29th Summer School and International Symposium on the Physics of Ionized Gases

Aug. 28 - Sep. 1, 2018, Belgrade, Serbia

CONTRIBUTED PAPERS

&

ABSTRACTS OF INVITED LECTURES, TOPICAL INVITED LECTURES, PROGRESS REPORTS AND WORKSHOP LECTURES

Editors:
Goran Poparić, Bratislav Obradović,
Duško Borka and Milan Rajković

Vinča Institute of
Nuclear Sciences

Serbian Academy
of Sciences and Arts

29th Summer School and International Symposium on the Physics of Ionized Gases

S P I G 2018

CONTRIBUTED PAPERS

&

ABSTRACTS OF INVITED LECTURES,
TOPICAL INVITED LECTURES, PROGRESS REPORTS
AND WORKSHOP LECTURES

Editors

Goran Poparić, Bratislav Obradović,
Duško Borka and Milan Rajković

Vinča Institute of
Nuclear Sciences

Serbian Academy
of Sciences and Arts

Belgrade, 2018

CONTRIBUTED PAPERS & ABSTRACTS OF INVITED LECTURES, TOPICAL INVITED LECTURES, PROGRESS REPORTS AND WORKSHOP LECTURES

of the 29th Summer School and International Symposium on the Physics of Ionized Gases

August 28 – September 1, 2018, Belgrade, Serbia

Editors:
Goran Poparić, Bratislav Obradović,
Duško Borka and Milan Rajković

Publisher:
Vinča Institute of Nuclear Sciences,
University of Belgrade,
P.O. Box 522,
11001 Belgrade, Serbia

Computer processing:
Tatjana Milovanov

Printed by
Skripta Internacional, Mike Alasa 54, Beograd

Number of copies
200

ISBN 978-86-7306-146-7

PREFACE

This publication contains the contributed papers and abstracts of Invited Lectures, Topical Invited Lectures, Progress Reports and Workshop Lectures that will be presented at the International Symposium on the Physics of Ionized Gases 2018. This is the 29th of a series of events which reflect the progress in this challenging field of science. The event is organized by the Vinča Institute of Nuclear Sciences in Belgrade and Serbian Academy of Sciences and Arts, with the support of the Ministry of Education, Science and Technological Development of the Republic of Serbia.

The aim of this book is to present new results in the fundamental and frontier theories and technology in the area of general plasma physics (including astrophysical and fusion plasmas), atomic collision processes and particle and laser beam interactions with solids. Also, the presented results and lectures of the 3rd Workshop on X-ray and VUV interaction with Biomolecules in Gas Phase - XiBiGP are also included.

Herein, the Editors would like to thank the authors and reviewers for their support of this event and to wish all participants a pleasant and productive stay in Belgrade. We are grateful to the Serbian Academy of Sciences and Arts for their long term commitment to support this event as well as the Serbian Ministry of Education, Science and Technological Development for their continuing help. We also acknowledge the support of the open access journal "Atom"

Editors: Goran Poparić, Bratislav Obradović,
Duško Borka and Milan Rajković

Belgrade, August 2018.

ACKNOWLEDGEMENT

29th SUMMER SCHOOL AND INTERNATIONAL SYMPOSIUM ON THE PHYSICS OF IONIZED GASES

is organized by

Vinča Institute of Nuclear Sciences, University of Belgrade, Serbia

and

Serbian Academy of Sciences and Arts

with the support of the

Ministry of Education, Science and Technological Development, Republic of Serbia

with the technical support of the

PANACOMP - Zemlja Čuda d.o.o.

and sponsored by:

Synchrotron SOLEIL
Institute of General and Physical Chemistry
Open Access Journal "Atom"

SPIG 2018

SPIG 2018 CONFERENCE TOPICS

Section 1.

ATOMIC COLLISION PROCESSES

- 1.1. Electron and Photon Interactions with Atomic Particles
- 1.2. Heavy Particle Collisions
- 1.3. Swarms and Transport Phenomena

Section 2.

PARTICLE AND LASER BEAM INTERACTION WITH SOLIDS

- 2.1. Atomic Collisions in Solids
- 2.2. Sputtering and Deposition
- 2.3. Laser and Plasma Interaction with Surfaces

Section 3.

LOW TEMPERATURE PLASMAS

- 3.1. Plasma Spectroscopy and Other Diagnostics Methods
- 3.2. Gas Discharges
- 3.3. Plasma Applications and Devices

Section 4.

GENERAL PLASMAS

- 4.1. Fusion Plasmas
- 4.2. Astrophysical Plasmas
- 4.3. Collective Phenomena

CONTENTS

Progress Reports

Contributed Papers

Section 2. PARTICLE AND LASER BEAM INTERACTIONS WITH SOLIDS

Invited Lecture

Topical Invited Lectures

Progress Reports

Contributed Papers

Section 3. LOW TEMPERATURE PLASMAS

Invited Lectures

Topical Invited Lectures

Progress Reports

Contributed Papers

Progress Reports

Contributed Papers

The Workshop on X-ray Interaction with Biomolecules in Gas Phase (XiBiGP)

Section 1.

ATOMIC COLLISION PROCESSES

USING X-RAYS TO LOOK AT QUANTUM MECHANICS IN ATOMS, MOLECULES AND CLUSTERS

John D. Bozek

Synchrotron SOLEIL
L'Orme des Merisiers, Saint-Aubin-BP 48, 91192 Gif-sur-Yvette, France

Since Roentgen first discovered mysterious rays emanating from his cathode ray tube in 1895 [1], x-rays have been a tool for scientific discovery and technological development. The rate of improvement in the brightness of x-ray sources was greatly enhanced in the 1960's with the development of synchrotron radiation light sources. More recently, around 2010, accelerator based x-ray free electron lasers (XFELs) were developed leading to a further increase in the rate of improvement in x-ray brightness.

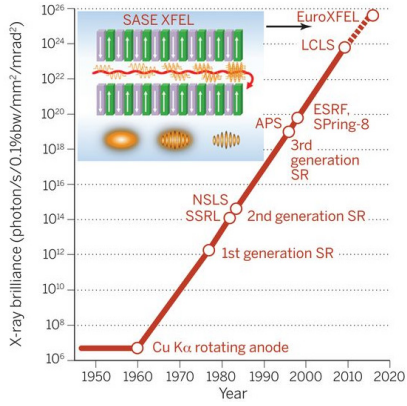

Figure 1. Development of the brightness of x-ray sources from x-ray tubes, to synchrotrons, to XFELs. From [2].

These technological developments in x-ray sources have resulted in an equally astonishing improvement in our ability to measure the physical and electronic structure of the matter that makes up our world as will be discussed in this talk.

REFERENCES

[1] O. Glasser, Am. J. Roentgenol **165**, 1033 (1995).
[2] J. Miao, T. Ishikawa, I.K. Robinsons and M.M. Murnane, Science **348**, 530 (2015).

ELECTRON-INDUCED CHEMISTRY IN THE CONDENSED PHASE

Jan Hendrik Bredehöft

University of Bremen, Institute for Applied and Physical Chemistry (IAPC), Leobener Str.5, 28359 Bremen, Germany

A lot of our knowledge about the interaction of electrons with atoms and molecules come from experiments using either crossed-beam experiments or observation and modelling of plasmas. In these situations, spectroscopic tools have allowed us to study electron-molecule interactions with high resolution and precision. In recent years, more and more studies have been undertaken that look at the role of electrons in chemical processes. These range from industrial applications such as e-beam curing of polymers [1], the writing of small structures on surfaces using tools such as focused electron beam induced deposition (FEBID) [2], understanding radiation damage to biological tissues [3], all the way to chemical processes on the surface of interstellar dust grains and comets [4]. All these studies have one thing in common: They are aimed at chemical transformations in condensed-phase samples. The host of available cross-sectional data for electron-induced processes in the gas phase are, however, not always applicable to these problems. Any process that produces at least one ion will have significantly different energy dependence due to the stabilization of charged particles in the condensed-phase matrix. Number densities of molecules are also orders of magnitude higher so that reactive species will only serve as short-lived intermediates to more stable products, making the observation of primary electron-molecule interaction products extremely difficult if not outright impossible. In order to further develop applications and to understand electron-driven chemical processes, a lot of experimental work is thus needed.

I will present recent work on the formation of small organic molecules in astrochemical settings that serve as examples for the challenges and rewards that electron-driven chemistry in the condensed phase offers.

REFERENCES

[1] C. E. Hoyle, J. F. Kinstle, *Radiation curing of polymers*, (ACS Publications, Washington DC, 1990).
[2] I. Utke, P. Hoffmann, J. Melngailis, J. Vac. Sci. Technol. B 26, 1197 (2008)
[3] P. Swiderek, Angew. Chem. Int. Ed. 45, 4056 (2006) and references therein
[4] K. I. Öberg, Chem. Rev. 116(17), 9631 (2016)

KINETIC AND FLUID MODELLING OF CHARGED-PARTICLE TRANSPORT IN GASES AND LIQUIDS AND THE GAS-LIQUID INTERFACE

R. D. White[1], D. Cocks[1,2], G. Boyle[1], M. Casey[1], N. Garland[1], D. Konovalov[1], J. de Urquijo[3], M. J. Brunger[2], R. P. McEachran[4], S. J. Buckman[4], S. Dujko[5], Z. Lj. Petrovic[5]

[1]*College of Science and Engineering, James Cook University, Australia*
[2] *School of Chemical and Physical Sciences, Flinders University, Australia*
[3] *Research School of Physics and Engineering, The Australian National University, Australia*
[4]*Instituto de Ciencias Físicas, Universidad Nacional Autónoma de México, 62251, Cuernavaca, Mor., México*
[5]*Institute of Physics, University of Belgrade, Serbia*

Modelling of electron transport in plasma-liquid interactions requires an accurate treatment of electron transport in the gaseous and soft-condensed phases, together with an understanding of the electron transport across the gas-liquid interface. In this presentation we present progress on an ab-initio formalism for electron transport in liquids through appropriate generalisations of Boltzmann's equation to account for spatio-temporal scattering correlations, screening of the electron potential and the effects of (self-) trapping. Application is considered for various atomic liquids as a starting benchmark to consider more complex polar liquids [1]. A consequent high order fluid model has been developed to consider non-local electron transport in liquids and gas-liquid interfaces In particular the explicit density effects across the gas-liquid interface have been considered including its impact on collisional processes and background energy/fields [2,3]. Propagation of ionization fronts between the gas and liquid phases are considered.

REFERENCES

[1] R. D. White, et al, Plasma Sources Sci. Technol. 27, 053001(2018)
[2] N. A. Garland, et al, Plasma Sources Sci. Technol. 27, 024002 (2018)
[3] N. A. Garland, et al, Plasma Sources Sci. Technol. 26 075003 (2017)

CAVITY-ENHANCED PHOTODETACHMENT OF H^- AS A MEANS TO PRODUCE ENERGETIC NEUTRAL BEAMS FOR PLASMA HEATING

Christophe Blondel[1], David Bresteau[2,†] and Cyril Drag[1]

[1]Laboratoire de Physique des plasmas, Centre national de la recherche scientifique, École polytechnique, F-91128 Palaiseau cedex, France
[2]Laboratoire Aimé Cotton, Centre national de la recherche scientifique, université Paris-sud, F-91405 Orsay cedex, France
[†]present address : LIDyL, Commissariat à l'énergie atomique et aux énergies alternatives, F-91191 Gif-Sur-Yvette Cedex, France

Neutral beam injection, for plasma heating, will supposedly be achieved, in ITER, by collisional detachment of a pre-accelerated D^- beam. Collisional detachment however makes use of a D_2-filled neutralisation chamber, which has severe drawbacks, including the necessity to set the D^- ion source at -1 MV.

Photodetachment, as a neutralisation method, would have several advantages, including the absence of gas injection, and the possibility to set the ion source close to the earth potential. Photodetachment however requires a very high laser flux. The presented work has consisted in implementing an optical cavity, with a finesse greater than 3000, to make such a high illumination possible with a state-of-the-art CW laser. A 1.2 keV H^- beam (only 20 times slower than the D^- ion beams to be prepared for ITER) was photodetached with a more-than-50% efficiency, with only 24 W of CW laser input. This experimental demonstration paves the way for developing real-size photoneutralizers, based on the implementation of refolded optical cavities around the ion beams of neutral beam injectors. Possible architectures will be examined at the conference.

Acknowledgements: This work was supported by grant ANR-13-BS04-0016-01 of the French *Agence nationale de la recherche*. It was also carried out within the framework of the *Eurofusion* consortium and has received funding from the *Euratom* research and training programme 2014-2018 under grant agreement No. 633053. The views and opinions expressed herein do not necessarily reflect those of the European Commission.

REFERENCE

D. Bresteau, C. Blondel & C. Drag, Rev. Sci. Instrum **88** (2017) 113103 (10 pp).

SYNCHROTRON RADIATION VUV ANGLE-RESOLVED PHOTOELECTRON SPECTROSCOPY ON FREE NANO-SYSTEMS

Dušan K. Božanić[1,2], Gustavo Garcia[1] and Laurent Nahon[1]

[1]*Synchrotron SOLEIL, L'Orme des Merisiers, St. Aubin, BP48, 91192 Gif sur Yvette, France*
[2]*Vinča Institute of Nuclear Sciences, University of Belgrade, P.O. Box 522, 11001 Belgrade, Serbia*

As intermediates between molecules and macroscopic matter, nanometer-sized objects exhibit specific and size-dependent properties. However, due to difficulties in their manipulation, the results of the conventional investigations are unavoidably linked to the nature of the substrates on which they are deposited. In this lecture, we will present the results of the vacuum-ultraviolet angle-resolved photoelectron spectroscopy (VUV ARPES) studies on isolated nano-systems, including metal nanoparticle aggregates conducted at the DESIRS beamline of Synchrotron SOLEIL. The influence of size, morphology and optical properties of a nano-system on the photoelectrons' angular distribution will be demonstrated and rationalized in terms of size-dependent photoabsorption and photoelectron transport.

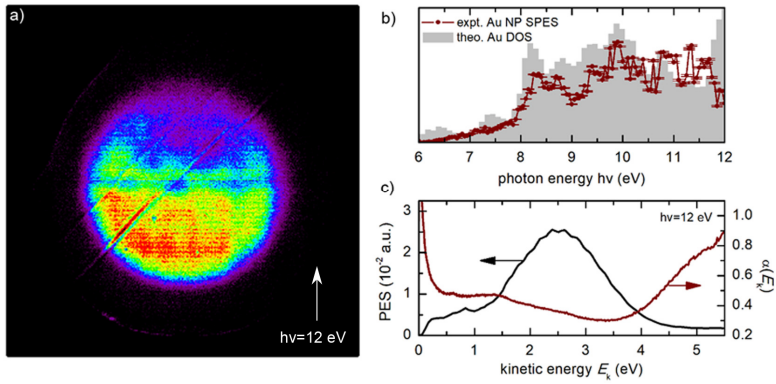

Figure 1. a) Photoelectron image showing a forward/backward anisotropy, b) slow photoelectron spectrum (SPES), and c) photoemission spectrum (PES) of gold nanoparticle aggregates. The dependence of the anisotropy parameter α, indicative of angular photoelectron distribution, on the kinetic energy is demonstrated in figure c).

THEORETICAL AND EXPERIMENTAL RESEARCH OF IONIC STATES OF ATOMS WITH MULTIELECTRON COINCIDENCE DETECTION

K. Jänkälä[1], F. Penent[2], J. Palaudoux[2], M. A. Khalal[2], J. Keskinen[1], D. Cubaynes[3], J.-M. Bizau[3], L. Andric[2] and P. Lablanquie[2]

[1]*Nano and Molecular Systems Research Unit, University of Oulu, 90014 Oulu, Finland* [2]*Sorbonne Universités, UPMC Université Paris 06, CNRS, LCP-MR (UMR 7614), 11 rue Pierre et Marie Curie, 75231 Paris Cedex 05, France* [3]*ISMO, Centre National de la Recherche Scientifique UMR 8214, Université Paris-Sud/Paris-Saclay, 91405 Orsay, France*

Nowadays it is understood that interaction between a photon and an atom can lead to emission of more than one electron. The emission can take place in a step-wise decay, i.e. Auger cascade, or via simultaneous processes such as direct many-electron photoemission or Auger decay. Simultaneous detection of these electrons emitted from a single photoionization event provides novel means to probe the electronic structure and dynamics of matter in neutral and ionic states. It can be used to, for example, gain access to exotic initial states [1], select initial ionic states [2, 3] or study many-electron interactions [4]. In this presentation an overview to the concept and main ideas of this research direction will be given with discussion of our recent results. The experimental works are carried out using a magnetic-bottle time-of-flight type electron energy analyzer that is capable of detecting up to seven electrons emitted from a single ionization event. The results are analyzed with modern atomic and molecular simulations.

REFERENCES

[1] J. Keskinen, *et. al.*, Phys. Rev. A 95, 043402 (2017).

[2] S.-M. Huttula, *et. al.*, Phys. Rev. Lett. 110, 113002 (2013).

[3] M. A. Khalal, *et. al.*, Phys. Rev. A 96, 013412 (2017).

[4] P. Lablanquie, *et. al.*, J. Elsp. 220, 125 (2017).

MAGNETIC FIELD CONTROL OF THE QUANTUM ENTANGLEMENT IN TWO-ELECTRON ARTIFICIAL ATOMS

R.G. Nazmitdinov[1], N. S. Simonović[2]

[1] *BLTP, Joint Institute for Nuclear Research, 141980 Dubna, Russia*
[2] *Institute of Physics, University of Belgrade, 11001 Belgrade, Serbia*

A few-electron quantum dots (QDs), so called "artificial atoms", attract an enormous experimental and theoretical attention [1]. It is expected that QDs could lead to novel device applications in fields such as quantum cryptography and information storage. It is also widely believed that the entangled states of electrons confined in a QD may give a natural realization of a quantum bit or qubit [2]. However, an entanglement being one of the most subtle and intriguing phenomena in nature is not yet well understood [3]. The questions how to efficiently produce and control it, for example, in QDs are among fundamental as well as technological problems.

In this contribution we discuss quantum entanglement in two-electron axially symmetric quantum dots under a perpendicular magnetic field. In particular, we focus on the entanglement variation at the transition from interacting to noninteracting particle regimes. The analytical expression for the entanglement measure based on the linear entropy is derived in the limit of noninteracting electrons. It reproduces remarkably well the numerical results for the lowest states with the magnetic quantum number $M \geq 2$ in the interacting regime. A method to estimate the experimental value of the entanglement of the ground state, with the aid of the magnetic field dependence of the addition energy, is proposed.

REFERENCES

[1] J.L. Birman, R.G. Nazmitdinov, and V.I. Yukalov, Phys. Rep. 526, 1 (2013).

[2] R. Hanson, L. P. Kouwenhoven, J. R. Petta, S. Tarucha, and L. M. K. Vandersypen, Rev. Mod. Phys 79, 1217 (2007).

[3] L. Amico, R. Fazio, A. Osterloh, and V. Vedral, Rev. Mod. Phys 80, 517 (2008).

MODIFICATIONS OF 2D-MATERIAL-ORGANIC THIN FILMS HETEROSTRUCTURES PRODUCED BY MONOENERGETIC ELECTRON BEAM

Radmila Panajotović and Jasna Vujin

Graphene Lab, Center for solid state physics and new materials, Institute of Physics, Pregrevica 118, 11080, Belgrade, Serbia

An extensive use of 2D-materials as solid support for organic materials, either as a base for electronic devices, such as organic Field-Effect Transistors, or scaffolds for growing organ tissue for implants, is not accidental. Graphene, MoS_2, WS_2, MgB_2, and quite recently hematene are extraordinary useful as mechanically resistant and allegedly non-toxic thin films with tunable electric properties. In biochemical sensors, interactions of various chemical agents with the 2D-material substrate change their electrical properties and can produce an electrical signal that corresponds to the concentration of molecules on their surface. Therefore, the molecular binding and charge transfer in these devices is governed by the chemical and electrical properties of the interface, as well as by its homogeneity and roughness.The same applies to the growth of organic tissue.
In our experiment we used the Scanning Electron Microscope (SEM) to modify the electrostatic status of thin lipid/graphene and lipid/WS_2 films. We showed that the SEM beam tuned to its typical values of power and energy for imaging organic samples could be used as a lithography tool for electrical and chemical modification of lipid/2D-material heterostructures, without inducing significant changes in the morphology of the surface.

Acknowledgements:

This work is supported by the Ministry of education, science and technological development of the Republic of Serbia under the grant IO 171005. We thank Mr. Vladimir Lazović for the technical help with the use of Scanning Electron Microscope.

REFERENCES

[1] Ann E. Oliver, Atul N. Parikh, Biochimica et Biophysica Acta, 1798, 839-850 (2010)
[2] Nathaniel S. Green, Michael L. Norton, Analytica Chimica Acta, 853, 127-142 (2015)
[3] Yuqing Wang, Yi Feng, Yangming Chen, Fei Mo, Gang Qian, Dongbo Yu, Yang Wang and Xuebin, Zhang, Phys.Chem.Chem.Phys, 17, 2678 (2015)

PECD ON CHIRAL AMINO-ACIDS

Rim Hadidi[1], Dusan Bozanic[1], Gustavo Garcia[1], Ivan Powis[2] and Laurent Nahon[1]

[1]*Synchrotron SOLEIL, St. Aubin BP 48, 91192 Gif sur Yvette, France*
[2]*School of Chemistry, University of Nottingham (Nottingham, UK)*

Photoelectron circular dichroism (PECD) is a chiroptical effect which manifests itself as a forward/backward asymmetry in the photoelectron angular distributions (PADs) of a chiral molecule with respect to the light's propagation axis when using circularly polarized light to ionize pure enantiomers.
PECD is highly sensitive to molecular structures (isomers, conformers, clusters, chemical substitution and vibrations…) and absolute configuration (and of course enantiomeric excess) [1]. (PECD) may shed light on the electronic and molecular structures of elementary bricks of life such as amino-acids in the gas phase. In addition PECD has been advanced as a symmetry-breaking astrophysical scenario which could therefore have a link with the origin of homochirality of life [2].

In the present work we studied over the VUV range the PECD of Proline (Pro) which is the only naturally occurring amino acid containing a pyrrolidine ring. Several temperatures were used to vary the conformer population of the nascent Pro in order to perform a comprehensive conformer analysis of the PECD with the help of ongoing CMS-Xα PECD calculations.
A large electron asymmetry of 12%, associated to the production of parent Pro ion, was found at the Lyman α (10.2 eV) energy, that is 3 times larger than the previous result on Alanine [4] but interestingly of the same sign, which strengthens the astrobiological scenario. Moreover we observed different spectral features and chiral electron asymmetries for the different types of Proline conformers which are formed.
We will highlight the observed marked conformer-specific fragmentation as well as the overall conformer population effect on PECD.

REFERENCES

[1] For a review see L. Nahon, G. A. Garcia, and I. Powis, J. Elec. Spec. Rel. Phen. 204, 322 (2015).
[2] M. Tia, B. C. de Miranda, S. Daly, F. Gaie-Levrel, G. A. Garcia, I. Powis, and L. Nahon, J. Phys. Chem. Lett. 4, 2698 (2013); R. Hadidi, D. K. Bozanic, G. A. Garcia, and L. Nahon, Advances in Physics X (2018). DOI: 10.1080/23746149.2018.1477530
[3] F. Gaie-Levrel, G. A. Garcia, M. Schwell and L. Nahon, Phys. Chem. Chem. Phys. 13, 7024 (2011).
[4] M. Tia, B. C. de Miranda, S. Daly, F. Gaie-Levrel, G. A. Garcia, L. Nahon, and I. Powis, J. Phys. Chem. A118, 2765 (2014).
[5] F. Fathi and H. Farrokhpour, ,Chem. Phys. Lett. 565, 102 (2013)

A CHEMICAL UNDERSTANDING OF THE LIMITED SITE-SPECIFICITY IN MOLECULAR INNER-SHELL PHOTOFRAGMENTATION

Ludger Inhester[1], Bart Oostenrijk[2], Minna Patanen[3], Esko Kokkonen[3], Stephen H. Southworth[4], Christoph Bostedt[4], Oksana Travnikova[5], Tatiana Marchenko [5], Sang-Kil Son [1], Robin Santra [1], Marc Simon [5], Linda Young [4] and Stacey L. Sorensen [1]

[1] *Center for Free-Electron Laser Science (DESY), Hamburg, Germany*
[2] *Department of Physics, Lund, Sweden*
[3] *Faculty of Science, Oulu, Finland*
[4] *Argonne National Laboratory, Lemont, USA*
[5] *LCPMR (CNRS), Paris, France*
bart.oostenrijk@sljus.lu.se

In many cases fragmentation of molecules upon inner-shell ionization is very unspecific with respect to the initially localized ionization site. Often this finding is interpreted in terms of an equilibration of internal energy into vibrational degrees of freedom after Auger decay. Here we investigate the x-ray photofragmentation of ethyl trifluoroacetate upon core electron ionization at environmentally distinct carbon sites using photoelectron-photoion-photoion coincidence measurements and ab-initio electronic structure calculations. For all the 4 carbon ionization sites, the Auger decay weakens the same bonds and transfers the two charges to opposite ends of the molecule, which leads to a rapid dissociation into 3 fragments followed by further fragmentation steps. The lack of site-specificity is attributed to the character of the dicationic electronic states after Auger decay, instead of a fast equilibration of internal energy.

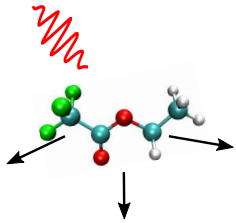

Figure 1. Visual representation of the process under study: does core ionization of different carbon atoms lead to a different breakup?

FORMATION OF SILVER NANOPARTICLES INTO SILICON WITH MASK-ASSISTED ION IMPLANTATION PROCESS

M. Novaković[1], A. Modrić-Šahbazović[2], E. Schmidt[3], I. Gazdić[2], V. Đokić[4], C. Ronning[3], N. Bibić[1] and Z. Rakočević[1]

[1]*University of Belgrade, Institute of Nuclear Sciences VINČA, 11351 Belgrade, Serbia*
[2]*University of Tuzla, Faculty of Natural Sciences and Mathematics, 75000 Tuzla, BiH*
[3]*Institute of Solid State Physics, Friedrich Schiller University Jena, Max-Wien-Platz 1, D-07743 Jena, Germany*
[4]*University of Belgrade, Faculty of Technology and Metallurgy, 11120 Belgrade, Serbia*

Mask-assisted ion beam processing of insulating substrates is a versatile tool for achieving nanopatterning of a material through the formation of ordered nanostructures. The possibility of producing self-assembled monolayers of nanospheres with size in the 100–1000 nm range on the substrate to be patterned can be considered a much simpler and cheaper alternative to conventional lithographic techniques. This paper reports on a nanostructuring of Si(100) wafers by means of 60 keV Ag ions implantation through self-organized polystyrene (PS) mask, consisting of ~150 nm diameter spheres. Different fluences were applied up to 2×10^{16} ions/cm^2 in order to create a distribution of different sizes and densities of buried metal nanoparticles. The characterization of the samples was done by Rutherford backscattering spectrometry, scanning electron microscopy, cross-sectional transmission electron microscopy and spectroscopic ellipsometry. It is demonstrated that the Ag is implanted into the Si only through the PS mask openings, thus forming a regular array of amorphized regions over the wide area of silicon substrate. These fragments are of the similar dimensions of about 190 nm width and 60 nm in depth. At the subsurface region of the implanted fragments, Ag nanoparticles are formed. Due to the formation of metal nanoparticles the optical spectra of the samples show a strong absorption peak in the long-wavelength region of 689.3-745.3 nm, characteristic for the surface plasmon resonance (SPR) excitations. The shift of SPR peak position was discussed based on the PS mask deformation and silver concentration.

DEVELOPMENT OF ELECTRON IMPACT IONIZATION SPECTROMETER

M. M. Vojnović[1], M. M. Ristić[2] and G. B. Poparić[1]

[1]*University of Belgrade, Faculty of Physics, Belgrade, Serbia*
[2]*University of Belgrade, Faculty of Physical Chemistry, Belgrade, Serbia*
e-mail: mvojnovic@ff.bg.ac.rs

Experimental setup containing an electron spectrometer and a time-of-flight mass spectrometer has been built for the purpose of measurement of electron-impact ionization cross sections and dissociative attachment cross sections. The device has been constructed in the conventional orthogonal arrangement of the two spectrometers and so far it has been successfully tested for positive ion detection.
Another similar composite spectrometer planned for ionization cross section measurements is under construction. This new spectrometer is peculiar in that it would work in a novel arrangement type – inline configuration of electron spectrometer and time-of-flight mass spectrometer, whereby ions are detected in the direction of electron motion. Positive ion detection would be performed. Electrons are collected on a grounded grid placed in front of the detector, which also serves to minimize penetration of the electric field from the detector into the mass analyzer. Electrons that pass through the grid are prevented from entering channeltron detector by a high negative voltage on its entrance. We expect the inline spectrometer arrangement to provide total ion collection, therefore much better detection efficiency than orthogonal setup.

Acknowledgements: This work is partially supported by the Ministry of Education, Science and Technological Development of the Republic of Serbia by the Project No. 171016.

STRONG FIELD MULTIPHOTON IONIZATION OF LITHIUM

A. Bunjac, D. B. Popović and N. S. Simonović

Institute of Physics, University of Belgrade, P.O. Box 57, 11001 Belgrade, Serbia

Abstract. Multiphoton ionization of lithium by 30 fs laser pulses of 785 nm wavelength is studied using a single-electron model where the valence electron moves in an effective core potential and in the external electromagnetic field. The photoelectron momentum distributions and energy spectra are calculated for several field strengths by numerically solving the time-dependent Schrödinger equation. Besides the nonresonant multiphoton ionization, which is the dominating process, structures related to the above threshold ionization are observed in the spectra. The present results are in good agreement with recent experimental and theoretical results.

1. THEORETICAL MODEL

The study of multiphoton ionization (MPI) of atoms, which has a much lower probability than the corresponding single-photon process, became experimentally accessible in last decades after appearance of a new generation of high intensity lasers. The MPI manifests itself as nonresonant multiphoton ionization (NRMPI), above threshold ionization (ATI) and resonantly enhanced multiphoton ionization (REMPI). The theoretical study of such strong field processes exclude any perturbative treatment, that is a valid approach in describing the single-photon ionization. Here we study the MPI of the lithium atom in strong laser fields using a single-electron approximation and solving numerically the time-dependent Schrödinger equation. The calculated photoelectron momentum distributions and energy spectra are compared with recently published experimental and theoretical results [1].

Within the single-electron model and the frozen core approximation the dynamics of the valence (active) electron of lithium atom in an alternating electric field $F(t)$ is described by Hamiltonian (in atomic units)

$$H = \frac{\mathbf{p}^2}{2} + V_{\mathrm{core}}(r) - F(t)z. \tag{1}$$

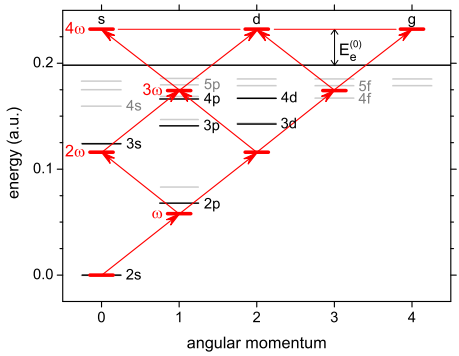

Figure 1. Energy scheme of lithium showing the lowest excited states (black lines - experimental values, gray lines - eigenenergies of pseudopotential (2)) and possible four-photon absorption pathways from the ground state to continuum in the case of laser of 785 nm wavelength ($\omega = 0.05804$ a.u.).

The effective core potential $V_{\text{core}}(r)$ describes the interaction of the valence electron with the atomic core (inner electrons + atomic nucleus). For this purpose we use the Hellmann's pseudopotential [2]

$$V_{\text{core}}(r) = -\frac{1}{r} + \frac{A}{r}\, e^{-ar}. \tag{2}$$

The parameters $A = 34$ and $a = 3.14331$ [3] provide the correct value for the ionization potential of lithium $I_{\text{p}} = 5.3917\,\text{eV} = 0.19814\,\text{a.u.}$ and reproduce approximately the energies of singly-excited states (see Fig. 1). Unfortunately, for lithium it is not possible to find a set of parameters providing sufficiently good agreement with experimental values for s and p states simultaneously. In this case the parameters are chosen to get the best agreement for s states.

We consider a linearly polarized laser pulse of the form

$$F(t) = F_{\text{peak}} \sin^2(\pi t/T_{\text{p}}) \cos(\omega t), \quad 0 < t < T_{\text{p}} \tag{3}$$

(otherwise $F(t) = 0$). Here ω, F_{peak} and T_{p} are the frequency of laser field, the peak value of its electric component and the pulse duration, respectively. Due to the axial symmetry of the system, the magnetic quantum number m of the valence electron is a good quantum number for all values of F (in contrast to the orbital quantum number l). Since the ground state of the field-free lithium atom is characterized by $l = m = 0$, we set $m = 0$ also for $F \neq 0$.

The photoionization process is simulated by calculating the evolution of the wave function of valence electron $\psi(\mathbf{r}, t)$, which is initially ($t = 0$) chosen to be the lowest eigenstate of Hamiltonian (1) (then $F = 0$) that describes the lithium ground state. The evolution is calculated by numerically

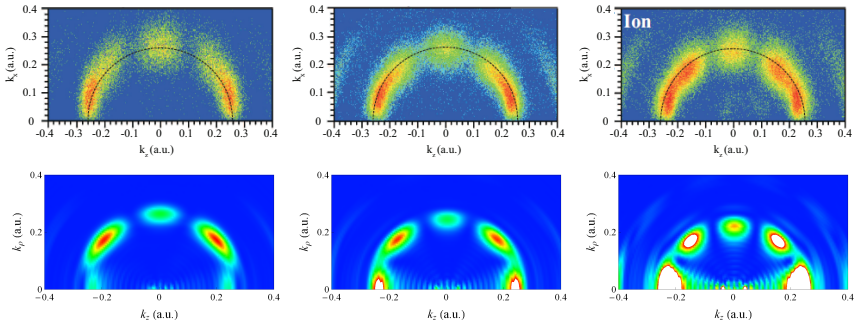

Figure 2. Photoelectron momentum distribution parallel (longitudinal) and transversal (perpendicular) to the polarization direction of 785 nm wavelength laser with 30 fs pulse duration and three different intensities (left: $I = 8 \times 10^{11}$ W/cm^2, middle: $I = 2 \times 10^{12}$ W/cm^2, right: $I = 4 \times 10^{12}$ W/cm^2). Top: experimental data obtained by recoil-ion momentum detection [1]. Bottom: calculated distribution $|\bar{\psi}(\mathbf{k}, t)|^2$ at $t = 1500$ a.u. Dashed semicircle denotes the nominal position of the four-photon line.

integrating the time-dependent Schrödinger equation [4]. The photoelectron momentum distribution (PMD) is obtained from the Fourier transform of the wave function at $t > T_p$ (PMD $\sim |\bar{\psi}(\mathbf{k}, t)|^2$).

2. RESULTS

Using the described model we study the photoionization of the lithium atom by a 785 nm ($\omega = 0.05804$ a.u., $\hbar\omega = 1.5794$ eV) laser pulse of the form (3) with three values of the peak intensities and 30 fs duration ($T_p = 1240$ a.u.) and compare our numerical results with recent experimental and numerical results obtained by Schuricke *at al* [1]. The energy level diagram (Fig. 1) illustrates that from the ground state (2s) at least four photons of energy 1.5794 eV are required to reach the continuum. In the low-intensity regime the NRMPI is the dominating process and the expected excess energy of the photoelectrons is $E_e^{(0)} = 0.03403$ a.u. (0.926 eV).

Fig. 2 shows the experimental (top) and calculated (bottom) momentum distributions for three values of the laser field strength. The nodal structure of the observed distributions can be related to superpositions of the accessible emitted partial waves. In the case of four-photon absorption s, d and g partial waves can be emitted (see Fig. 1). Both the experimental and calculated distribution indicate that the d partial wave (two nodes) is dominant at lower laser intensities, whereas the g partial wave is dominant (four nodes) at higher intensities. As expected, the distribution maxima are approximately located at semicircles of radius $k_e^{(0)} = (2E_e^{(0)})^{1/2} = 0.2609$ a.u.

Besides NRMPI, already for the lowest intensity considered here, the ATI, i.e. five-photon absorption, can be identified at the radius $k_e^{(0)\prime} =$

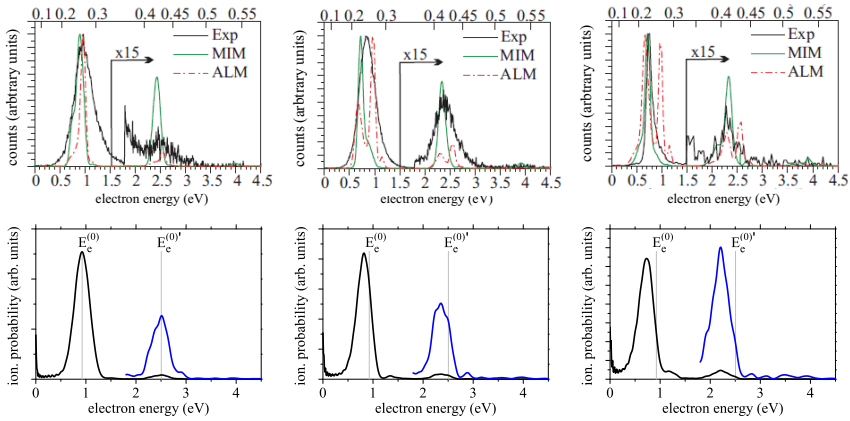

Figure 3. Photoelectron energy spectra extracted from the experimental and theoretical momentum data shown in Fig. 2 (left: $I = 8 \times 10^{11}\,\mathrm{W/cm^2}$, middle: $I = 2 \times 10^{12}\,\mathrm{W/cm^2}$, right: $I = 4 \times 10^{12}\,\mathrm{W/cm^2}$). Top: Results by Schuricke *et al* [1]. Bottom: Present calculations. The count rates and probabilities for energies $E > 0.18\,\mathrm{eV}$ are multiplied by 15.

$(2E_e^{(0)\prime})^{1/2} = 0.4291\,\mathrm{a.u.}$ $(E_e^{(0)\prime} = E_e^{(0)} + \hbar\omega = 2.5054\,\mathrm{eV})$. In this case p, f and h partial waves can be emitted. The corresponding ATI semicircle contains five nodes which is a feature of h waves.

The photoelectron energy spectrum is obtained by averaging the probability distribution $|\bar{\psi}(\mathbf{k}, t)|^2$ at a time $t > T_p$ along semicircles $k_\rho^2 + k_z^2 = 2E_e$ corresponding to different photoelectron excess energies E_e. The spectra at three values of the field strength, with clearly visible NRMPI and the first ATI peaks, are shown in Fig. 3. The difference between the NRMPI and ATI peak positions and $E_e^{(0)}$ and $E_e^{(0)\prime}$ values, respectively, can be attributed to the dynamic Stark shift.

Acknowledgements

This work was supported by the COST Action No. CM1204 (XLIC). We acknowledge support from the Ministry of Education, Science and Technological Development of Republic of Serbia under Project No. 171020.

REFERENCES

[1] M. Schuricke et al, Phys. Rev. A **83**, 023413 (2011).
[2] H. Hellmann, J. Chem. Phys. **3**, 61 (1935).
[3] M. Z. Milošević and N. S. Simonović, Phys. Rev. A **91**, 023424 (2015).
[4] A. Bunjac, D. B. Popović and N. S. Simonović, Phys. Chem. Chem. Phys. **19**, 19829 (2017).

HIGH RESOLUTION AUTOIONIZING STATES OF KRYPTON IN KINETIC ENERGY REGION 8 – 35 eV

Bratislav P. Marinković[1], Jozo J. Jureta[1] and Lorenzo Avaldi[2]

[1]Institute of Physics Belgrade, University of Belgrade, Laboratory for Atomic Collision Processes, Pregrevica 118, 11080 Belgrade, Serbia
[2]CNR-Istituto di Struttura della Materia, Area della Ricerca di Roma 1, CP10, 00015 Monterotondo Scalo, Italy

Abstract. High resolution electron spectroscopy has been used to investigate the spectra of ejected electrons of krypton at 90° ejection angle in the kinetic energy region 7.8-36 eV at high incident electron energies of 505 and 2019 eV. The energies of the observed features have been compared with previous experiments and a good agreement has been found.

1. INTRODUCTION

The measurement of the ejected electron spectra produced by the decay either of an excited state of a neutral atom to the ground or excited state of the singly charged ion (autoionizing transitions) or of an inner shell ionized atom to the states of the doubly charge ion (Auger transition) is one of the most suited methods to reconstruct the electronic structure of an atom. In this work, we present high resolution ejected electron spectra of krypton in the region of the autoionizing transitions between 7.8 and 24 eV and in the low energy MNN Auger region between 24 and 35 eV and compare them with previous electron impact studies.

Kr ejected electron spectra have been reported by Siegbahn *et al* (1971) [1] and Tweed *et al* (1976) [2], while Srivastava and Trajmar (1978) [3] and Baxter et al (1982) [4] measured electron energy loss spectra. The Kr MNN Auger spectra have been studied by Werme *et al* (1972) [5]. Kikas *et al* (1996) [6] made an extensive investigation of Kr^+ satellite spectrum by photoelectron spectroscopy.

2. EXPERIMENT

The apparatus used in the present measurements has been described previously [7], thus only a brief report is presented here. It consists of a non-monochromatic electron gun (10-2500 eV) which can rotate from 10^o to 130^o around the analyzer axis, and a high - resolution hemispherical analyzer with a

mean radius of 125 mm. The ejected electrons are detected with seven channeltrons. A 20 mm long platinum-iridium non-biased needle with internal diameter of 0.5 mm has been used to produce an atomic beam in the perpendicular direction to the scattering plane.

The background pressure in the vacuum chamber was $6x10^{-8}$ mbar, while the working pressure with krypton gas was $2x10^{-6}$ mbar. With an electron current of about 10^{-6} A the typical accumulation time for most of the spectra was 60 min with energy step of 0.020 or 0.050 eV per channel. The transmission was not uniform in low energy part and all spectra are presented with subtracted background without any further normalization of the data. The calibration of the kinetic energy scale was achieved using the line at 11.72 eV from the Ar [$3s3p^6 3d(^1D)$] excited state (27.48 eV excitation energy). The scale of the incident energies was calibrated using the elastic channel. For higher energies until 2000 eV, the fit made below 200 eV was applied. The FWHM of the elastic peak was roughly 0.80 eV.

3. RESULTS AND DISCUSSION

Figure 1 shows two high resolution ejected electron spectra obtained at 505 and 2019 eV at 90°. The spectrum at 2019 eV is obtained with energy step of 0.020 eV at lower statistics, while the spectrum at 505 eV with energy step of 0.050 eV has been recorded with better statistics. Despite this both spectra display the same number of features produced by the decay of single and double excited states with $4s4p^6nl$ and $4s^24p^4nln'l'$configurations to Kr^+ states. The spectrum can be divided in two regions: one due to the decay of the $4s4p^6nl$ singly excited states converging to the 4s ionization threshold and another one above this threshold where the decay of neutral doubly excited and satellite states contribute. In the first region the most pronounced features are due to the decay of the $5s(^3S_1)$, $4d(^1D_1)$ and $5d(^1D_1)$ states at 9.44 eV, 11.58 eV and 12.48 eV respectively. Above the 4s ionization threshold, the prominent features are due to the $4s^24p^4$ excited ionic states: the $(^3P)5s\ ^2P_{3/2}$, $(^1D)5s\ ^2D_{5/2}$ and $(^3P)4d\ ^2D_{5/2}$ at 28.70 eV, 29.86 eV and 31.06 eV, respectively. A good agreement among measurements is achieved, but still large number of features stayed unassigned. A detailed analysis will be presented at the conference.

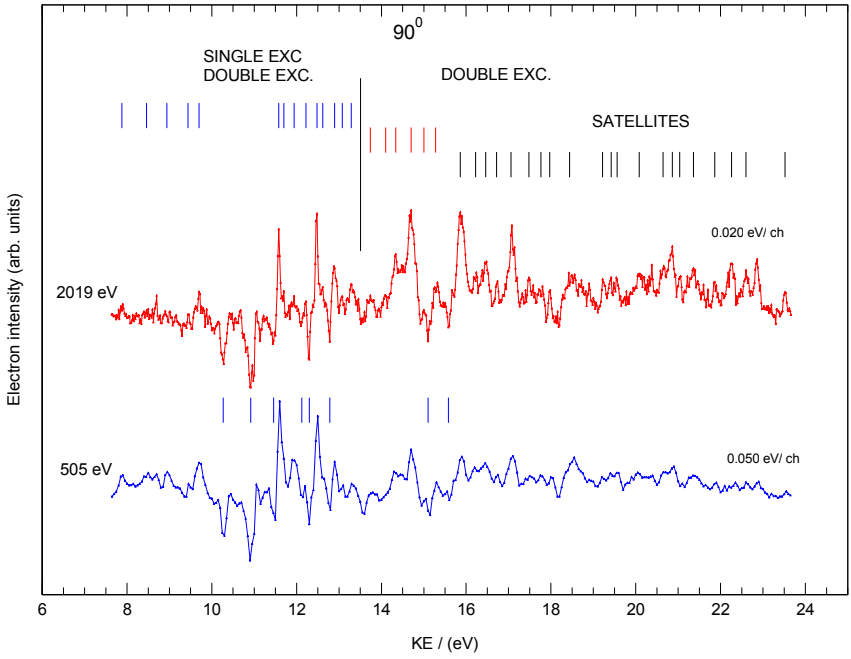

Figure 1. Ejected electron spectra obtained between 7.8 and 24 eV. The energies of the peaks are indicated by short bars on the top spectrum, while the ones of the dips by the bars between two spectra. The vertical line shows the limit of the $4s4p^6nl$ series.

Figure 2 shows low energy part of the Kr MNN Auger spectra with features labeled from 1 to 20 measured at 505 and 2019 eV incident energy and angle of 90°. The present spectra well compare with the one by Werme *et al* (1972) [6], although a different approach in calibration procedure leads to a systematic difference in energies of about 0.150-0.170 eV. Both Auger transitions and their satellites contribute to the observed spectra. The first two features at 24.16 and 25.42 eV are due to transitions from the initial vacancies in the $3d_{5/2,3/2}$ (M_5 and M_4) with the final $4s^24p^3(^2P)6s\ ^1P_1$ state, while the peaks labeled 12 and 16 at 31.06 and 32.30 eV correspond to the $4s^04p^6\ ^1S_0$ final state. A detailed analysis of the spectra will be presented at the conference.

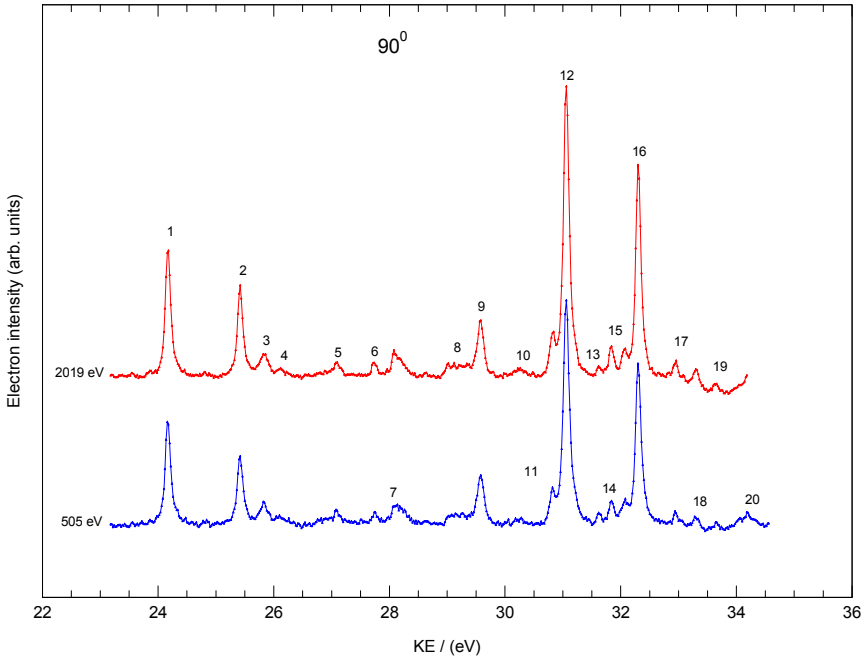

Figure 2. Low energy part of the $M_{4,5}NN$ Auger krypton spectra.

Acknowledgements

This work is partially supported by MESTD under the grant OI 171020 and Grande Rilevanza programme between Italian Republic and Republic of Serbia "*A nanoview of radiation-biomatter interaction*" of the MAE-CI.

REFERENCES

[1] K. Siegbahn *et al, ESCA Applied to free Molecules* p. 153, (North-Holland, Amsterdam, 1971).
[2] R. J. Tweed, F. Gelebart and J. Peresse, J. Phys. B 9, 2643 (1976).
[3] S. K. Srivastava and S. Trajmar, J. Phys. B 11, 3433 (1978).
[4] J. A. Baxter, P. Mitchell, J. Comer, J. Phys. B 15, 1105 (1982).
[5] L. O. Werme, T. Bergmark and K. Siegbahn, Phys. Scripta 6, 141 (1972).
[6] A. Kikas, S. J. Osborne, A. Ausmees, S. Svensson, O. P. Sairanen, S. Aksela, J. El. Spec. Rel. Phenom. 77, 241 (1966).
[7] J. J. Jureta, B. P. Marinković and L. Avaldi, Eur. Phys. J. D 70, 199 (2016).

BEAMDB AND MOLD – COLLISIONAL AND RADIATIVE DATABASES AT THE SERBIAN VIRTUAL OBSERVATORY

Bratislav P. Marinković[1], Vladimir A. Srećković[1], Darko Jevremović[2], Veljko Vujčić[2,3], Ljubinko M. Ignjatović[1], Milan S. Dimitrijević [2,4], Stefan Ivanović[1,5], Nebojša Uskoković[1,5], Milutin Nešić[5] and Nigel J. Mason[6]

[1] *Institute of Physics Belgrade, University of Belgrade, Pregrevica 118, 11080, Belgrade, Serbia;*
[2] *Astronomical Observatory, Volgina 7, 11060 Belgrade 38, Serbia;*
[3] *Faculty of Organizational Sciences, University of Belgrade Jove Ilića 154, 11000 Belgrade, Serbia*
[4] *Observatoire de Paris, 92195 Meudon Cedex, France;*
[5] *The School of Electrical Engineering and Computer Science of Applied Studies 283, Vojvode Stepe St., 11000 Belgrade, Serbia*
[6] *Department of Physical Sciences, The Open University, MK7 6AA, Milton Keynes, UK*

Abstract. In this contribution we present a progress report of two atomic and molecular databases, BEAMDB and MolD, which are web services at the Serbian virtual observatory (SerVO) and nodes within the Virtual Atomic and Molecular Data Center (VAMDC). The Belgrade Electron/Atom(Molecule) Data Base (BEAMDB) provides collisional data for electron interactions with atoms and molecules. The MolD database contains photo-dissociation cross-sections for individual rovibrational states of diatomic molecular ions and rate coefficients for the chemi-ionisation/recombination processes. We also present a progress report on the major upgrade of these databases and plans for the future.

1. INTRODUCTION

Databases in atomic and molecular physics have become essential for develop of models and simulations of complex physical and chemical processes and for the interpretation of data provided by observations measurements e.g. in laboratory plasmas [1] and plasma chemistries and reactions in planetary atmospheres [2]. In order to solve the problem of analysis and mining of such large amounts of data, the creation of a Virtual Observatory and Virtual Data Center has been crucial [3 and refs. therein]. In this contribution we present a progress report of two atomic and molecular databases, BEAMDB and MolD,

which are web services at the Serbian virtual observatory (SerVO) [4] and nodes within the Virtual Atomic and Molecular Data Center (VAMDC) [5].

This branch of science often entitled 'Data management' or 'Data mining' is undergoing rapid expansion and development, however nowadays it is not enough for these databases to satisfy the standards of Virtual centers etc., but they have to deal with new challenges such as inputs of large amounts of data i.e. Big Data. Thus, we can expect major investment and activity in this field in the next decade.

2. REPORTS FROM BG NODES

The Belgrade nodes of VAMDC are hosted by SerVO (see Fig.1) and currently consists of two databases BEAMDB (servo.aob.rs/emol) and MolD (servo.aob.rs/mold). These databases have been created using the standards developed and operated by the VAMDC project [5], (see Fig 2). VAMDC and SerVO have been through different stages of development. SerVO (http://www.servo.aob.rs/) is a project formally created in 2008 but its origins date from 2000 when the first attempts to organize data and to create a kind of webservice was made in the BELDATA project, the precursor of SerVO. VAMDC started, on July 1st 2009 as a FP7 funded project. It began with about twenty databases and now there are more than 33 currently running [6].

Figure 1. The home page of the SerVO [4]

We are currently in a transition phase updating the software "platform" (Python update, Django, XSAMS evolution, new Query Store on VAMDC, etc.) as the consequence of the rapid development and expansion.

Some current technical characteristics and aspects of these databases will be briefly introduced here (for details see [3]). Access to the BEAMDB and MolD data is possible via Table Access Protocol (TAP), a Virtual Observatory standard for a web service or via AJAX (Asynchronous JavaScript and XML)-enabled web interface (http://servo.aob.rs/). Both queries return data in XSAMS (XML Schema for Atoms, Molecules and Solids) format. The XSAMS schema provides

a framework for a structured presentation of atomic, molecular, and particle-solid-interaction data in an XML file. The underlying application architecture is written in Django, a Python web framework and represents a customization and extension of VAMDC's NodeSoftware [7,8].

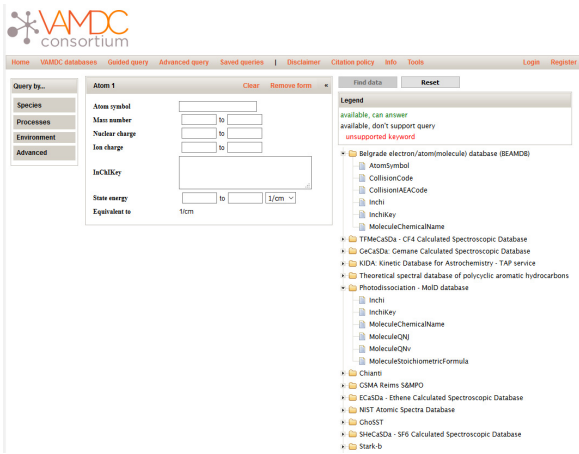

Figure 2. VAMDC [5] portal query snapshot (http://www.portal.vamdc.eu).

MolD: The MolD database has undergone three stages of development [9,10]. The initial stage of development was completed at the end of 2014, when the service for all the photodissociation data for hydrogen H_2^+ and helium He_2^+ molecular ions was constructed together with the web interface and some utility programs. At the end of 2016 MolD completed the stage 2 of development when it added averaged thermal photodissociation cross-sections H_2^+ and helium He_2^+ molecular ions and new cross-section for processes which involve species such as diatomic molecular ions HX^+, where X=Mg, Li, Na. During 2017, MolD entered stage 3 of its development in which MolD includes cross-section data for processes which involve species such as MgH^+, HeH^+, LiH^+, NaH^+, H_2^+, He_2^+... The third stage also improved the design of the web interface and developed utility programs that allow online data visualization of a wide range of data. This phase of development was completed at the beginning of 2018. The database is currently in the phase of a major upgrade.

BEAMDB: The origins of this database date from the early ideas of developing an Information System in Atomic Collision Physics [11] and at first it provided only cross sections for electron interactions with neutral atoms and molecules [12]. However the database has now been extended to cover electron spectra (energy-loss and threshold) and ionic species [3].

3. CONCLUSIONS AND FUTURE WORK

Both databases, BEAMDB and MolD databases are in transition and working progress that involves:

- XSAMS evolution to deal with Big Data (resources to be accessed by diverse client platforms across the network; generating and transferring data over a network without requiring human-to-human or human-to-computer; provide security and data quality; etc.)
- Python, Django updates
- Installing the Query Store on VAMDC node that should have a plan store for holding the execution plan information, and a runtime stats store for carrying on the execution statistics information.

In this contribution we have presented a progress report and recent developments of the Belgrade atomic and molecular databases hosted by the SerVO. These databases have been developed using protocols developed by the VAMDC. We expect advances in many fields once VAMDC and the BEMDB/ MolD are functionalised and adopted by the whole community.

Acknowledgements

This work has been supported by the MESTD of the Republic of Serbia Grants OI171020, OI176002, III44002. Part of this work has been supported by the VAMDC and the SUP@VAMDC projects funded under the 'Combination of Collaborative Projects and Coordination and Support Actions' Funding Scheme of The Seventh Framework Program.

REFERENCES

[1] N. J. Mason, J Phys. D 42, 194003 (2009).
[2] J. Tennyson, et al., Plasma Sources Sci. Technol. 26, 055014 (2017).
[3] B.P. Marinković, D. Jevremović, V.A. Srećković, V. Vujčić, L.M. Ignjatović, M.S. Dimitrijević and N.J. Mason, Eur. Phys. J. D 71, 158 (2017).
[4] D. Jevremović, M. Dimitrijević, L. Popović, M. Dačić, V.P. Benišek, E. Bon, N. Gavrilović, J., Kovačević, V., Benišek, and A. Kovačević, New Astron. Rev. 53, 222 (2009).
[5] M.-L. Dubernet, et al., J. Phys. B 49, 074003 (2016).
[6] https://portal.vamdc.eu/vamdc_portal/home.seam
[7] https://github.com/VAMDC/NodeSoftware
[8] https://www.djangoproject.com/
[9] V.Vujčič, D. Jevremović, A.A. Mihajlov, Lj.M. Ignjatović, V.A. Srećković, M.S. Dimitrijević, and M. Malović, J. Astrophys. Astron. 36, 693 (2015).
[10] V.A. Srećković, L.M. Ignjatović, D. Jevremović, V. Vujčić, and M.S. Dimitrijević Atoms 5, 31 (2017).
[11] V. Cvjetković, B. Marinković, D. Šević, *Information System in Atomic Collision Physics*, p. 485, In: Elleithy K. (eds) *Advances and Innovations in Systems, Computing Sciences and Software Engineering*. (Springer, Dordrecht, 2007).
[12] B.P. Marinković, V. Vujčić, G. Sushko, D. Vudragović, et al., Nucl. Instrum. Methods Phys. Res. B 354, 90 (2015).

COMPLEX-ROTATION CALCULATIONS OF IONIZATION RATES FOR HELIUM IN STRONG ELECTRIC FIELD

M. Z. Milošević[1] and N. S. Simonović[2]

[1] *Faculty of Science and Mathematics, University of Niš, Višegradska 33, 18000 Niš, Serbia*
[2] *Institute of Physics, University of Belgrade, P.O. Box 57, 11001 Belgrade, Serbia*

Abstract. The lowest state energies and widths (ionization rates) of the helium atom in static electric field are calculated for different field strength by the complex rotation method using a single-electron and the full two-electron model. The results are compared with the values obtained using the Stark shift expansion and the Ammosov-Delone-Krainov rate formula. It is found that the single-electron description is a good approximation for weak fields, but it fails in over-the-barrier ionization regime and partially in the tunnelling regime.

1. SINGLE-ELECTRON DESCRIPTION

Ionization of atoms in electric field can be well described by the quantum-mechanical tunnelling model. The field distorts the potential $V(\mathbf{r})$ of atomic residue forming a potential barrier through which the electron can tunnel. This mechanism explains the resonant character of atomic states when the field is present. If static electric field F is directed along the z-axis, the active (tunnelling) electron is moving in total potential $V_{\rm tot}(\mathbf{r}) = V(\mathbf{r}) - Fz$ and position of the barrier saddle point $\mathbf{r}_{\rm sp} = (0, 0, z_{\rm sp})$ and its hight $V_{\rm sp} = V_{\rm tot}(\mathbf{r}_{\rm sp}; F)$ can be determined from the rule $(\partial V_{\rm tot}/\partial z)_{x=y=0} = 0$. Atomic potential $V(\mathbf{r})$ is usually calibrated in such a way that the lowest energy level corresponds to the negative value of ionization potential $I_{\rm p}$ of the atom. Therefore, if $\epsilon(F)$ is the energy of the lowest resonant state in the total potential, one has $\epsilon(0) = -I_{\rm p}$. For a sufficiently strong field the barrier is suppressed below the energy $\epsilon(F)$ and we talk about over-the-barrier ionization (OBI). The field strength $F_{\rm S}$ that separates the tunnelling and OBI regimes is defined by the condition $\epsilon(F_{\rm S}) = V_{\rm sp}(F_{\rm S})$.

1.1 The ADK theory

Within this single-electron approach, the semiclassical Ammosov-Delone-Krainov (ADK) formula [1] gives approximate tunnelling rates for an arbitrary atom. For the helium (He) atom in the ground state the orbital and magnetic quantum number of the active (tunnelling) electron are $l = m = 0$ and the ADK formula (for static fields) reduces to

$$w = |C_{n^*0}|^2 I_\mathrm{p} \left(\frac{2F_0}{3F}\right)^{2n^*-1} \exp\left(-\frac{2F_0}{3F}\right), \tag{1}$$

where $n^* = (2I_\mathrm{p})^{-1/2}$ is the effective principal quantum number, $F_0 = (2I_\mathrm{p})^{3/2}$ and $|C_{n^*0}|^2 = 2^{2n^*}/[n^*\,\Gamma(n^*+1)\,\Gamma(n^*)]$. Here $I_\mathrm{p} = 0.9037244$ a.u. (24.5916 eV) is the ionization potential of helium (nonrelativistic theoretical value). For stronger fields, however, this formula significantly overestimates the exact rates, particularly in the OBI regime (see Fig. 1(b)).

1.2 Complex-rotation calculations

Alternatively, we calculated the ionization rates of helium in static electric field numerically using the complex-rotation (CR) method [2]. In the present calculations the wave function of the active electron, which represents the lowest (resonant) state, is expanded in the Sturmian basis [3]. The method determines the associated complex energy $\epsilon - i\Gamma/2$ whose real and imaginary parts determine the energy ϵ (position) and width Γ of resonance. The decay rate of the resonant state is then $w = \Gamma/\hbar$ (hereafter we set $\hbar = 1$ and use atomic units). The interaction between the active electron and the atomic residue (He^+) is here described by the effective potential (pseudopotential) of Hellmann's type [4]

$$V(r) = -\frac{1 + e^{-ar}}{r}, \tag{2}$$

which in limits $r \to 0$ and $r \to \infty$ reduces to $-2/r$ (e-He^{++} interaction) and $-1/r$ (asymptotic e-He^+ interaction), respectively, and for $a = 2.1324052$ reproduces the correct value of the helium ionization potential. Using potential (2) we obtain $F_\mathrm{S} = 0.22$ a.u.

The lowest state energy and width of the helium atom at different field strengths, obtained using this single-electron model and the CR method, are shown in Fig. 1. The energy values are there shifted by -2 a.u. (the negative value of the 2nd ionization potential of helium) and represent the total energy of two electrons $E(F) = \epsilon(F) - 2$, which can be directly compared with the results obtained using the full two-electron description.

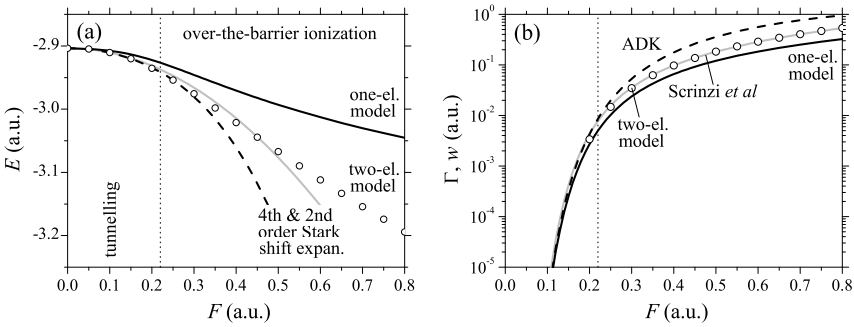

Figure 1. (a) The lowest state energy E and (b) width Γ (ionization rate w) of the helium atom in static electric field as functions of the field strength F. The results obtained numerically using the full two-electron and the single electron model with pseudopotential (2) are denoted by circles and full lines, respectively. The full gray and dashed black lines in part (a) represent the lowest state energy $E(F)$ obtained using the 2nd and the 4th order expansion for the Stark shift, respectively. The dashed line in part (b) shows the rate $w(F)$ given by the ADK formula (Eq. (1)). Full gray line represents the results from Ref. [5] obtained using the two-electron model and the CR method.

2. TWO-ELECTRON DESCRIPTION

The Hamiltonian describing the full dynamics of two electrons in the helium atom in static electric field of strength F reads

$$H = -\frac{1}{2}(\Delta_1 + \Delta_2) - \frac{2}{r_1} - \frac{2}{r_2} + \frac{1}{r_{12}} - F(z_1 + z_2), \tag{3}$$

where $\mathbf{r}_i$ and $-\frac{1}{2}\Delta_i$ are the position and the kinetic energy operator of the i-th electron, respectively, and $r_{12} = |\mathbf{r}_1 - \mathbf{r}_2|$. The energy and width of the lowest eigenstate of this Hamiltonian for different values of the field strengths are calculated using the CR method. The calculations are performed in the two-electron basis whose elements are the symmetrized products of Sturmian functions for each electron. The energy E (position) and width Γ (ionization rate w) of the lowest resonant state at a given field strength F are extracted from the associated complex energy $E - i\Gamma/2$. The results are shown in Fig. 1, together with the results obtained using the single-electron approach described in the previous section and the results for rates from Ref. [5] obtained using the two-electron model and the CR method.

3. RESULTS

The results for energies are shown in Fig. 1(a). One can see that for small values of the field strength the lowest state energy of helium obtained using the CR method and the single-electron model approximately agrees with the results of the full two-electron CR calculations. At stronger fields, however, the difference between these results increases, particularly in the OBI area. In addition, for $F < F_S$ the results of two-electron CR calculations agree well with the Stark shift expansion formula

$$E(F) = E(0) - \frac{1}{2}\alpha F^2 - \frac{1}{24}\gamma F^4 - \cdots \tag{4}$$

of the 2nd or 4th order. Here $E(0) = -I_\mathrm{p} - 2$ is the ground state energy of the free atom, whereas $\alpha = 1.3837$ and $\gamma = 43.104$ are the corresponding values for the dipole polarizability and the second dipole hyperpolarizability. This agreement confirms the validity of this formula in the tunnelling regime.

Results for the ionization rate are shown in Fig. 1(b). The results obtained by the CR method using the two-electron model agree very well with earlier CR calculations of other authors [5, 6, 7], who used a different basis set. The ADK rates and those obtained by the CR method within the single-electron approach agree well with rates obtained from the full two-electron CR calculations for $F < F_S$ (tunnelling regime). In the OBI regime, however, they overestimate and underestimate, respectively, the results of the two-electron calculations.

Acknowledgements

This work is supported by the COST Action CM1204 (XLIC). N. S. S. acknowledges support by the Ministry of education, science and technological development of Republic of Serbia under Project 171020.

REFERENCES

[1] M. V. Ammosov, N. B. Delone, and V. P. Krainov, Sov. Phys. JETP **64**, 1191 (1986).

[2] Y. K. Ho, Phys. Rep. **99**, 1 (1983); A. Buchleitner, B. Grémaud and D. Delande, J. Phys. B: At. Mol. Opt. Phys. **27** 2663 (1994).

[3] J. Avery and J. Avery, *Generalized Sturmians and Atomic Spectra* (Singapore: World Scientific, 2006)

[4] H. Hellmann, J. Chem. Phys. **3**, 61 (1935).

[5] A. Scrinzi, M. Geissler, and T. Brabec, Phys. Rev. Lett. **83**, 706 (1999).

[6] S. I. Themelis, T. Mercouris,1 and C. A. Nicolaides1, Phys. Rev. A **61**, 024101 (1999).

[7] J. S. Parker, G. S. J. Armstrong, M. Boca and K. T. Taylor, J. Phys. B: At. Mol. Opt. Phys. **42**, 134011 (2009).

RATE COEFFICIENTS FOR EXCITATION OF THE $^1\Pi_u$ STATE OF CO_2 IN RF ELECTRIC FIELD

M. M. Ristić[1], M. M. Aoneas[2], M. M. Vojnović[2] and G. B. Poparić[2]

[1]*Faculty of Physical Chemistry, University of Belgrade, Studentski trg 12-16, P. O. Box 47, 11158 Belgrade, Serbia*
[2]*Faculty of Physics, University of Belgrade, Studentski trg 12-16, P. O. Box 44, 11000 Belgrade, Serbia*

Abstract. We present rate coefficients for excitation of the $^1\Pi_u$ state of CO_2 by electrons in the presence of time-dependent electric field. Non-equilibrium electron energy distribution functions obtained by using a Monte Carlo simulation of electron movement in CO_2 gas under the influence of radio-frequency electric field have been used. Distribution functions were obtained for 200 and 500 MHz frequencies of radio-frequency (RF) electric field and for the reduced electric field values of 500 and 700 Td. The behavior of excitation rate coefficients for these values of frequencies and reduced electric fields is analyzed. The results of our research provide the data useful for modeling carbon dioxide RF plasma.

1. INTRODUCTION

The CO_2 molecule has been intensively studied as one of the major gases responsible for the greenhouse effect on Earth. It is also the most abundant molecule on atmospheres of Venus and Mars. The CO_2 gas is widely used in plasma devices based on radio-frequency discharge [1, 2]. Electron impact excitation of electronic states of the carbon dioxide molecule is, beside ionization, important process in plasmas that contain CO_2. To accurately model CO_2 plasma one needs rate coefficients for as many different processes as possible.

This work was aimed to study the time modulation behavior of the $^1\Pi_u$ excitation rate coefficients at different electric field frequencies and reduced electric field magnitudes. The study was achieved by applying Monte Carlo simulation in order to obtain non-equilibrium electron energy distribution functions (EEDFs). A similar calculation had been performed earlier by our group for N_2 and CO molecules [3, 4].

2. MONTE CARLO SIMULATION

The Monte Carlo simulation code has been used that treats transport of electrons through CO_2 gas, influenced by spatially uniform RF electric field. The cold gas approximation was used in the simulation. Electrons are tracked in each time step (Δt) by application of numerical Runge-Kutta method [5] in solving differential equations of motion. It was assumed that there are no electron-electron interactions. The EEDFs are sampled in each time step within one period. After many subsequent time steps, steady state is reached and the necessary results are statistically averaged over many periods.

Simulation reads an input database consisting of differential and integral effective cross sections for electron scattering on CO_2 molecule. Greater part of the vibrational excitation data was earlier obtained by measurements performed by our group [6].

3. RESULTS AND DISCUSSION

The calculations have been performed at E_R/N (electric field reduced to number density N) value of 500 and 700 Td (1 Td = 10^{-21} Vm^2). The time modulation of the uniform external electric field $E(t)$ is given by the following equation:

$$\vec{E}(t) = \sqrt{2} E_R \vec{k} \cos(\omega t) \tag{1}$$

where E_R denotes the effective reduced field strength, ω is angular frequency of the RF field and k is the unit vector in the field direction.

In order to minimize the simulation running time, the initial kinetic energy value for each electron was chosen to be 5 eV. The number density of neutrals was $3.22 \cdot 10^{22}$ m^{-3}, which corresponds to the gas pressure of 1 Torr (133.3 Pa). Rate coefficients for $^1\Pi_u$ state excitation have been calculated at given conditions by using the relation [7]:

$$K(\langle\varepsilon\rangle) = \sqrt{2/m_e} \int_{\varepsilon_{thres}}^{+\infty} \sigma(\varepsilon)\sqrt{\varepsilon} \cdot f_e(\langle\varepsilon\rangle, \varepsilon) d\varepsilon \tag{2}$$

where $< \varepsilon >$ stands for the mean electron energy, ε_{thres} is threshold energy $f_e(< \varepsilon >, \varepsilon)$ is the normalized EEDF and $\sigma(\varepsilon)$ is the excitation cross section. We used cross section values for excitation of $^1\Pi_u$ state of CO_2 measured by Kawahara et al. [8] in the calculation of the integral above and as a part of input data for the simulation.

Figure 1 shows the excitation rate coefficients at frequencies of 200 and 500 MHz and reduced electric field magnitudes of 500 and 700 Td. Rate coefficients increase with increasing the applied magnitudes of electric field, because then the number of electrons that have got sufficient kinetic energy to excite the $^1\Pi_u$ state increases. The rate coefficients' decrease with increasing frequency follows from the incapability of electrons to adjust to temporal

variations of the external electric field due to scattering. This also causes an increasing phase delay with increasing frequency between rate coefficients and electric field.

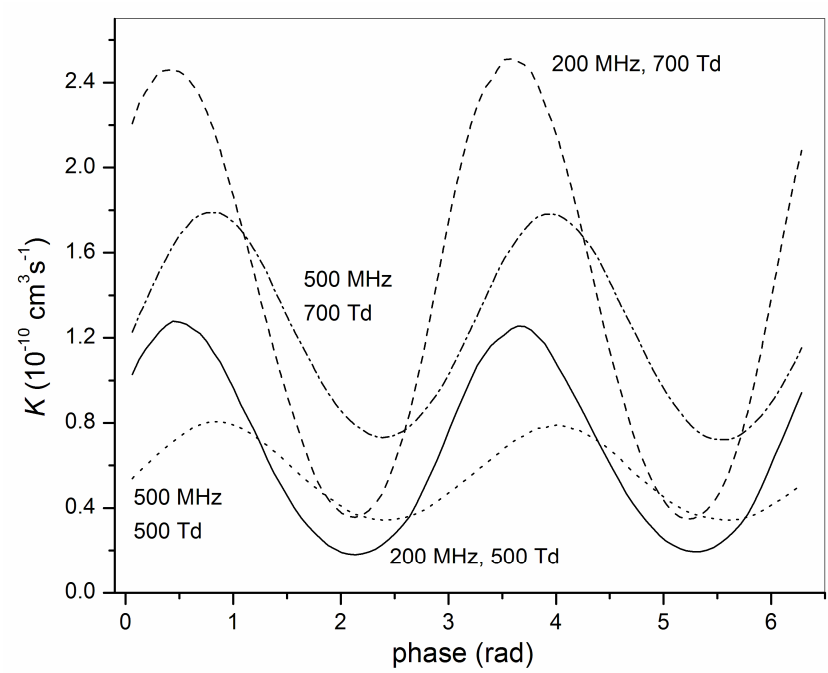

Figure 1. Time modulations of the $^1\Pi_u$ electronic state excitation rate coefficients, K_{exc}, for E_R/N value of 500 and 700 Td, in carbon dioxide at 1 Torr for 200 and 500 MHz.

4. CONCLUSIONS

Rate coefficients for the $^1\Pi_u$ state excitation of carbon dioxide in radio-frequency electric field have been calculated. The Monte Carlo simulation of electron movement through CO_2 gas in the presence of RF electric field was applied in order to obtain non-equilibrium EEDFs. The obtained results provide an insight into collision dynamics under conditions considered in this study. The rate coefficient dependence within the period of oscillation upon different applied electric field frequencies and magnitudes was discussed. This study provides necessary input data for modeling rf plasmas.

Acknowledgements

This work is supported in part by the Ministry of Education, Science and Technological Development of the Republic of Serbia, under the Project No 171016.

REFERENCES

[1] L.F. Spencer and A. D. Gallimore, Plasma Chem Plasma Process 31, 79 (2011).
[2] M.P. Srivastava and A. Kobayashi, Transactions of JWRI 39, No. 1 (2010).
[3] M.P. Popović, M. M. Vojnović, M. M. Aoneas, M. M. Ristić, M. D. Vićić and G. B. Poparić, Physics of Plasmas 21, 063504 (2014).
[4] M. M. Ristić, M. M. Aoneas, M. M. Vojnović, S. M. D. Galijaš and G. B. Poparić, Plasma Chem. Plasma Process, 1-14 (2018).
[5] R. Morrow, J. Comp. Phys. 43, 1 (1981).
[6] G. B. Poparić, M. M. Ristić and D. S. Belić, J. Phys. Chem. A, 114(4), 1610 (2010).
[7] P. Chantry, Final Technical Report ARPA, Order No 3342 (1978).
[8] H. Kawahara, H. Kato, M. Hoshino, H. Tanaka, L. Campbell and M. J. Brunger, J. Phys. B: At. Mol. Phys. 41, 085203 (2008).

ELECTRON SCATTERING ON $X(CH_3)_4$ MOLECULES: APPLICABILITY OF SIMPLE ADDITIVITY RULE AND ROLE OF METHYLATION

S. Stefanowska, P. Możejko, E. Ptasińska-Denga, Cz. Szmytkowski

Department of Atomic, Molecular and Optical Physics,
Faculty of Applied Physics and Mathematics, Gdańsk University of Technology,
ul. G. Narutowicza 11/12, 80-233 Gdańsk, Poland

Abstract. To investigate influence of target methylation (substitution of a hydrogen atom by methyl group) on electron-collision processes we compare absolute total cross sections for XH_4 and $X(CH_3)_4$ molecules, where X is Si and Ge, respectively. We also compare experimental TCSs energy dependencies with estimated data obtained using simple formula and TCSs for methyl group and those for SiH_4 and GeH_4. Electron-scattering TCSs for mentioned compounds are measured using linear transmission method.

1. INTRODUCTION

Processes induced by electron collisions are significant in many fields of science, like astrochemistry [1] and biology [2], they are also used in industry. Low-energy electrons play a key role in a lithographic technique FEBID (Focus Electron Beam Induced Deposition). This method can be applied in semiconductor industry [3] using metalorganic precursors, like $Si(CH_3)_4$. FEBID is commonly used in photolithographic mask repair [4] and nano-optics structures production [5]. Systematic studies on the interaction of electrons with gas-phase precursors can provide information needed to improve purity and spatial resolution of deposited layers. To describe and understand crucial mechanisms occurring in mentioned applications, data concerning collisions for variety of molecular targets in wide electron energy function are required.

Total cross section (TCS) as a basic quantity describing electron-scattering processes, contains summary information about all actions taking place during collision and shows efficiency of scattering for individual targets. Unfortunately, due to experimental difficulties, for many important targets TCS is still not available. Hence, for obtaining necessary data the applicability of TCS estimation methods, like simple additivity rule, should be investigated. Some observed regularities in TCS function for molecular families can be also helpful. Here, with the silicon and germanium compounds, we study the compatibility of

group additivity rule with experimental results. Moreover, influence of methyl group substitution on magnitude and shape of TCS electron energy dependence is investigated.

2. EXPERIMENT

TCS data have been obtained using electrostatic electron spectrometer working in the linear-transmission mode. The electron beam with given energy E, within the limits from 0.6 up to 300 eV and resolution of about 80 - 100 meV, is directed into scattering chamber filled with studied molecules. Electrons leaving the collision volume by exit orifice, are energy discriminated by retarding-field analyzer and collected in Faraday cup. TCS is determined by the Bouguer-de Beer-Lambert attenuation formula, in which thermal transpiration effect was included:

$$TCS(E) = \frac{k\sqrt{T_t T_m}}{pL} \ln \frac{I(E,0)}{I(E,t)} \quad , \tag{1}$$

where $I(E,0)$ and $I(E,t)$ are transmitted electron currents taken in the absence and presence of target in the scattering chamber of the length L, p is the pressure of studied molecules, T_t is the scattering cell temperature, T_m is the temperature of manometer head and k – Boltzmann constant. Statistical uncertainties (about 1%) were estimated as standard deviation of the weighted mean of the results obtained in the successive measurement series. Potential systematic uncertainties are less than 7% at low energies and decrease to 4% at intermediates. Detailed description of the experimental equipment and measurements procedure can be found in our earlier work [6].

3. RESULTS AND DISCUSION

The dependence of the TCSs values on geometrical size of molecules suggests [7], that TCS in some electron energy range can be estimated using simple additivity rule. Figure 1 shows comparison of absolute experimental and estimated TCS for $Si(CH_3)_4$ (up) and $Ge(CH_3)_4$ (down) [8]. TCSs were estimated in two ways: first, results were obtained using data only from our laboratory (SiH_4 [9], GeH_4 [10], CH_3 as 0.5TCS for C_2H_6 [11] and H_2[12]) and the second set - using experimental TCS data for atomic hydrogen [13]:

$$TCS_{Si(CH_3)_4} = TCS_{SiH4} + 4TCS_{CH_3} - 2TCS_{H_2} \tag{2}$$

$$TCS_{Si(CH_3)_4} = TCS_{SiH4} + 4TCS_{CH_3} - 4TCS_{H} \tag{3}$$

Results for $Ge(CH_3)_4$ were calculated from analogous formulas. For energies above 15 eV data from Eq. (2) and (3) practically overlap. The agreement between measured and estimated data is much better in high energy range, what

indicates that in this region scattering is dominated by electron collision with individual constitutes of molecule.

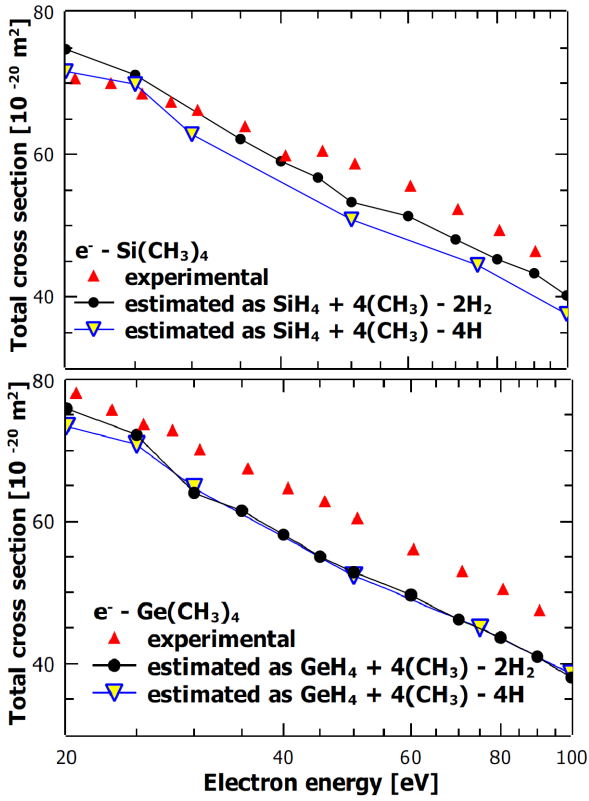

Figure 1. TCSs measured and estimated for $Si(CH_3)_4$ and $Ge(CH_3)_4$ molecules.

To investigate how substitution of methyl group (CH_3) affects on TCS electron energy dependence, we carried out detailed analysis of experimental TCS for molecules without methyl group - SiH_4 and GeH_4, and for their methylated derivatives - $Si(CH_3)_4$ and $Ge(CH_3)_4$. Comparison of these results is shown in Figure 2. Significant differences appear on high energy slope of TCSs curves for SiH_4 and $Si(CH_3)_4$ and similarly for GeH_4 and $Ge(CH_3)_4$: methylated molecules have enhancement extending between 12 and 20 eV. The enhancement of this structure is visible with the increasing number of methyl groups in targets.

4. CONCLUSION

In intermediate and high electron energy range, TCS for complex compounds can be estimated using simple empirical additivity rule with reasonable accuracy. Substitution of successive hydrogen atoms by CH_3 groups

leads to general growth of TCSs magnitudes, but also has the influence on the shape of TCS dependencies, especially at low energies.

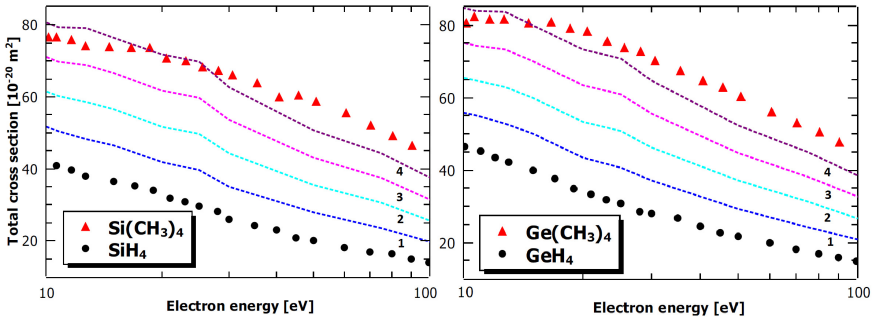

Figure 2. Measured TCSs for SiH_4, $Si(CH_3)_4$ and GeH_4, $Ge(CH_3)_4$ molecules. Dot-dot lines mean estimated TCSs for once (1), twice (2), three times (3) and four times (4) methylated SiH_4 and GeH_4.

Acknowledgements

This work is partially supported by the Polish Ministry of Science and Higher Education (MNiSzW). S. Stefanowska acknowledge the support of the MNiSzW within the Diamond Grant program (Project No. DI2015 018945).

REFERENCES

[1] N. J. Mason, B. Nair, S. Jheeta and E. Szymańska, Faraday Discuss. DOI:10.1039/c4fd00004h (2014).
[2] L. Sanche, Eur. Phys. J. D 35, 367 (2005).
[3] A. Perentes and P. Hoffmann, Chem. Vap. Deposition 13, 176-184 (2007).
[4] T. Bert, T. Hofmann and K. Edinger, Appl. Phys. A 117, 1607-1614 (2014).
[5] A. Perentes, A. Bachmann, M. Leutenegger, I. Utke, C. Sandu and P. Hoffmann, Microelectron. Eng. 412, 73-74 (2004).
[6] Cz. Szmytkowski and P. Możejko, Vacuum 63, 549 (2001).
[7] A. Domaracka, P. Możejko, E. Ptasińska-Denga and Cz. Szmytkowski, Publ. Astron. Obs. Belgrade 84, 35-38 (2008).
[8] S. Stefanowska, Cz. Szmytkowski, E. Ptasińska-Denga and P. Możejko (to be published)
[9] Cz. Szmytkowski, P. Możejko and G. Kasperski, J. Phys. B 30, 4363 (1997).
[10] P. Możejko, G. Kasperski and Cz. Szmytkowski, J. Phys. B 29, 571 (1996).
[11] Cz. Szmytkowski and A. M. Krzysztofowicz, J. Phys. B 28, 4291 (1995).
[12] Cz. Szmytkowski, K. Maciąg and G. Karwasz, Phys. Scr. 54, 271 (1996).
[13] S. Zhou, H. Li, W. E. Kauppila, C. K. Kwan and T. S. Stein, Phys. Rev. A 55, 361-368 (1997).

SYMMETRIC STRETCH MODE EXCITATION RATES OF CO_2 IN E AND B FIELDS

M. M. Vojnović[1], M. M. Ristić[2] and G. B. Poparić[1]

[1]*Faculty of Physics, University of Belgrade, Studentski trg 12-16, P. O. Box 44, 11000 Belgrade, Serbia*
[2]*Faculty of Physical Chemistry, University of Belgrade, Studentski trg 12-16, P. O. Box 47, 11158 Belgrade, Serbia*

Abstract. We report rate coefficients for the electron-impact excitation of the CO_2 molecule from its ground state to eight levels of symmetric stretch mode of vibration. Computations were performed for conditions of electron transport under the influence of crossed electric and magnetic fields. Rate coefficients were calculated by using electron energy distribution functions (EEDFs) generated by a Monte Carlo simulation we developed and cross sections (CSs) measured earlier in our laboratory. Results were obtained for different combinations of the reduced electric field strength, E/N, (20-1000 Td) and the reduced magnetic field strength, B/N, (0,1000, 2000 and 3000 Hx). This interval of the parameter changes corresponds to the mean electron energy variation from 0 to 15 eV.

1. INTRODUCTION

In electron collision studies CO_2 has very often been used as a target gas molecule. The reason for such great interest in this molecule is its presence in nature as an important atmospheric constituent of Earth, Mars and Venus, and in laser and plasma devices. Its great impact on the greenhouse effect is still a burning subject. At low electron energies the vibrational excitation is the dominant process. The vibrational excitation of carbon-dioxide is found to be an important process leading to dissociation [1], [2]. This fact has initiated efforts in enhancement of dissociation efficiency through vibrational excitation [3], since dissociation of CO_2 is, on the other hand, essential for conversion of CO_2 to environmentally friendly fuels [1].

All of this has led to the development of CO_2 plasma models for astrophysical, environmental and technological investigation purposes. Models of these environments require a complete set of collision cross sections and rate coefficients (preferably obtained for non-equilibrium conditions) as input data.

In the present work we present our results of rates for electron-impact vibrational excitation to symmetrical modes of CO_2, calculated for conditions when E and B fields are present. The inclusion of magnetic field in our study comes from the fact that devices that generate plasma usually operate in the

presence of magnetic field to achieve the electron confinement. Our study covers a wide range of conditions of E and B fields for more general purpose.

2. MONTE CARLO SIMULATION

A simulation has been developed that tracks the electrons on their way through infinite space containing CO_2 gas molecules, whereby electrons are exposed to the action of mutually crossed homogeneous electric and magnetic fields. Electrons move in each time step of the simulation according to analytical solutions of Newton's differential equations of motion.

Scattering processes are simulated by generating random numbers and their comparison with probabilities calculated on the basis of the input CS data from the base (experimentally and theoretically estimated values) for each process. After a sufficient number of time steps, the mean energy of the ensemble is stabilized. When ensemble reaches this steady state, EEDF is sampled in every step.

Alongside distribution, the electron transport parameters meaningful for different tests prior to use are sampled as well. These are the drift velocity, longitudinal and transversal diffusion coefficients. The simulation code was validated by computing the values of these quantities for conservative collision (Reid [4]) and non-conservative collision (modified Ness-Robson [5]) model gases, and comparing them with benchmark data. The input CS database for electron collisions with CO_2 was successfully tested by comparison of the resulting transport parameters with those obtained in swarm experiments.

3. RESULTS AND DISCUSSION

Rates have been calculated by implementing the formula:

$$K(\overline{E}_{el}) = \sqrt{2/m_e} \int_{\varepsilon thr}^{+\infty} \sigma(\varepsilon)\sqrt{\varepsilon} \cdot f_e(\overline{E}_{el}, \varepsilon) d\varepsilon \qquad (1),$$

where $\overline{E}_{el}$ is the mean electron energy, m_e is the electron mass, ε is its actual energy, $\sigma(\varepsilon)$ is the CS for excitation to the given symmetric stretch vibrational mode, ε_{thr} is the threshold energy and $f_e(\overline{E}_{el}, \varepsilon)$ is the normalized EEDF [6]. We used integral CSs for excitation to (n,0,0) vibration modes, whereby the vibrational quantum number, n, extends from 1 to 8. These CSs had been measured in our laboratory earlier [7]. Our results are presented in figures 1-3.

Figure 1 shows rates for excitation to specific symmetric stretch mode from (1,0,0) to (8,0,0) for E/N values ranging from 20 up to 1000 Td (1 Td = 10^{-21} Vm^2), when no magnetic field is present. Cross sections for these excitations are also shown for better insight. Naturally, the predominant process is excitation of the lowest (1,0,0) state, due to the large cross sections.

Figure 2 represents total symmetric stretch excitation rates, obtained after summation of partial rates. Results have been shown for zero magnetic field

case and for B/N having values of 1000, 2000 and 3000 Hx (1 Hx = 10^{-27} Tm^3), while E and B fields are crossed at right angle.

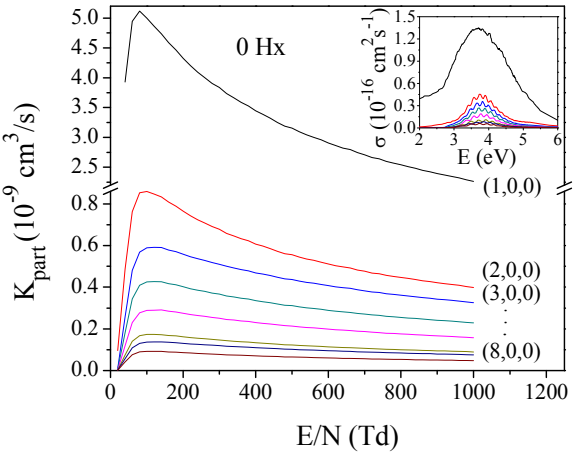

Figure 1. Partial symmetric stretch excitation rates as a function of reduced electric field strength. The inset shows partial cross sections for electron-impact excitation of CO_2 vibrational symmetric states [7].

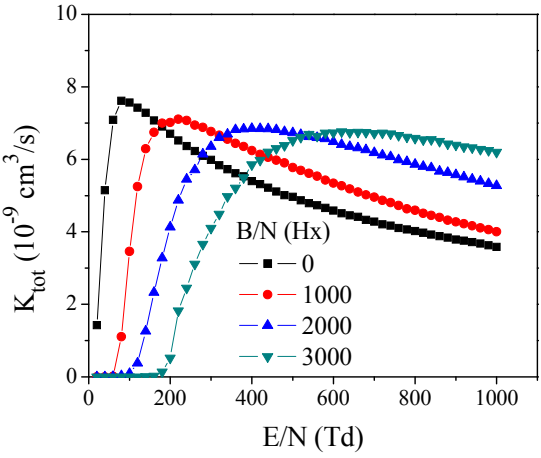

Figure 2. Total symmetric stretch excitation rates as a function of reduced electric field strength for various values of reduced magnetic field strength.

In Figure 3 total symmetric stretch rates have been shown in dependence of angle between the fields, obtained at 500 Td for different values of B/N. This dependence has been fitted with the following function:

$$K = \frac{K_0 + K_{90}}{2} + \frac{K_0 - K_{90}}{2} \cos 2\beta \qquad (2),$$

where K is the rate for the specific value of B/N, for E/N = 500 Td, K_0 and K_{90} are rates at 0 and 90 degrees respectively, and β is the angle between the fields. Situation of 0 degrees is identical to the case when no magnetic field is present. Therefore, it is possible to estimate K for any angle between the fields, based on our results for magnetic field free case and for orthogonal configuration of the fields. However, this approximation holds only if there is a monotonic decrease/increase of rates in the mean electron energy range covered by angle change from 0 to 90 degrees. This is equal to the demand of monotonic behavior of rates while B/N value rises from zero to the applied value, for chosen fixed value of E/N, which can easily be made certain from figure 2.

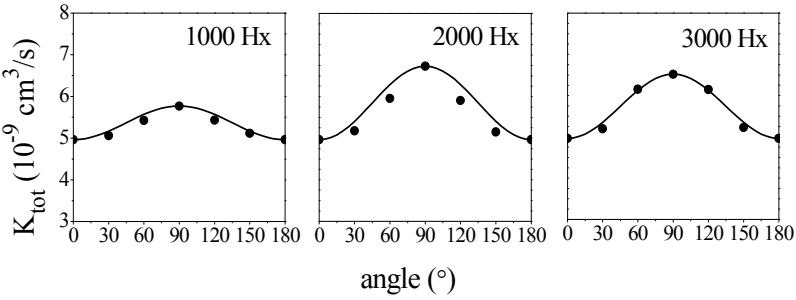

Figure 3. Variation of total symmetric stretch rates with angle between the fields, obtained at 500 Td for 1000, 2000 and 3000 Hx. The points represent the simulation results, whereas full line shows the application of eq (2).

Acknowledgements

This work is supported in part by the Ministry of Education, Science and Technological Development of the Republic of Serbia, under the Project No 171016.

REFERENCES

[1] Tomáš Kozák and Annemie Bogaerts, Plasma Sources Sci. Technol. **24** 015024 (2015).
[2] L. D. Pietanza, G. Colonna, G. D'Ammando, A. Laricchiuta and M. Capitelli, Plasma Sources Sci. Technol. **24** 042002 (2015).
[3] L. D. Pietanza, G. Colonna, V. Laporta, R. Celiberto, G. D'Ammando, A. Laricchiuta and M. Capitelli, J. Phys. Chem. A **120** 2614 (2016).
[4] R. D. White, K. F. Ness, R. E. Robson, B. Li, Phys. Rev. E **60** 2231 (1999).
[5] A. M. Nolan, M. J. Brennan, K. F. Ness, A. B. Wedding, J. Phys. D: Appl. Phys. **30** 2865 (1997).
[6] M. Ristić, G. B. Poparić and D. S. Belić, Chem. Phys. **331** 410 (2007).
[7] G. B. Poparić, M. M. Ristić, D. S. Belić, J. Phys. Chem. A **114** 1610 (2008).

SINGLE ELECTRON CAPTURE IN $H^+ - N$ COLLISIONS

Nenad Milojević and Ivan Mančev

Department of Physics, Faculty of Sciences and Mathematics, University of Niš, P.O.Box 224, 18000 Niš, Serbia

Abstract. Single electron capture from the K-shell of nitrogen atomic target by fast protons is investigated by means of the prior form four-body boundary-corrected BCIS-4B and CB1-4B methods. The obtained results are compared with the available experimental measurements and good agreement is noted especially at intermediate and high energies above 0.75 MeV.

1.Introduction

Charge transfer process in fast ion-multielectron atoms collisions is very important not only in physics such as astrophysics, plasma physics but also in medicine such as hadron therapy. In this process single electron capture plays important role. At low impact energies, capture from the outer target shells is dominated, but with the increase incidence energy of projectiles electron capture from K-shell is becoming more significant. In the present work, the four-body boundary-corrected first Born (CB1-4B) and continuum intermediate state (BCIS-4B) methods are used to examine single electron capture from K-shell nitrogen atomic target. Both of the K-shell electrons are considered as being active and the other electrons are considered as the passive. These active electrons move in an effective field of the target nucleus and the passive electrons. This is known as frozen core approximation. Such an approximation is a reduction of a many-body problem to a four-body problem. The CB1-4B and BCIS-4B methods are a fully quantum-mechanical four-body formalism and they strictly preserve the correct boundary conditions in both collisional channels. The boundary conditions or equivalently the asymptotic convergence problem [1, 2] are of essential importance for ion-atom collisions whenever the aggregates are charged in the asymptotic channels. Atomic units will be used throughout unless otherwise stated.

2. Theory and results

We consider single electron capture in collision of fast proton with nitrogen targets considering both e_1 and e_2 K-shell electrons as a active:

$$\mathrm{H}^+ + \mathrm{N}(1\mathrm{s}^2 2\mathrm{s}^2 2\mathrm{p}^3) \longrightarrow \mathrm{H}(\Sigma) + \mathrm{N}^+(1\mathrm{s}^1 2\mathrm{s}^2 2\mathrm{p}^3), \tag{1}$$

or symbolic

$$\begin{aligned} &Z_\mathrm{P} + (Z_\mathrm{T}, e_1, e_2; \{e_3, e_4, e_5, e_6, e_7\}) \\ &\longrightarrow (Z_\mathrm{P}, e_1)_\Sigma + (Z_\mathrm{T}, e_2; \{e_3, e_4, e_5, e_6, e_7\}), \end{aligned} \tag{2}$$

where the set $\{e_3, e_4, e_5, e_6, e_7\}$ denotes the five non-captured electrons which are considered as passive and $Z_\mathrm{P} = 1$ and $Z_\mathrm{T} = 7$. The symbol Σ denotes the formation of atomic hydrogen $\mathrm{H}(\Sigma)$ in any state. In frozen core approximation multielectron problem (2) can be reduced to four body problem:

$$Z_\mathrm{P} + (Z_\mathrm{T}^\mathrm{eff}, e_1, e_2)_{1s^2} \longrightarrow (Z_\mathrm{P}, e_1)_\Sigma + (Z_\mathrm{T}^\mathrm{eff}, e_2)_{1s}, \tag{3}$$

where $Z_\mathrm{T}^\mathrm{eff} = Z_\mathrm{T} - 5/16 = 6.6875$ is the effective charge. In non-relativistic scattering theory the electrons can be considered as distinguishable from each other, because we shall consider that e_1 is captured, while e_2 remains in the target rest.

Therefore, the prior form of the transition amplitudes in the BCIS-4B [3] and CB1-4B [4] approximations for process (3) become:

$$\begin{aligned} T_\mathrm{if}^\mathrm{BCIS}(\vec{\eta}) &= [N^-(\nu_\mathrm{T})]^* \iiint d\vec{x}_1 d\vec{x}_2 d\vec{R} \varphi_\mathrm{P}^*(\vec{s}_1)\varphi_\mathrm{T}^*(\vec{x}_2) \left(\frac{2}{R} - \frac{1}{s_1} - \frac{1}{s_2}\right) \\ &\times \varphi_\mathrm{i}(\vec{x}_1, \vec{x}_2) \mathrm{e}^{i\vec{\beta}\cdot\vec{R} - i\vec{v}\cdot\vec{s}_1} {}_1F_1(i\nu_\mathrm{T}, 1, ivx_1 + i\vec{v}\cdot\vec{x}_1)(vR + \vec{v}\cdot\vec{R})^{i\xi_1}, \end{aligned} \tag{4}$$

$$\begin{aligned} T_\mathrm{if}^\mathrm{CB1}(\vec{\eta}) &= \iiint \mathrm{d}\vec{x}_1 \mathrm{d}\vec{x}_2 \mathrm{d}\vec{R} \varphi_\mathrm{P}^*(\vec{s}_1) \left(\frac{2}{R} - \frac{1}{s_1} - \frac{1}{s_2}\right) \\ &\times \varphi_\mathrm{T}^*(\vec{x}_2)\varphi_\mathrm{i}(\vec{x}_1, \vec{x}_2) \mathrm{e}^{i\vec{\beta}\cdot\vec{R} - i\vec{v}\cdot\vec{s}_1} (vR + \vec{v}\cdot\vec{R})^{i\xi_2}, \end{aligned} \tag{5}$$

respectively, where the momentum transfer $\vec{\beta}$ is: $\vec{\beta} = -\vec{\eta} - \beta_z \hat{\vec{v}}$, $\beta_z = v/2 + \Delta E/v$, with $\Delta E = \epsilon_\mathrm{i} - \epsilon_\mathrm{f}$ and $\epsilon_\mathrm{f} = -1/(2n^2) - (Z_\mathrm{T}^\mathrm{eff})^2/2$. The transverse component of the change in the relative linear momentum of a heavy particle is denoted by $\vec{\eta} = (\eta\cos\phi_\eta, \eta\sin\phi_\eta, 0)$ where $\vec{\eta}\cdot\vec{v} = 0$. The position vectors of e_1 and e_2 relative to the projectile H^+ (target N^{7+}) are denoted by $\vec{s}_1$ and $\vec{s}_2$ ($\vec{x}_1$ and $\vec{x}_2$). The one-electron functions $\varphi_\mathrm{P}(\vec{s}_1)$ and $\varphi_\mathrm{T}(\vec{x}_2)$ denote the bound-state wave function of H and $(Z_\mathrm{T}^\mathrm{eff}, e_2)$, respectively. Furthermore, $N^-(\nu_\mathrm{T}) = \mathrm{e}^{\pi\nu_\mathrm{T}/2}\Gamma(1+\nu_\mathrm{T})$, $\nu_\mathrm{T} = (Z_\mathrm{T}^\mathrm{eff} - 1)/v$ and exponential factors $\xi_1 = Z_\mathrm{P}/v$ and $\xi_2 = (Z_\mathrm{P} - Z_\mathrm{T}^\mathrm{eff} + 1)/v$ where v is velocity of the projectile. The symbol Γ stands for the standard Gamma function and the ${}_1F_1(i\nu_\mathrm{T}, 1, ivx_1 + i\vec{v}\cdot\vec{x}_1)$ denotes the regular hypergeometric

function. The wave function of the two-electron ground state of the target $(Z_{\rm T}^{\rm eff}, e_1, e_2)_{1s^2}$ is labeled by $\varphi_{\rm i}(\vec{x}_1, \vec{x}_2)$. In the present work both of the K-shell target electrons (active electrons) are described by one-parameter Hylleraas like wave function $\varphi_{\rm i}(\vec{x}_1, \vec{x}_2) = (\alpha^3/\pi){\rm e}^{-\alpha(x_1+x_2)}$ with binding energies $\epsilon_{\rm i} = -\alpha^2$. We shall use two value of parameter α. In first case we set $\alpha = \alpha_1 = Z_{\rm T} - 5/16 = 6.6875$ obtained from a variational calculation, minimizing the binding energy for a two-electron atom with nuclear charge $Z_{\rm T} = 7$. In this variant we have BCIS-4Ba and CB1-4Ba methods. In second case we have BCIS-4Bb and CB1-4Bb with $\alpha = \alpha_2 = Z_{\rm T}^{\rm eff} - 5/16 = 6.375$ obtained from a variational calculation, minimizing the binding energy for a two-electron target system with nuclear charge $Z_{\rm T}^{\rm eff} = 6.6875$.

The original nine-dimensional integral for the matrix elements T_{if} from eqs. (4) and (5) can be reduced to a two-dimensional integral over real variables τ and t from 0 to 1. The total cross sections become:

$$Q^{\rm BCIS,CB1}(a_0^2) = \frac{1}{2\pi v^2} \int\limits_0^\infty {\rm d}\eta\eta |T_{if}^{\rm BCIS,CB1}(\vec{\eta})|^2 \,. \tag{6}$$

The Gauss-Legendre quadrature is employed for numerical integration this three-dimensional integral over τ, t and η. The numbers of integration points are varied until convergence to two decimal places. Total cross sections into all the final states are obtained by applying Oppenheimer scaling law via:

$$Q_{tot}^{\rm BCIS} = 1.202 Q_{1s}^{\rm BCIS}, \quad Q_{tot}^{\rm CB1} = Q_1^{\rm CB1} + Q_2^{\rm CB1} + Q_3^{\rm CB1} + 2.561 Q_4^{\rm CB1}, \tag{7}$$

where $Q_n = \sum_{l=0}^{n-1} Q_{nl}$ $(n = 1, 2, 3, 4)$ and $Q_{nl} = \sum_{m=-l}^{+l} Q_{nlm}$ are partial cross sections.

The results of the computations of total cross sections for process (1) are presented in Fig. 1 in the energy range from 0.3 to 40 MeV. The solid and dotted curves present CB1-4Bb and CB1-4Ba results respectively, whereas the results from then BCIS-4Bb and BCIS-4Ba methods are shown by dash and dash-dotted lines respectively. As can be seen at lower energies the four curves display different behaviour. The BCIS-4Ba and BCIS-4Bb methods give excellent agreement with experimental results of Cocke et al. [5] over the entire energy region, while CB1-4Bb and CB1-4Ba results slightly overestimate these measurements. For process (1) only the measurement of Cocke et al. [5] correspond to electron capture from K-shell of the nitrogen. The other experimental results overestimate all theoretical curves due to contribution from the L-shell, which become significant at lower energies. At high energies the four curves have similar shape. In this region the contribution from the K-shell becomes dominant over that from the L-shell and good agreement is obtained among all our presented results and available experimental data, especially notable is excellent agreement with the measurement of Acerbi et al. [6] at 24.7, 27.3, 32.5 and 37.7 MeV.

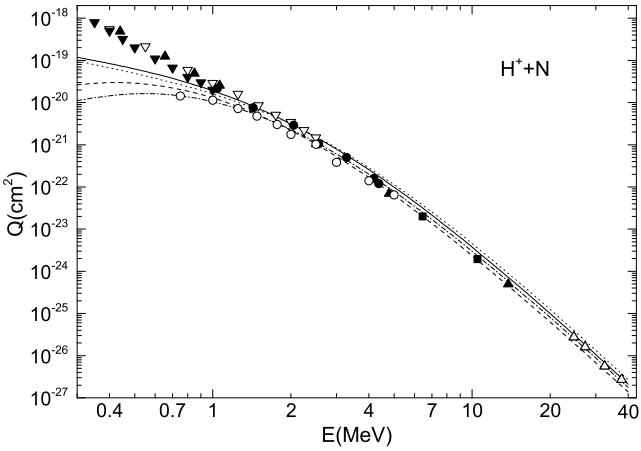

Figure 1. Full line: CB1-4Bb, dotted line: CB1-4Ba, dash line: BCIS-4Bb and dash-dotted line: BCIS-4Ba. Experimental data: ○ Cocke *et al.* [5], △ Acerbi *et al.* [6], • Schryber *et al.* [7], ▲ Welsh *et al.* [8], ▽ Toburen *et al.* [9], ■ Berkner *et al.* [10], ▼ Allison *et al.* [11].

Acknowledgements Authors thank the Ministry of Education, Science and Technological Development of the Republic of Serbia for support through Project No. 171020.

REFERENCES

[1] Dž. Belkić, *Principles of Quantum Scattering Theory* (Institute of Physics, Bristol, 2004).

[2] Dž. Belkić, *Quantum Theory of High-Energy Ion-Atom Collisions* (Taylor & Francis, London, 2008).

[3] I. Mančev, N. Milojević and Dž. Belkić, Phys. Rev. A 91, 062705 (2015).

[4] I. Mančev, N. Milojević, Dž. Belkić, Phys. Rev. A 86, 022704 (2012).

[5] C.L. Cocke, R.K. Gardner, B. Curnutte, T. Bratton and T.K. Saylor, Phys. Rev. A 16, 2248 (1977).

[6] E. Acerbi, B. Candoni, M. Castiglioni, G. Dutto, G. Fait, F. Resmini and C. Succi, Nuovo Cimento A 64, 1068 (1969).

[7] U. Shryber, Helv. Phys. Acta 40, 1023 (1967).

[8] L.M. Welsh, K.H. Berkner, S.N. Kaplan and R.V. Pyle, Phys. Rev. 158, 85 (1967).

[9] L.H. Toburen, M.Y. Nakai and R.A. Langley, Phys. Rev. 171, 114 (1968).

[10] K.H. Berkner, S.N. Kaplan, G.A. Paulikas and R.V. Pyle, Phys. Rev. 140, A729 (1965).

[11] S.K. Allison, Rev. Mod. Phys. 30, 1137 (1958).

ELECTRON TRANSPORT AND STREAMER PROPAGATION IN CF_3I-SF_6 GAS MIXTURES

J. Atić, D. Bošnjaković, Z. Lj. Petrović and S. Dujko

Institute of Physics, University of Belgrade,
Pregrevica 118, 11080 Belgrade, Serbia

Abstract. A Monte Carlo simulation technique has been used to calculate electron transport coefficients in the mixtures of trifluoromethyl iodide (CF_3I) and sulfur hexafluoride (SF_6). The calculated transport coefficients are then used as an input into the fluid equation based models with the aim of investigating the transition from an avalanche into a streamer and streamer propagation. It was found that CF_3I and its mixture with SF_6 and N_2 have the good insulation properties to be regarded as viable gaseous dielectrics.

1. INTRODUCTION

In this work we investigate electron transport and streamer propagation in the mixtures of strong electronegative gases CF_3I and SF_6 as well as in the mixtures of CF_3I and N_2. In high voltage technology, strong electronegative gases and their mixtures with other appropriate gases such as N_2 and/or CO_2, are used with the aim of controlling and preventing the electrical breakdown in electric power systems. The most important gaseous dielectric in high voltage technology is SF_6. SF_6 is a strongly electronegative gas, with a high dielectric strength, and a breakdown voltage nearly three times higher than that of air at atmospheric pressure. However, in electrical discharges, SF_6 creates highly toxic and corrosive compounds such as S_2F_{10} and SOF_2. In addition, SF_6 has extremely high global warming potential (23900 times higher than CO_2) and extremely long atmospheric lifetime (3200 years) [1]. These facts have moved scientists and engineers into finding possible substitutes of SF_6. One of the most promising candidates is CF_3I. CF_3I is also a strongly electronegative gas, but with much higher dielectric strength than SF_6. The global warming potential of CF_3I is much less than that of SF_6, and its lifetime in the atmosphere is very short. Using these facts as motivational factors, we have undertaken a program to understand electron interactions with CF_3I as well as the basic properties of streamer propagation in pure CF_3I and its mixtures with SF_6 and N_2.

In the present work, we discuss the variation of transport coefficients with the applied electric field. Calculations are performed for electrons in the CF_3I-SF_6 and CF_3I-N_2 mixtures. Values of mean energy, drift velocity, diffusion tensor, and rate coefficients are reported here. Among many important points, we

discuss the occurrence of kinetic phenomena such as negative differential conductivity, induced by the explicit effects of electron attachment. Transport coefficients for electrons are then used as an input into the fluid equation based models with the aim of investigating the transition from an avalanche into a streamer and streamer propagation. Two fundamental issues have been discussed: (i) how to use two different families of transport coefficients, the flux and the bulk in the modeling of streamers, and (ii) how streamer properties, including the electron density, electric field and streamer velocity are affected by introducing CF_3I into SF_6 and N_2 into CF_3I.

2. METHODS OF CALCULATION

In our Monte Carlo simulations, we follow a large number of electrons (typically 10^6-10^7) moving in an infinite gas under the influence of electric field. The electrons gain the energy from the electric field and dissipate this energy through binary collisions with background neutral molecules. The motion of a single electron is followed until collision with the background molecule of a neutral gas occurs. The equation for the collision probability is solved numerically by using the appropriate set of random numbers. The type of collision determines the scattering parameters after collision, including the electron speed and direction of motion. Due to extensive vanishing of the seed electrons in strongly electronegative gases, we have employed the rescaling procedures in our Monte Carlo simulation code with the aim of compensating the number of electrons in simulations without disturbing the distribution function [2]. Transport coefficients are determined after relaxation to steady state using formulae given in our previous publications [3].

Transition from an avalanche into a streamer, and propagation of streamers have been considered by the fluid equation based models. We employ the so-called classical fluid model in which the equation of continuity is combined with the drift-diffusion approximation. The resulting equation is coupled with the Poisson equation for the space charge electric field calculations. The resulting system of partial differential equations is solved numerically assuming the local field approximation [3].

3. RESULTS AND DISCUSSION

In this section, we firstly show our results for transport coefficients of electrons in the CF_3I-SF_6 mixtures. We consider the reduced electric field range: 1-10000 Td (1Td = 1×10^{-21} Vm^2) while the temperature of the background gas is 293 K. Cross sections for electron scattering in SF_6 are taken from Itoh *et al.* [4] while for electron interactions with CF_3I, we use a set of cross sections developed in our laboratory [2]. Our set of cross sections provides an excellent agreement between calculated and measured transport coefficients under the Pulsed-Townsend conditions in pure CF_3I and a fairly good agreement for the mixtures of CF_3I with Ar and CO_2.

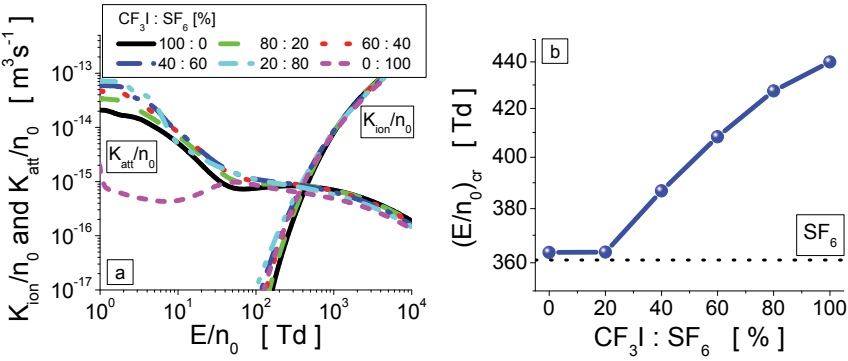

Figure 1. (a) Variation of the ionization and attachment rate coefficients with E/n_0, and (b) critical electric field in the CF_3I-SF_6 mixtures.

Figure 1 (a) shows the variation of ionization and attachment rate coefficients with E/n_0 in the CF_3I-SF_6 mixtures. As expected, the ionization rate coefficient is a monotonically increasing function of E/n_0 and becomes significant at the higher values of E/n_0 when sufficient electrons have enough energy to undergo ionization. The behavior of the attachment rate coefficient is more complex, but generally it tends to be decreased with an increasing E/n_0. When the attachment and ionization rates are equal, the E/n_0 corresponds to the so-called critical electric field. The critical electric field is shown in Figure 1 (b) for various CF_3I-SF_6 mixtures. We see that by introducing CF_3I into SF_6 the critical electric field is increased. It should be noted that in our simulations the transition from an avalanche into a streamer occurs in electric fields higher than the critical electric field.

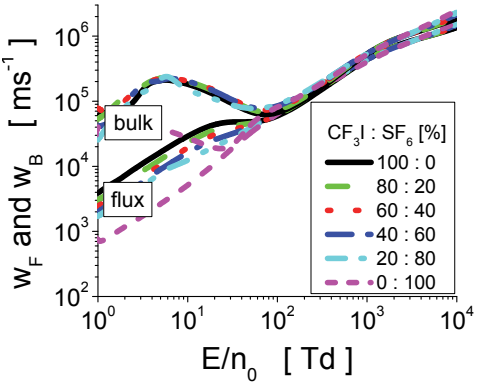

Figure 2. Variation of the flux and bulk drift velocities in various CF_3I-SF_6 mixtures.

Figure 2 shows the variation of the flux and bulk drift velocities with E/n_0 for various CF_3I-SF_6 mixtures. We observe that over the entire range of E/n_0 the flux drift velocity is a monotonically increasing function of E/n_0 while the bulk drift velocity in pure CF_3I and in pure SF_6, as well as in the mixtures shows

a strong negative differential conductivity (NDC). The phenomenon is induced by the explicit effects of electron attachment. Due to attachment heating and explicit effects of ionization the bulk drift velocity is greater than the flux drift velocity over the entire range of E/n_0 considered in this work.

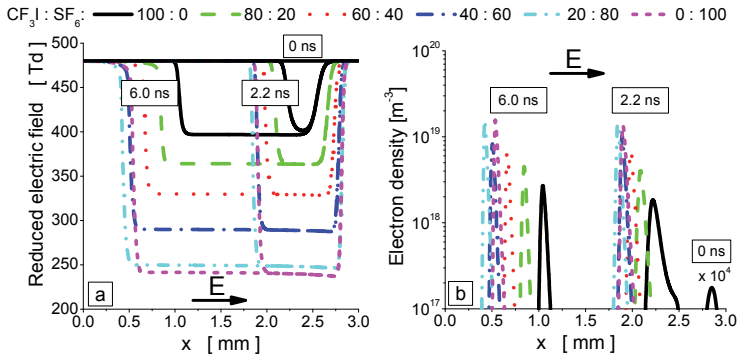

Figure 3. Temporal evolution of the electric field (a) and electron density (b) in a planar front in various CF_3I-SF_6 mixtures. The externally applied electric field is 480 Td and streamers move from the right to the left.

In Figures 3 (a) and 3 (b) we show the temporal evolution of the electric field and electron density, respectively for various CF_3I-SF_6 mixtures. Calculations are performed in a 1-dimensional setup. The initial Gaussian grows due to the ionization and then charge separation occurs due to the drift of positive ions in the opposite direction. As a consequence, the initial homogeneous electric field is disturbed and the field in the ionized region becomes more and more screened. Due to space charge effects the electric field drops off to the level in which the ionization stops and only attachment occurs. As a consequence, the electron density in the streamer channel is significantly reduced. By introducing CF_3I into SF_6, the streamers become slower and the screening of the externally applied electric field is less pronounced.

Acknowledgements

This work is supported by MPNTRRS Projects OI171037 and III41011.

REFERENCES

[1] J. de Urquijo, J. Phys: Conf. Ser. 86, 012008 (2007).
[2] J. Mirić, D. Bošnjaković, I. Simonović, Z. Lj. Petrović and S. Dujko. Plasma Source Sci. Technol. 25, 065010 (2016).
[3] D. Bošnjaković, Z. Lj. Petrović and S. Dujko, J. Phys. D: Appl. Phys. 49, 405201 (2016).
[4] H. Itoh, T. Matsumura, K. Satoh, H. Date, Y. Nakano and H. Tagashira, J. Phys. D: Appl. Phys. 26, 1975 (1993).

FLUID MODELING OF RPC'S: IMPACT OF COLLISIONAL DATA ON STREAMERS AND INDUCED SIGNALS

D. Bošnjaković[1], O. Šašić[2], Z. Lj. Petrović[1] and S. Dujko[1]

[1] *Institute of Physics, University of Belgrade, Pregrevica 118, 11070 Belgrade, Serbia*
[2] *Faculty of Transport and Traffic Engineering, University of Belgrade, Vojvode Stepe 305, 11010 Belgrade, Serbia*

Abstract. A 1.5-dimensional classical fluid model is employed to investigate the development of streamers and signals in a Resistive Plate Chamber (RPC) detector used for triggering purposes in ATLAS experiment at CERN. For comparison, the results are calculated with different transport data corresponding to different cross section sets for electron scattering in $C_2H_2F_4$ — the main component of ATLAS RPC gas mixture.

1. INTRODUCTION

Resistive Plate Chambers (RPCs) are gaseous parallel plate detectors widely used for large area timing and triggering purposes in high energy physics experiments [1, 2]. They have been introduced in high-energy physics in the 1980s of the last century, but owing to their low cost, good efficiency and outstanding timing resolution, these detectors found their way into other areas of physics and technology, including cosmic ray physics, medical imaging and geophysics [3].

There were many approaches in modeling of RPCs [4, 5, 6]. However, all RPC models rely on accurate electron collisional and transport data used as an input. Still, the accuracy of these data was often neglected. For example, most RPCs operated in the avalanche mode use a gas mixture composed of tetrafluoroethane ($C_2H_2F_4$), iso-butane (iso-C_4H_{10}) and sulfur hexafluoride (SF_6). In these mixtures, tetrafluoroethane is used as a main component which gives high primary ionization. Isobutane is a UV-quencher gas while sulfur hexafluoride is a strongly electronegative gas used to suppress the development of streamers. Several cross section sets for electron scattering in $C_2H_2F_4$ can be found in the literature. Previously, we found that these different sets used as input in the microscopic RPC model can

have a significant effect on the calculated RPC performance characteristics [4].

In this work, we employ a 1.5-dimensional classical fluid model to investigate the development of streamers and signals in ATLAS triggering RPC [1] which uses a gas mixture of 94.7% $C_2H_2F_4$ + 5% iso-C_4H_{10} + 0.3% SF_6. Particular emphasis is placed on sensitivity of the simulated signals with respect to the cross section sets for electron scattering in $C_2H_2F_4$.

2. THEORETICAL METHODS

In the present work we use a 1.5-dimensional classical fluid model based on balance equations for the number densities of electrons and ions with the local field approximation [5]. Assuming one-dimensional scenario and that the electric field is oriented along the x-axis, the continuity equation for electrons can be written as

$$\frac{\partial n_\mathrm{e}}{\partial t} = \frac{\partial}{\partial x}\left(W\,\mathrm{sgn}(E)\,n_\mathrm{e} + D_\mathrm{L}\,\frac{\partial n_\mathrm{e}}{\partial x}\right) + (\nu_\mathrm{i} - \nu_\mathrm{a})\,n_\mathrm{e} + S_\mathrm{ph}\,, \qquad (1)$$

where ν_i and ν_a are the ionization and attachment frequencies, respectively, W, D_L are bulk drift velocity and bulk longitudinal diffusion coefficient, and S_ph represents the photoionization source term.

The ions can be considered as immobile on the timescale of fast electron signal. Therefore, the balance equations for number densities of positive (n_p) and negative ions (n_n) are written as

$$\frac{\partial n_\mathrm{p}}{\partial t} = \nu_\mathrm{i}\,n_\mathrm{e} + S_\mathrm{ph} \quad \text{and} \quad \frac{\partial n_\mathrm{n}}{\partial t} = \nu_\mathrm{a}\,n_\mathrm{e}\,. \qquad (2)$$

We assume that the charge is contained inside a cylinder, with radius R_0 along the x axis, and distributed uniformly in the radial direction. For this case, the expression for electric field along the x axis is given in [5]. Source term due to photoionization is calculated as in [5] and assumes that the photon production rate is proportional to the ionization rate.

Equations (1) and (2) are solved numerically imposing homogeneous Dirichlet boundary conditions at the gas gap boundaries. The numerical scheme uses second-order central finite differences for discretization of spatial derivatives and classical fourth-order Runge–Kutta 4 scheme for integration in time. Finally, the induced current is calculated using Ramo's theorem [5, 7].

3. RESULTS AND DISCUSSION

The fluid model presented in the previous section is used to investigate the effect of input data on streamer development and calculated signal in ATLAS triggering RPC [1] which uses a 2 mm gas gap with a gas mixture

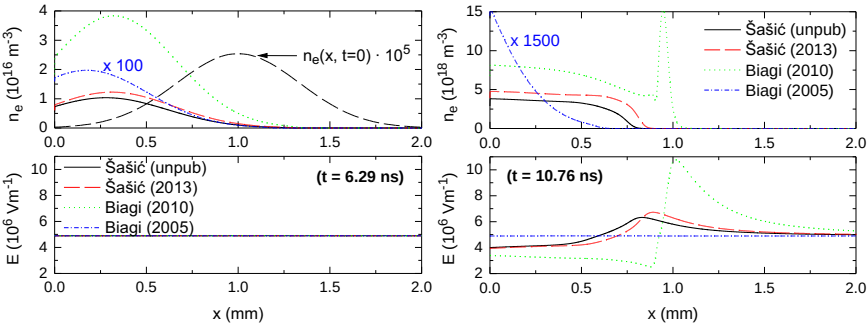

Figure 1. Electron number density and electric field along the gas gap of ATLAS triggering RPC at $t = 6.29$ ns during avalanche development (left), and $t = 10.76$ ns during positive streamer formation (right). The external electric field is set to 196 Td. Results are calculated using four different $C_2H_2F_4$ cross sections sets.

of 94.7% $C_2H_2F_4$ + 5% iso-C_4H_{10} + 0.3% SF_6. For comparison, the transport data are calculated by our Monte Carlo code [8] using four different cross section sets for electron scattering in $C_2H_2F_4$: 1) Šašić (unpub) [9], developed by our group, 2) Šašić (2013) [10], 3) Biagi (2010), taken from MAGBOLTZ 8.9 code developed by S. Biagi [11], 4) Biagi (2010), taken from MAGBOLTZ 7.9. The cross sections for iso-C_4H_{10} are taken from MAGBOLTZ 7.1 and cross sections for SF_6 are taken from Itoh et al. [12].

We assume that the initial electron distribution at $t = 0$ is a Gaussian representing 60 primary electrons. Figure 1 (left) shows the electron number density and electric field at time instant $t = 6.29$ ns during avalanche development in ATLAS RPC. At this moment, there are no space charge effects and the induced current grows exponentially with time (Figure 2, left). Afterwards, the exponential rise gradually stops due to both space charge effects and electron absorption at the anode. At about 10.76 ns, the positive streamer starts to develop (Figure 1, right) and the current rises again while the streamer progresses towards the cathode (Figure 2, left). When the positive streamer stops before the cathode and starts to diminish, the induced current slowly drops to zero. We observe both quantitative and qualitative differences between the profiles and induced currents for the four data sets. The differences arise mainly due to different drift velocities and effective ionization rates. In the avalanche phase, these differences can be explained using the exponential law of avalanche growth. Still, this is not true for the streamer phase where space charge effects take place. Figure 2 (right) shows the induced charge (defined as an integral of the induced current) calculated over a range of applied electric field strengths with four different data sets used as input. At low electric fields, where the avalanche phase is dominant, we observe that the differences between the four scenarios can reach several orders of magnitude.

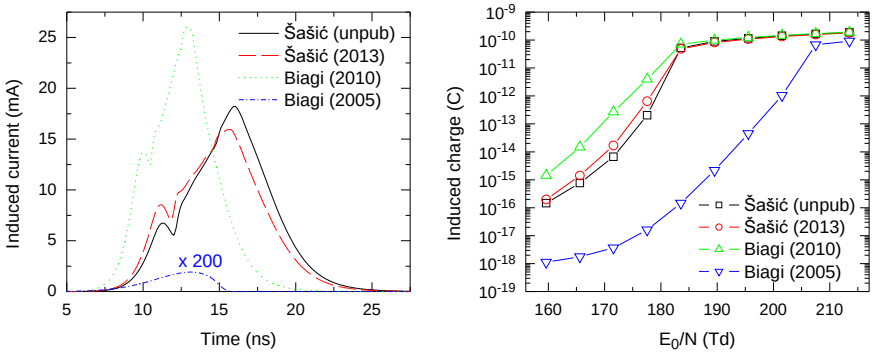

Figure 2. Induced current (left) and induced charge (right) in ATLAS triggering RPC. The induced current is obtained for the external electric field of $E_0/N = 196$ Td. Results are calculated using four different $C_2H_2F_4$ cross sections sets.

However, the differences start to diminish at higher electric fields where the space charge effects begin. This saturation effect is further enhanced by photoionization since it generates additional space charge.

Acknowledgements

This work is supported by MPNTRRS Projects OI171037 and III41011.

REFERENCES

[1] The ATLAS Collaboration, J. Instrum. 3, S08003 (2008).
[2] The ALICE Collaboration, J. Instrum. 3, S08002 (2008).
[3] R. Santonico, Nucl. Instrum. Meth. A 661, S2 (2012).
[4] D. Bošnjaković, Z. Lj. Petrović and S. Dujko, J. Instrum. 9, P09012 (2014).
[5] D. Bošnjaković, Z. Lj. Petrović and S. Dujko, J. Phys. D: Appl. Phys. 49, 405201 (2016).
[6] A. Moshaii et al., Nucl. Instrum. Meth. A 661, S168 (2012).
[7] S. Ramo, Proc. I.R.E. 27, 584 (1939).
[8] Z. M. Raspopović et al., IEEE Trans. Plasma Sci. 39, 2566 (2011).
[9] O. Šašić et al., unpublished.
[10] O. Šašić et al., J. Phys. D: Appl. Phys. 46, 325201 (2013).
[11] S. Biagi, Nucl. Instrum. Meth. A 421, 234 (1999).
[12] H. Itoh et al., J. Phys. D: Appl. Phys. 26, 1975 (1993).

ELECTRON TRANSPORT AND PROPAGATION OF STREAMERS IN THE ATMOSPHERE OF TITAN

S. Dujko[1], I. Simonović[1], D. Bošnjaković[1] and C. Köhn[2]

[1] *Institute of Physics, University of Belgrade, Pregrevica 118, 11080 Belgrade, Serbia*
[2] *Technical University of Denmark, National Space Institute (DTU Space), Elektrovej 328, 2800 Kgs Lyngby, Denmark*

Abstract. Electron transport coefficients in the atmosphere of Titan are calculated from the solution of the non-conservative Boltzmann equation. Calculations are performed in various N_2-CH_4 mixtures and values of the mean energy, drift velocity, diffusion tensor and rate coefficients are reported here. These transport coefficients are then used as an input in fluid equation based models to investigate the propagation of streamers with the aim of investigating the possibility for the occurrence of lightning in Titan's atmosphere.

1. INTRODUCTION

There are numerous evidences of lightning activity in the atmospheres of the planets of our solar system. In particular, since the era of the Voyager missions in 1980s the possibility of lightning on Titan has been investigated by theoretical and experimental studies of its complex atmospheric chemistry. Titan is the largest satellite of Saturn and its atmosphere is mostly composed of N_2 and CH_4 and trace amounts of H_2 and HCN. The presence of C_2H_2, C_2H_4 and C_2H_6 and other hydrocarbons and nitriles has also been detected. The modeling studies of Titan's atmospheric chemistry suggested the existence of lightning since the amount of HCN and C_2H_2 in the atmosphere cannot be explained as the results of photo-chemistry or charged-particle chemistry [1]. Additionally, another promising factor for the development of lightning is the presence of convective CH_4 clouds over the South pole of Titan as observed by the Cassini spacecraft [2]. However, no electromagnetic signatures of lightning were detected with either Voyager or Cassini flybys of Titan. This suggests that lightning is most probably a rare event with a very low rate of occurrence. On the other hand, it is well

known that Titan's upper atmosphere and ionosphere have a rather high conductivity due to very efficient ionization by galactic cosmic rays. As a consequence, the electromagnetic waves produced by lightning cannot penetrate Titan's upper atmosphere and ionosphere and hence their signatures were not detected by Voyager and Cassini. So, the question arises: does the lightning on Titan exist or not?

2. METHODS OF CALCULATION

In order to resolve the issue surrounding the existence of lightning on Titan, we have recently undertaken a program to understand the possible occurrence of lightning in the atmosphere of Titan. In the present work we approach this by investigating electron transport in various N_2-CH_4 mixtures in the presence of electric fields by solving the non-conservative Boltzmann equation and by applying Monte Carlo simulations [3]. We are focused how the transport coefficients are influenced by the amount of CH_4 in the mixture and by the temperature of the background gas. Calculations have also been performed in time-dependent electric and magnetic fields aiming to understand the response of electrons towards the electromagnetic pulses generated by lightning discharges.

As a second step of our analysis, we apply the calculated transport coefficients as input for fluid equation based models with the aim of investigating the transition from an electron avalanche into a streamer. Streamers are thin channels of low-temperature plasma whose dynamics is entirely controlled by the highly-localized non-linear regions of space charge and steep gradients of the electron number density. They occur in the initial stages of lightning and in sprite discharges above thunderclouds. We employ the classical fluid model which combines the equation of continuity for electrons and ions as well as the drift-diffusion approximation for electrons, and Poisson's equation for the calculation of the space charge electric field [4]. These fluid equations are closed by the local-field approximation in which all transport properties are assumed to be functions of the local electric field. In addition, we use our recently developed fluid model in which the electron collisional term in the continuity equation is expanded in terms of gradients of the electron number density. The expansion coefficients are calculated in Monte Carlo simulations. Both fluid models are numerically implemented in a 1.5-dimensional setup.

Finally, in addition to fluid models, we also use a 2.5D PIC/MC (Particle in cell/Monte Carlo) model with a cylindrical symmetry to simulate the development of both positive and negative streamers in the ambient electric field [5]. In order to simulate positive streamers, the photoionization model initially developed by Zheleznyak and co-workers [6] is implemented into the code.

3. RESULTS AND DISCUSSION

On Titan clouds form between 20 and 35 km altitude with the pressure varying between approximately 0.1 bar and 0.6 bar, the ambient temperature varying between 70 and 75 K and the level of CH_4 varying between 1.6% and 2.0%. In our calculations we choose 1.6% of CH_4 while the pressure and temperature are set to 0.3 bar and 75 K, respectively. We cover a range of the reduced electric field E/N between 10^{-3} and 10^{3} Td where 1 Td $= 1 \times 10^{-21}$ Vm^2.

In figure 1 we show the variation of the mean energy (a), drift velocity (b) and rate coefficients for ionization and attachment (c) for a mixture with 1.6% CH_4 as a function of E/N. We observe that the mean energy is a monotonically increasing function of E/N. The properties of the cross sections are reflected in the E/N-profile of the mean energy. From the profile of the drift velocity, we see that there are no signs of a negative differential conductivity effect (NDC), i.e., the drift velocity is a monotonically increasing function of E/N. In pure CH_4, however, the drift velocity exhibits a very strong NDC.

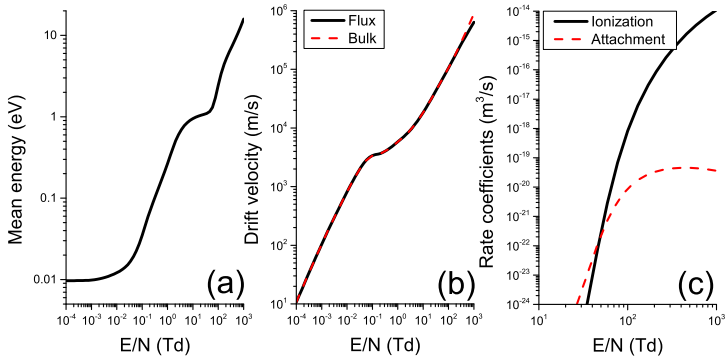

Figure 1. Variation of the mean energy (a), drift velocity (b) and rate coefficients for ionization and attachment with E/N.

Figure 2 displays the spatio-temporal evolution of the electron density and the electric field for different percentages of CH_4 when the reduced electric field E/N ahead of the front is fixed to 480 Td. The simulation is started with the same initial Gaussian-type distribution of electrons and positive ions reflecting the macroscopic plasma neutrality (panel a). In the early stage of evolution we see that the electron density grows due to electron impact ionization (panel b). The electrons drift in the direction opposite to the electric field while positive ions slowly drift in the opposite direction. The mobility of positive ions is much lower and as a consequence, the charge separation starts to distort the initial homogeneous electric field (panel c).

As the evolution continues, for mixtures with the higher concentrations of CH_4, the electric field in the ionized region gets almost completely screened, and further ionization processes cannot occur in this region (panel d). We observe that by adding CH_4 to N_2 the electron density and streamer velocity are increased. This can be expected, since the addition of CH_4 to N_2 increases the electron drift velocity and ionization rate.

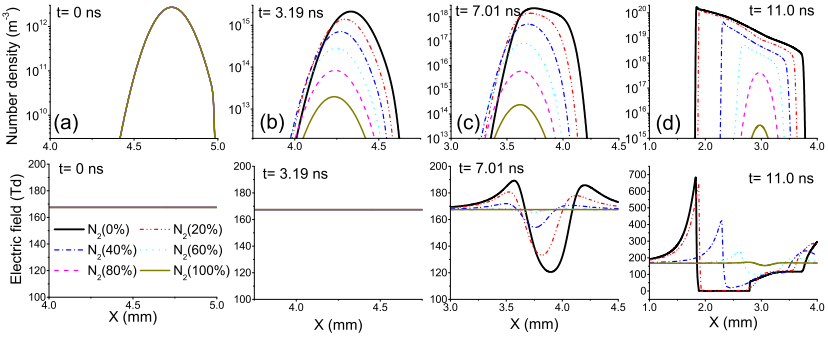

Figure 2. Evolution of the electron density (upper row) and the electric field (bottom row) in a negative planar ionization front for various N_2-CH_4 mixtures.

Acknowledgements

This work is supported by the MPNTRRS Projects OI171037 and III41011. CK acknowledges support from the Marie Curie Actions of the European Unions Seventh Framework Programme (FP7/2007-2013) under REA grant agreement no. 609405 and from the Horizon 2020 research and innovation program under the Marie Sklodowska-Curie grant agreement 722337.

REFERENCES

[1] S. J. Desch, W. J. Borucki, C. T. Russell and A. Bar-Nun, Rep. Prog. Phys. 65, 955 (2002)

[2] C. C. Porco et al., Nature 434, 159 (2005)

[3] S. Dujko, R. D. White, Z. Lj. Petrović and R. E. Robson, Phys. Rev. E 81, 046403 (2010)

[4] D. Bošnjaković, Z. Lj. Petrović and S. Dujko, J. Phys. D: Appl. Phys. 49, 405201 (2016)

[5] O. Chanrion and T. Neubert, J. Geophys. Res. 115, A00E32 (2010)

[6] M. B. Zhelznyak, High. Temp. 20, 357 (1982)

TRANSPORT COEFFICIENTS FOR Li^+ IN DIMETHOXYETHANE

Ž. Nikitović[1], M. Gilić[1], Z. Raspopović[1], M. Ćurčić[1] and V. Stojanović[1]

[1] *Institute of Physics, University of Belgrade, Pregrevica 118, 11080 Belgrade, Serbia*

Abstract. In this paper we present most probable reactions of alkali metal ion Li^+ with dimethoxyethane (DXE) molecule. Appropriate gas phase enthalpies of formation for the products were used to calculate scattering cross section as a function of kinetic energy. These data are needed for modeling in numerous applications of technologically important DXE discharges. Results for transport coefficients as a function of *E/N* (*E* -electric field; *N*-gas density) were obtained by using the Monte Carlo technique.

1. INTRODUCTION

Cold plasmas are often used in new technologies where they offer methods for nonintrusive production or modification of specific substances. Main characteristics of these plasmas are their high electron temperature and low gas temperature. Dimethoxy-containing compounds, such as dimethoxy ethane (DXE), can be produced from dimethyl ether by using dielectric barrier discharge (DBD) plasmas containing water vapor at atmospheric pressure [1]. As clear and colorless liquid at room temperature and atmospheric pressure, DXE is used as a precursor in production of ceramics or as a sole compound to make other chemicals such as those used in lithium batteries production, superconductor production and nanoparticles synthesis.

In this paper we firstly selected the most probable reactions of alkali metal ion Li^+ with DXE molecule (and its most probable products) for thermodynamic threshold energies below about 15 eV. Appropriate gas phase enthalpies of formation [2] for the products were used to calculate thermodynamic thresholds.

2. CROSS SECTION SETS

The scattering cross section of alkali ion Li^+ on DXE are calculated by using the Denpoh-Nanbu (DN) theory [3] separating elastic from reactive

collisions. DXE is known not to have dipole moment in its ground state. The dipole polarizability of 9.94×10^{-30} m^3 [4] is used for the DXE target. Similar to our recent papers [5] DN method is used to separate elastic from reactive endothermic collisions by accounting the thermodynamic threshold energy and branching ratio according to the Rice-Rampsperger-Kassel (RRK) theory [3]. Within the RRK theory the internal energy is being distributed among an empirical number of ***s*** equivalent effective modes of the complex selected from the total number of atoms involved in the complex.

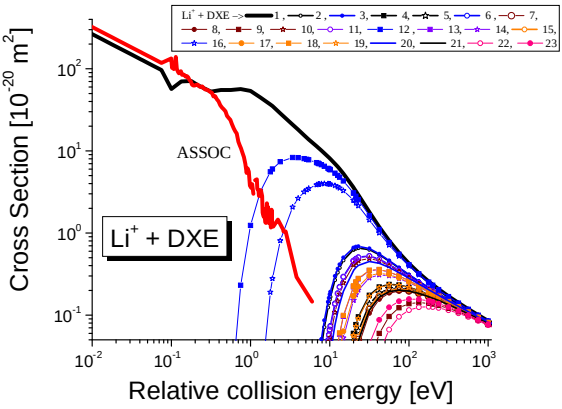

Figure 1. Cross section sets for Li^+in DXE.

Elastic momentum transfer cross section is modified in order to fit approximate mobility peak characteristic for presented systems. Swarm method [5, 6] is exploited to modify the cross section for elastic momentum transfer where for reduced mobility in the peak region (experimental [7] or theoretical values [8]) similarity with ions of equal or similar reduced mass is targeted. Appropriate gas phase enthalpies of formation for the products were used to calculate thermodynamic thresholds [9]. Elastic momentum transfer cross section for elastic collisions of Li^+ with DXE is presented in Figure 1.

3. DISCUSSION AND RESULTS

Swarm parameters as a function of reduced electric field *E/N* in DC electric fields are generally applied to plasma modeling and simulations.

We have used a Monte Carlo code that properly takes into account thermal collisions [10]. The code has passed all the relevant benchmarks and has been tested in our work on several types of charged particles.

Flux and bulk drift velocities for Li^+ in DXE as a function of *E/N* are given in Fig.2. The drift velocities obtained by Monte Carlo simulation

calculated in real space (bulk) and in velocity space (flux) values which are obtained as $\langle v \rangle$ and dx/dt, respectively. The mass of Li^+ is smaller than the mass of K^+, so as a consequence the drift velocity of Li^+ is bigger [9].

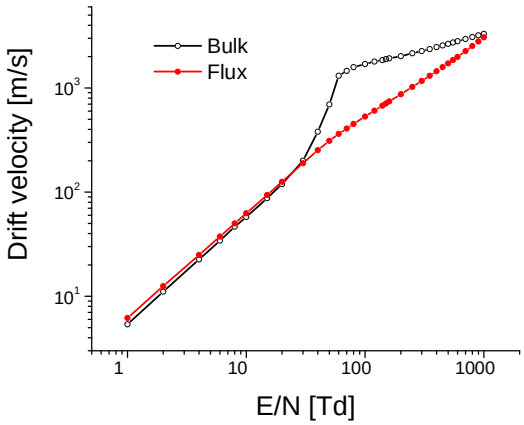

Figure 2. Drift velocity of Li^+ ions in DXE gas as a function of *E/N* at *T* = 300 K.

In Figure 3. we show the results of Monte Carlo simulation for reduced mobility as a function of *E/N*. Due to reactive collisions bulk and flux values of reduced mobility are separated.

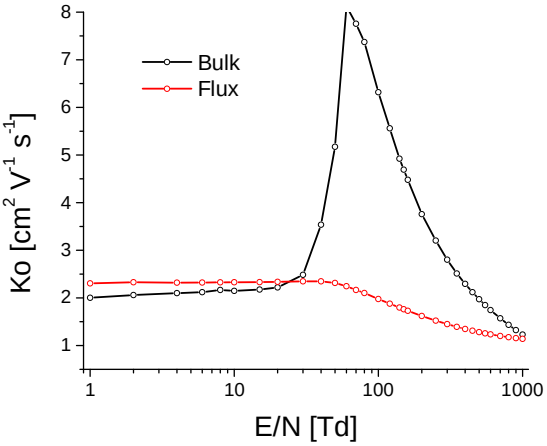

Figure 3. Reduced mobility of Li^+ ions in DXE as a function of *E/N* at *T*=300 K.

The mobility K of an ion is the quantity defined as the velocity attained by an ion moving through a gas under the unit electric field. One often exploits the reduced or standard mobility defined as:

$$K_0 = \frac{v_d}{N_0 E} N \,, \qquad (1)$$

where v_d is the drift velocity of the ion, N is the gas density at elevated temperature T and E is the electric field.

4. CONCLUSION

Calculated cross sections are used to obtain transport coefficients for alkali metal ion Li^+ in DXE gas.

The cross sections and transport data for technologically very important gas DXE have been determined by using simple theory. Peak for flux reduced mobility values is shifted in energy and intensity with respect to peak for bulk values. While it is a good basis for modeling it would be much better to add a data base of measured transport coefficients and then to perform the analysis again.

Acknowledgements

Results obtained in the Institute of Physics University of Belgrade under the auspices of the Ministry of Education, Science and Technology, Projects No. 171037 and 410011.

REFERENCES

[1] Y. Wang, C. Liu, Y. Zhang, Plasma Sci. & Technology 7, No. 3, 2839 (2005).
[2] S. G. Lias, J. E. Bartmess, J. F. Xebman and J. L. Holmes, R. D. Levin and W. G. Mallard, J. Phys. Chem. Ref. Data, Supl. 1 Vol. 17, 1 (1988).
[3] K. Denpoh and K. Nanbu, J. Vac. Sci. Technol. A 16 (3), 1201 (1998).
[4] H. Koizumi, P. B. Armentrout, J. Chem. Phys. 119, 12819 (2003).
[5] V. Stojanović, Z. Raspopović, J. Jovanović, Ž. Nikitović and Z. Lj. Petrović, EPL 101, 45003 (2013).
[6] Ž. Nikitović, Z. Raspopović, V. Stojanović and J. Jovanović, EPL 108, 35004 (2014).
[7] L. A. Viehland and E. A. Mason, At. Data. Nucl. Data Tables 60, 37 (1995).
[8] http://nl.lxcat.net/data/set type.php.
[9] Ž. Nikitović, M. Gilić, Z. Raspopović and V. Stojanović, EPL 116, 15002 (2016).
[10] Z. Ristivojević and Z. Lj. Petrović, Plasma Sources Sci. Technol. 21, 035001 (2012).

THERMALIZATION OF POSITRONS IN PENNING – MALMBERG - SURKO TRAP AT DIFFERENT BACKGROUND TEMPERATURES

Vladan Simić[1], Joan P. Marler[2], Gordana Malović[1], Srđan Marjanović[1] and Zoran Lj. Petrović[1, 3]

[1]*Institute of Physics, University of Belgrade, POB 68 11080 Zemun, Serbia*
[2]*Clemson University, Clemson SC, USA*
[3]*Serbian Academy of Sciences and Arts, 11001 Belgrade, Serbia*

Abstract. In this paper we investigate positron thermalization in a three stage Penning-Malmberg-Surko trap (buffer gas trap). We focus on the role of inelastic energy losses and try to identify the relative importance of the contribution from different processes. In order to investigate the effect of buffer gas temperature on cooling, our first simulation is conducted initially at constant background gas temperature of 300 K until positrons are thermalized and after that the trap is cooled down to 77.2 K. The second simulation is conducted at a constant background gas temperature of 77.2 K. It is shown that rotational excitation provides the key contribution during the thermalization only upon transition towards 77 K.

1. INTRODUCTION

A buffer gas positron trap is, basically, a Penning-Malmberg trap, consisting of cylindrical electrodes in an external magnetic field. However, in the buffer gas trap (also known as the Penning-Malmberg-Surko trap) the cylindrical electrodes have increasing radii effectively creating two or three stages of gas pressure with the possibility for a different electric potential in each stage [1]. As a buffer gas, we used a standard setup with N_2 in the first two stages and a mixture of N_2 and CF_4 in the third. Vibrational excitation of CF_4 is very effective in later stages of positron thermalization. Normally one would assume, however, that when the energy drops down below 100 meV rotational excitation will become the dominant energy loss process. That is the reason why we postulated that even for a CF_4 filled trap in the last stage nitrogen should be added [2]. On the other hand it was found that dominant energy losses in thermalization to the room temperature are due to vibrational energy inelastic processes [3]. The calculation was performed by using a Maxwellian distribution at all time and calculating energy loss in order to follow the decay of the effective temperature (mean energy). However, it is known that a full kinetic treatment of the swarm

like development of the positron energy distribution functions (PEDF) indicate that PEDF may have complex shapes favoring some processes and being depleted in the range of other processes even in the region of the mean energy [1, 4]. Thus we have performed a full kinetic modeling of thermalization (i.e. never assuming the PEDF energy dependence) and we have tried to identify the dominant inelastic processes. Optimizing cooling rates is beneficial for several reasons. Simply, losses of positrons would be reduced if shorter times are required to thermalize positrons. Additionally, and equally important for most applications, is that longer cooling processes result in a greater number of *elastic* (momentum transfer) collisions. Elastic collisions disperse the ensemble and broaden the radial distribution thus reducing the density that needs to be high for antimatter experiments. Thus the optimal cooling scheme minimizes the growth of the radial dimension and may include further compressing (e.g. which can be performed by rotating compression technique [5]). Finally, we note that Natisin *et al.* [6] have studied the thermalization of positrons in a cryogenically cooled trap with the background temperature in the proximity of the temperature of liquid nitrogen (i.e. in their experiment electrodes cooled to 50 K).

We used a Monte Carlo simulation of positron swarms in a three segment Penning-Malmberg-Surko trap. The code has been well tested for electrons and for positrons both in an infinite swarm-like case and for the realistic geometry and conditions of existing traps. The parameters used in both simulations are given in Table 1.

Table 1. Conditions in the trap used in simulation.

Stage	I	II	III
Background gases	N_2	N_2	$50\%\ N_2, 50\%\ CF_4$
Pressure (Torr)	10^{-3}	10^{-4}	10^{-5}
Electrode potential (V)	20	10	0
Length (m)	0.5	0.5	0.5
Radius (mm)	5	20	20
Magnetic field (T)	0.053	0.053	0.053
Pre-electrode potential (V)		10	
e^+ source bias (V)		0.1	

We present the data for two situations. First the trap is thermalized to room temperature and then suddenly cooled to the liquid nitrogen temperature, and second the trap is held at liquid nitrogen gas temperature throughout. The cross sections used for N_2 and CF_4 have been taken from our previous papers [7, 8] and include rotational excitation represented by a non-resonant Born approximation (Gerjuoy and Stein formulae) [3].

2. RESULTS AND DISCUSSION

We first present the results for the two stage (300 K-77.2 K) thermalization (Fig. 1a and 1b). The relative contributions of the different

inelastic processes are shown in Fig. 1b. We have chosen to sample only in the last stage as in each crossing between the stages positrons gain energy of around 10 eV. So the final thermalization occurs in the last stage.

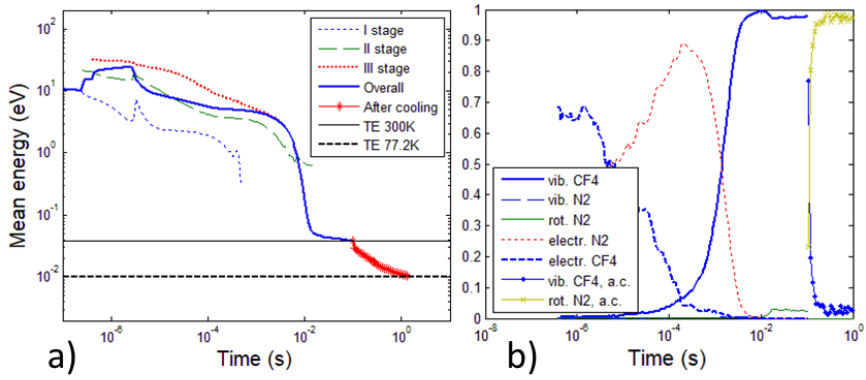

Figure 1. a) Mean energy of the positrons in the three different stages of the trap and overall during thermalization to room temperature (300 K, solid horizontal line) and then to liquid nitrogen temperature (77.2 K, dashed horizontal line). **b)** Relative contributions of each inelastic loss process to the total inelastic losses in the third segment, before and after cooling trap to 77.2 K that occurs at 0.1 s.

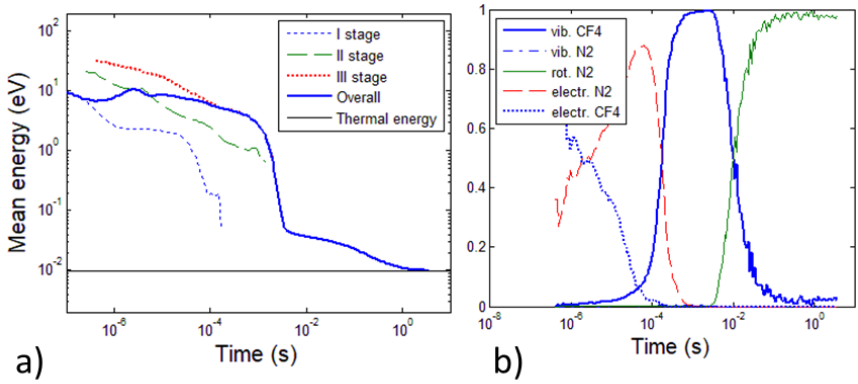

Figure 2. a) Mean energy of positrons in all three stages of the trap for 77.2 K (solid horizontal line) trap temperature. **b)** Relative contributions of each inelastic loss to the total inelastic losses in the third segment at 77.2 K.

Positrons appear first in the third stage at just before 1 μs and the most important inelastic process in that stage is electronic excitation of CF_4. Electronic excitation of CF_4 and also N_2 dominates thermalization over the initial 0.1 ms followed by the turn on of the vibrational excitation of CF_4. (Vibrational excitation of N_2 is negligible at this temperature). Surprisingly, even when the mean energy drops well below the threshold for vibrational losses, vibrational

excitations maintain their dominance in inelastic energy transfer while rotations contribute only by a couple of percent. While for electrons one may expect rotational excitation to dominate thermalization below 100 meV, for positrons, due to the lack of a resonance, rotational cross sections are very small. Thus one needs to go to mean energies less than 30 meV for rotational inelastic losses to become the dominant inelastic process with positrons, as can be seen in Fig. 1b. Results for the trap maintained at 77.2 K (Fig. 2a and 2b) clearly show that rotational energy losses become important only at positron mean energies below 30 meV.

3. CONCLUSION

This paper presents relative contributions to positron thermalization in a buffer gas trap from the different inelastic processes possible as a function of trap (gas) temperature. As one may expect, at high positron energies, thermalization is dominated by electronic excitation. As the positrons cool, vibrational excitation becomes dominant. Specifically (and unexpectedly) the rotational contribution turns on only after positron mean energy is below 30meV (room temperature). This is due to the very small values of the non-resonant excitation of rotational transitions in nitrogen.

Acknowledgements

This work is partially supported by our Ministry under the grants OI 171037 and III 41011, as well as by project F155 of the Academy of Sciences and Arts of Serbia.

REFERENCES

[1] S. Marjanović and Z. Lj. Petrović, Plasma Sources Sci. Technol. 26, 024003 (2017).
[2] S. Marjanović, A. Banković, D. Cassidy, B. Cooper, A. Deller, S. Dujko and Z. Lj Petrović, J. Phys. B: At. Mol. Opt. Phys. 49, 215001 (2016).
[3] M. R. Natisin, J. R. Danielson and C. M. Surko, J. Phys. B: At. Mol. Opt. Phys. 47, 225209 (2014).
[4] Z. Lj. Petrović, I. Simonović, S. Marjanović, D. Bošnjaković, D. Marić, G. Malović and S Dujko, Plasma Phys. Control. Fusion 59, 014026 (2017).
[5] R. G. Greaves and J. M. Moxom, Physics of Plasmas 15, 072304 (2008).
[6] M. R. Natisin, J. R. Danielson and C. M. Surko, Appl. Phys. Lett. 108, 024102 (2016).
[7] A. Banković, J. P. Marler, M. Šuvakov, G. Malović and Z.Lj Petrović, Nucl. Instrum. Methods B 266, 462–5 (2008).
[8] A. Banković, S. Dujko, S. Marjanović, R. D. White and Z. Lj. Petrović, Eur. Phys. J. D 68, 127 (2014).

THE NON-HYDRODYNAMIC BEHAVIOR OF THE THIRD ORDER TRANSPORT COEFFICIENTS FOR ELECTRONS IN GASES

I. Simonović[1], D. Bošnjaković[1], Z.Lj. Petrović[1,2], R.D. White[3] and S. Dujko[1]

[1] *Institute of Physics, University of Belgrade, Pregrevica 118, Belgrade, 11080, Serbia*
[2] *Serbian Academy of Sciences and Arts, Knez Mihailova 35, Belgrade, 11000, Serbia*
[3] *College of Science and Engineering, James Cook University, Townsville, QLD 4811, Australia*

Abstract. Third-order transport coefficients (the skewness tensor) for electron swarms in gases are studied by using the multi term method for solving the Boltzmann equation. In this work, we investigate the sensitivity of the third order transport coefficients with respect to the presence of pressure-dependent processes in neutral gases. Particular emphasis is placed upon the non-hydrodynamic behavior of the third-order transport coefficients in mercury vapor. It is found that the non-hydrodynamic effects are caused by the presence of mercury dimers.

1. Introduction

The third-order transport coefficients (TOTC) have been systematically ignored in the traditional interpretation of swarm experiments. However, the TOTC could be important under conditions in which the hydrodynamic approximation is in the limit of applicability as in the presence of physical boundaries or sources and sinks of charged particles. Moreover, the standard swarm procedure of deriving cross sections for charged particle scattering would be greatly improved by including the TOTC if they were both calculated and measured [1]. Furthermore, it has been shown that the TOTC are required for the conversion of the hydrodynamic transport coefficients into transport data which are measured in the arrival time spectra

and steady state Townsend experiments [2, 3].

The theoretical study of the TOTC has been performed by several authors. Koutselos has calculated the TOTC for ions in rare gases by using the molecular dynamics simulations and the three temperature treatment of the Boltzmann equation [4]. Penetrante and Bardsley have investigated the TOTC for electrons in rare gases by using the Monte Carlo simulations and the numerical solutions of the Boltzmann equation [5]. The TOTC have been further studied by Vrhovac et al. by employing the fluid equation based models [1].

In the present work, we extend the previous studies by determining the structure of the TOTC by using the group projector method. In addition, we have calculated the TOTC for electrons in a wide range of gases by employing the Monte Carlo simulations and the multi term solution of the Boltzmann equation. The influence of elastic, inelastic and non-conservative collisions on the TOTC has been thoroughly investigated. In the present work, however, the emphasis is placed upon the non-hydrodynamic effects observed in the E/n_0-profiles of the TOTC, where E/n_0 is the reduced electric field. We consider the electrons in mercury vapor and molecular oxygen. In particular, the pressure dependence of the TOTC in mercury vapor is attributed to inelastic collisions of electrons and mercury dimers.

2. THEORETICAL METHOD

In this work we employ the multi term method for solving the Boltzmann equation. The Boltzmann equation is given by [6]

$$\left(\frac{\partial}{\partial t} + \vec{c}\cdot\frac{\partial}{\partial \vec{r}} + \frac{q\vec{E}}{m}\cdot\frac{\partial}{\partial \vec{c}}\right) f(\vec{r},\vec{c},t) = -J(f(\vec{r},\vec{c},t), f_0) \qquad (1)$$

where $\vec{r}$, $\vec{c}$ and t denote position and velocity coordinates and time respectively, while q and m are the charge and mass of the charged particles, while $\vec{E}$ is the applied external electric field, which is oriented along the z-axis, and $f(\vec{r},\vec{c},t)$ is the phase-space distribution function. The collision operator J represents the rate of change of $f(\vec{r},\vec{c},t)$ due to collisions of charged particles with the background molecules of a neutral gas. The background molecules are assumed to be in a thermal equilibrium and they are represented by a Maxwellian distribution function f_0.

The angular dependence of the phase-space distribution function in the velocity space and the speed dependence can be resolved by expansions in terms of spherical harmonics and Sonine polynomials respectively. In the hydrodynamic regime, the phase space distribution function can be further expanded in terms of gradients of the number density. By representing the phase-space distribution function in terms of these expansions

the Boltzmann equation can be converted into a set of matrix equations. These matrix equations are solved numerically [6].

The independent components of the skewness tensor in the magnetic field free case are $n_0^2 Q_{zzz}$, $n_0^2 Q_{xxz}$ and $n_0^2 Q_{zxx}$, where n_0 is the number density of the neutral background molecules. The remaining non-zero components in the magnetic field free case can be expressed as $Q_{xzx} = Q_{xxz} = Q_{yzy} = Q_{yyz}$ and $Q_{zyy} = Q_{zxx}$ [1].

3. RESULTS AND DISCUSSION

In this work, we study the influence of the pressure dependent processes on the TOTC for electrons in mercury vapor and gaseous oxygen. The pressure dependence of transport properties in mercury vapor can be attributed to the energy losses of electrons to vibrational excitation and dissociation of mercury dimers (Hg_2). The mercury dimers are always present in mercury vapor and their concentration is directly proportional to the number density of mercury atoms [7]. At low electric fields the transport properties of electrons are determined by the elastic collisions with mercury atoms and by inelastic collisions with mercury dimers. The cross section for elastic scattering of electrons in gaseous mercury has a maximum close to 0.5eV. This maximum has a strong influence on the third order transport coefficients for E/n_0 between 0.1 Td and 2 Td, since the mean energy of electrons varies between around 0.08 eV and 0.3 eV in this field region [7].

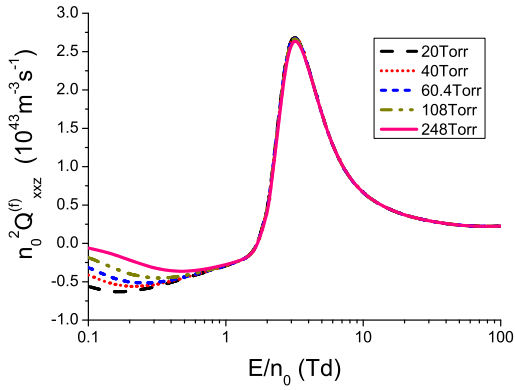

Figure 1. The field and pressure dependence of the $n_0^2 Q_{xxz}$ component of the third order transport coefficients for electrons in gaseous mercury.

The $n_0^2 Q_{xxz}$ component of the TOTC for electrons in gaseous mercury is shown in figure 1 at several values of pressure of the background gas. For the values of E/n_0 around 0.1 Td $n_0^2 Q_{xxz}$ is negative and it decreases

with increasing field, due to a rising rate for elastic collisions of electrons with mercury atoms at low electric fields. However, $n_0^2 Q_{xxz}$ rises for E/n_0 between approximately 0.2 Td and 4 Td. This rise is especially sharp for E/n_0 higher than 2 Td. The increase of $n_0^2 Q_{xxz}$ can be attributed to a decrease of the collision frequency for elastic scattering of high energy electrons in this field region. For E/n_0 higher than 4 Td $n_0^2 Q_{xxz}$ decreases due to energy losses to electronic excitations and ionization. At low electric fields the absolute value of $n_0^2 Q_{xxz}$ decreases with increasing pressure, due to a rising number density of mercury dimers. The pressure dependence is reduced with increasing field and it is negligible for E/n_0 higher than 1Td.

Acknowledgements

This work was supported by the Grant Nos. OI171037 and III41011 from the Ministry of Education, Science and Technological Development of the Republic of Serbia and also by the project 155 of the Serbian Academy of Sciences and Arts. RDW acknowledges support from the Australian Research Council.

References

[1] S. B. Vrhovac et al., J. Chem. Phys., 110, 2423 (1999)

[2] K. Kondo and H. Tagashira, J. Phys. D: Appl. Phys., 23, 1175 (1990)

[3] S. Dujko et al., J. Phys. D: Appl. Phys., 41, 245205 (11pp) (2008)

[4] A. D. Koutselos, Chemical Physics, 315, 193 (2005)

[5] B. M. Penetrante and J. N. Bardsley, "Nonequilibrium Effects in Ion and Electron Transport", ed J. W. Gallagher et al., 49-66 (1990)

[6] S. Dujko et al., Phys. Rev. E, 81, 046403 (2010)

[7] J. Miric et al., Eur. Phys. J. D, 71, 289 (2017)

Section 2.

PARTICLE AND LASER BEAM INTERACTION WITH SOLIDS

LASER ASSISTED SYNTHESIS OF MAGNETO-PLASMONIC AND UV-vis-NIR PLASMONIC NANOPARTICLES

Vincenzo Amendola

Department of Chemical Sciences, University of Padova (Italy)
vincenzo.amendola@unipd.it

In recent years, laser-based methods for the synthesis of nanomaterials in liquid have proven to be peculiar and efficient techniques to generate, excite, fragment, and conjugate elemental, nano-alloy, semiconductor, perovskite and ceramic nanoparticles (Nps) [1]. This emerging synthetic approach provides strong advantages, such as the direct access to a library of stable or metastable nanoalloys, the purity of NPs, the limited manual operation, the possibility to scale up to grams/hour of NPs. This talk will provide an overview of laser assisted synthesis of nanomaterials in liquid environment, and will discuss several examples of laser-generated plasmonic nanoparticles and nanoalloys with plasmonic and magnetic properties. These examples include, for instance, noble metal nanoparticles with easy surface bioconjugation [2], gold nanocorals with broadband visible-near infrared plasmon resonances [3], Fe-doped Au nanospheres for magnetic-plasmonic nanomedicine applications [4,5] and Fe-doped Ag nanotruffles for magnetic assembly of surface enhanced Raman Scattering (SERS) substrates [6,7].

REFERENCES

[1] V. Amendola, Phys. Chem. Chem. Phys. 15 3027-3046 (2013).
[2] V. Amendola, Phys. Chem. Chem. Phys.11 3805-3821 (2009).
[3] A. Poletti, G. Fracasso, G. Conti, R. Pilota, V. Amendola, Nanoscale 7 13702-13714 (2015).
[4] V. Amendola, M. Meneghetti, O. M. Bakr, P. Riello, S. Polizzi, D. H. Anjum, S. Fiameni, P. Arosio, T. Orlando, C. de Julian Fernandez, F. Pineider, C. Sangregorio, A. Lascialfari, Nanoscale 5 5611-5619 (2013).
[5] V. Amendola, S. Scaramuzza, L. Litti, M. Meneghetti, G. Zuccolotto, A. Rosato, E. Nicolato, P. Marzola, G. Fracasso, C. Anselmi, M. Pinto, M. Colombatti, Small 10 2476–2486 (2014).
[6] V. Amendola, S. Scaramuzza, S. Agnoli, G. Granozzi, M. Meneghetti, G. Campo, V. Bonanni, F. Pineider, C. Sangregorio, P. Ghigna, S. Polizzi, P. Riello, S. Fiameni, L. Nodari, Nano research 8 (12) 4007–4023 (2015).
[7] S. Scaramuzza, D. Badocco, P. Pastore, D. F. Coral, M. B. Fernandez van Raap, V. Amendola, ChemPhysChem 18 1026 – 1034 (2017).

ATOMIC AND MOLECULAR PROCESSES IN A STRONG BICIRCULAR LASER FIELD

Dejan B. Milošević

[1]*Faculty of Science, University of Sarajevo, Zmaja od Bosne 35, 71000 Sarajevo, Bosnia and Herzegovina*
[2]*Academy of Sciences and Arts of Bosnia and Herzegovina, Bistrik 7, 71000 Sarajevo, Bosnia and Herzegovina*
[3]*Max-Born-Institut, Max-Born-Strasse 2A, 12489 Berlin, Germany*

With the development of intense femtosecond laser sources it has become possible to study atomic and molecular processes on their own subfemtosecond time scale. Table-top setups are available that generate intense coherent radiation in the XUV and soft-X-ray regime which have various applications in strong-field physics and attoscience [1]. More recently, the emphasis is moving from the generation of linearly polarized pulses using a linearly polarized driving field to the generation of more complicated elliptically polarized polychromatic ultrashort pulses. The transverse electromagnetic field oscillates in a plane perpendicular to its propagation direction. Therefore, the two dimensions of field polarization plane are available for manipulation and tailoring of these ultrashort pulses. In this talk we present a field that allows such a tailoring, the so-called bicircular field. This field is the superposition of two circularly polarized fields with different frequencies that rotate in the same plane in opposite directions. We consider various atomic [2-4] and molecular [5,6] processes in bicircular field. We also present a possibility of introducing spin into attoscience with spin-polarized electrons produced by this field [7].

REFERENCES

[1] F. Krausz and M. Ivanov, Rev. Mod. Phys. 81, 163 (2009).
[2] D. B. Milošević, Opt. Lett. 40, 2381 (2015).
[3] T. Fan et al., Proc. Natl. Acad. Sci. USA 112, 14206 (2015).
[4] S. Odžak, E. Hasović, W. Becker, and D. B. Milošević, J. Mod. Opt. 64, 971 (2017).
[5] S. Odžak, E. Hasović, and D. B. Milošević, Phys. Rev. A 94, 033419 (2016).
[6] A. Gazibegović-Busuladžić, M. Busuladžić, E. Hasović, W. Becker, and D. B. Milošević, Phys. Rev. A 97, 043432 (2018).
[7] D. B. Milošević, Phys. Rev. A 93, 051402(R) (2016).

INTENSE LASER FILAMENT-SOLID INTERACTIONS FROM NEAR-ULTRAVIOLET TO MID-INFRARED

Miloš Burger[1,2], Patrick J. Skrodzki[1,2], Jinpu Lin[1,2], John Nees[2], Karl Krushelnick[1,2] and Igor Jovanovic[1,2]

[1] *Department of Nuclear Engineering and Radiological Sciences, University of Michigan, Ann Arbor, MI 48109, USA*
[2] *Center for Ultrafast Optical Science, University of Michigan, Ann Arbor, MI 48109, USA*

Abstract. Studies of high-power ultrashort laser pulse interaction with matter are not only of fundamental scientific interest, but are also highly relevant to applications in the domain of remote sensing. Here, we investigate the effect of laser wavelength on coupling of femtosecond laser filaments to solid targets. Three central wavelengths have been used to produce filaments: 0.4, 0.8, and 2.0 μm. We find that, unlike the case of conventional tight focusing, use of shorter wavelengths does not necessarily produce more efficient ablation. This is explained by increased multi-photon absorption arising in near-UV filamentation. Investigations of filament-induced plasma dynamics and its thermodynamic parameters provide the foundation for unveiling the interplay between wavelength-dependent filament ablation mechanisms. In this way, strategies to increase the sensitivity of material detection via this technique may be better understood, thereby improving the analytical performance in this class of applications [1].

REFERENCES

[1] M. Burger, P.J. Skrodzki, J. Lin, J. Nees, K. Krushelnick, and I. Jovanovic, Optics Express 26(13), (2018) 16456.

ELECTRONIC EXCITATIONS IN ALKALI-INTERCALATED GRAPHENE

Leonardo Marušić[1] and Vito Despoja[2]

[1]*University of Zadar, M. Pavlinovića 1, HR-23000 Zadar, Croatia*
[2]*Institut za fiziku,,Bijenička 46, HR-10000 Zagreb, Croatia*

Nowadays graphene is being intercalated with various alkali and alkali earth metals. The intercalated metal donates electrons to the graphene causing the electronic doping of the graphene π band, in a way that the metallic σ band remains partially filled. This results in the formation of two quasi two-dimensional plasmas and also adds new bands to the band structure, opening possibilities for the intraband [1] and interband [2] electronic transitions not possible in the pristine or doped graphene, as can be seen in Fig.1. Because of the heavy doping, the Dirac plasmon is very strong, while the interband and especially the inter-layer modes can be optically active in the visible and UV frequency region and therefore interesting for optical applications.

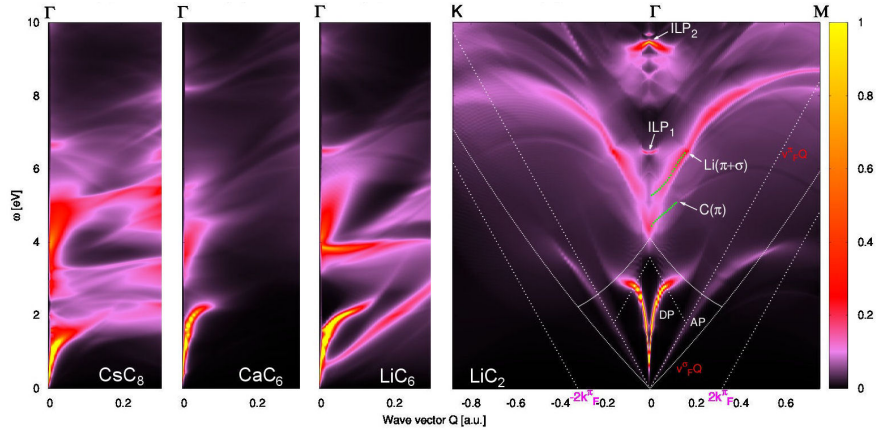

Figure 1. The intensities of the electronic excitations in CsC_8, CaC_6, LiC_6 and LiC_2 monolayer

REFERENCES

[1] L. Marušić and V. Despoja, Phys. Rev. B **95** (2017) 201408(R)
[2] V.Despoja and L. Marušić, Phys. Rev. B **97** (2018) 205426

LASER BEAM MODIFICATION OF MULTILAYERED THIN FILM STRUCTURES

Davor Peruško and Suzana Petrović

VINČA Institute of Nuclear Sciences, University of Belgrade, P .O. Box 522, 11001 Belgrade, Serbia

Laser surface alloying is a relatively new technique for improving hardness, wear, as well as corrosion resistance and some other surface characteristics of materials. Laser irradiation induces several complex phenomena such as melting, mixing of the components and alloy solidification. These processes are confined to a relatively shallow depth from the surface within a very short interaction time.

Nanometric multilayered thin film materials became very interesting due to their properties, such as enormous hardness or unusual phase composition, not achievable in a uniform bulk form. Intermetallic compounds belong to a unique class of materials which retain their structures up to their melting point and possess good mechanical properties.

Al/Ti and Ni/Ti multilayers, deposited by ion sputtering method on Si substrates, were irradiated by 1064 nm picoseconds pulsed laser beam (Nd:YAG) operated in a defocused regime. Multi-pulse action with relatively low fluence was used to prevent ablation/evaporation of material in the irradiated areas. All laser treatments were performed in air.

The applied defocused laser pulses did not cause evaporation of the material, but provided sufficient energy for melting and chemical interaction between components. Although the processing was performed in air, the growth of oxide was limited to the top layer. Deeper inside, the deposited energy enabled formation of intermetallic compounds. However, only layers included within the heat-affected zone take part in the processes of intermixing and intermetallic formation. Another interesting phenomena is formation of the laser-induced periodic surface structure (LIPSS), observed for both multilayer structures. Intensity and period of LIPSS depend on laser beam parameters (energy, incidence angle, polarization).

QUANTUM RAINBOWS IN POSITRON TRANSMISSION THROUGH CARBON NANOTUBES

Marko Ćosić[1], Srđan Petrović[1] and Nebojša Nešković[1]

[1]*Laboratory of Physics, Vinča Institute of Nuclear Sciences, University of Belgrade,*
P.O. Box 522, 11001 Belgrade, Serbia

Abstract. Here we report results of the theoretical investigation of the transmission of channeled positrons through various short chiral single walled carbon nanotubes (SWCNT). The main question answered by this study is, "*What are manifestations of the rainbow effect in the channeling of quantum particles, which happens in channeling of classical particles?*" To answer it corresponding classical and quantum problems were solved in parallel, critically examined, and compared with each other.

Positron energies were taken to be 1 MeV when quantum approach is necessary. The continuum positron-nanotube potential was constructed from the thermally averaged Molière's positron-carbon potential. In classical approach positron beam is considered as an ensemble of noninteracting particles, in quantum as an ensemble of noninteracting wave packages. Distributions of transmitted positrons were constructed from numerical solutions of Newton's equation and time-dependent Schrödinger equation.

For transmission of 1-MeV positrons through 200-nm long SWCNT (11; 9), besides central maximum, quantum angular distribution have a prominent peak (close to the classical rainbow) and two smaller peaks. We have shown that even though semi-classical approximation is not applicable the observation can be explained in terms of ray interference. In vicinity of the prominent peak *i.e.* the primary rainbow peak, rays interfere constructively. Beyond it they become complex, and below it their interference alternates between constructive and destructive thus generating two observed supernumerary rainbow peaks. Developed model was than applied for explanation of the angular distributions of 1-MeV positrons transmitting through 200 nm long (7; 3), (8; 5), (9; 7), (14; 4), (16; 5) and (17; 7) SWCNTs. It has shown that it explains most but not all rainbow patterns. Therefore, a new method for identification and classification of quantum rainbows was developed relaying only on the morphological properties of positron wave function amplitude and phase function families. This led to a detailed explanation of the way how quantum rainbow are generated. All wave packets wrinkle due to their internal focusing in mutually coordinated way and are concentrated near position of the corresponding classical rainbow. This explanation is general and applicable to investigations of quantum effects occurring in various other atomic collision processes.

DEVELOPING THE TECHNIQUES FOR SOLVING THE INVERSE PROBLEM IN PHOTOACOUSTICS

Mioljub V. Nesic[1], Marica N. Popovic[1], Slobodanka P. Galovic[1]

[1]*INS Vinca, University of Belgrade, PO Box 522, Belgrade 11000*

In this work, theoretically/mathematically simulated models are derived for the photoacoustic (PA) frequency response of both volume and surface optically absorbing samples in a minimum volume PA cell. In the derivation process, thermal memory influence of both the sample and the air of the gas column are accounted for, as well as the influence of the measurement chain.

Within the analysis of the TMS model, the influence of optical, thermal and elastic properties of the sample was investigated. This analysis revealed that some of the processes, characterized by certain sample properties, exert their dominance only in limited modulation frequency ranges, which are shown to be dependent upon the choice of the sample material and its thickness. Based on the described analysis, two methods are developed for TMS model parameter determination, i.e. sample properties which dominantly influence the PA response: a self consistent procedure for solving the exponential problems of mathematical physics and a well trained three-layer perceptron with back propagation, based upon theory of neural networks. The results of the application of both inverse problem solving methods are compared and discussed. The first method is shown to have the advantage in the number of properties which are determined, while the second one is advantageous in gaining high accuracy in the determination of thermal diffusivity, explicitly. Finally, the execution of inverse PA problem is implemented on experimental measurements done on macromolecule samples, the results are discussed and the most important conclusions are derived and presented.

Acknowledgements: This work is supported by the Ministry of Science as the contribution to the project III-45005.

REFERENCE

[1] M. V. Nesic, ”Developing the techniques for solving the inverse problem in photoacoustics – doctoral dissertation”, School of Electrical Engineering, University of Belgrade, Belgrade (2018)

TUNING THE PLASMONIC PROPERTIES OF TITANIUM NITRIDE

M. Popović*[1], M. Novaković[1], E. Schmidt[2], P. Schöppe[2], N. Bibić[1], C. Ronning[2] and Z. Rakočević[1]

[1]*University of Belgrade, Institute of Nuclear Sciences VINČA, 11351 Belgrade, Serbia*
[2]*Institute of Solid State Physics, Friedrich Schiller University Jena, Max-Wien-Platz 1, D-07743 Jena, Germany*

Polycrystalline titanium nitride (TiN) thin films were irradiated with Ag ions, and the irradiation induced modifications on structural and optical properties of the films were investigated. TiN thin films were deposited by dc reactive sputtering onto Si(100) substrates to a thickness of 260 nm. After deposition the films were implanted at room temperature with 200 keV Ag ions to the fluences of 5×10^{15} - 6×10^{16} ions/cm^2. The films were then annealed at 200 and 400^{o}C in vacuum for 2h. The combination of Rutherford backscattering spectrometry (RBS) and transmission electron microscopy (TEM) was used for analyzing structural properties, while changes in optical properties were monitored by spectroscopic ellipsometry. RBS analysis reveals that the concentration of Ag in the layers increases with ion fluence reaching the value of around 5 at.% for the highest ion dose, at a depth of approximately 50-70 nm. TEM studies demonstrate that after irradiation to the highest ion fluence the columnar microstructure is partially destroyed within ~100 nm. Also, the formation of cubic Ag nanoparticles with size of 1-2 nm was observed. Spectroscopic ellipsometry analysis shows that the silver ions within the TiN matrix drastically changes both the real and imaginary component of the dielectric function and provides low optical losses. The silver influence on the optical behavior of TiN was described using a Drude Lorentz dielectric analysis based on free electron and oscillator model. The analysis showed that the unscreened plasma frequency decreased and broadening increased with increasing silver concentration. The changes in fitting parameters were nicely correlated with the microstructural changes induced in TiN films.

SHOCK WAVE EXPANSION IN LASER INDUCED PLASMA

Miloš Skočić, Dejan Dojić and Srdjan Bukvić

University of Belgrade, Faculty of Physics, Studentski trg 12 11001, Belgrade, Serbia

Relying on classical spectroscopic approach we measured fast expansion of copper plasma created by nanosecond Nd:YAG laser. Significant Doppler splitting caused by fast radiall expansion is used to estimate expansion velocity [1, 2]. Radial velocity of copper atoms/ions attains maximum value of $\sim$ 50 km/s (800 eV) approximately 30 ns after the laser pulse. We found that number of fast copper atoms/ions is significant, and it cannot be interpret relying on usually assumed thermal initial condition. A possible explanations is that relatively small number of high speed, energetic, electrons escapes the plasma forming a double layer [3, 4] which results in formation of an electric field that accelerate ions to velocities $\sim$ 50 km/s.

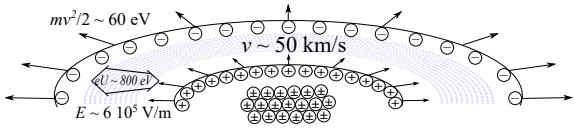

Figure 1. Schematic representation of double layer in laser induced plasma.

Acknowledgements: This work is supported by our Ministry under the project ON171008.

REFERENCES

[1] Srdjan Bukvić, Miloš Skočić, Spec. Acta Part B 132, 56 (2017)

[2] Dejan Dojić, Miloš Skočić, Srdjan Bukvić, JQSRT, 207, 73 (2018)

[3] A. V. Gurevich et al., Soviet Physics JETP 22, 2 (1966)

[4] N. M. Bulgakova et al., Phys.Rev.E 62, 4 (2000)

WAKE EFFECT DUE TO EXCITATION OF PLASMON-PHONON HYBRID MODES IN A GRAPHENE–SAPPHIRE–GRAPHENE STRUCTURE BY A MOVING CHARGE

V. Despoja[1], I. Radović[2], L. Karbunar[3] and Z. L. Mišković[4]

[1] *Institute of Physics, Bijenička 46, Zagreb, Croatia*
[2] *Vinča Institute of Nuclear Sciences, University of Belgrade, P.O. Box 522, Belgrade, Serbia*
[3] *School of Electrical Engineering, University of Belgrade, Bulevar Kralja Aleksandra 73, Belgrade, Serbia*
[4] *Department of Applied Mathematics, and Waterloo Institute for Nanotechnology, University of Waterloo, Waterloo, Ontario, Canada*

Abstract. We study the wake effect due to excitation of a plasmon-phonon hybrid mode in a sandwich-like structure consisting of two doped graphene sheets, separated by a layer of Al_2O_3 (sapphire), which is induced by an external charged particle moving parallel to the structure.

1. INTRODUCTION

Using doped graphene shows great promise for plasmonic applications in the range of frequencies from the terahertz (THz) to the infrared (IR) owing to long propagation distances and tunability of its Dirac (or sheet) plasmon [1]. Properties of that plasmon can be efficiently probed by inelastic scattering of low-energy electrons in the technique known as High-Resolution Electron Energy Loss Spectroscopy [2]. Both the energy and momentum transfers from the incident electron to graphene are significantly influenced by excitation of the Dirac plasmon, which can give rise to the wake effect in the induced potential, as shown in Refs. [3,4].

However, the dynamic response of graphene in the THz to IR frequency range is adversely affected by the presence of the transverse optical phonons in a nearby polar substrate, typically an oxide [2,5]. As a result, strong hybridization takes place between the Dirac plasmon and the resulting Fuchs-Kliewer, or surface optical phonon modes in the oxide, which can profoundly affect the damping of the collective modes in layered structures

involving graphene sheets [1,5]. Moreover, such hybridization also affects the energy loss of an incident electron [6], as well as the resulting wake effect [7]. For example, while in Ref. [3] it was shown that there exists a velocity threshold for the wake to be excited in a single, free graphene by an incident charged particle, given by the Fermi speed of graphene $v_{\rm F} \approx 10^6$ m/s, we have found in Ref. [7] that a hybrid mode between graphene and an SiO_2 substrate gives rise to a noticeable, phonon-dominated wake effect.

Since in nanoscale devices graphene typically appears in stacks separated by insulating layers [1], we have recently studied a sandwich-like structure with two graphene sheets, placed in the planes $z = a/2$ and $z = -a/2$ of a Cartesian coordinate system (x, y, z), as shown in Fig. 1, with the space between them being the air or a layer of Al_2O_3 (sapphire) of thickness a [8]. The dynamic response of each graphene was described by a two-dimensional (2D) independent-electron polarization function $\chi_1^0(\mathbf{q}, \omega)$ and $\chi_2^0(\mathbf{q}, \omega)$, with $\mathbf{q} = (q_x, q_y)$ being the 2D wavevector, whereas the response of the sapphire layer was described by a dielectric function $\varepsilon_{\rm S}(\omega)$ consisting of several Lorentzian terms [8]. For the microscopic model of χ_j^0 we used random phase approximation with two models: *ab initio* calculations with a full range of electronic bands in graphene [9], and analytical description of low-energy portions of graphene's π electronic bands in a massless Dirac fermion (MDF) approximation. While in Ref. [8] we analyzed the dispersion relations of the hybrid plasmon-phonon modes of this structure, we present here results on the wake effect due to the excitation of these modes by a charged particle moving parallel to the structure at the speed of v, a distance $b > 0$ from the top graphene sheet with the polarization χ_2^0. As in Ref. [8], we take $a = 5$ nm and assume that graphene sheets are equally doped, each having the same Fermi energy of $E_{\rm F} = 0.2$ eV.

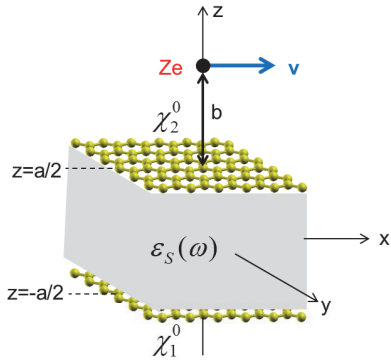

Figure 1. Diagram of a sandwich-like structure with point charge Ze moving at the speed v, a distance b above the top graphene with χ_2^0.

2. RESULTS AND DISCUSSION

In Ref. [8] we used a Feynman diagram technique, as well as analytical solution of Dyson-Schwinger equation, to express the screened Coulomb interaction $W(\mathbf{q}, \omega, z, z')$ between the points in Fig. 1 with $z, z' \geq a/2$ as

$$W(\mathbf{q}, \omega, z, z') = V_q \left\{ {\rm e}^{-q|z-z'|} + \left[\frac{1}{\varepsilon(\mathbf{q}, \omega)} - 1 \right] {\rm e}^{-q(z+z'-a)} \right\}, \qquad (1)$$

where $q = \|\mathbf{q}\| = \sqrt{q_x^2 + q_y^2}$ and $V_q = 2\pi/q$ is the Fourier transform of the bare Coulomb potential between unit point charges in 2D, whereas the effective 2D dielectric function $\varepsilon(\mathbf{q}, \omega)$ is defined as

$$\varepsilon(\mathbf{q},\omega) = \frac{1}{2}\left\{\left[1 + \varepsilon_{\rm S}\coth(qa) - 2V_q\chi_2^0\right] - \frac{\varepsilon_{\rm S}^2\,\mathrm{cosech}^2(qa)}{1 + \varepsilon_{\rm S}\coth(qa) - 2V_q\chi_1^0}\right\}. \quad (2)$$

For a point charge Ze moving parallel to the x axis with constant speed v, the 2D translational invariance of the structure in Fig. 1 renders the induced electrostatic potential stationary in the moving frame of reference attached to that particle, so that the total potential at a point (x, y, z) with $z \geq a/2$ may be written as

$$\Phi_{\rm tot}(x - vt, y, z) = Ze \iint \frac{dq_x\, dq_y}{(2\pi)^2}\, W(\mathbf{q}, q_x v, z, \tfrac{a}{2} + b)\, \mathrm{e}^{iq_x(x-vt)+iq_y y}. \quad (3)$$

In Fig. 2 we show the cross section of this potential with $y = 0$, in the plane of the upper graphene sheet, $z = a/2$, normalized by $\Phi_0 = Ze/b$ with $b = 0.5$ nm, for a particle moving at the sub-threshold speed of $v = v_{\rm F}/2$.

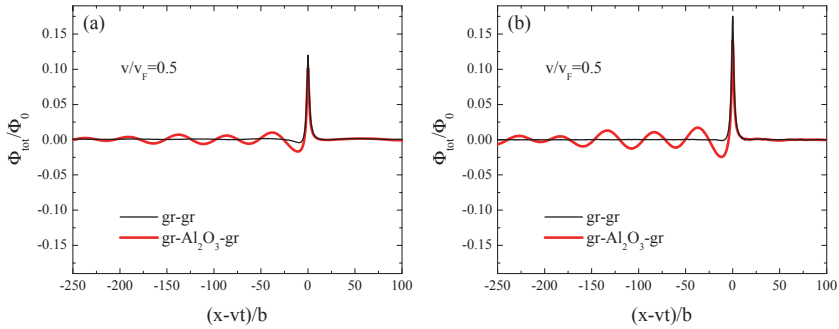

Figure 2. The total potential, normalized by $\Phi_0 = Ze/b$ with $b = 0.5$ nm, shown as a function of the normalized distance $(x - vt)/b$, when the space of thickness $a = 5$ nm between graphene sheets is filled by air (thin black lines) or Al_2O_3 (thick red lines). The polarization functions of graphene sheets are obtained from (a) *ab initio* calculations and (b) MDF approximation [8].

One notices that, when the space between graphene sheets is air, there is only a sharp, somewhat asymmetric peak in the potential at the position of the particle. This is due to the fact that the condition of kinematic resonance for exciting a collective mode, $v > \omega/q$ [3,7], is not fulfilled because the phase velocities of the two hybridized Dirac plasmon modes are $> v_{\rm F}$ in this case. On the other hand, when the space is filled with sapphire, there is a prominent wake pattern in the potential behind the particle, $x - vt < 0$, resulting from a low-frequency plasmon-phonon mode, $\omega_{\rm low}$ [8], which does not disperse as q increases, thereby enabling the kinematic resonance for a sufficiently large wavenumber, $q > \omega_{\rm low}/v_{\rm F}$ [7].

At the same time, it is remarkable in Fig. 2 that the analytical MDF model reproduces the overall shape and the period of quasi-oscillations in the wake potential obtained from the *ab initio* calculations. The main quantitative difference is seen to be in the magnitude of the main peak and in the amplitudes of quasi-oscillations, which appear larger in the MDF model than in the *ab initio* case. For example, the ratio of the MDF to *ab initio* data is ≈ 1.4 for the main peak and it increases from about 1.5 to about 2 for the amplitudes as the distance from the charged particle increases. Since the wake in Fig. 2 arises due to excitation of a low-frequency mode $\omega_{\rm low}$, it is possible that the observed difference arises due to the fact that the MDF model underestimates the static limit of the graphene polarization function, $\chi_j^0(q, \omega \to 0)$, in comparison to the *ab initio* calculations [10].

Acknowledgements

V.D. acknowledges support from the QuantiXLie Center of Excellence (Grant No. KK.01.1.1.01.0004). I.R. and L.K. acknowledge support from the Ministry of Education, Science and Technological Development of the Republic of Serbia (Projects No. 45005 and 32039). Z.L.M. acknowledges support from the Natural Sciences and Engineering Research Council of Canada (RGPIN-2016-03689).

REFERENCES

[1] H. Yan, X. Li, B. Chandra, G. Tulevski, Y. Wu, M. Freitag, W. Zhu, P. Avouris and F. Xia, Nat. Nanotech. 7, 330 (2012).

[2] A. Politano, Crit. Rev. Solid State Mater. Sci. 42, 99 (2017).

[3] I. Radović, D. Borka and Z. L. Mišković, Phys. Lett. A 375, 3720 (2011).

[4] V. Despoja, K. Dekanić, M. Šunjić and L. Marušić, Phys. Rev. B 86, 165419 (2012).

[5] H. Yan, T. Low, W. Zhu, Y. Wu, M. Freitag, X. Li, F. Guinea, P. Avouris and F. Xia, Nat. Photonics 7, 394 (2013).

[6] K. F. Allison and Z. L. Mišković, Nanotechnology 21, 134017 (2010).

[7] T. Marinković, I. Radović, D. Borka and Z. L. Mišković, Plasmonics 10, 1741 (2015).

[8] V. Despoja, T. Djordjević, L. Karbunar, I. Radović and Z. L. Mišković, Phys. Rev. B 96, 075433 (2017).

[9] V. Despoja, D. Novko, K. Dekanić, M. Šunjić and L. Marušić, Phys. Rev. B 87, 075447 (2013).

[10] T. Sohier, M. Calandra and F. Mauri, Phys. Rev. B 91, 165428 (2015).

INTERPLAY OF THE ION-SURFACE-COLLISION PARAMETERS AND THEIR ROLE IN THE NANOSTRUCTURE FORMATION

M. D. Majkić[1], N. N. Nedeljković[2] and R. J. Dojčilović[3]

[1] *University of Priština, Faculty of Technical Sciences, Kneza Miloša 7, 38220 Kosovska Mitrovica, Serbia*
[2] *University of Belgrade, Faculty of Physics, P.O. Box 368, 11001 Belgrade, Serbia*
[3] *University of Belgrade, Vinča Institute of Nuclear Sciences, P.O. Box 522, 11001 Belgrade, Serbia*

Abstract. We consider the highly charged Xe^{30+} ion impinging upon a metal surface covered with a thin dielectric film at moderate velocity, under arbitrary collision geometry. During the cascade neutralization inside the dielectric film the formation of the surface nanostructures (craters) occurs. The dependence of the neutralization energy on the system parameters (angle of incidence and dielectric constant) is demonstrated. The corresponding equipotential curves are used to discuss the values of the system parameters relevant for the crater formation.

1. INTRODUCTION

The formation of the surface nanostructers by the impact of individual highly charged ions (HCI) on the solid surface has been intensively studied both experimentally [1, 2] and theoretically [3]. However, only the normal incidence case has been analysed. In the present study, we consider the formation of the surface nanostructures (during the population of the intermediate Rydberg states) by the impact of HCI of charge Z upon a metal surface covered with thin dielectric film (relative dielectric constant ϵ) under arbitrary angle of incidence $\Phi_{\rm in}$ at moderate ionic velocity v. The relevant physical quantity for the analysis of the surface modification in the metal-dielectric-vacuum (MDV) system is the neutralization energy $W^{(Z,\rm MDV)}$, which we calculate within the framework of the quasi-resonant two-state vector model and micro-staircase model [4].

We extend our previous study [3] in which the influence of different dielectric materials on the value of the neutralization energy has been considered for the normal incidence case. We consider the behaviour of the neutralization energy for different combinations of the system parameters $(\Phi_{\rm in}, \epsilon)$. In order to stress the interplay of these parameters, we construct the equipotential curves for some characteristic values of the ionic neutralization energy.

2. INTERPLAY OF THE SYSTEM PARAMETERS

The interaction of the HCI with metal surface covered with a thin dielectric film induces both the cascade neutralization of these ions along their trajectories inside the film and the formation the surface nanostructures (craters) [2]. During the population of the intermediate Rydberg states the neutralization energy $W^{(Z,\mathrm{MDV})}$ is deposited into the dielectric. For moderate ionic velocity, which we consider in this study, both the deposited ionic kinetic energy $E^{(Z)}_{\rm k,dep}$ and ionic neutralization energy determine the size of the nanocrater, i.e., the total deposited energy is given by $E^{(Z)}_{\rm dep} = E^{(Z)}_{\rm k,dep} + W^{(Z,\mathrm{MDV})}$.

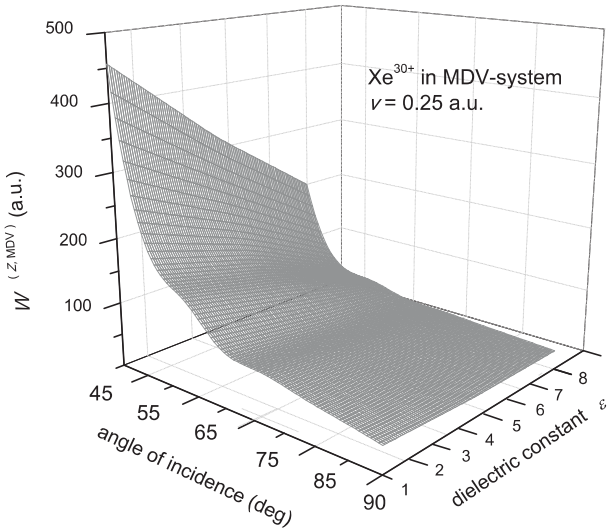

Figure 1. Neutralization energy $W^{(Z,\mathrm{MDV})}$ of the Xe^{30+} ion impinging at velocity $v = 0.25$ a.u. upon a metal surface ($\phi = 5$ eV and $U_0 = 15$ eV) covered with a thin dielectric film via angle of incidence $\Phi_{\rm in}$ and dielectric constant ϵ.

Within the TVM and micro-staircase model [4], modelling by a concept of the effective ionic charge the influence of dielectric film [3], we

calculate the neutralization energy for different angle of incidence [5]; deposited kinetic energy is determined by the corresponding stoping power [2]. The obtained deposited energy can be directly compared with experiment concerning the nanocraters formation [2], for the case of Xe^{Z+} ions impinging upon the Co surface covered with a thin Al_2O_3 film at normal incidence geometry. The agreement of the results with experiment has been found for the mean $< \epsilon >$ [3]. The aim of the present article is to emphasize the interplay of the angle of incidence and the dielectric constant and their simultaneous influence on the neutralization energy.

In Fig. 1 we present the neutralization energy $W^{(Z,\mathrm{MDV})} = W(\Phi_{\mathrm{in}}, \epsilon)$ for Xe^{30+} impinging a solid surface covered with thin dielectric film. The maximal value of the neutralization energy, which determines the maximal size of the surface nanostructures, corresponds to the minimal value of the angle of incidence Φ_{in} and minimal value of the dielectric constant ϵ. On the other hand, the minimal crater can be obtained by using the Xe^{30+} ion impinging on the metal surface covered with a thin dielectric material of the maximal value of ϵ under normal angle of incidence $\Phi_{\mathrm{in}} = \pi/2$.

3. EQUIPOTENTIAL CURVES

The relevance of the system parameters can be seen more directly if we consider the equipotential curves

$$W(\Phi_{\mathrm{in}}, \epsilon) = const \ . \tag{1}$$

In Fig. 2 we present the equipotential curves $\Phi_{\mathrm{in}} = \Phi_{\mathrm{in}}(\epsilon)$ for the given values of the neutralization energy $W^{(Z,\mathrm{MDV})} = 50$ a.u., 100 a.u., 150 a.u., ... 400 a.u., for Xe^{30+} ion. These curves are constructed by using the characteristic behaviour of the neutralization energy. From Fig. 2 one can see the existence of the continuous set of parameters Φ_{in} and ϵ for which the neutralization energy is of a given value. For example, for $Z = 30$ and angle of incidence $\Phi_{\mathrm{in}} = \pi/2, 3\pi/8$ and $\pi/4$, neutralization energy $W = 200$ a.u. can be obtained (approximately) by the film with $\epsilon = 1, 1.5$ and 2, while the neutralization energy $W = 50$ a.u. for $\epsilon = 3.5, 5.5$ and 7, respectively.

The equipotential curves presented in Fig. 2 give the information which system parameters yield the energy necessary for the crater formation. That is, we take into account that the neutralization energy necessary for the crater formation for the Xe^{30+} ion impinging upon a Co surface covered with dielectric thin film at normal angle of incidence, obtained in experimentally [2] (averaged value), is $W^{(Z,\mathrm{MDV})}_{\mathrm{expt}} = 81.4$ a.u. The corresponding equipotential curve is presented by dashed line in Fig. 2. We see that, for example, for the considered characteristic angles of incidence $\Phi_{\mathrm{in}} = \pi/2, 3\pi/8$ and $\pi/4$ this energy can be achieved within the dielectric films with $\epsilon = 1.8$, 3.5, and 4.2, respectively.

According to the previous discussion, we see that, by using the particular collision geometry and dielectric material, one can select the system

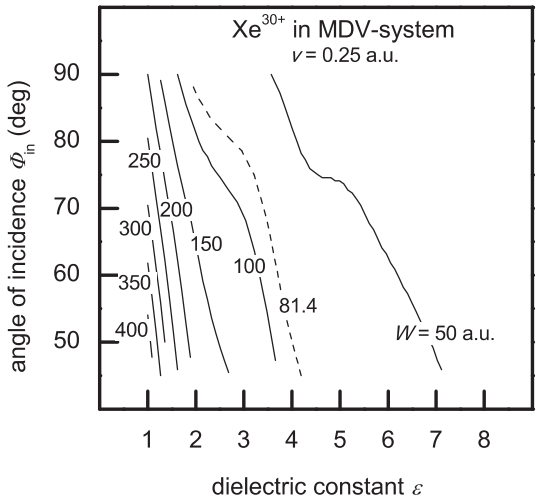

Figure 2. Equipotential curves for the neutralization energies $W^{(Z,\mathrm{MDV})} =$ 50 a.u, 100 a.u., 150 a.u., ... 400 a.u. of the Xe^{30+} ion impinging at velocity $v = 0.25$ a.u. upon a metal surface ($\phi = 5$ eV and $U_0 = 15$ eV) covered with a thin dielectric film. Dashed curve is the equipotential curve $W^{(Z,\mathrm{MDV})}_{\mathrm{expt}} = 81.4$ a.u. from [2] necessary for the crater formation.

parameters necessary for the fabrication of the nanostructures of a desired size (directly proportional to the value of the HCI neutralization energy).

This work is partially supported by the Ministry of Education, Science and Technological Development of the Republic of Serbia under the grants NO 171016, 172056, 45020.

REFERENCES

[1] A. S. El-Said, R. A. Wilhelm, R. Heller, M. Sorokin, S. Facsko and F. Aumayr, Phys. Rev. Lett. 117, 126101 (2016).

[2] R. E. Lake, J. M. Pomeroy, H. Grube and C. E. Sosolik, Phys. Rev. Lett. 107, 063202 (2011).

[3] M. D. Majkić, N. N. Nedeljković and R. J. Dojčilović, Mater. Res. Express 4, 095027 (2017).

[4] N. N. Nedeljković, M. D. Majkić, D. K. Božanić and R. J. Dojčilović, J. Phys. B: At. Mol. Opt. Phys. 49, 125201 (2016).

[5] N. N. Nedeljković, M. D. Majkić and M. A. Mirković, this conference (2018).

EFFECT OF THE IONIC CORE POLARIZATION ON THE NEUTRALIZATION IN A DIELECTRIC FILM AT METAL SURFACE

M. D. Majkić[1], N. N. Nedeljković[2], R. J. Dojčilović[3] and M. A. Mirković[4]

[1] *University of Priština, Faculty of Technical Sciences, Kneza Miloša 7, 38220 Kosovska Mitrovica, Serbia*
[2] *University of Belgrade, Faculty of Physics, P.O. Box 368, 11001 Belgrade, Serbia*
[3] *University of Belgrade, Vinča Institute of Nuclear Sciences, P.O. Box 522, 11001 Belgrade, Serbia*
[4] *University College of Civil Engineering and Geodesy, Belgrade, Serbia*

Abstract. We consider the highly charged Ar^{Z+}, Kr^{Z+} and Xe^{Z+} ions impinging upon a metal surface covered with a thin dielectric film at moderate velocity, under arbitrary angle of incidence. These ions are partially neutralized after successive population of the intermediate Rydberg states, which occurs inside the dielectric film. We calculate the corresponding neutralization energy, by taking into account the ionic core polarization. The influence of the type of the ion on the surface nanostructures is briefly discussed.

1. INTRODUCTION

The highly charged ions (HCI) have been intensively used as a tool for the solid surface modifications, see [1] and references therein. For low ionic velocity, the ions are totaly neutralized and only the neutralization energy contributes to the formation of the surface nanostructures. On the other hand, at moderate velocity the ions could be partially neutralized, and both the kinetic energy and neutralization energy, determine the size of the nanofeatures obtained by their individual impact on surface.

The ArVIII, KrVIII and XeVIII ions colliding with a metal surface have been studied considering the population probabilities in the grazing incidence case [2] and ArXV, KrXV and XeXV ions for arbitrary collision geometry [3], both in the metal-vacuum system (MV-system). In this article

we extend our analysis to the Ar^{Z+}, Kr^{Z+} and Xe^{Z+} ions in the metal-dielectric-vacuum system (MDV-system) and consider the influence of the core polarization on the neutralization energy $W^{(Z,\mathrm{MDV})}$, deposited in the system during the neutralization cascade $Z \to Z-1 \to Z-2$ ....

2. ROLE OF THE IONIC CORE POLARIZATION

During the ionic motion, inside the dielectric film, at each micro-step (of a given macro cascade) the intermediate ionic Rydberg state of the ion with core charge Q are populated through the quasi-resonant electron pick-up from the metal surface. We take into account that the electron capture is into the field of polarized ionic core. The neutralization process is finished at minimal ion-surface distance $R = R_{\mathrm{min}}$, with nonzero final ionic charge Q_{fin}, the quantity which determines the neutralization energy. During the neutralization cascade, the ionic neutralization energy is deposited (together with the kinetic energy) into the dielectric and the nanostructures are formed.

For describing the fine structure of the neutralization process we use the quasi-resonant two-state vector model (TVM) and micro-staire case model [4]. The neutralization energy in the MDV-system is defined within the framework of the recently developed concept of the effective ionic charge [5]. That is, we use the equivalence between the Rydberg state neutralization process in the MDV-system and MV-system, from the standpoint of the population probabilities. By this procedure we obtain the effective ionic charges Z_{eff} for the Ar^{Z+}, Kr^{Z+} and Xe^{Z+} ions, which are independent on the ionic velocity and the collision geometry. In the first approximation, considering the interactions in the MDV-system, we obtain the quantities Z_{eff}, which are also independent on the type of the ions.

The second important fact is the equality of the final ionic charges of these ions, which is a direct consequence of the behaviour of the intermediate population probabilities $P^{(Q,j)}$, used for determination of the Q_{fin} by the following expression:

$$Q_{\mathrm{fin}}^{MV} = Q_{\mathrm{min}}^{(Z)}(R) - \sum_{j=j_{\mathrm{min}}^{(Q)}}^{\tilde{j}_{\mathrm{max}}^{(Q)}} P^{(Q,j)}, \quad Q = Q_{\mathrm{min}}^{(Z)}, R = R_{\mathrm{min}} \ , \qquad (1)$$

where $Q_{\mathrm{min}}^{(Z)}$ is the ionic charge characteristic for the last macro step at ion-surface distance R. That is, the population cascades of these ions (in which the characteristic different Rydberg levels are populated) are localized at nearly the same ion-surface distances, with the probabilities of the same order of magnitude. This circumstance is known for the grazing incidence case [2] and for low ionic velocity, but also holds for moderate ionic velocity and for arbitrary collision geometry.

These facts give us the possibility to use the same value of $Z_{\rm eff}$ for all considered geometries and ions in the definition of the neutralization energy:

$$W^{(Z,\rm MDV)} = W_{Z_{\rm eff},\rm pot} - W_{Q_{\rm fin,eff},\rm pot} = W^{(Z_{\rm eff},\rm MV)} \ , \qquad (2)$$

where $Q_{\rm fin,eff}$ is defined by (1) for $Z = Z_{\rm eff}$.

3. RESULTS

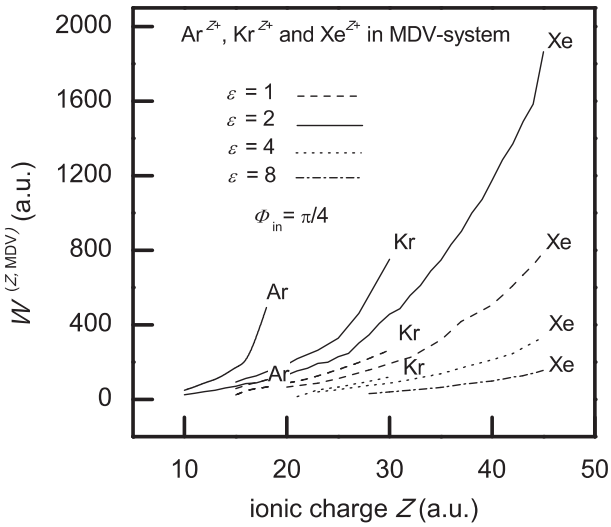

Figure 1. Neutralization energies $W^{(Z,\rm MDV)}$ of the $\rm Ar^{Z+}$, $\rm Kr^{Z+}$ and $\rm Xe^{Z+}$ ions impinging at velocity $v = 0.25$ a.u. upon a metal surface ($\phi = 5$ eV and $U_0 = 15$ eV) covered with a thin dielectric film (dielectric constant $\epsilon = 2, 4$ and 8) for the angle of incidence $\Phi_{\rm in} = \pi/4$. Case $\epsilon = 1$ (solid curves) is the $W^{(Z,\rm MV)}$ energy.

In Fig. 1 we present the neutralization energy $W^{(Z,\rm MDV)}$ for $\rm Ar^{Z+}$, $\rm Kr^{Z+}$ and $\rm Xe^{Z+}$ ions in the MDV-system, for moderate ionic velocity $v = 0.25$ a.u. relevant for the nanocraters formation [6]. These ions have the same core charge Z but different core polarization. As an example, we present the results for the angle of incidence $\Phi_{\rm in} = \pi/4$.

For $\rm Ar^{Z+}$ considered in Fig. 1 we present only the values for $\epsilon = 1$ (MV-system) and $\epsilon = 2$. For larger ϵ, the quantity $Q_{\rm fin,eff}$, which determines the state of the ion in front of the surface, necessary for the calculation of the neutralization energy in the MDV-system, can not be obtained within the framework of our model [5] because the effective core charge is small: $Z_{\rm eff} < 10$ for $Z < 18$. For the similar reason, in Fig. 1 we present the

results for Kr^{Z+} and dielectric constants $\epsilon = 1, 2$ and 4, and for Xe^{Z+} and $\epsilon = 1, 2, 4$ and 8.

With increasing of the ionic core polarization, $Ar^{Z+} \rightarrow Kr^{Z+} \rightarrow Xe^{Z+}$, the neutralization energy decreases. This is a direct consequence of the behaviour of the corresponding potential energies, i.e., of the electronic structures of these ions. With increasing of the relative dielectric constant the difference between the values of the neutralization energies is smaller.

The obtained core-polarization dependence of the neutralization energy represents important information for the energy partition in the considered system. That is, beside the influence of the particular collision geometry and dielectric properties of the film, the type of the ion also plays a role in the nanostructure formation.

This work is partially supported by the Ministry of Education, Science and Technological Development of the Republic of Serbia under the grants NO 171016, 172056, 45020.

REFERENCES

[1] F. Aumayr, S. Facsko, A. S. El-Said, C. Trautmann and M. Schleberger, J. Phys: Condens. Matter 23, 393001 (2011)

[2] N. N. Nedeljković, M. D. Majkić and S. M. D. Galijaš, J. Phys. B: At. Mol. Opt. Phys. 45, 215202 (2012)

[3] M. D. Majkić, N. N. Nedeljković, D. K. Božanić and R. J. Dojčilović, Contributed papers (28th SPIG, Belgrade) p 166 (2016).

[4] N. N. Nedeljković, M. D. Majkić, D. K. Božanić and R. J. Dojčilović, J. Phys. B: At. Mol. Opt. Phys. 49, 125201 (2016).

[5] M. D. Majkić, N. N. Nedeljković and R. J. Dojčilović, Mater. Res. Express 4, 095027 (2017).

[6] R. E. Lake, J. M. Pomeroy, H. Grube and C. E. Sosolik, Phys. Rev. Lett. 107, 063202 (2011).

INFLUENCE OF THE COLLISION GEOMETRY ON THE NEUTRALIZATION OF HIGHLY CHARGED IONS AT METAL SURFACE COVERED WITH A THIN DIELECTRIC FILM

N. N. Nedeljković[1], M. D. Majkić[2] and M. A. Mirković[3]

[1] *University of Belgrade, Faculty of Physics, P.O. Box 368, 11001 Belgrade, Serbia*
[2] *University of Priština, Faculty of Technical Sciences, Kneza Miloša 7, 38220 Kosovska Mitrovica, Serbia*
[3] *University College of Civil Engineering and Geodesy, Belgrade, Serbia*

Abstract. We consider the population of the intermediate Rydberg states of the highly charged Xe^{Z+} ions impinging upon a metal surface covered with a thin dielectric film at moderate velocity, under arbitrary collision geometry. Within the quasi-resonant two-state vector model and micro-staircase model we calculate the final ionic charge, the quantity necessary for the calculation of the neutralization energy deposited in the dielectric after neutralization cascade $Z \to Z-1 \to Z-2 \ldots$. The influence of the interaction geometry and the film properties on the value of the neutralization energy is demonstrated, and the relevance of this energy for the formation of the surface nanostructures is briefly discussed.

1. INTRODUCTION

The interaction of the slow highly charged ions (HCI) with solid surfaces and the formation of nanostructures by their impact has been intensively studied, see [1] and references therein. That is, depending on their structure and properties the materials respond differently to the energy deposition by HCIs, resulting in different types of nanostructures. In the case of CaF_2, BaF_2, SiO_2, HOPG ... nanohillocks were observed, craters (pits) in Si, PMMA, KBr, KCl, and carbon nanomembranes, caldera structures were formed in TiO_2,... For very low ionic velocity only the neutralization energy, equal to the ionic potential energy, contributes to the surface modification.

For moderate ionic velocity, what we consider in this study, the required energy consists both of the deposited kinetic energy and the ionic neutralization energy [2] (craters in Co surface covered with thin Al_2O_3 film [3]). This study is devoted to the influence of the collision geometry on the HCI neutralization in the interaction with metal surface covered with a thin dielectric film (MDV-system). To obtain the final ionic charge $Q_{\rm fin}^{(Z)}$, the quantity necessary for the calculation of the ionic neutralization energy, we use the quasi-resonant two-state vector model (TVM) and micro-staircase model [4], which take into account the specific quantum features of the population dynamics. The cascade neutralization process with decreasing of the ionic charge $Q = Z \to Q = Z-1... \to Q_{\rm fin}^{(Z)}$ occurs inside the dielectric which is perturbed due to the ionic motion and the surface nanostructure formation.

2. NEUTRALIZATION ENERGY

We consider the population of the HCI intermediate Rydberg states during the neutralization cascade, which occurs in front of the metal surface inside the perturbed dielectric film at arbitrary collision geometry, see Fig. 1. Simultaneously with the neutralization process inside the dielectric film the formation of the nanocraters occurs [3].

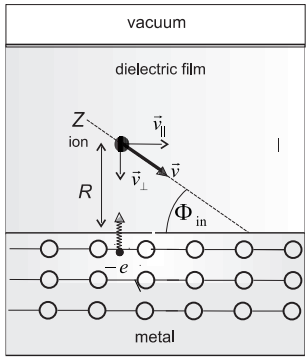

Figure 1. Neutralization of the Xe^{Z+} ion impinging at velocity v upon a metal surface covered with a thin dielectric film at arbitrary angle of incidence $\Phi_{\rm in}$.

In our previous study of the cascade neutralization concerning the neutralization energy necessary for the nanocrater formation in the MDV-system [2], only the normal incidence case $\Phi_{\rm in} = \pi/2$ has been considered. The influence of the collision geometry is known only in the absence of dielectric film (metal-vacuum, MV-system) [5]. In this study we calculate the neutralization energy of the Xe^{Z+} ion impinging upon a solid surface at arbitrary angle of incidence $\Phi_{\rm in}$, at velocity $v = 0.25$ a.u.

To calculate the neutralization energy inside the dielectric we use the TVM and micro-staircase model [4] accompanied by the concept of the effective ionic charge [2]. That is, we consider as equivalent the population of the Rydberg level E of the HCI of the core charge Z in the MDV-system and the population of the effective Rydberg level $E_{\rm eff}$ of the HCI of the effective ionic charge $Z_{\rm eff}$ in the MV-system. From the standpoint of the electron tunnelling process, the effective ionic charge follows from the equality of the barrier widths δ of the potential barriers $U^{(Z)}_{\rm MDV}$ and $U^{(Z_{\rm eff})}_{\rm MV}$ in the MDV-system and MV-system, respectively:

$$\delta\{U^{(Z)}_{\rm MDV} atE\} = \delta\{U^{(Z_{\rm eff})}_{\rm MV} atE_{\rm eff}\} \ . \tag{1}$$

The HCI of the initial charge $Q = Z$ (in vacuum) enters the dielectric with the potential energy $W_{Z_{\rm eff},{\rm pot}}$, where $Z_{\rm eff}$ is defined according to Eq. (1). Inside the dielectric, the neutralization cascade begins and causes the perturbation of the dielectric, which contributes (together with the deposition of the kinetic energy) to the dielectric modification and crater formation at film surface. After the neutralization cascade, at ion-surface distance $R = R_{\rm min}$, the ions have the nonzero potential energy $W_{Q_{\rm fin,eff},{\rm pot}}$, which corresponds to the final ionic charge $Q^{\rm MDV}_{\rm fin} \neq 0$. The neutralization energy in the MDV-system can be expressed by the relation:

$$W^{(Z,{\rm MDV})} = W_{Z_{\rm eff},{\rm pot}} - W_{Q_{\rm fin,eff},{\rm pot}} = W^{(Z_{\rm eff},{\rm MV})} \ . \tag{2}$$

3. RESULTS

In the case of the moderate ionic velocity v, which we analyze in this article, the required energy for the nanocrater formation consists of the deposited kinetic energy and neutralization energy $W^{(Z,{\rm MDV})}$ [2, 3]. In Fig. 2 we present the quantity $W^{(Z,{\rm MDV})}$ via angle of incidence $\Phi_{\rm in}$ for the ionic charge $Z \in [20, 45]$, for three different values of the dielectric constant $\epsilon = 2, 4$ and 8 and in the absence of the film ($\epsilon = 1$). With increasing the angle of incidence the neutralization energy decreases, which is a direct consequence of the behaviour of the final ionic charge. That is, with increasing of the angle of incidence the normal component of the ionic velocity $v_\perp$ increases and, simultaneously, the parallel component $v_\parallel$ decreases, which induces the decreasing of the population probabilities. Consequently, the final ionic charge increases and, according to Eq. (2), the neutralization energy decreases.

For a given collision geometry the neutralization energy depends on the film properties. With an increase of the dielectric constant, the quantity $W^{(Z,{\rm MDV})}$ decreases, compare solid, dashed, dotted and dash-dotted curves in Fig. 2. This decreasing can be easily understood if we take into account that the effective core charges decrease with increasing of ϵ.

With the knowledge of the neutralization energy we are able to discuss the total deposited energy necessary for the formation of the particular

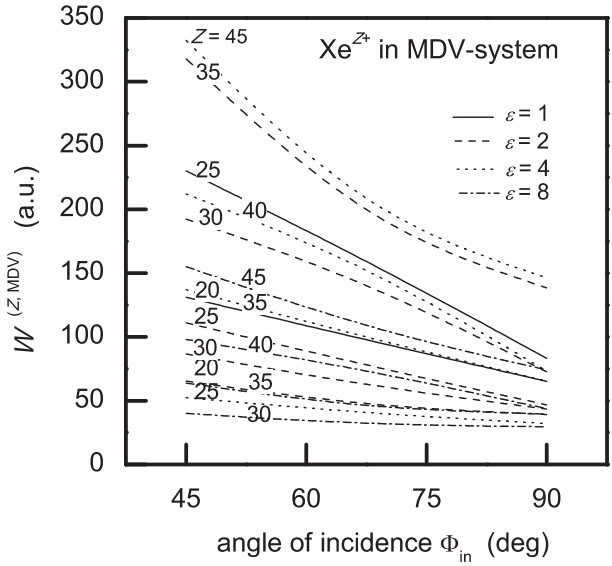

Figure 2. Neutralization energy $W^{(Z,\mathrm{MDV})}$ of the Xe^{Z+} ion impinging at velocity $v = 0.25$ a.u. upon a metal surface ($\phi = 5$ eV and $U_0 = 15$ eV) covered with a thin dielectric film ($\epsilon = 2, 4$ and 8) via angle of incidence Φ_{in}. Solid line ($\epsilon = 1$) is the $W^{(Z,\mathrm{MV})}$ energy.

nanostructure and to specify the system parameters for which this energy could be achieved.

This work is partially supported by the Ministry of Education, Science and Technological Development of the Republic of Serbia under the grant NO 171016.

REFERENCES

[1] A. S. El-Said, R. A. Wilhelm, R. Heller, M. Sorokin, S. Facsko and F. Aumayr, Phys. Rev. Lett. 117, 126101 (2016).

[2] M. D. Majkić, N. N. Nedeljković and R. J. Dojčilović, Mater. Res. Express 4, 095027 (2017).

[3] R. E. Lake, J. M. Pomeroy, H. Grube and C. E. Sosolik, Phys. Rev. Lett. 107, 063202 (2011).

[4] N. N. Nedeljković, M. D. Majkić, D. K. Božanić and R. J. Dojčilović, J. Phys. B: At. Mol. Opt. Phys. 49, 125201 (2016).

[5] M. D. Majkić, R. J. Dojčilović and N. N. Nedeljković, Contributed papers (28th SPIG, Belgrade) p 162 (2016).

INVESTIGATIONS INTO PROPERTIES OF YTTRIUM-DOPED ZIRCONIUM OXIDE FILMS

A. N. Chumakov[1], A. A Shevchenok[2], L. V. Baran[3],
V. V. Malyutina-Bronskaya[4], A. G. Karoza[1], N. A. Bosak[1], A. A. Ivanov[1]

[1]*State Scientific Institution "B. I. Stepanov Institute of Physics National Academy of Sciences of Belarus"*
[2]*Powder Metallurgy Institute, National Academy of Sciences of Belarus*
[3]*Belarusian State University*
[4]*SSPA "Optics, Optoelectronics and Laser Technology" of the National Academy of Sciences of Belarus*

Abstract. Zirconium oxide films doped with yttrium oxide were deposited on a silicon substrate using high-frequency (20-30 kHz) multi-pulse laser evaporation of a ceramic target in vacuum. The structure of the films was investigated using an atomic force microscope. Transmission spectra in the visible, near IR, and middle IR regions, and current-voltage and capacity-voltage characteristics were studied. It is shown that doping of zirconium oxide with yttrium oxide causes a significant reduction in the transmission of the film in the spectral region from 1 to 10 μm.

INTRODUCTION.

Zirconium dioxide-based nanomaterials are of considerable interest for the development of nanotechnology [1, 2]. The production of ZrO_2-based materials with required performance characteristics rests on the doping of zirconium dioxide with oxides of alkaline- or rare-earth metals. This makes possible the obtaining of the high-temperature ZrO_2 (either tetragonal or cubic) forms at relatively low temperatures [3]. The ZrO_2 compounds are used to produce both the structural (turbine blades, cutting tools) and functional materials (solid-state current sources, medical products, sputtering targets) [4]. The high-frequency laser impact on a ceramic sputtering target [5] is capable of providing the efficient film deposition. The work is aimed at making the laser-deposited zirconium oxide films doped with yttrium oxide and conducting a complex research of their properties.

EXPERIMENTAL DETAILS AND RESULTS.

The experimental setup included an Nd:glass laser (λ = 1.06 μm), an optical system to transport laser radiation to a sputtered target, a vacuum chamber, and measuring and diagnostic facilities. To get a multi-pulse mode of laser generation with a high pulse repetition rate, a passive Q-switch (γ-irradiated crystalline lithium fluoride, LiF, with F_2^--color centers) was placed in the laser cavity. The repetition frequency of laser pulses was varied by changing the laser

pump level and the Q-switch optical density; the laser pulse duration at a half-height was ~ 85 ns. Effective deposition of thin films was achieved at a 100 MW/cm^2 laser power density and a 20 − 30 kHz pulse repetition rate. The films were deposited at a pressure of 2.7 Pa.

To produce the thin films under consideration, ceramic targets obtained from a high purity zirconium oxide powder (with a base material content of 99.96% by weight) were employed. Yttrium oxide powder was used as an alloying additive with a concentration of 5% by weight. Ceramic targets were fabricated by static moulding with subsequent annealing in air at a temperature of 1580° for 2 hours. The topography of the sample surface was investigated using a Solver P47-Pro scanning probe microscope (NT-MDT, Russia) in a semi-contact mode. Measurements of electrophysical characteristics of doped zirconium oxide films were carried out with an E7-20 automated immittance meter (Belarus) at room temperature. Capacitance was measured at two frequencies: 1 MHz and 100 kHz.

Transmission of optical radiation by thin films in the near infrared (IR) spectral region was measured with a Carry 500 Scan spectrophotometer. Transmission spectra in the far IR region were recorded using a NEXUS infrared Fourier spectrometer (Thermo Nicolet) in the 400–4000 cm^{-1} range with a 2 cm^{-1} resolution after 128 scans. The microstructure of yttrium oxide-doped zirconium oxide thin films on a KDB-12 (100) silicon substrate was studied by way of atomic force microscopy images with the 2×2 μm field of vision (Fig. 1).

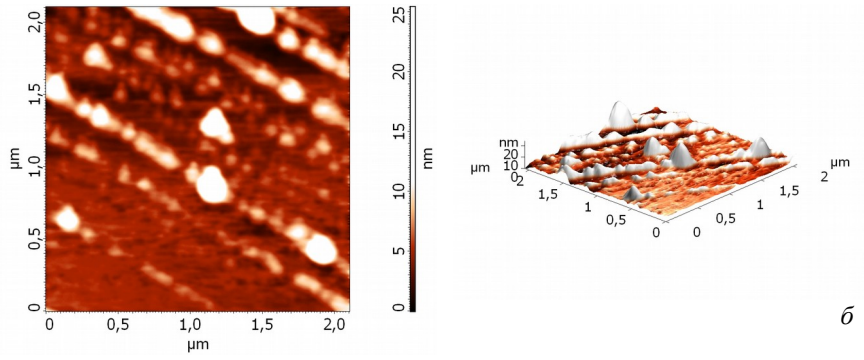

а *б*

Figure 1. Topography of laser-deposited (ZrO_2 + 5%Y_2O_3) thin film surface.

It was found that the average lateral size of the particles was 55.9 nm and their height did not exceed 25 nm.

The surface structure of the doped zirconium oxide thin film on the 20*20 μm silicon surface and the film profile along the scanning line are shown in Fig. 2. Craters 50 nm in depth and up to 2 μm wide were found on the film surfaces.

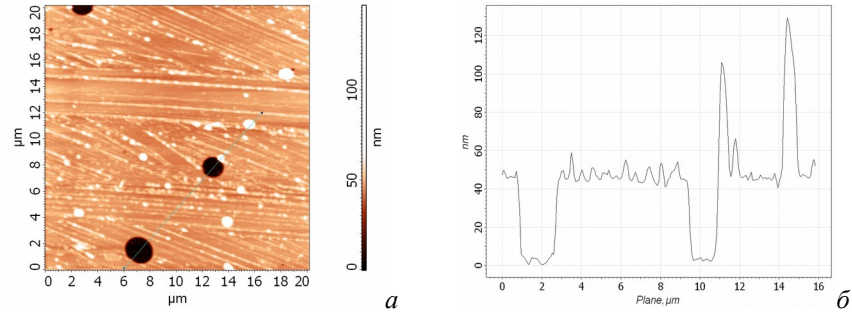

а *б*

Figure 2. Surface structure (a) and profile (b) along the scanning line of the zirconium oxide thin film on silicon.

The transmission spectrum of the ZrO_2+5%Y_2O_3 film on a silicon substrate in the visible and near IR regions is shown in Fig. 3.

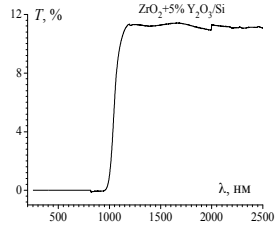

Figure 3. Transmission spectrum of ZrO_2 + 5% Y_2O_3 film on a silicon substrate in the visible and near IR regions.

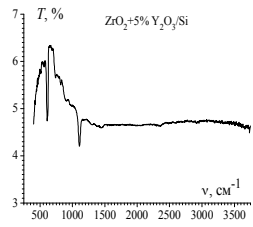

Figure 4. Transmittance spectrum of the ZrO_2+5%Y_2O_3 film on a silicon substrate in the mid-infrared region.

In the range from 1 μm to 2.5 μm, the transmission of the film reaches 12%, and in the middle IR range from 3 μm to 6 μm it is around 5% (Fig. 4).

Current-voltage (I-V) and capacity-voltage (C-V) characteristics of the test film on a silicon substrate are shown in figures 5 and 6. The analysis of the I-V curve shows that the mechanism for the current flow is mainly governed by the film morphology, in particular by the presence of nanoscale particles, and has a hopping and tunneling character. On the I-V curves, the areas with negative differential resistance are visible (Fig. 5), which are reproduced in the repeated measurement. The presence of such sites indicates a possible blocking of conductivity caused by the recharge processes of discrete surface states associated with nanoparticles and nanocrystalline inclusions. It should also be noted that in the matrix surrounding the nanocrystalline inclusions, there may be additional energy states associated with individual nanoparticles which are beyond the nanocrystalline inclusion. The presence of nanoparticles in the dielectric layer or the surface states of the interface can contribute to the occurrence of hysteresis effects.

Zirconium oxide, ZrO_2, is a material with high dielectric permeability (k ≈23). Its C-V characteristic should have a form typical of MOS-structures, but

the presence of discrete states associated with the morphology of the film is manifested on the CV curve as multiple maxima and hysteresis. This suggests that discrete states have a wide energy spectrum.

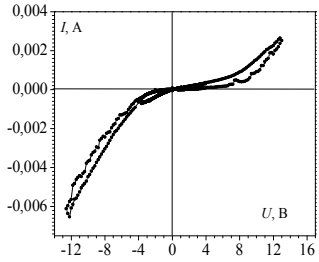

Figure 5. Volt-ampere characteristic of doped zirconium oxide film on silicon.

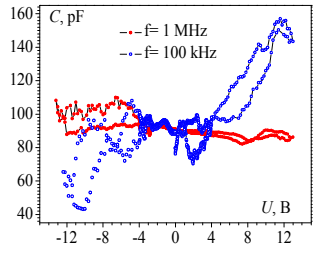

Figure 6. Capacity-voltage characteristic of the structure of zirconium doped oxide on silicon.

CONCLUSION.

High-frequency pulsed laser deposition was used to produce zirconium oxide films doped with yttrium oxide (a mass fraction of 5%) on a silicon substrate. The obtained films feature a granular structure with an average lateral size of individual particles of 56 nm and a height of 25 nm. The transmission of the zirconium oxide films on the silicon substrate reaches 12% in the spectral range from 1 μm to 2.5 μm, and in the 3 – 6 μm range, it is around 5%. Current-voltage and capacity-voltage curves of zirconium oxide films are characterized both by nonlinearity and by the presence of hysteresis.

Acknowledgements

This work is partially supported by the BRFFI Projects No. F17-108.

REFERENCES

[1] I. P. Suzdalev, the Success chemistry. 70, № 3, 203 (2001).
[2] V. F. Petrunin, Inorganic materials. 40, № 3, 303 (2004).
[3] V. Ya. Shevchenko, S. M. Barinov. Technical ceramics, p. 3. 197 (M.: "Science", 1993).
[4] A. Neubrand, R. Schafer. "Proc. of the 5 Int. Conf. "HT CMC", Seattle, 2005, 253.
[5] L. I Minko, A. N. Chumakov, N. A. Bosak, Quantum electronics, 17, No 11, 1480 (1990).

SYNTHESIS AND SURFACE ENGINEERING OF CARBON NANOPARTICLES BY ELECTRICAL DISCHARGES GENERATED INSIDE AND IN CONTACT WITH LIQUID

V. S. Burakov, V. V. Kiris, N. N. Tarasenka, A. A. Nevar, M. I. Nedelko, N. V. Tarasenko

B. I. Stepanov Institute of Physics, National Academy of Sciences of Belarus, 68 Nezalezhnasti Ave., 220072 Minsk, Belarus

Abstract. The capabilities of high-voltage discharge between two electrodes submerged into liquid and a gas-liquid interfacial discharge generated between a capillary (hollow needle) with flowing argon and liquid surface were studied for synthesis of carbon quantum dots. The results of the solution chemistry induced at the plasma-liquid interface for surface engineering of nanoparticles are discussed.

1. INTRODUCTION

Among the different discharge systems used for the generation of atmospheric-pressure plasmas, electrical discharges ignited inside or in contact with liquid have attracted much attention for various technological applications, including synthesis of nanoparticles (NPs) [1-4]. The main advantages of electrical discharges between two electrodes submerged in liquid (EDL) for the NPs synthesis include high production rates, versatility and possibility of control over the particle size and size distribution function during the synthesis process.

The other type of liquid assisted electrical discharges is based on the gas-liquid interfacial discharge produced in contact with liquid. Igniting the plasma between an electrode in the gas phase and another immersed into the electrolyte solution results in the current flow through the electrolyte and in the reactions at the anode and cathode. At the anode, oxidation reactions lead to dissolution of the solid metal into metal cations which are then reduced by the microplasma to nucleate metal NPs.

To generate stable glow discharges at atmospheric pressure, spatial confining of plasmas to dimensions of 1 mm or less are required [5]. As a result, the formed microplasma is characterized by relatively high current densities (high electron concentrations), non-thermal characteristics (relatively low gas temperatures) and non-Maxwellian electron energy distributions [5]. For nanomaterials synthesis atmospheric-pressure microplasmas offer many advantages such as reduction in cost, non-equilibrium chemistry, self-

organization phenomena, high densities of radicals and new possible chemical reaction pathways.

It should be noted that the liquid assisted electrical discharges both within a liquid and at the gas-liquid interface were successfully applied for synthesis of NPs of metals, their oxides and carbides.

In this paper electrical discharge plasma in liquid was used for synthesis of carbon NPs. In addition, the targeted changes of the NPs surface properties could be selectively achieved via treatment of the as-prepared NPs in the gas-liquid interfacial discharge produced in contact with the colloidal solution.

2. EXPERIMENTAL

The two types of plasma-liquid systems used in this work i.e. high-voltage discharge between two electrodes submerged into liquid and gas-liquid interfacial discharge have been described elsewhere [4, 6]. Briefly, a spark discharge was ignited in the solution between two graphite rods employed as electrodes immersed in water. The distance between the electrodes during the experiment was less than 1 mm and controlled to maintain the discharge parameters approximately constant. The alternating current discharge was initiated by applying a high-voltage pulse of 8.5 kV. The peak current was about 17 A with a duration of a single discharge pulse of 25 μs.

The discharge in contact with liquid was ignited between a stainless-steel capillary electrode served as cathode and the surface of the liquid. The stainless steel capillary tube (800 μm outer, 500 μm inner diameter, 5 cm length) was located at the distance of 1-8 mm above the liquid surface. The experiments were performed with argon flowing through the capillary tube. The argon flow rate was measured with a mass flow controller and could be varied from 10 to 60 sccm. The discharge was ignited by applying the high voltage of 3.6 kV using a dc power supply. The discharge current was kept constant in the range of 1 - 5 mA.

The composition, morphology and optical properties of the synthesized and plasma treated NPs were studied by TEM, EDX, PL, FTIR, Raman and ultraviolet–visible spectroscopy.

3. RESULTS AND DISCUSSION

The NPs obtained by the spark discharge in water looked like isolated spherical NPs with the average diameter about 3 nm as it followed from the TEM analysis. The sizes of the NPs were mainly distributed in the range of 2–5 nm (Fig. 1). The HRTEM images (Fig. 1b) of separate particles revealed that particles are monocrystalline and the measured interplanar distances were found to be 2.06 Å that correspond to the reflections between (111) planes in cubic carbon having diamond-like structure. The SAED analysis further proves the formation of diamond-like structures. In the SAED patterns obtained the rings attributable to the (111) plane of the C with diamond-like structure and orthorhombic carbon phases were observed, while the rings corresponding to graphitic structure were absent.

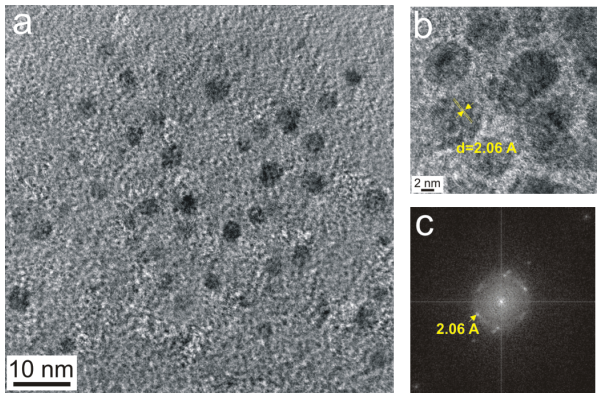

Figure 1. Morphology of C NPs prepared by electrical discharge in water: a – TEM image; b – HRTEM of the selected group of particles with the interplanar spacing of 2.06 A indicated that the NPs have diamond-like structure; c – FFT of the 1b image

For the further studies of the sample Raman and XRD techniques were used. The Raman spectrum contained two distinct peaks: narrow G-band near 1578 cm^{-1} attributable to the ordered graphite and the broadened D-band at 1349 cm^{-1} which is associated with disodered carbon and the presence of a carbon sp^3 defects in the prepared C-NPs. It should be noted that the D-band is rather broad thus covering the range 1310-1320 cm^{-1}, typical to the diamond and orthorhombic carbon structures.

Analogically, the results of the X-ray diffraction studies exhibited the broad peak in the region 20-40˚, so-called halo, indicated a presence of small particles with various carbon phases in the sample. Nevertheless, the diamond-like phases, observed in TEM measurements most probably are presented in the sample but only as very small particles that are produced through the condensation mechanism. It is known that NPs in electrical discharge are formed through two competing mechanisms namely via the condensation of the evaporated electrode material that are atoms, ions and small clusters with their subsequent growth into the NPs; and in result the destroying of the electrodes with the formation of the particles of much larger sizes. As for Raman studies all the colloid was deposited onto the substrate the larger and better crystallized particles with graphite structure formed by the second route are dominant that can explain the contradiction of Raman and TEM results.

To modify the properties of NPs the colloidal solution of C NPs synthesized by spark discharge in liquids was treated by reactive non-equilibrium gas-liquid discharge plasma contacting with the solution. The results of these studies showed that the different surface chemistry activated in different

solutions could be due to different reactions induced by plasma electrons at the plasma–solution interface compared to plasma–water one. Changing the surface groups is believed to be effective in improvement of photoluminescence properties of the synthesized C-dots.

4. CONCLUSION

Thus, the EDL technique has been demonstrated to be suitable for the preparation of carbon quantum dots with sizes 2-5 nm and narrow size distribution that are the part of the requirements for the practical applications. In addition, the treatment of NPs by reactive non-equilibrium gas-liquid discharge plasma contacting with a colloidal solution can offer great opportunities for the NPs surface engineering and an improvement of the photoluminescent properties. Carbon NPs with size less than 10 nm – so called quantum dots due to their excellent biocompatibility, chemical inertness, and size-selective photoluminescence properties may find increasing applications in modern biotechnology as more suitable alternatives to the traditional semiconductor quantum dots.

Acknowledgements

The work was supported by the National Academy of Sciences of Belarus under project Convergence 2.4.06 and the Belarusian Foundation for Fundamental Researches under Grant No. F18 MS-020. The authors would like to thank Dr. A.G. Karoza for the FTIR and Dr. A.P. Stupak for luminescence measurements and fruitful discussions.

REFERENCES

[1] W.G. Graham, K.R. Stalder, J. Phys. D: Appl. Phys., **44**, 174037 (2011).
[2] J. Patel, L. Nemcova, P. Maguire, W.G. Graham and D Mariotti, Nanotechnology, **24** 245604 (2013).
[3] G. Saito and T. Akiyama, J. of Nanomaterials, **2015**, 123696 (2015).
[4] V.S. Burakov, V.V Kiris, M.I. Nedelko, N.N. Tarasenka, A.A. Nevar, N. V. Tarasenko, Eur. Phys. J. Appl. Phys., 79 10801 (2017).
[5] D. Mariotti, R.M. Sankaran, J. Phys. D: Appl. Phys. **44,** 174023 (2011)D. Mariotti, J. Patel, V. Švrček, P. Maguire, Plasma Processes Polym. 9, 1074 (2012).
[6] V.S. Burakov, A.A. Nevar, M.I. Nedelko and N.V. Tarasenko, Rus. J. Gen. Chem. **85**, 17 (2015).

SURFACE ENGINEERING OF SILICON NANOCRYSTALS BY PLASMA CONTACTING WITH COLLOIDAL SOLUTION

V.S. Burakov, V.V. Kiris, N.N. Tarasenka, A.A. Nevar, M.I. Nedelko, N.V. Tarasenko

B. I. Stepanov Institute of Physics, National Academy of Sciences of Belarus, 68 Nezalezhnasti Ave., 220072 Minsk, Belarus

Abstract. The gas-liquid interfacial microplasma was used for surface modification of silicon nanoparticles (NPs) directly in solution. The possibility of the improvement of photoluminescent (PL) properties of silicon NPs by their treatment with non-equilibrium gas-liquid discharge plasma was demonstrated.

1. INTRODUCTION

Currently the post-synthesis surface modification of NPs is mostly relying on the traditional wet-chemical approaches. A promising alternative route for tuning the NPs surface chemistry to desirable characteristics can be developed based on the plasma-surface interactions. Electrical discharges generated in contact with liquid can initiate a variety of physical and chemical processes including the formation of various reactive species, which can be involved in particle surface passivation process. This effect can be applied for the improvement of NPs properties such as solubility, biocompatibility and photoluminescence adjusting them for achieving the optimal parameters suitable for practical applications. In this case the solvent composition is a crucial factor influencing the NPs surface change. For example, Mariotti et.al. [1] showed that the surface modification of silicon nanocrystals in ethanol by the formation of Si–O–R terminations resulted in the significant improvement of their optical characteristics. In the present paper the dc plasma in contact with colloidal solution was used for the modification of the Si-NPs surface and improvement of their PL properties.

2. EXPERIMENTAL

The initial Si colloids were prepared by electrical discharge ignited in the solution between two silicon plates employed as electrodes The detailed description of the experimental procedure can be found elsewhere [2]. To tailor surface properties of the NPs synthesized, the prepared colloids were treated by

the atmospheric pressure microplasma ignited in contact with the colloidal solution. In our experiments the microplasma of the gas-liquid interfacial discharge was generated in the double plasma jets regime. A schematic diagram of the microplasma-liquid system with double plasma jets is shown in Figure 1a. Two similar stainless steel capillary tubes (500 μm inside diameter, 5 cm length) that served as electrodes were located at a distance of 2 mm above the liquid surface. The experiments were carried out with argon flowing through the capillary tubes. The gas flow rate was measured with a mass flow controller and can be varied from 10 to 45 sccm. The discharge was ignited by applying a high voltage (about 3 kV). The dc voltage applied between two nozzle electrodes by a regulated power source in a constant current mode, resulted in the generation of two glow discharges that were in contact with the liquid surface. A ballast resistor (0.1 - 0.4 MΩ) limited the current and provided the stability of the discharge in the range of 1 - 5 mA.

The composition, morphology and optical properties of the synthesized and plasma treated NPs were studied by TEM, EDX, PL, FTIR, Raman and ultraviolet–visible spectroscopy.

3. RESULTS AND DISCUSSION

The typical TEM images of the silicon NPs prepared by the electrical discharge between two Si electrodes in water and ethanol showed separate and quasi-spherical particles with slightly different size distributions. The NPs obtained by the spark discharge in water were isolated and spherical with the average diameter about 5 nm. The sizes of the NPs prepared in ethanol were mainly distributed in the range of 6–13 nm.

Absorption and Raman scattering studies of the synthesized particles confirm their polycrystalline nature and cubic structure as the Raman peak centered at 518 cm^{-1} was shifted to higher energy relative to its position in bulk crystalline silicon (~ 521 cm^{-1}) thus indicating the presence of nanocrystalline particles. The observed shift can be attributed to the small size of synthesized particles and is in agreement with the calculated value for the nanocrystals with sizes of 4 nm [2]. The lines corresponding to the amorphous phase of silicon or oxide inclusions were not recorded, that indicates that the crystalline silicon phase is dominant in the resulting nanoparticles.

The chemical nature of the surface groups introduced onto the particles surface was studied by FTIR spectroscopy. For this purpose, the colloids were deposited on the Al foil and dried at ambient conditions. The knowledge of the surface groups formed in result of Si NPs processing is important for determination of the possibility of their optical properties improvement to fit the criteria determined by the practical applications. The FTIR results for the Si NPs prepared in ethanol before (sample A) and after discharge treatment (sample B) are presented in Figure 1b. The analysis of the surface properties by FT-IR revealed the following characteristic features of the samples: a presence of the oxide layer on the surface of the particles that is confirmed by the observation of weak bands at 3300 cm^{-1}, 1650 cm^{-1} and 651 cm^{-1}, corresponding to the

stretching and bending vibrations of OH, as well as a wide absorption band in the range of 1050-1200 cm^{-1} in the spectrum corresponding to the characteristic Si-O-Si stretching vibrations. In addition, the CH_3 and CH_2 groups are detected most probably due to the decomposition of ethanol. The distinctive feature that appears after the plasma treatment (spectrum B) is the formation of rather strong carbonyl group at around 1600 cm^{-1} possibly due to the OH groups oxidation by the plasma created reactive species.

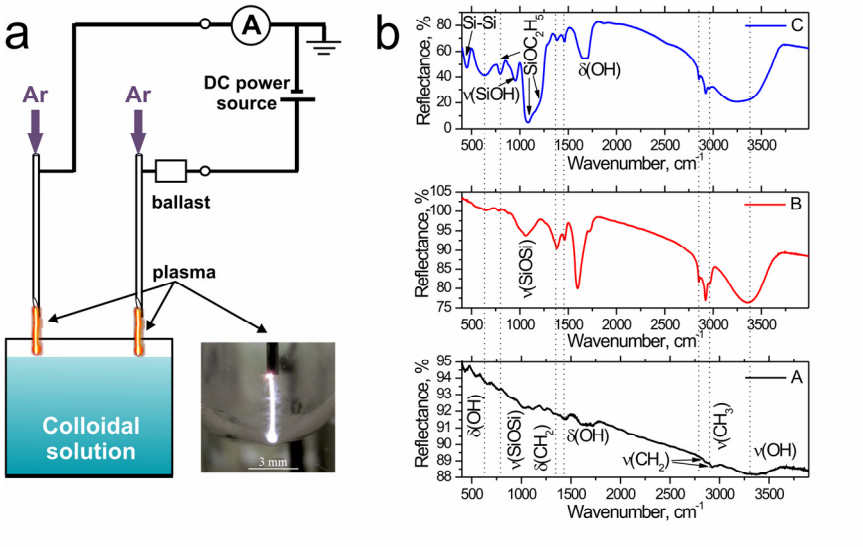

Figure 1. (a) Schematic diagram representing the double plasma–liquid system for surface engineering of NPs; (b) FTIR spectra of the Si NPs prepared by electrical discharge in ethanol: A – as-prepared sample, B – sample A after dc-plasma treatment, C – sample A plasma treated after the addition of HF solution.

To remove the surface oxide layer covering the particles the as-prepared colloid was mixed with the hydrofluoric acid solution (40%) in the proportion Si colloid: HF solution = 9:1 and further treated by two plasma jets. The FTIR spectrum (Fig.1bC) reveals the change of the surface groups in result of the plasma treatment. In addition to the OH and Si-O-Si groups, that still remain at the NPs surface, the Si-O-C_2H_5 groups appeared. We suggest that the different surface chemistry activated in different solutions could be due to different reactions induced by plasma-electrons at the plasma–solution interface compared to the plasma–water surface. Changing the surface groups is believed to be effective in improvement of photoluminescence properties of the synthesized Si NPs. Indeed, our experiments showed that the colloidal solution after the plasma treatment with HF showed strong blue photoluminescence (PL) centered at approximately 450 nm when excited at 360 nm (Fig.2). Therefore, surface

passivation can be used for tailoring NPs luminescent properties and increase PL intensity.

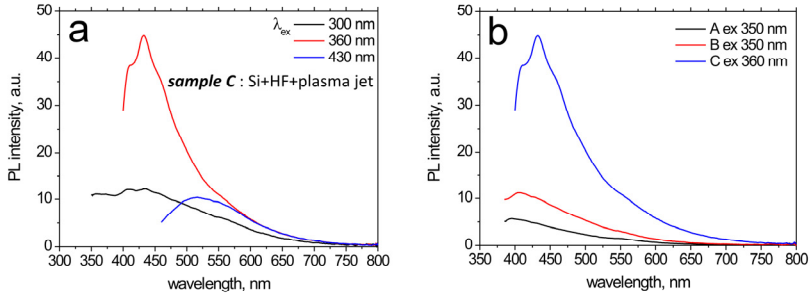

Figure 2. PL emission of Si NPs prepared by electrical discharge in ethanol: (a) – PL spectra of the colloid C at different excitation wavelength showing the excitation dependent behavior and maximal efficiency of excitation at 360 nm; (b) – the PL spectra of the colloids excited at 350-360 nm: A – as prepared, B – after plasma treatment, C – after plasma treatment with the addition of HF.

4. CONCLUSION

The capabilities of the non-equilibrium gas-liquid discharge plasma for surface modification and an improvement of photoluminescent properties of Si NPs have been demonstrated. The interaction of energetic plasma species with the colloidal solution initiates liquid-based non-equilibrium chemistry that results in surface functionalization of the particles present in the solution. Although experimental evidence indicates the possibility of PL enhancement after plasma treatment, still detailed studies are required to understand the reaction kinetics of microplasma-induced processes and plasma-induced mechanisms that contribute to the surface modification of NPs.

Acknowledgements

The work was supported by the National Academy of Sciences of Belarus under project Convergence 2.4.06 and the Belarusian Foundation for Fundamental Researches under Grant No. F18 MS-020. The authors would like to thank Dr. A.G. Karoza for the FTIR and Dr. A.P. Stupak for luminescence measurements and fruitful discussions.

REFERENCES

[1] D. Mariotti, J. Patel, V. Švrček, P. Maguire, Plasma Processes Polym. 9, 1074 (2012).
[2] A. Nevar, V. Kiris, M. Mardanian, M. Nedelko, N. Tarasenko, High Temper. Mater. Proc. 20, 251 (2016).

FEATURES OF PULSED LASER PLASMA EXPANSION IN VACUUM IN MAGNETIC FIELD

A. Chumakov, P. Chekan

B.I. Stepanov Institute of Physics of the NASB,
68 Nezavisimosti Ave., Minsk, 220072 Belarus,
e-mail: a,chumakov@dragon.bas-net.by

Abstract. Expansion of erosion laser plasma in vacuum and generation of magnetic field by moving plasma (in particular, in the presence of external static magnetic field oriented along the direction of plasma motion) are experimentally studied. Radial confinement of the expansion of plasma, a decrease in the electrification of target upon plasma formation, and an increase in the induction of the plasma magnetic field by a factor of 10–15 are revealed at an induction of the external magnetic field of about 0.35 T. Dependences of the induction of the plasma magnetic field on the power density of the laser radiation are determined for the above regimes.

1. INTRODUCTION

Formation and propagation of plasma jets in the presence of magnetic field are important theoretical and applied problems in the study of laser plasma. Theoretical calculations of [1, 2] and experimental results of [3] show that longitudinal magnetic field provides significant radial confinement of the expansion of erosion laser-plasma jet, so that the spread of plasma along the radial direction is virtually terminated at an external magnetic induction of greater than 2 T and plasma exhibits rectilinear motion. In this case, the density and homogeneity of plasma bunch remain almost unchanged and the effect of energy transfer inside plasma on the plasma dynamics becomes stronger. Under such conditions, the maximum plasma temperature slightly decreases and the temperature distribution in plasma becomes more uniform. External magnetic field can be used to control dynamic parameters of laser plasma and, hence, employed in practical applications in science and technology (in particular, laboratory astrophysics [4], pulsed laser deposition [5], emission laser spectroscopy [6], and laser drilling [7]) in which the field is used for the compression of plasma plume and control of its expansion. In plasma jet engines, longitudinal magnetic field can be used as magnetic nozzle for compression and acceleration of plasma jet [8–11].

Moving laser plasma generates magnetic fields, which depend on the laser power density on the irradiated surface, target material, size of irradiation

spot, ambient gas pressure, and regimes of laser irradiation [12]. Comparable effects of external magnetic fields and spontaneous magnetic fields generated by moving erosion laser plasma on the formation of laser-plasma jets need to be studied in detail for optimization of laser microjet engines. Thus, the purpose of this work is the study of specific features of the expansion of erosion laser plasma and generation of spontaneous magnetic fields by moving plasma at relatively low air pressure versus laser power density on the target and longitudinal magnetic field.

2. EXPERIMENTAL

Laser plasma is studied with the aid of an experimental setup based on the LS-2135M Nd:YAG laser with a second-harmonic radiation wavelength of 532 nm. A target is irradiated using singe laser pulses with a duration of 10 ns and a radiation energy of up to 84 mJ. The target represents a copper cylinder covered with an indium layer and is placed in a vacuum chamber evacuated to a pressure of about 10^{-3} mmHg. The laser radiation is delivered to the chamber via a side window and focused to a spot with a diameter of 0.5 mm, so that the laser power density on the target is up to 5×10^9 W/cm^2. Magnetic field is generated by a combination of three permanent magnets that are put on the target in such a way that the direction of magnetic field lines at the irradiation spot on the target coincides with the direction of motion of the plasma bunch. The magnetic field at the end surface of the system of magnets is up to 0.35 T.

The speed of plasma motion is measured using the time-of-flight method with the aid of an electric probe that represents a plane copper plate with a hole for the laser beam. The probe is placed at a distance of 7 mm from the surface of the target. The second probe is used to simultaneously measure variations in the electric potential on the target. The magnetic induction of the moving laser plasma is determined using an induction magnetic probe the coil of which is placed in the plane of the irradiation spot at a distance of 5 mm from the center of the spot and oriented perpendicularly to the axis of the plasma motion. Such probes detect only ac magnetic field and are insensitive to static field, so that the effect of permanent magnets on the measured results is eliminated. The probe signal that is proportional to the magnetic flux through the surface of the coil is detected using the DPO 3034 digital oscilloscope and used to determine the amplitude of magnetic induction with the aid of numerical integration.

3. RESULTS

Figure 1 shows the photographs of the pulsed plasma jet resulting from the laser irradiation of the target. We observe the integral emission of a single bunch of laser plasma that is detected in the visible spectral range with the aid of a video camera with a CCD array. It is seen that the plasma plume obtained in the presence of the longitudinal magnetic field (Fig. 1b) is more elongated along the propagation direction in comparison with the plasma plume obtained in the absence of magnetic field (Fig. 1a).

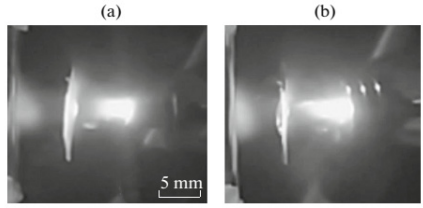

Figure 1. Photographs of the plasma plume (a) in the presence and (b) in the absence of magnetic field.

Variations in the electric potential on the target and the potential induced by the plasma in the electric probe are detected using the DPO 3034 digital oscilloscope (Fig. 2).

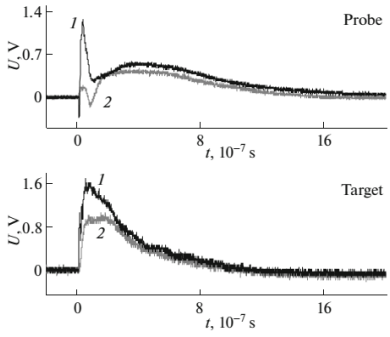

Figure 2. Oscillograms of the signals of electric probe and electric potential on the target (*1*) in the absence and (*2*) in the presence of magnetic field.

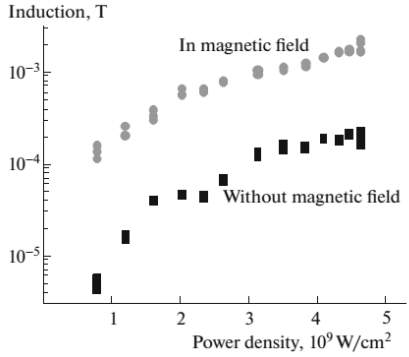

Figure 3. Effect of external magnetic field on the induction of the pulsed magnetic field generated by the plasma.

Normally, erosion laser plasma contains nonequilibrium ion component that is accelerated due to the interaction with the emission electrons and equilibrium component that is responsible for the thermal expansion of the laser plasma. Figure 2a shows that the magnetic field insignificantly affects the velocities of both components but causes a decrease in the electric charge that is transferred from the plasma to the electric probe. For the first positive peak in Fig. 2a that corresponds to the nonequilibrium ion component of the laser plasma, we observe a significant decrease in the potential jump by a factor of 4–5 in the presence of the external magnetic field and a minor decrease in the signal of the equilibrium component. Such results can be due to an increase in the density of the plasma plume in the presence of the magnetic field and the radial confinement, which lead to a decrease in the number of particles that interact with the electric probe. The oscillogram of variations in the electric potential induced on the target upon plasma formation in the presence of the longitudinal magnetic field (Fig. 2b) also shows a decrease in the maximum

value by approximately 30%, which can be caused by an increase in the energy transfer in plasma.

The induction of the plasma magnetic field is measured at laser energies ranging from 10 to 70 mJ and laser power densities on the target ranging from 0.8×10^9 to 4.6×10^9 W/cm^2. Figure 3 shows the experimental results. It is seen that the external longitudinal magnetic field causes an increase in the density of the plasma plume and provides radial confinement, so that the induction of the plasma magnetic field increases by a factor of 10–15.

4. CONCLUSIONS

The experimental results show that external magnetic field substantially affects the motion of erosion laser plasma at a magnetic induction of about 0.35 T. Such an effect is manifested as variations in the shape of the plasma plume related to radial confinement of plasma expansion. We also observe the effect of the nearsurface plasma formation on the electrification of target and an increase in the induction of the magnetic field that is generated by moving plasma by more than an order of magnitude, which can be due to an increase in the density of the plasma bunch and an increase in the energy flux of plasma. However, the effect of magnetic field on the axial velocity of the plasma jet is not revealed under the above conditions.

Acknowledgements

This work was supported by the Belarusian State Program “Convergence-2020" (project no. 2.4.02).

REFERENCES

[1] D. O. Ustyugov et al., Math. Models Comput. Simul. **2**, 362 (2010).
[2] R. Amitava et al., IEEE Trans. Plasma Sci. **44**, 574 (2016).
[3] T. Pisarczyk et al., Phys. Scr. **50**, 72 (1994).
[4] B. A. Remington, R. P. Drake, and O. O. Ryutov, Rev. Mod. Phys. **78**, 755 (2006).
[5] T. Tajima and J. M. Dawson, Phys. Rev. Lett. **43**, 267 (1979).
[6] X. K. Shen et al., J. Appl. Phys. **100**, 053303 (2006).
[7] C. Ye, G. J. Cheng, S. Tao, and B. Wu, J. Manuf. Sci. Eng. **135**, 061020 (2013).
[8] T. M. York, B. A. Jacoby, and P. Mikellides, J. Propul. Power **8**, 1023 (1992).
[9] M. Inutake, A. Ando, K. Hattori, H. Tobari, and T. Yagai, J. Plasma Fusion Res. **78**, 1352 (2002).
[10] M. Merino and E. Ahedo, Phys. Plasmas **17**, 073501 (2010).
[11] M. Merino and E. Ahedo, Plasma Sources Sci. Technol. **25**, 040512 (2016).
[12] 12. A. N. Chumakov and P. V. Chekan, Quantum Electron. **45**, 224 (2015).

DETERMINATION OF THE ELECTRON-CAPTURE DISTANCES OF THE RYDBERG ION-SURFACE INTERACTIONS

S. M. D. Galijaš

University of Belgrade, Faculty of Physics, P. O. Box 368, 11000 Belgrade, Serbia

Abstract. We analyze the non-resonant character of the electron capture into the Rydberg state of highly charged ions escaping a solid surface with intermediate velocity. Based on the two-state description of the single active electron in the ion-surface system, we are able to characterize the process and to calculate the electron-capture distances.

1. INTRODUCTION

In the case when we have metal-vacuum interface, the charge transfer play a significant role in surface science, especially for photo-emission, thermionic-emission and field-emission of electrons from metal surface. Specially, in spectroscopy such as low-energy electron diffraction, low-energy positron diffraction, inverse photoemission spectroscopy and scanning tunneling microscopy, charge transfer between a metal and the vacuum is also involved.

The electron transiton process has been studied theoretically [1] and experimentally [2]. Theoretical two-state vector model research is particularly interesting [3]. Here, we focus on the evaluation of the electron-capture distances R_c for the ions finally detected into the Rydberg state with high principal quantum number n_A, low values of the orbital quantum number l_A at the intermediate ionic velocities $v \approx 1$ a.u. It is important to point out that at sufficiently large values of the principal quantum number, we are able to consider electron capture processes only outside the bulk. Even more, small values of the orbital quantum number reduce the potential barrier $l_A(l_A+1)/r^2$, which means that the presence of a leaving ion significantly influences on the dynamic of the electron capture process, especially in the case of the very small ion-surface distances $R(t)$. The coupled-angular-mode

method (CAM) [4] calculations are in agreement with our estimates as well as results calculated by using the first-order transition rates [5].

2. THEORETICAL MODEL

We investigate interaction between a multiply charged ion ($Z \gg 1$), moving away with intermediate velocity v in normal direction in respect to the metal surface, and metal. In order to quantify the process of neutralization, we introduce the so-called normalized rate by using the following formula:

$$\tilde{\Gamma}_{\nu_A}(t) = \frac{d}{dt}\left(\frac{P_{\nu_A}(t)}{\lim_{t\to t_{fin}} P_{\nu_A}(t)}\right) \ , \tag{1}$$

where the neutralization probability $P_{\nu_A}(t)$ is expressed through the wave functions of the first $\Psi_1(\vec{r},t)$ and second $\Psi_2(\vec{r},t)$ scenarios as

$$P_{\nu_A}(t) = \int_{\sqrt{2\phi}}^{\sqrt{2U_0}} \sum_{n_{1M},m_M} \left| \int_{t_{in}}^{t} dt \left(\frac{i}{2} \int_{S_F} \left(\frac{\nabla\Psi_1(\vec{r},t)}{\Psi_1(\vec{r},t)} - \frac{\nabla\Psi_2^*(\vec{r},t)}{\Psi_2^*(\vec{r},t)} \right.\right.\right.$$

$$\left.\left.\left. -2iv\left(1 - \frac{da(t)}{dR}\right)\vec{e}_z\right)\Psi_2^*(\vec{r},t)\Psi_1(\vec{r},t)d\vec{S}\right)\right|^2 d\gamma_M \ , \tag{2}$$

where the work function and the depth of the potential well of the metal are denoted with ϕ and U_0, respectively. Parabolic quantum numbers γ_M, n_{1M} and m_M characterized the state $\Psi_1(\vec{r},t)$, which evolves from the fixed initial state at the time t_{in}, while the spherical quantum numbers ν_A characterized the final $\Psi_2(\vec{r},t)$ state, evolves from the fixed final state at the time t_{fin}. The advantage of the two-state vector model is reflected in the fact that the one same active electron is described by two Hamiltonians, depending on whether the representative active electron is close to the metal (first scenario) or to the ion (second scenario).

In Eq. (2), the movement of ions is defined by the orth $\vec{e}_z$ while the position of the Firsov plane S_F (typical for two-state vector model) in respect to the ion $a(t)$ is defined by variational requirement; the distance between the surface and the ion is indicated by R.

For intermediate ionic velocities and for ionic states of the low angular momentum l_A, we obtain the following analytical expression for normalized neutralization rate:

$$\tilde{\Gamma}_{\nu_A}(R,\gamma_M=\gamma_{max}) = \omega\sin 2\xi + 2v\left(|A(R)|e^{-\frac{\Omega}{v}R} - \cos\xi\right)$$

$$\times\left(e^{-\frac{\Omega}{v}R}\left(|A(R)|\left(\frac{\alpha+1}{R} - \frac{\Omega}{v}\right) - \frac{\alpha+1}{R}\right) + \frac{\omega}{v}\sin\xi\right) \ , \tag{3}$$

where $\xi = \omega R/v + \arg A(R)$, $A(R) \approx (1 + (|\beta|R)^{\alpha+1}/\Gamma(\alpha+2))e^{-i\arctan T}$, $T = (|\beta|R)^{\alpha+1}\sin\delta/(\Gamma(\alpha+2) + (|\beta|R)^{\alpha+1}\cos\delta)$, $\delta = (\alpha+1)\arctan(\omega/\Omega)$,

$\alpha = Z/\tilde{\gamma}_A - 1.5 + 1/4\gamma_M$, $\beta = \Omega/v - i\omega/v$, $\Omega = v\gamma_M + v(\tilde{\gamma}_A - \gamma_M)g$, $\omega = (\gamma_M^2 - \gamma_A^2)/2 - v^2(1-2g)/2$ and $g = a(R)/R$. By solving the eigenvalue problem of the second scenario, we get discrete energy spectrum $-\gamma_A^2/2 \approx -\gamma_A^2/2 + (2\tilde{Z} - 1)/4R$, with experimentally observed parameter $\tilde{\gamma}_A$. In the last equation, we have indicated that $\gamma_M = \gamma_{max}$, where value γ_{max} gives the main contribution, together with $n_{1M} = m_M = m_A = 0$, to the population of the Rydberg states.

3. RESULTS AND DISCUSSION

Electron-capture distances can be estimate, in the case of the intermediate ion-surface velocities, from the position of the last maximal values of the $\tilde{\Gamma}_{\nu_A}$ rates, Eq. (3). To illustrate that, in Fig. 1 we present (empty dots) the electron-capture distances R_c for the OVIII ion escaping the Al surface, for the velocities in the range between 0.8 a.u. and 1.2 a.u. Full dots are the electron-capture distances calculated by using the first-order transition rates [5]; empty square is the CAM result [4], and the distance R_c at the $v = 0.01$ a.u. is taken from Ref. [3].

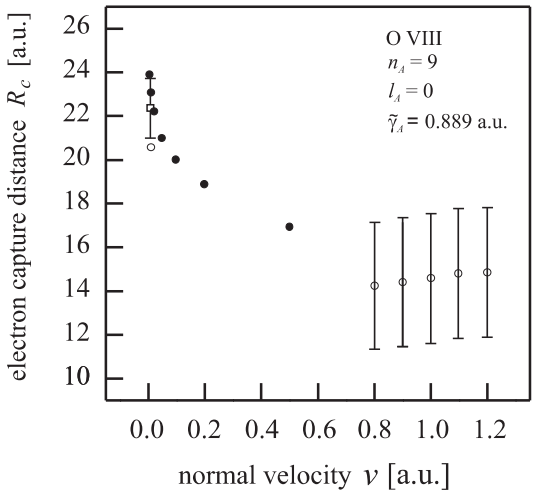

Figure 1. Electron-capture distances R_c for the OVIII ion escaping the Al surface as a function of the normal intermediate velocity v; full dots are the distances calculated by using first-order transition rates [5].The empty square result is available CAM assessment [4].

Figure 2 shows the electron-capture distances R_c for the population of Rydberg states of the SVI ion for different values of the principal quantum number ($n_A = 5 - 10, l_A = 0, 1, 2, m_M = m_A = n_{1M} = 0$). It should be noted that the widths of the normalized rates (given by Eq. (3)), is related to the delocalization of the electron-capture process in ion-surface

interaction. The increase of the projectile velocity leads slightly to the increase of delocalization of the neutralization process, as we can conclude from Figure 1.

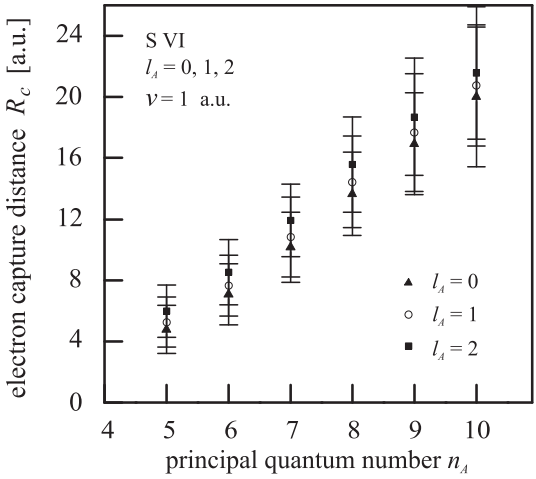

Figure 2. Neutralization distances R_c for the SVI ion escaping the Al surface, for the electron capture into the high Rydberg state ($n_A, l_A = 0, 1, 2, m_A = 0$).

Acknowledgements

This work was supported by the Ministry of Education, Science and Technological Development, Republic of Serbia (Project 171016). Author express huge gratitude to professor N. N. Nedeljković for discussion and valuable remarks.

References

[1] J. Sjakste, A. G. Borisov and J. P. Gauyacq, Phys. Rev. A 73, 042903 (2006).

[2] G. R. Lloyd, S. P. Procter and T. P. Softley, Phys. Rev. Lett. 95, 133202 (2005).

[3] N. N. Nedeljković and M. D. Majkić, Phys. Rev. A 76, 042902 (2007).

[4] A. Borisov, R. Zimny, D. Teillet-Billy and J. P. Gauyacq, Phys. Rev. A 53, 2457 (1996).

[5] A. Borisov and U. Wille, Nucl. Instr. Meth. Phys. Res. B 115, 137 (1996).

OXIDATION AND NITRIDING OF TITANIUM PRODUCED BY MICRO- AND NANOSECOND LASER IRRADIATION

I. Nikonchuk[1], A. Chumakov[1], O. Kuznechik[2]

[1]B.I. Stepanov Institute of Physics of the NASB,
68-2 Nezavisimosti Ave., Minsk, 220072 Belarus,
e-mail: i.nikanchuk@ifanbel.bas-net.by
[2]Powder Metallurgy Institute,
41 Platonova Str., Minsk, 220072 Belarus

Abstract. Results of laser-induced (1–50 Hz frequency, 1064 nm wavelength, and 0.085-200 μs pulse duration) oxidation, nitriding and structuring of the surface of porous titanium alloy (0.5 wt. % Fe, 0.15 wt. % N, 0.15 wt. % Cl) are presented. The surfaces were examined by scanning electron microscopy and energy-dispersive X-ray microanalysis. It was found that the parameters of millisecond laser action are more effective for the nitriding of the titanium, whereas multi-pulse action with nanosecond pulse duration is more suitable for the structuring and formation of oxides.

1. INTRODUCTION

Porous titanium is promising material for various applications (creating of medical implants, photo catalysis etc.). The quality of products based on titanium depends on the elemental composition and structure of the surface. One of the most effective methods of controllably changing of the composition and morphology of metal surfaces is laser treatment [1-4]. The purpose of this work is to identify effective modes of laser modification of the surface properties of porous titanium in atmospheric air.

2. EXPERIMENTAL DETAILS

In the present study the multipulse laser irradiation (1–50 Hz frequency, 1064 nm wavelength, and 0.085-200 μs pulse duration) with parameters shown at the Table 1 was used to create different oxide and nitride composition on the surface of porous titanium alloy (0.5 wt. % Fe, 0.15 wt. % N, 0.15 wt. % Cl). Titanium samples were mounted on a computer-driven X–Y table that moved along the track specified in a special program with a velocity of v = 0.6 –1.2 mm/s.

Table 1. Modes of laser irradiation

№	Spot area, м^2	Frequency, Hz	Pulse duration, μs	Power density, W/cm^2
1	$0{,}85\cdot10^{-6}$	25	0,085	$5{,}5\cdot10^{7}$
2	$1{,}77\cdot10^{-6}$	50	200	$1{,}1\cdot10^{4}$
3	$0{,}63\cdot10^{-6}$	25	200	$3{,}2\cdot10^{4}$
4	$1{,}77\cdot10^{-6}$	1	200	$1{,}1\cdot10^{4}$
5	$0{,}38\cdot10^{-6}$	25	0,085	$1{,}24\cdot10^{8}$

Surface structures and composition analysis were examined by methods of scanning electron microscopy and energy dispersive X-ray microanalysis using microscope MIRA-3 with X-Max extreme silicon drift detector.

3. RESULTS AND ANALYSIS

The laser action on the titanium samples was accompanied by the formation of a near-surface plasma. Registered emission spectra of the plasma are shown in Figure 1. In the spectra of the near-surface laser plasma the lines of Ti I atoms and the first titanium ions Ti II predominate. The temperature of titanium plasma ~ $1.3\cdot10^4$ K was estimated from the "normal" temperature of the Ti II line at 375.9 nm (excitation energy 3.9 eV, ionization energy of the Ti II ion 13.637 eV), which was calculated in accordance with [5].

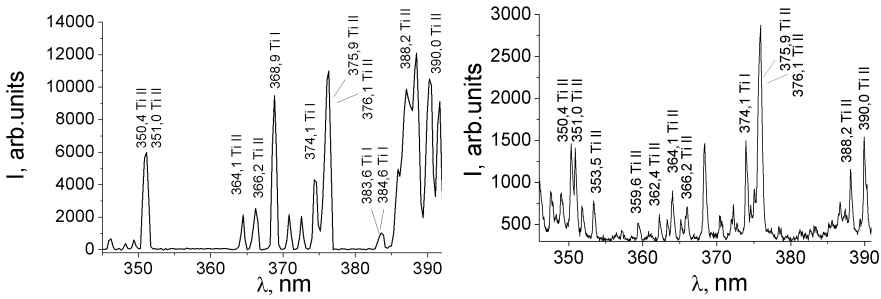

a) pulse duration of 200 μs *b) pulse duration of 85 ns*

Figure 1. Typical emission spectra of the plasma produced by pulsed laser action on titanium.

Scanning electron microscopy showed that laser treatment reduces the number and size of pores, probably due to the triggering of mechanisms for laser sintering of titanium grains. In this case, the effect of laser irradiation with a pulse duration of 200 μs (modes 3-5), treatment leads to a surface melting (liquid-phase sintering), and a nanosecond laser action produces a developed structure on the surface with substantially smaller grain and pore sizes compared to the original surface.

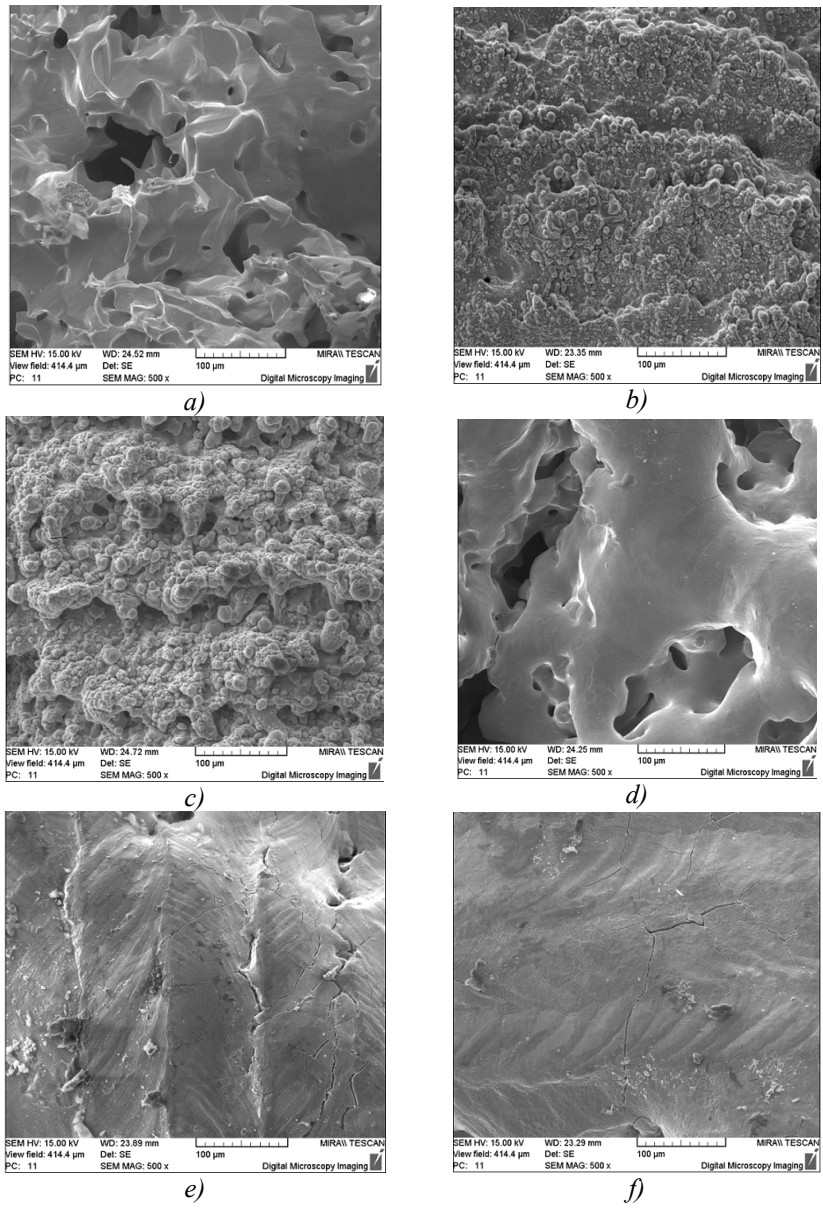

a) initial sample; b) mode №1; c) mode №2;
d) mode №3; e) mode №4; f) mode №5

Figure 2. SEM images of porous titanium irradiated in various regimes

Analysis of the elemental composition of the samples with the X-ray microanalyzer EDX X-Max revealed several variations in the chemical composition of the irradiated surface (Table 2).

Table 2. Intensity of X-rays of oxygen and nitrogen

Element	Intensity, pulses/s					
	Initial surface	mode №1	mode №2	mode №3	mode №4	mode №5
O	143	760	911	683	299	641
N	604	298	431	869	773	335

The results of the X-ray microanalysis presented in Table 2 and the analysis of the surface structures by SEM showed that laser action on the porous titanium substrate facilitates its transition in a monolithic state that is characteristic of metal alloys obtained by casting. It was found that the oxidation of the titanium surface induced by laser irradiation in atmospheric air increases with the increasing of number of laser pulses and has a weak dependence on pulse duration and power density ($q \sim 10^4$-10^8 W/cm^2). Nitriding of titanium increases with a decrease of repetition rate and power density from 10^4 to 10^6 W/cm^2.

4. CONCLUSIONS

Thus, by varying the modes of laser action on porous titanium alloy, it is possible to significantly change the morphology of surface and selectively increase the content of nitrides or oxides in the surface layer. It was found that the parameters of millisecond laser action are more effective for the nitriding of the titanium, whereas multi-pulse action with nanosecond pulse duration is more suitable for the structuring and formation of oxides.

Acknowledgments

This work is partly supported by the Belarusian Republican Foundation for Fundamental Research (Grant No. T15CO-055).

REFERENCES

[1] Trtica, M. et al. // Appl. Surface Sci. 2006., vol. 253, pp. 2551–2556.
[2] L. Lavisse et al. // Appl. Surf. Sc. 2007. 294, 916-920.
[3] M. Bussoli et al. // Radiation Effects & Defects in Solids. 2008. Vol.163, 349-356.
[4] A.N. Chumakov et al. // Physica Scripta. 2014. T162, 014016.
[5] Л. П. Пилиневич., Е.М. Харуки. // Доклады БГУИР, 2014 - № 5 (83) - с. 56-61.(in Russian)
[6] В. Лохте-Хольтгревен. Методы исследования плазмы // Пер. под ред. С. Ю. Лукьянова. М.: Мир, 1971, 126 с.(in Russian)

MODIFICATION OF NICKEL-TITANIUM THIN LAYERS BY PLASMA FLOW ACTION

Nora Trklja[1], Ivan Krstić[1], Bratislav M. Obradović[1], Milorad M. Kuraica[1] and Jagoš Purić[1]

[1]*Faculty of Physics, University of Belgrade, Belgrade, Serbia*

Abstract. Morphological changes occurring on nickel-titanium thin films, deposited on the silicon substrate, when treated with a compressed plasma flow have been investigated. The energy density delivered to the surface is about 10 J/cm^2. Main effects of compressed plasma flow treatment are surface uniform melting, perturbation action on melted surface layer and quenching of the produced surface wave structures.

1. INTRODUCTION

Titanium alloys are used in a wide variety of fields – in microelectronics, aerospace and biomedical industries. Nickel-titanium (Ni-Ti) alloys have very good physicochemical characteristics that make them useful for high-temperature wear and corrosion protection in mechanical applications. The main focus of this study is analysis of morphological changes occurring on Ni-Ti thin films when treated with a compressed plasma flow (CPF) which was formed in the magnetoplasma accelerator.

2. EXPERIMENTAL SETUP AND PROCEDURE

The plasma source is a quasistationary plasma accelerator which operates in the mode of ion current transfer. The plasma acceleration by the Ampere force in MPC interelectrode gap is accompanied by formation of a compression plasma flow at the outlet of the discharge device. The plasma flow is compressed due to interaction of longitudinal current component with intrinsic azimuthal magnetic field (pinch effect) [1]. The stable CPF is formed 20 μs after the beginning of the discharge. Relatively high values of plasma parameters of the compressed plasma flows (electron density in the order of 10^{23} m^{-3}, and plasma temperature of 20000 K) together with large plasma flow velocity (of 100 km/s in hydrogen plasmas) and discharge duration (of up to 100-150 μs) makes them suitable and efficient for studies of surface modifications under high thermal loads. In addition, we are able to investigate the formation of specific micro- and nanostructures, the occurrence of morphological characteristics

arising from the movement of the molten material pieces, and the formation of craters caused by ablation of the target. Scheme of the experimental setup is shown in Fig.1. In present investigation helium with addition of 5% of hydrogen was used as a working gas at 6 mbar pressure. Maximum current in discharge was about 50 kA with time duration of the plasma flow up to 150 μs.

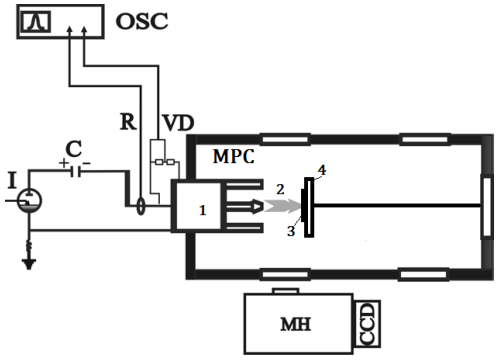

Figure 1. Scheme of the experimental setup: 1. Magnetoplasma accelerator, 2. CPF, 3. Sample, 4. Sample brass holder

Ni-Ti multilayer systems have been created by alternate deposition of nanometer-thick layers on a single silicon substrate, by sputter deposition method represented in [2]. The thickness of each individual layer is roughly 20 nm. Wafers of Si(100) was used as substrate. The deposited structures consisted of 10 alternate Ni and Ti layers, five of each and 20 alternate Ni and Ti layers, ten of each. The surface of the sample before plasma treatment is shown in Fig 2. The image was made by atomic force microscope (AFM).

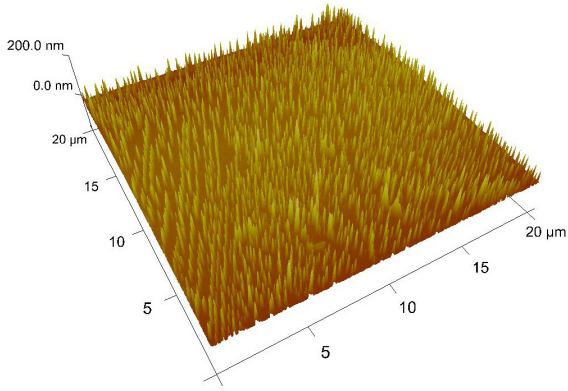

Figure 2. AFM analysis of the 5x(Ni-Ti)/Si samples before plasma treatment.

Samples treated by the compressed plasma flows have been analyzed by atomic force microscope (AFM) and scanning electron microscope (SEM).

3. EXPERIMENTAL RESULTS AND DISCUSSION

The energy density delivered to the surface is about 10 J/cm^2 [2] and surface is uniformly melted. Due to the fast cooling of the melted surface layer, the surface structures formed during melt phase are freezing (quenched) during a process of the melt resolidification. The central area of the treated surface contains craters with a diameter of 5 or 10 μm and mosaic structures with well-defined boundaries of the characteristic dimension of 1-2 μm (Fig.3.). Orientation of these structures corresponds to the orientation of the silicon substrate. These microstructures originate from the redeposition of thin film materials on the partially destroyed structure of the Si substrate.

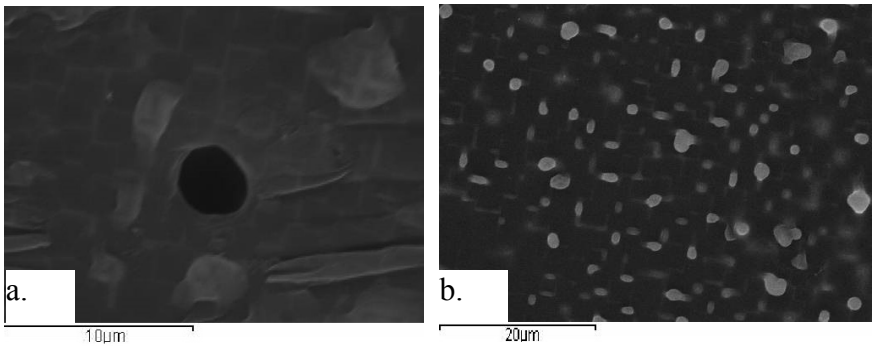

Figure 3. SEM analysis of the 5x(Ni-Ti)/Si multilayer target after CPF treatment (a) crater (b) mosaic microstructure

The periphery area of the treated surface contains periodical structures which are smooth, homogeneously and sinusoidally shaped, as would be expected from the frozen capillary waves (Fig. 4.). Typical wavelength of the periodical structures is 10 μm.

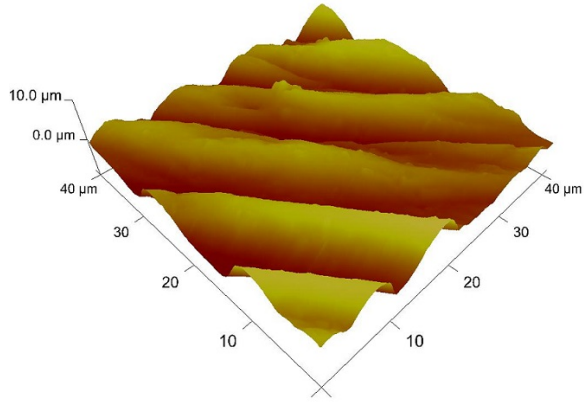

Figure 4. AFM analysis of the 10x(Ni-Ti)/Si after CPF treatment.

These modifications are comparable to the (Ni-Ti)/Si and (Al-Ti)/Si surface modifications during laser treatment [3, 4].

Results of the CPF with the silicon surface have shown formation of the periodical structures very similar to those observed in present experiment. Wavelengths of silicone periodical structures are 4-8 μm. Thickness of near-surface molten layer is estimated at 6-10 μm. It can be concluded that, in present experiment, periodical structures come from interaction of thin films with plasma, as well as from silicon – plasma interaction

4. CONCLUSIONS

The basic effects of the CPF action on a solid target are surface melting, formation of different surface patterns and their freezing during fast cooling (quenching effect). Modifications of treated surfaces – craters, mosaic structures and periodical periphery structures, are similar to those formed by laser beam - target interaction. Present study is important for investigations related with material of interest for mechanical applications, for fusion experiments, biomedical implant applications, etc.

Acknowledgements

This work is financially supported by the Ministry of Education, Science and Technological Development of the Republic of Serbia within the project 171034.

REFERENCES

[1] I. P. Dojčinović et al., Vauum, 80, 1381 (2006)
[2] S. Petrovic et al., Physica Scripta T149, 014082 (2014)
[3] B. Salatić et al., Applied Surface Science 360, 559 (2016)
[4] S. M. Petrovic et al., Optics and Laser Technology 54, 22 (2013)

FEMTOSECOND LASER-ASSISTED SURFACE MODIFICATION OF ODS STEEL WITH 10^{14} W/cm^2 INTENSITY IN AIR AND VACUUM AMBIENCE

M. Trtica[a*], J. Limpouch[b], X. Chen[c], J. Stasic[a], P. Gavrilov[b], M. Kuzmanovic[d]

[a]*Institute of Nuclear Sciences „Vinča", University of Belgrade, P.O. Box 522, 11001 Belgrade, Serbia*
[b]*Czech Technical University in Prague, Faculty of Nuclear Sciences and Physical Engineering, CZ-115 19 Praha, Czech Republic*
[c]*School of Mechanical and Electrical Engineering, Wenzhou University, Wenzhou 325035, China*
[d]*University of Belgrade, Faculty of Physical Chemistry, Studentski trg 12-16, 11158 Belgrade, 118, PAC 105305, Serbia*

Abstract. Irradiation of oxide dispersion strengthened (ODS) steel with high fs-laser intensity (order of 10^{14} W/cm^2) in air and vacuum ambience was studied. It was evident that induced damages, i.e. surface features, strongly depend on applied ambience. In case of vacuum, they were more drastic - probably due to enhanced coupling between laser radiation and sample surface.

1. INTRODUCTION

Laser processing/modification of materials with extraordinary characteristics, like ODS steel, is of high importance nowadays. Due to specific elemental content, ODS steel shows excellent properties [1], e.g. mechanical, thermal, creep and radiation resistance. Today, this modern material can be applied in industry, in nuclear field, etc. In context of the latter usage, it should be mentioned that ODS steels having Cr contents of about 14 wt.%, as in our case, are one of the candidates for structural components of the first wall and blanket in fusion reactors [2].

Generally, significance of the laser treatment of ODS steel can be twofold: (i) it is one of the most efficient techniques for processing of high-strength materials and, (ii) exposition of the target to high electromagnetic fluxes can serve for a laboratory simulation of some processes in nuclear fusion reactor [2]. In this context, it must be mentioned that inside the reactor a material is exposed to different fluxes such as neutron, electromagnetic, particles, etc., plus thermal loads. The goal of this work was to study ODS steel behavior under the action of ultrashort, femtosecond laser pulses of high intensity, ~10^{14} W/cm^2, in air and vacuum ambience, which was scarcely reported in literature.

2. EXPERIMENTAL

ODS steel used in this work, with the elemental content (wt%) of Fe:Cr:Al:W-Y_2O_3 = Fe (balance):Cr (16):Al (3):W (1.5)-Y_2O_3 (0.35), was synthesized in China by mechanical alloying and hot isostatic pressing [3] in argon atmosphere. Average sizes of Y_2O_3 and pre-alloyed powders were 40 nm and 50 μm, respectively. The dimensions of the sample were 10 mm × 10 mm × 0.4 mm (length × width × thickness). Target was metallographically prepared before irradiation. Experimental setup is same as in reference [4] - laser beam with 15 mm diameter was focused through lens (150 mm focal length) perpendicularly on the steel surface. The employed femtosecond laser was Ti:sapphire system (PULSAR, Amplitude Technologies based on CPA technique) with radiation wavelength 804 nm; laser pulse duration 60 fs; pulse energy up to 12 mJ; TEM_{00} operation; linearly, vertically polarized beam. Irradiations were performed at 1013 and ~1 x 10^{-4} mbar pressure for air and vacuum environment, respectively. Characterization of the induced surface features was done using optical, scanning electron microscopy (SEM) and optical interferometric profilometry. Elemental content of the target was observed by energy dispersive analyser (EDS) connected to SEM device.

3. RESULTS AND DISCUSSION

Material surface modification by laser generally depends on laser characteristics (e.g. energy, pulse length, wavelength), sample state (for example, its absorptivity), as well as surrounding ambience. Irradiation in this work was carried out in air and vacuum with the obtained surface effects given in the following text.

3.1. Irradiation in air ambience

Irradiation of ODS steel sample by fs-laser, in air atmosphere, at the intensity of I_1 ~10^{14} W/cm^2 (fluence ~6.6 J/cm^2) is shown in Fig. 1. Morphological changes and phenomena can be summarized as follows: (a) damage appearance in the form of crater with great aureole (Fig. 1 A1, B1,2). The crater had nearly conical cross-section (Fig. 1 B1) with maximum depth of ~3.5 μm; (b) smooth melting areas with surface cracking can be registered in the central zone (Fig. 1 A2); (c) appearance of material barrier at the rim (Fig. 1 A3, B2) due to material redeposition; and (d) plasma creation in front of the sample (several mm long). It should be mentioned that filamentation effects were not observed in the course of irradiation. Appearance of black and white aureoles at the surface implies possible chemical reaction of primary oxidation process, which was confirmed by EDS.

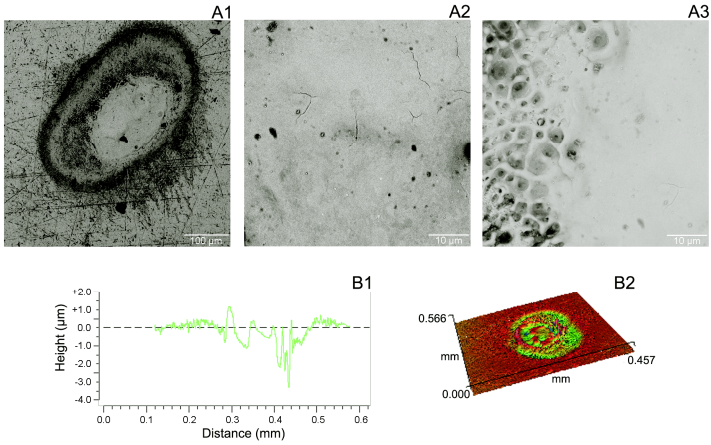

Fig. 1. SEM (A) and profilometric (B) analysis of the ODS steel target after irradiation with 50 laser pulses. Air atmosphere; laser output energy E ~5.20 mJ ($\Phi_1 \approx 6.6$ J/cm^2, $I_1 \approx 1.1 \times 10^{14}$ W/cm^2). A1,A2,A3 –entire spot, central and periphery zone. B1,B2 –2D and 3D-view of the damage (cross-section is visible).

3.2. Irradiation in vacuum ambience

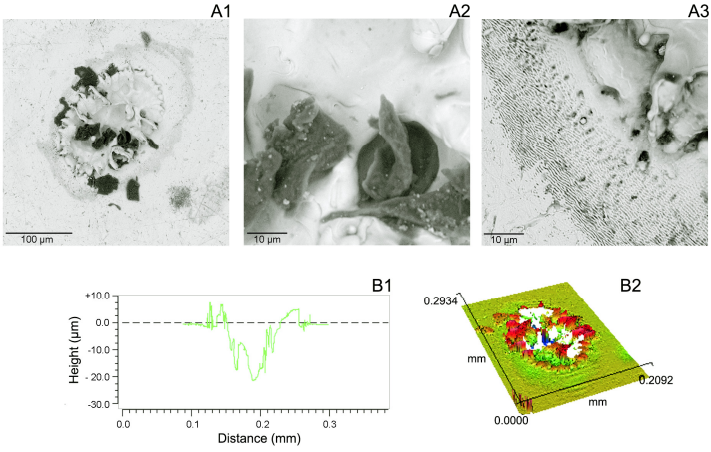

Fig. 2. SEM (A) and profilometric (B) analysis of the ODS steel target after irradiation with 50 laser pulses. Vacuum ambience; laser output energy E ~5.20 mJ ($\Phi_2 \approx 26.0$ J/cm^2, $I_2 \approx 4.4 \times 10^{14}$ W/cm^2). A1,A2,A3 –entire spot, central and periphery area. B1,B2 –2D and 3D-view of the damage (cross-section is visible).

Irradiation of the ODS sample at almost the same intensity in vacuum ambience is shown in Fig. 2. Morphological features and phenomena can be summarized as follows: (a) damage appearance in the form of crater was

registered as well (Fig. 2 A1, B1,2). Crater depth (Fig. 2 B1) was larger (~23 μm) compared to that obtained in air ambience; (b) almost melting areas can be registered in the central irradiation zone (Fig. 2 A2); (c) partial redeposition of the material with creation of periodic surface structures at the rim (Fig. 2 A3, B2); and (d) plasma generation in front of the sample was observed, with larger dimensions than in air (over 20 mm in length). In case of vacuum irradiation, the damage spots were well defined with smaller overall dimensions. Coronas at the periphery were drastically reduced, with no color changes, which implied low oxidation.

Generally, femtosecond laser-ODS steel interaction is very complex [5], and in the first step comprises the absorption of laser radiation by free electrons (which lasts several to tens of fs). Then, thermalization of electron sub-system takes place. Finally, the transfer of energy to the lattice sub-system occurs within the period of less than several picoseconds. Assuming that initial laser intensity is high enough, the process of material removal/ablation can occur.

4. CONCLUSIONS

Irradiation of ODS steel with high fs-laser intensity (order of 10^{14} W/cm^2) in air and vacuum ambience was studied. It was evident that the used intensity induced damage, while surface features strongly depend on the applied ambience. In case of vacuum, the coupling between laser radiation and sample surface is probably enhanced.

Acknowledgements

The research was sponsored by: (i) The Ministry of Education, Science and Technology of the Republic of Serbia through project No. 172019); (ii) International Atomic Energy Agency (IAEA), Contract No. 20636; (iii) Ministry of Education, Youth and Sports of the Czech Republic. Projects: LD14089 and LG15013.

REFERENCES

[1] J. Macías-Delgado, T. Leguey, V. de Castro, M.A. Auger, M.A. Monge, P. Spatig, N. Baluc and R. Pareja, Nuclear Mater. and Energy 9, 372 (2016).
[2] R. Montanari, E. Pakhomova, R. Pizzoferrato, M. Richetta and A. Varone, Metals 7, 454 (2017).
[3] H. Dong, L. Yu, Y. Liu, C. Liu, H. Li and J. Wu, Fusion Engineering and Design 125, 402 (2017).
[4] M. Trtica, J. Limpouch, P. Gavrilov, P. Hribek, J. Stasic, G. Brankovic and X. Chen, Laser and Particle Beams 35, 534 (2017).
[5] B.N. Chichkov, C. Momma, S. Nolte, F. von Alvensleben and A. Tunnermann, Appl. Phys. A 63, 109 (1996).

Section 3.

LOW TEMPERATURE PLASMAS

THERMOCHEMICAL NON EQUILIBRIUM IN THERMAL PLASMAS

Arnaud Bultel[1], Vincent Morel[1] and Julien Annaloro[2]

[1]CORIA UMR 6614 – CNRS and Normandy University, 76801 St-Etienne du Rouvray, France
[2] CNES, French Spatial Agency, 31400 Toulouse, France

The modelling of plasmas in thermodynamic non equilibrium requires the development of dedicated kinetic mechanisms that must be subsequently validated. Even if heavy particles are less effective than electrons from the collisional point of view to induce significant changes in the plasma composition, the sometimes low ionization degree leads to take them into account in the mechanism. The non equilibrium degree can even be sufficiently high to prevent a satisfactory coupling between the excited atomic and molecular states. The excited states then behave freely due to the different elementary electron and heavy particle induced collisions. The modelling becomes very challenging since different types of collisional elementary processes are involved, whose collision partners can follow an energy distribution function at different temperatures if the concerned distributions are Maxwellian. The difficulty is increased if the plasma density is sufficiently low to induce a significant influence of the radiative elementary processes on the excited states. The set of elementary data relative to the collisional and radiative processes forms a Collisional-Radiative (CR) model and can be implemented in a State-to-State (StS) modelling of the plasma in order to reproduce its behaviour.
Two situations remarkably illustrate the benefit provided by such a sophisticated strategy.

(1) **Laser-induced plasmas**. The interaction between a powerful laser pulse and a solid sample generally leads to plasma formation with a significant departure from equilibrium resulting from the hypersonic expansion.
(2) **Atmospheric entry plasmas**. During the hypersonic entry of a spacecraft in the upper layers of a planetary atmosphere, the sudden decrease in the velocity close to the fuselage leads to the formation of a shock layer where the relaxation of the flow composition takes place at high temperature. The related time scales are short and induce a sometimes significant departure from equilibrium.

The present lecture will be the opportunity to thoroughly discuss these situations based on reference experiments. The StS modelling using relevant CR models elaborated in CORIA will be described. Their results will be finally discussed in the light of the experimental results.

INFLUENCE OF NITROGEN ADMIXTURE ON PLASMA CHARACTERISTICS IN A DC ARGON GLOW DISCHARGE AND IN AFTERGLOW

N. A. Dyatko[1], Yu. Z. Ionikh[2], A. P. Napartovich[1]

[1]*Troitsk Institute for Innovation and Fusion Research, Troitsk, Moscow, 108840 Russia*
[2]*St. Petersburg State University, St. Petersburg, 199034 Russia*

It is well known that an addition of a molecular gas to a rare gas can significantly change characteristics of a discharge. The degree and tendency of these changes depend on the discharge conditions: the sort of a rare gas, sort and percentage of the admixture, gas pressure, etc. In this paper, we restrict ourselves to examining the effect of nitrogen admixture (0.1-1%) on the characteristics of a dc glow discharge (maintained in a tube) in argon and on the characteristics of afterglow plasma. In particular, the following effects are discussed.

- Influence on the current-voltage characteristic of a diffuse glow discharge. At relatively low pressures (several Torr) the addition of nitrogen leads to an increase in the discharge voltage, while at intermediate gas pressures (tens of Torr) it leads to a noticeable decrease in the discharge voltage.
- Influence on the population of Ar metastable states.
- Influence on the rate of plasma decay in the afterglow. A high degree of a vibrational excitation of molecules is achieved in the Ar:N_2 discharge, which provides a high electron temperature in the afterglow due to superelastic collisions of electrons with vibrationally excited molecules. This, in turn, leads to an increase in the rate of ambipolar diffusion process.
- Influence on discharge constriction. At intermediate gas pressures a stepwise transition of the positive column from the diffuse to the constricted form is observed when the discharge current exceeds a certain critical value. The addition of nitrogen to argon leads to a noticeable increase in the critical current value.
- Influence on the constriction process. According to observations, the constriction starts near one of the electrodes and then the constricted region boundary propagates towards the other electrode. For the Ar:N_2 mixture, the transition time is considerably longer than in pure argon.
- Partially constricted discharge. In the case of the Ar:N_2 mixture there can be formed a steady-state partially constricted discharge in which the constricted and diffuse forms of the positive column simultaneously exist in the discharge tube.

Acknowledgements: This work was partially supported by the Russian Foundation for Basic Research, Project No. 16-02-00861-a.

ELECTRON HEATING IN ELECTRONEGATIVE CAPACITIVELY COUPLED DISCHARGES OF COMPLEX CHEMISTRY

Jón Tómas Gudmundsson[1,2]

[1]*Science Institute, University of Iceland, Reykjavik, Iceland*
[2]*Department of Space and Plasma Physics, School of Electrical Engineering and Computer Science, KTH Royal Institute of Technology, Stockholm, Sweden*

An overview is given on the oxygen discharge chemistry, in particular on the creation and destruction of the negative ion O^-. The one-dimensional object-oriented particle-in-cell Monte Carlo collision code `oopd1` is then applied to explore the electron heating mechanism in a single frequency capacitively coupled oxygen discharge. We explore how including and excluding detachment by the singlet metastable molecules $O_2(a^1\Delta_g)$ and $O_2(b^1\Sigma_g)$ influences the electron heating mechanism and the discharge electronegativity. We demonstrate that the detachment processes have a significant influence on the discharge properties, in particular at the higher pressures [1,2]. We show that at a low driving frequency and low pressure (5 and 10 mTorr), a combination of stochastic (α-mode) and drift ambipolar (DA) heating in the bulk plasma (the electronegative core) is observed and the DA-mode dominates the time averaged electron heating [3]. As the driving frequency or pressure are increased, the heating mode transitions into a pure α-mode, where electron heating in the sheath region dominates [3]. This transition coincides with a sharp decrease in electronegativity.

REFERENCES

[1] J. T. Gudmundsson and M. A. Lieberman, Plasma Sources Sci. Technol. **24**, 035016 (2015).

[2] J. T. Gudmundsson and B. Ventéjou, J. Appl. Phys. **118**, 153302 (2015)

[3] J. T. Gudmundsson, D. I. Snorrason and H. Hannesdottir, Plasma Sources Sci. Technol. **27**, 025009 (2018).

HIGH-RESOLUTION HIGH-SENSITIVITY SPECTROSCOPIC AND ELECTRICAL DIAGNOSTICS OF BARRIER DISCHARGES

Tomáš Hoder

Department of Physical Electronics, Masaryk University, Brno, Czechia

The barrier discharge is widely studied plasma source with multiple industrial applications [1,2]. Big effort was dedicated to the understanding of the fundamental physics of this discharge type within last twenty years. Especially for the case of volume barrier discharge in air, the task to follow its spatiotemporal development on its characteristic spatiotemporal scales and to quantify accordingly the electric field was initiated in the article of Kozlov et al. [3]. This contribution will present the fulfilment of the mentioned task achieved in the last years using high-resolution (single photons counted at picosecond and micrometer scales) optical emission spectroscopy [4,5] enhanced by numerical verification of kinetic models [6,7]. The talk will also include the presentation of the precise current measurements on volume barrier discharge in air where the approximate electronic and ionic components of the transferred charge were determined [8]. Charge transfer down to femtocoulombs is reported with sub-nanosecond resolution at the same time and responsible mechanisms discussed.

Acknowledgements: This work is supported by Czech Science Foundation project nr.16-19721Y and by the projects CZ.1.05/2.1.00/03.0086 funded by European Regional Development Fund and project LO1411 (NPU I) funded by Ministry of Education Youth and Sports of the Czech Republic.

REFERENCES

[1] U. Kogelschatz, J. Phys. D: Appl. Phys. 50, 051001 (2017).
[2] R. Brandenburg, Plasma Spources Sci. Technol. 26, 053001 (2017).
[3] K. V. Kozlov et al., J. Phys. D: Appl. Phys. 34, 3164-3176 (2001).
[4] T. Hoder et al., J. Appl. Phys. 117, 073302 (2015).
[5] T. Hoder et al., Plasma Phys. Control. Fusion 59, 074001 (2017).
[6] P. Bílek et al., Plasma Spources Sci. Technol. - under review
[7] A. Obrusník et al., Plasma Spources Sci. Technol. - under review
[8] P. Synek et al., Plasma Sources Sci. Technol. 27, 045008 (2018).

AN EQUIVALENT CIRCUIT APPROACH FOR THE ELECTRICAL DIAGNOSTICS OF DIELECTRIC BARRIER DISCHARGES

Andrei V. Pipa and Ronny Brandenburg

Leibniz Institute for Plasma Science and Technology (INP),
Felix-Hausdorff-Straße 2, 17489 Greifswald, Germany

Measurements of current and voltage is a basic diagnostics for electrical discharges. However, in the case of dielectric barrier discharge (DBD) the measured current and voltage waveforms are determined by the properties of the discharge reactor (geometry) and the discharge itself (gas gap voltage, discharge current). Thus, interpretation of measured quantities is required to determine discharge characteristics. After the formulation of the classical sinusoidal operated ozoniser electrical theory [1] the technical possibilities to measure and analyze electrical signals has been improved. In parallel other DBD geometries and driving voltage waveforms were developed, and required extension or revision of the electrical theory [2, 3]. The contribution will present the historical development of these electrical DBD theories, which are based on lumped electrical elements. Further development of the simplest equivalent circuit for its application on partially discharged DBDs [4], surface DBDs [5], and packed-bed reactors [6] will be discussed.

REFERENCES

[1] T.C. Manley, Trans. Electrochem. Soc. 84, 83-96 (1943)
[2] A.V. Pipa, J. Koskulics, R. Brandenburg and T. Hoder, Rev. Sci. Instrum. 83, 115112 (2012).
[3] A.V. Pipa, T. Hoder and R. Brandenburg, Contrib. Plasm. Phys. 53, 469-480 (2013).
[4] F.J.J. Peeters and M.C.M. van de Sanden, Plasma Sources Sci. Technol. 24, 015016 (2015).
[5] J. Kriegseis, S. Grundmann, and C. Tropea, J. App. Phys. 110, 013305 (2011)
[6] T. Butterworth and R.W.K. Allen, Plasma Sources Sci. Technol. 26, 065008 (2017)

RADIO-FREQUENCY PLASMAS AT ATMOSPHERIC PRESSURE: FROM PHYSICS OF SUSTAINING TO MATERIALS ENGINEERING AND BIOMEDICINE

Lei Wang[1], Gheorghe Dinescu[2], Xiaolong Deng[3], Bratislav Obradović[4], Christophe Leys[1], Anton Yu Nikiforov[1]

[1]*Department of Applied Physics, Ghent University, Sint-Pietersnieuwstraat 41 B4, 9000 Gent, Belgium*
[2] *National Institute of Laser, Plasma and Radiation, Magurele-Bucharest, MG-36, Ilfov RO 077125, Romania*
[3]*College of Aerospace Science and Engineering, National University of Defense and Technology, Deya Road 109, Changsha 410073, China*
[4] *University of Belgrade, Faculty of Physics, Studentski trg 12-16, 11000 Belgrade, Serbia*

Low temperature plasma technology, as an interdisciplinary field combining physics, chemistry, and material science, turns out to bear great potential in both scientific explorations and industrial applications. Operation of plasma sources at high pressure up to 100's of kPa results in low costs and relative simplicity of in-line installation of plasma sources. However, industrial applications encountered certain drawbacks including low processing efficiency due to limited plasma dimensions, problems of uniformity, heating of the electrodes and many others that can strongly affect successful valorization of atmospheric pressure plasma technology. With this contribution we present an overview of recent research activities related to study of the atmospheric pressure co-planar radio-frequency (APRF) discharge as a source suitable for biomedical applications and polymer material processing. Special attention is paid to time and spatial resolved plasma diagnostics, measurements of main discharge parameters including electrical field and electron density as well as to study physics of the RF sheath formation. It is shown that despite atmospheric pressure operation the discharge sustaining is similar to low pressure operation and high density and fluxes of active species can be obtained in the sheath region that is of particular interest for biomedical applications and surface processing.

Acknowledgements: This work is partially supported by M.Era-Net project "PlasmaTex".

ELECTRON HEATING IN RADIO FREQUENCY HOLLOW CATHODES

Scott J. Doyle[1], Andrew R. Gibson[1], Jason Flatt[1], Teck S. Ho[2], Rod W. Boswell[2], Christine Charles[2], Mark J. Kushner[3] and James Dedrick[1]

[1] *York Plasma Institute, Department of Physics, University of York, Heslington, York, YO10 5DD, UK*
[2] *Space Plasma, Power and Propulsion Laboratory, Research School of Physics and Engineering, The Australian National University, ACT 0200, Australia*
[3] *University of Michigan, Dept. of Electrical and Computer Engineering, 1301 Beal Ave., Ann Arbor, MI 48109-2122, USA*

The development of low-power and compact propulsion sources is of significant interest for meeting the increasingly demanding challenges of space missions. Radio-frequency (rf) hollow cathode plasma thrusters operate by heating the neutral propellant gas and therefore do not require a space-charge neutralizer. To maximise thrust-power efficiency, it is important to control the spatial and temporal deposition of electrical power into the plasma. In this study, we investigate the mechanisms for electron heating in the recently developed *Pocket Rocket* electrothermal microthruster. Measurements of the electron-impact excitation rate via phase-resolved optical emission spectroscopy are corroborated by fluid-kinetic simulations undertaken with the Hybrid Plasma Equipment Model. Electron power deposition, and the ion and neutral-gas heating this underpins, is investigated across an α-γ mode transition and pressure gradient on-axis. The results highlight the importance of local collisionality and the surface potential of the radial wall. Prospects for achieving enhanced control of plasma heating, e.g. rf voltage waveforms comprising multiple harmonics, are discussed.

Acknowledgements: We wish to thank R. Armitage, K. Niemi and P. Hill for their technical assistance and acknowledge financial support from the Engineering and Physical Sciences Research Council (EP/M508196/1). The participation of M. J. Kushner was supported by the US National Science Foundation and the US Department of Energy Office of Fusion Energy Science.

MEASUREMENT OF STARK HALFWIDTHS OF SPECTRAL LINES OF IONIZED OXYGEN AND SILICON, EMITTED FROM T-TUBE PLASMA

Lazar Gavanski

University of Novi Sad, Faculty of Sciences, Department of Physics, Trg Dositeja Obradovića 4, 21000 Novi Sad, Serbia

Experimental Stark halfwidths of spectral lines of singly ionized oxygen and silicon and double ionized silicon are presented in this work and in [1]. Stark halfwidths of 37 O II spectral lines, 10 Si II lines and 12 Si III lines were determined. The experimentally obtained values were compared to experimental values given by other authors. All experimental values were also compared to theoretical values from [2] and calculated values by using the semi-empirical formula [3] and the modified semi–empirical formula [4]. The spectral lines were emitted from an electromagnetically driven T-tube plasma. The plasma electron temperature of 15000 K was determined by using the Boltzmann plot method. The electron density of 1.45×10^{23} m^{-3} was determined by the method and formula given in [5]. The shock front velocity in the T-tube was determined by the method [6], since properties of the produced plasma strongly depend on it.

Acknowledgements: This work was supported by the Ministry of Education, Science and Technological development of Republic Serbia, under Project 171014.

REFERENCES

[1] L. Gavanski, M. T. Belmonte, I. Savić and S. Djurović, Month. Not. Roy. Astron. Soc. 457, 4038 (2016).
[2] H. R. Griem, *Specttral Line Broadening by Plasmas*, (Academic Press, New York, 1974).
[3] M. S. Dimitrijević and N. Konjević, J. Quant. Spectrosc. Radiat. Transfer 24, 451 (1980).
[4] M. S. Dimitrijević and N. Konjević, Astron. Astrophys. 172, 345 (1987).
[5] M. Ivković, M. Á. González, S. Jovićević, M. A. Gigosos, N. Konjević, Spectrochim. Acta B 65, 234-240 (2010).
[6] S. Djurović, Z. Mijatović, B. Vujičić, R. Kobilarov, I. Savić and L. Gavanski, Phys. Plasmas 22, 013505 (2015).

STUDY OF Ar I AND Ne I SPECTRAL LINES SHAPES IN THE CATHODE SHEATH REGION OF ABNORMAL GLOW DISCHARGE

Nikola V. Ivanović

Faculty of Agriculture, University of Belgrade, Nemanjina 6, 11080 Belgrade, Serbia

One of the distinguished features of the cathode sheath (CS) region of abnormal glow discharges (GD) is the distribution of electric field strength F, which is of crucial importance for charged particles acceleration, their trajectories, kinetic energies and collisions with other particles and cathode sputtering. All these processes are relevant for the operation of GD, as well as for numerous applications in the field of spectroscopic analysis, plasma etching, thin film deposition and depth profiling of cathode material. Thus, the importance of non-perturbing technique for F distribution measurement in a tiny CS region was recognized long time ago.

Within this work, a simple technique, based on the standard optical emission spectroscopy (OES) and standard laboratory equipment, has been used for F mapping in the CS region of abnormal GDs of Grimm type in argon and neon. This is in essence the well known Lo Surdo technique used for studies of Stark effect, but employed with a modern CCD detector [1-3].

The profiles of two neutral argon lines (Ar I 518.775 nm and 522.127 nm) and several neutral neon lines were observed in the CS region side-on to the discharge axis. It was found that some of the studied lines manifest the Stark splitting, and that all lines exhibit Stark shifts, whose measured values are subsequently used for estimating the distributions of the electric field strength in the cathode sheath region of the studied glow discharges.

Acknowledgements: This work is supported by the Ministry of Education, Science and Technological Development of the Republic of Serbia under Projects 171014.

REFERENCES

[1] G. Lj. Majstorović, N. V. Ivanović, N. M. Šišović, S. Djurović and N. Konjević, *Plasma Sources Sci. Technol.* **22,** 045015 (2013).
[2] N. M. Šišović, N. V. Ivanović, G. Lj. Majstorović and N. Konjević *J. Anal. At. Spectrom.* **29,** 2058 (2014).
[3] N. V. Ivanović, N. M. Šišović, Dj. Spasojević and N. Konjević, *J. Phys. D: Appl. Phys.* **50**, 125201 (2017).

DIAGNOSTICS OF DIELECTRIC BARRIER DISCHARGES IN CONTACT WITH LIQUID TARGET

Vesna V. Kovačević

Universityof Belgrade, Faculty of Physics, PO Box 44, 11001 Belgrade, Serbia

Dielectric barrier discharge (DBD) is one the most widely used source of non-thermal atmospheric pressure plasma in different fields of applications, particularly in water purification processes and biomedical applications. The subject of the presented study is diagnostics of complex plasma-liquid interaction in plasma sources based on dielectric barrier discharge. For a spatio-temporally resolved study of plasma-liquid interaction helium plasma jet with liquid target was used [1]. The discharge development, spatial distribution of the excited species, electric field measurement results and the results of the Schlieren imaging are presented. It was shown that the slight change of the non-electrical parameters, such as target distance and the gas flow rate can completely change the nature of the discharge. In a specially designed water falling film DBD reactor, chemical processes induced in liquids by discharge generated in different gases are studied, with the emphasis on the physical and chemical properties of the gas phase and the liquid phase [2]. The formation of hydroxyl radical ($^{\bullet}OH$) and long-living chemical species (H_2O_2, O_3, NO_3^- and NO_2^-) generated in the liquid phase of the reactor in dependence on the gas atmosphere (air, nitrogen, oxygen, argon and helium) were investigated. It was found that formation of hydrogen peroxide in air, nitrogen and argon discharges is determined by recombination reaction of hydroxyl radicals.

Acknowledgements: This work was supported by the Ministry of Education and Science of the Republic of Serbia through Project 171034, Project 33022 and Action COST TD1208 for the financial support for a short-term scientific mission.

REFERENCES

[1] V. V. Kovačević, G. B. Sretenović, E. Slikboer, O. Guaitella, A. Sobota and M. M. Kuraica, J. Phys. D. Appl. Phys. 51, 65202 (2018).
[2] V. V. Kovačević, B. P. Dojčinović, M. Jović, G. M. Roglić, B. M. Obradović and M. M. Kuraica, J. Phys. D. Appl. Phys. 50, 155205 (2017).

PROCESSING OF CELLULOSE TEXTILE MATERIALS WITH NON THERMAL ATMOSPHERIC PRESSURE PLASMA

Ana Kramar

Faculty of Technology and Metallurgy, Department of textile engineering, University of Belgrade, Karnegijeva 4, 11000 Belgrade, Serbia

Conventional processing of textile materials in general includes wet chemical procedures for cleaning, scouring, functionalization, dissolving, etc. However, plasma processing could become one of the leading processes in the future of textile industry since it comprises little to no chemical use, no chemical waste and low production cost. This work will give an overview of current research and future prospects of using atmospheric pressure plasma (APP) for treatment of cellulose textile materials. From the processing of pure natural cellulose fibers such is cotton [1,2], over regenerated cellulose in the form of viscose fibers [3,4], to the multicomponent lignocellulosic fibers such is hemp, APP treatment can provide the wide range of effects which improve general properties and add new values to the existing textile products.

Acknowledgements: This study is supported by the Ministry of Education, Science and Technological development of the Republic of Serbia through projects OI 171034 and OI 172029.

REFERENCES

[1] M. Kostić, N. Radić, B. M. Obradović, S. Dimitrijević, M.M. Kuraica, P. Škundrić, Plasma. Process. Polym. 6, 58 (2009).
[2] V. Prysiazhnyi, A. Kramar, B. Dojcinovic, A. Zekic, B. M. Obradovic, M. M. Kuraica, M. Kostic, Cellulose 20, 315 (2013).
[3] A. Kramar, V. Prysiazhnyi, B. Dojcinovic, K. Mihajlovski, B. M. Obradovic, M. M. Kuraica, M. Kostic, Surf. Coat. Tech. 234, 92 (2013).
[4] A. Kramar, B. M. Obradovic, A. Vesel, M. M. Kuraica, M. Kostic, Plasma. Process. Polym. 12, 1095 (2015).

ATMOSPHERIC PLASMA JETS: DEVELOPMENT, DIAGNOSTICS AND APPLICATION FOR BACTERIA STERILIZATION

Dejan Maletić[1], Nevena Puač[1], Gordana Malović[1] and Zoran Lj. Petrović[1, 2]

[1]*Institute of Physics, University of Belgrade, Pregrevica 118, 11080 Belgrade*
[2]*Serbian Academy of Sciences and Arts, Knez Mihajlova 35, 11001 Belgrade, Serbia*

In the last several years plasma jets attracted great interest due to the unique physical phenomena. Unlike the classical streamers that are travelling stochastically in space, plasma jets or guided ionization waves have highly reproducible trajectories. They are confined with the buffer gas column. We will present diagnostics of plasma jet in pure helium and in gas mixtures for several electrode configurations. Two diagnostic techniques are used: iCCD imaging and electrical probe measurements [1, 2]. From electrical measurements we calculated voltages, powers and impedances of the plasma jet and from iCCD images we obtained spatial and temporal development of plasma for various experimental parameters. In some configurations velocity of the PAPS (Pulsed Atmospheric Pressure Streamers) can reach speeds up to 20 km/s, which are several orders of magnitude higher than the speed of the buffer gas. By adjusting the width of the electrodes, their mutual distance and distance from the edge of the tube, the range of plasma jet can be tuned. Our plasma jet was used for MRSA bacteria treatment in form of biofilms. The inhibition zones were measured and reduction of the bacteria number in samples was quantified by using MTT assay. We also investigated the influence of the plasma jet on the bacteria DNA. Based on these results it can be concluded that the plasma jet is a very flexible plasma source in operating parameters and can be used for surface sterilization.

Acknowledgements: This research has been supported by the Ministry of Education and Science, Serbia, under projects ON171037 and III41011.

REFERENCES

[1] D. Maletić, N. Puač, N. Selaković, S. Lazović, G. Malović, A. Đorđević and Z. Lj. Petrović, Plasma Sources Sci. Technol. 24, 025006 (2015)
[2] D. Maletić, N. Puač, G. Malović, A. Đorđević and Z. Lj Petrović, J. Phys. D: Appl. Phys. 50, 145202 (2017)

BERYLLIUM SPECTRAL LINE STUDIES IN THE PRESENCE OF BERYLLIUM DUST

Biljana D. Stankov[1,2]

[1]*Institute of Physics, University of Belgrade, P.O.Box 68, 11080 Belgrade, Serbia*
[2]*University of Novi Sad, Faculty of Sciences, Department of Physics, Trg Dositeja Obradovića 4, 21000 Novi Sad, Serbia*

Beryllium is the element which has six times the specific stiffness of steel and at the same time it's one-third lighter than aluminum which makes it suitable for a wide range of applications: aerospace, information technologies, energy exploration, medical and other. Since Be is also naturally occurring element in metal-poor stars [1] study of the spectral lines emission of beryllium is important for astrophysics. Also, the beryllium has been chosen as the element to cover the first wall of ITER (International Thermonuclear Experimental Reactor) [2]. Hence, basic knowledge about beryllium spectral emission is available but still spectroscopic investigations and Stark parameters studies are almost exclusively limited to Be II resonance lines at 313 nm. In this research special plasma source was made in order to broaden the studies of spectral line shapes of beryllium [3]. Guideline during the construction of the source was to prevent exposure to formed dust, considering the toxicity of beryllium. Plasma source characterization through determination of optimal working conditions is described. It is found that the optimal conditions for Be spectral line shapes measurements are achieved with C = 5 μF, U = 7 kV, gas Ar +3% H_2, p = 1.2 mbar. Beryllium lines appeared as a result of the ablation of the discharges tube made of ceramic, BeO. The presence of dust particles is also observed. The electron density, Ne, and temperature, Te, were determined by using the iterative method. The electron number density during plasma afterglow was estimated using the peak separation $\Delta\lambda_{ps}$ of the hydrogen Balmer beta line, and the electron temperature is determined from the ratios of the relative intensities of Be spectral lines emitted from successive ionized stages of atoms.

REFERENCES

[1] G. Gilmore et al, Nature 357, 379 (1992)
[2] International Thermonuclear Fusion Experimental Reactor Project, ITER Report, ITER D 2X6K67 v1.0 Plant Description (PD), Cadarache (2009)
[3] B. D. Stankov et al, Rev. Sci. 89, 053108 (2018)

CURRENT DISTRIBUTION IN AN EXPERIMENT OF Z-PINCH WITH PRE-EMBEDDED AXIAL MAGNETIC FIELD

M. Cvejić[1], D. Mikitchuk[1], R. Doron[1], E. Kroupp[1], C. Stollberg[1], Y. Maron[1]

[1]*Weizmann Institute of Science, Rehovot, 7610001, Israel*

Abstract. Temporally and spatially resolved spectroscopic measurements of the magnetic field in the experiment of z-pinch with pre-embedded axial magnetic field clearly showed that the azimuthal magnetic field is substantially smaller than expected from Ampere's law, considering the driving current and the imploding plasma radius. This situation is very different from measurements performed without preembedded axial magnetic field, demonstrating the dramatic effect of the pre-embedded field on the current distribution. Subsequent measurements revealed that the missing current flows through the slowly-imploding, low-density-plasma residing at radii larger than the main imploding plasma radii.

1. INTRODUCTION

The subject of compression of magnetic flux and magnetized plasma is a fundamental problem manifested in a variety of conducting fluid phenomena in laboratory plasmas and astrophysics. Magnetic flux can be compressed within a conducting shell when the shell is collapsed by the application of an external force. In z-pinch scheme, the conductor is plasma that implodes by the J×B force due to a large current flowing through it. Recently, this subject has gained particular interest due to the advances in producing plasmas of high temperature and density for fusion purposes, based on the approach of magnetized plasma compression [1].

2. EXPERIMENTAL SETUP

In our configuration (see Figure 1a), a cylindrical argon gas-puff shell (initial radius 19 mm and mass per length 30 μg/cm), in which a quasi-static axial magnetic flux ($B_{z0} \leq 0.4$ T) is pre-embedded, pre-fills the anode-cathode gap (10 mm). Subsequently, a pulsed-current (rising to 300 kA in 1.6 μs) is driven through the gas, ionizes it, and generates an azimuthal magnetic field, B_{θ}, creating a pressure that compresses the plasma radially inward together with the embedded B_z-field. The initial B_{z0} is generated by a pair of Helmholtz coils (HC)

carrying a long current pulse (~5 ms) to allow for the diffusion of B_z into the anode-cathode gap.

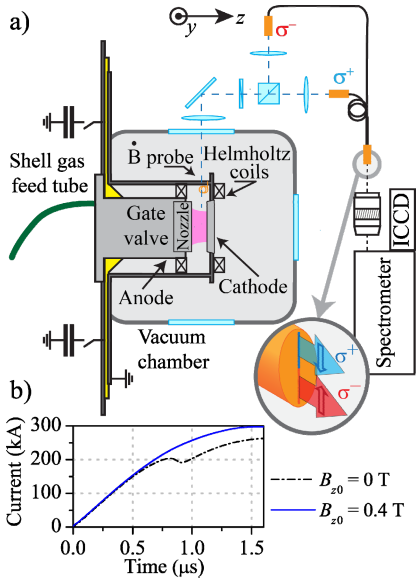

Figure 1. a) Schematic description of the experimental setup and spectroscopic system used for B_θ measurements. b) Current traces for B_{z0} =0 and B_{z0} = 0.4 T.

Spectroscopic technique for B_θ measurements is recently developed and described in Refs. [2,3]. When the plasma emission is viewed parallel to the B-field, σ^+ and σ^- circularly polarized Zeeman components are observed. These two components are separated using polarization optics, consisting of a quarter wave plate and a polarizing beam splitter. Each of the two components, now linearly polarized, is imaged on a separate linear array of 50 optical fibers. The two ends of the fiber arrays are imaged along the entrance slit of a high-resolution imaging spectrometer, coupled with ICCD. This setup allows for a simultaneous recording of the two polarization components (σ^+ and σ^-), emitted from the same plasma volume in a single discharge, on different parts of a single ICCD detector. Within addition to the spectroscopic measurements, a calibrated B-dot probe is used for measuring the total load current that flows through the discharge.

3. RESULTS

B_θ is determined using the σ^+ and σ^- Zeeman components of the Ar III line (^{4}S)4s $^5S_2$ - (^{4}S)4p $^5P_2$ at λ=3301.85 Å. Figure 2a presents a typical spectral image obtained at z = 5 mm, for B_{z0} = 0 (z=0 is the anode surface) and at t = 806 ns (t = 0 is the beginning of the current pulse, gate time is 10 ns). The upper and lower halves of the figure show the spatially resolved (in the r-direction) plasma emission of the σ^+ and σ^- components, respectively. The upper branch of the

fiber array is flipped, such that the emission from the plasma outer radii are recorded close to the center of the ICCD, to minimize the effects of optical aberrations. Figure 2b shows the lineouts shapes of the σ^+ and σ^- Zeeman components at the outermost plasma radius (r_{imp} = 7.8 mm, marked by the rectangles in Fig. 2a), along with their best fits.

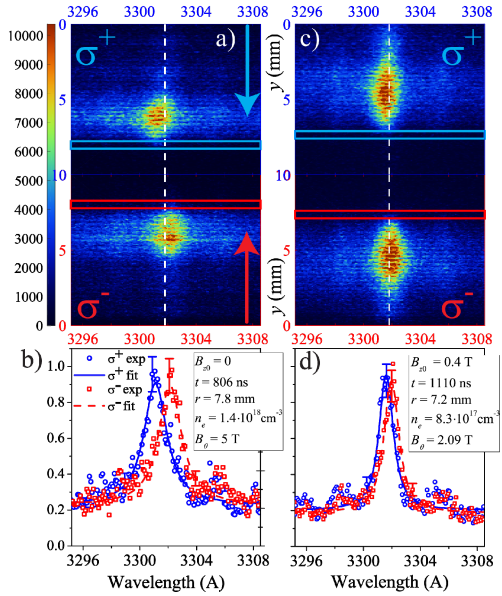

Figure 2. a) Spectral image of the Ar III 4*s*-4*p* transition (λ = 3301.85 Å), for B_{z0} = 0; b) spectral line shapes of the σ^+ (blue circles) and σ^- (red squares) Zeeman components along with the best fits (blue solid and red dashed lines); c) spectral image for B_{z0} = 0.4 T; d) explanations are the same as in b). The dashed white vertical line in a) and c) represents un-shifted position of the line center (B_θ = 0). The horizontal lines mark the lineout positions.

Each of σ^+ and σ^- line shapes are fitted with a Voigt profile, where the Gaussian part accounts for both the instrumental and Doppler broadenings, and the Lorentzian part that is due to the Stark broadening. The influence of the Zeeman effect on the spectral shape of each of the σ-component is small. B_θ is then extracted from the wavelength difference between the peaks of the best fits. Figures 2c-d are the same as Figures.2a-b, but for B_{z0} = 0.4 T, obtained at t = 1100 ns.

The imploding plasma radii observed from the spectral images in Figures 2a and c are similar. Assuming the entire current is flowing through the imploding plasma, we expect that B_θ would be lower for the case of B_{z0} = 0, due to the significantly smaller current measured by the B-dot probe at the time of the spectra recording (~195 kA for B_{z0} = 0 compared to ~270 kA for B_{z0} = 0.4 T, as seen from Figure 1b). However, while the measured B_θ in the case of B_{z0} = 0, is B_θ = 5 T, as expected, in the case of B_{z0} = 0.4 T, the measured B_θ = 2.1 T is much lower than expected from Ampere's law. Measurements during the

implosion phase at different z-position also confirm the discrepancy between expected and measured values of B_θ for $B_{z0} > 0$ T. In contrast, for B_{z0}=0, the expected and measured B_θ values are practically the same. This means that for $B_{z0} = 0$ the entire current flows within the imploding argon shell. On the other hand, for $B_{z0} = 0.4$ T, only ~ ¼ of the current is flowing through the imploding argon plasma.

Spectroscopic measurements revealed the existence of low-density-plasma (LDP) at $20 \le r \le 27$ mm, for $B_{z0} = 0.4$ T, that consists of argon and hydrocarbon impurities ($10^{16} \le n_{e\mathrm{LDP}} \le 10^{17}$ cm^{-3}, $4 \le T_{e\mathrm{LDP}} \le 6.5$ eV, while the typical plasma parameters of the main imploding argon plasma are $n_{e(\mathrm{Ar})} \sim 10^{18}$ cm^{-3} and $T_{e(\mathrm{Ar})} \sim 5$ eV). B_θ measurements at the outer edge of this LDP ($r \approx 27$ mm), obtained using Zeeman splitting of the C IV, $\lambda = 5801.33$ Å revealed that the current flowing within $r \le 27$ mm accounts for nearly the entire current measured by the B-dot, providing a definite answer for the missing current in the imploding plasma. LDP is also observed when $B_{z0} = 0$, but it is of lower density and temperature ($n_e \le 3 \cdot 10^{16}$ cm^{-3} and $T_e \le 2$ eV), that remain low throughout the implosion, consistent with the absence of a significant current flowing through the LDP. It is only in the presence of $B_{z0} > 0$ that the LDP carries a significant part of the current. Although, much of the current flows through the LDP at large radii, this LDP is only slowly imploding. The development of a force-free current configuration can be an explanation to this phenomenon.

4. CONCLUSIONS

The significant effects of B_{z0} on the implosion dynamics are due to current loss to the LDP. Previously unpredicted observations in high-power magnetized-plasma experiments, like (*i*) formation of helical structures (observed in the Magnetized Liner Inertial Fusion experiment [1]), (*ii*) larger-than-predicted implosion time and plasma radius at stagnation, and (*iii*) reduction of the continuum and K-shell emission, may be connected and explained by the present discovery.

Acknowledgements

This work is supported in part by the Cornell Multi-University Center for High Energy Density Science (USA), Israel Science Foundation and United States-Israel Binational Science Foundation.

REFERENCES

[1] M. R. Gomez, et. al., Phys. Rev. Lett., 113, 155003, (2014)
[2] G. Rosenzweig, E. Kroupp, A. Fisher, and Y. Maron, JINST 12, P09004 (2017)
[3] D. Mikitchuk, M. Cvejć, R. Doron, E. Kroupp, C. Stollberg, Y. Maron, A. L. Velikovich, N.D. Ouart, J. L. Giuliani, T.A. Mehlhorn, E.P. Yu and A. Fruchtman, submitted to Phys. Rev. Lett.

Doppler spectroscopy of shock waves in laser induced plasma

Dejan Dojić, Miloš Skočić and Srdjan Bukvić

University of Belgrade, Faculty of Physics, 11000 Belgrade, Serbia

Abstract. Relying on classical, laterally resolved spectroscopy we present measurements of plasma expansion which is generated by interaction of nanosecond laser with copper target. Radial expansion velocity is estimated from Doppler splitting of resonant Cu I 324.75 nm spectral line. The measurements are conducted in atmosphere of air, argon and hydrogen at low pressure of 60 Pa. We found that expansion velocity of copper atoms have the highest value in argon (∼50 km/s) and the smallest speed in air (∼42 km/s).

1.Indroduction

Diagnostics of Laser Induced Plasma (LIP) provides relevant data related to laser-metal interaction. For high pressure of background gas, plasma is close to state of local thermodynamic equilibrium [1] (LTE). Details related to initial plasma metal interaction are less pronounced at atmospheric pressure. At low pressure of ambient gas plasma can departure from state of LTE. This makes diagnostics more difficult, but some specifics related to laser metal interaction are preserved - expansion velocity, temperature of heavy particles etc.

In this paper we present measurements of the plasma expansion relyling on Doppler splitting of resonant copper line (see Fig.1) [2]. This method allows us to estimate expansion velocity of copper plasma created by Nd:YAG laser for different types of surrounding gas.

2.Experimental setup

For plasma creation we employed the Nd:YAG laser, EKSPLA NL 311, operating at 532 nm. Duration of the laser pulse was 5 ns, with repetition rate of 1 Hz and output energy in the range 125 - 400 mJ. Flat copper sample (99.9% purity) was placed inside the home made chamber. Measurements of expansion speed presented in this work are conducted in

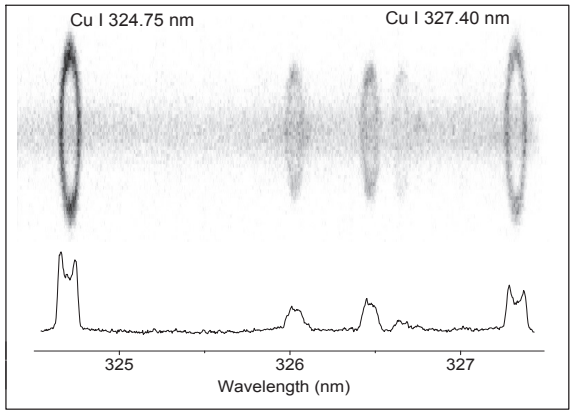

Figure 1. Spectrum of Cu I lines 324.75 nm and 327.40 nm recorded side-on in the imaging mode. Characteristic oval shape is caused by Doppler splitting due to fast radial expansion. At the bottom is presented the same spectrum but without lateral resolution (FVB camera mode). Clear deep seen in the resonant Cu I lines is, therefore, caused by strong Doppler splitting, not by strong self-absorption [2].

air, hydrogen and argon atmosphere at 60 Pa background gas. The detection system is based on the Andor DH740-18F-03 iStar intensified CCD camera, cooled down to -20°C and mounted on McPherson model 209 spectrograph (1.33 m focal length) equipped with a holographic grating of 2400 grooves/mm. The overall instrumental profile (spectrograph + ICCD camera) can be approximated by the Voigt function with a FWHM of 8.7 pm. The image of the plasma is collected side-on and projected onto a 50 μm wide entrance slit with unit magnification.

3.Laterally resolved spectra

In Fig.1 we present uncommon, oval shape, of spectral lines recorded in the imaging mode of the camera. This oval shape is caused by significant Doppler splitting due to fast radial expansion, Fig.1.

In the early stage of plasma expansion, the fastest particle leave the volume which is heated by the absorption of laser light. These particles in interaction with surrounding gas create a hot expanding front with more or less spherical form , Fig.2. When the image of the plasma is projected on spectrograph, the entrance slit cuts only 50 μm wide line of the whole image. This line comes from a narrow slice of the hot expanding front. The slice has a ring shape.

Due to Doppler effect, light emitted from the parts of the ring mow-

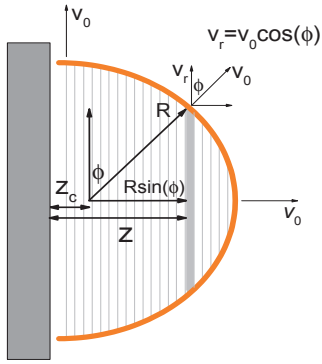

Figure 2. Schematics of expansion process. Only radial component $v_r = v_0 \cos\phi$ of the expansion velocity v_0 introduces Doppler splitting. With light gray we marked the slice of the plume projected on the entrance slit of the spectrograph. Z is distance of the recorded slice from the target while Z_c is geometrical center of the hot expanding front [3].

ing toward the observer will be shifted towards the blue. Consequently, the light emitted from the parts of the ring which move away will be shifted towards the red. Accordingly, the CCD camera will record the spectral line whose shape satisfy equation of ellipse [2]

$$\frac{c^2}{v_0^2}\left(\frac{\Delta\lambda}{\lambda}\right)^2 + \frac{y^2}{R^2} = 1. \tag{1}$$

In equation (1) c is speed of light, $\Delta\lambda$ is separation between red and blue arc, y represents distance from the central line of sight, R is radius of the expanding ring, v_0 expansion velocity, while λ is wavelenght of the emitted light. From equation (1) it is clear that separation of the red and blue arc is proportional to the expansion velocity v_0, if y and λ are constant. Maximum value of expansion velocity is for $y = 0$, while for $y = R$ it is minimal. Height of the oval corresponds to the radius of the expanding ring at the moment when recording is made.

Equation (1) is obteined under the assumption that the expanding ring is thin, that all parts have the same radial velocity v_0 and the same monochromatic emission λ. It is clear that these assumptions are only approximately satisfied in reality.

4.Experimental results and discusion

We measured profiles of Cu I 324.75 nm spectral line for 8 different distances from the target starting from 1 mm to 4.25 mm with 0.25 mm step [3]. For given position from the copper target, the spectrum was recorded

for several time delays in respect to the laser pulse (60 ns, 90 ns and 140 ns). The plasma was created in air, hydrogen and argon atmosphere at a pressure of 60 Pa. All spectra were recorded in the imaging mode of the camera. To improve S/N ratio every spectrum is obtained by averaging 50 images of successive laser shots.

In Fig.3 we present velocities of radial expansion measured for three delays at various distances from the copper target. As we move away from target, the expansion velocity, for the same delay decreases, Fig.3. This behavior is explained by the fact that the projection of the expansion speed to the direction of observation is smaller as we move away from the target. Experimental data shows good agreement with calculated values of radial velocity assuming that the expanding front has spherical geometry. In this case $v_r = v_0\sqrt{1-\frac{(Z-Z_c)^2}{R^2}}$. Meaning of the quantities v_r, v_0, Z, Z_c and R is illustrated in Fig.2. The corresponding best fit curves are shown in Fig.3 as the solid lines.

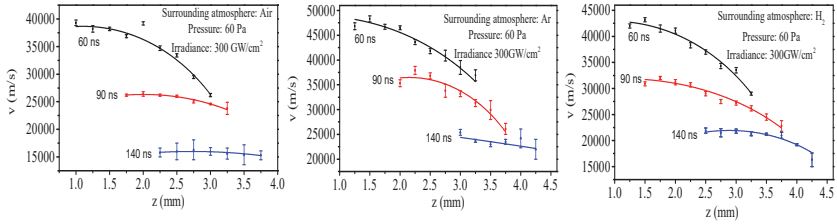

Figure 3. Radial expansion velocities measured for delays of 60 ns, 90 ns and 140 ns at several distances from the target surface relying on Cu I 324.75 nm line [3].

5. Acknowledgements

This work is part of the project "Determination of atomic parameters on the basis of spectral line profiles" (ON171008) supported by Ministry of Education and Science of the Republic of Serbia.

REFERENCES

[1] G. Cristoforetti et al. Spectrochim. Acta Part B 65 (2010) 86-95

[2] S.Bukvić and M.Skočić, Spectrochemica Acta part B, Volume 132, 56-60, (2017)

[3] D.Dojić et al. JQSRT, Volume 207, 73-77, (2018)

TRANSITION PROBABILITIES FOR Kr III SPECTRAL LINES TABULATED BY STRIGANOV AND SVENTITSKII TABLES ONLY

L. Gavanski[1], M. T. Belmonte[2], J. A. Aparicio[2], S. Mar[2], and S. Djurović[1]

[1]*University of Novi Sad, Faculty of Sciences, Department of Physics, Trg Dositeja Obradovića 4, 21000 Novi Sad, Serbia*
[2]*Universidad de Valladolid, Departamento de Física Teórica, Atómica y Óptica, Paseo de Belén 7, E-47011 Valladolid, Spain*

Abstract. Experimentally obtained transition probabilities for some ultraviolet Kr III lines, expressed in absolute units, are presented in this paper. For the measurement, intensities of spectral lines emitted by a plasma generated in a low-pressure pulsed arc were used. The electron density was in the range of (1.5 - 3.4) × 10^{22} m^{-3}, while the temperature was between 28000 K and 31000 K.

1. INTRODUCTION

In this paper, we report new experimental results of transition probabilities for some UV lines of doubly ionized krypton. The transition data for the considered lines can only be found in the Striganov and Sventitskii Tables [1]. The transition probabilities are derived by using experimentally obtained spectral intensities and reference transition probabilities calculated from theoretical oscillator strengths given in Raineri et al. [2].

These data can be of interest for plasma diagnostic purposes, especially for the determination of the plasma temperature using a method based on spectral line intensities [3]. The transition probability data are also important for the development of light and laser sources [4, 5] as well as in astrophysics [6, 7].

2. EXPERIMENT

A low pressure pulsed arc was used as the plasma source. The lamp consists of a Pyrex glass tube, 19 mm in internal diameter and 175 mm long. The pulses were made by discharging a 20 μF capacitor bank, charged up to 7.8 kV. The plasma life was about 200 μs. Pure krypton was continuously flowing through the discharge tube under a pressure of 120 Pa.

The spectra were recorded by using a 1.5 m spectrometer equipped with a 2400 lines/mm grating. At the exit of the spectrometer, an ICCD camera was mounted. The spectra were observed along the discharge tube, 2 mm off the tube axis at the instants 50, 60, 100 and 110 μs after the beginning of the discharge.

The exposure time ranged between 2 and 5 μs. Every line profile was checked for the presence of the self-absorption.

The electron density was measured by using a two-wavelength interferometric technique with two He-Ne lasers at 543.5 nm and 632.8 nm. This density ranged between (1.5 - 3.4) × 10^{22} m^{-3}, with an estimated experimental error of 5%. The axial homogeneity of the plasma and the cylindrical symmetry enabled simultaneous optical and interferometric measurements. According to [8, 9] the plasma was in pLTE. This enabled us to use the Boltzmann plot of several Kr III lines to calculate the electron temperature, which ranged from 28000 K to 31000 K with estimated errors lower than 10%. Since there are not previous experimental transition probability data, the theoretical oscillator strengths from Raineri et al. [2] were used to obtain the corresponding transition probabilities needed for the Boltzmann plot.

3. RESULTS

The results, arranged in increasing wavelength, are shown in Table 1. The first column contains the line wavelengths in nanometers. The next four columns include the configuration and energy of the upper and lower energy levels of the transition, respectively. The wavelengths and energy levels were taken from the Striganov and Sventitskii Tables [1]. In the last column, our measured transition probabilities (in absolute units) are given. The experimental errors are estimated to be lower than 20%.

Table 1. Measured transition probability data for some UV Kr III spectral lines.

Wav. (nm)	Upper level Configuration	Energy (eV)	Lower level Configuration	Energy (eV)	A_{ki} (10^7 s^{-1})
245.772	5d $^3D°_3$	27.37	5p $^3P_2$	22.33	12.854
247.837	6s'' $^1P°_1$	31.30	5p'' $^1D_2$	26.30	10.546
249.135	5p'' $^1D_2$	26.30	4d' $^1P°_1$	21.32	1.415
252.032	5d $^3D°_1$	27.19	5p $^3P_1$	22.27	2.513
254.951	5d $^3D°_1$	27.19	5p $^3P_2$	22.33	1.097
323.521	5p' $^1D_2$	25.15	4d' $^1P°_1$	21.32	0.242

The intensities of all the spectral lines considered here are very low in comparison with other doubly ionized krypton lines. Fig. 1 and Fig. 2 show two examples for the 249.135 nm and 254.951 nm spectral lines.

There are not previous transition probability data for the considered lines in the literature, and the present data are given here for the first time.

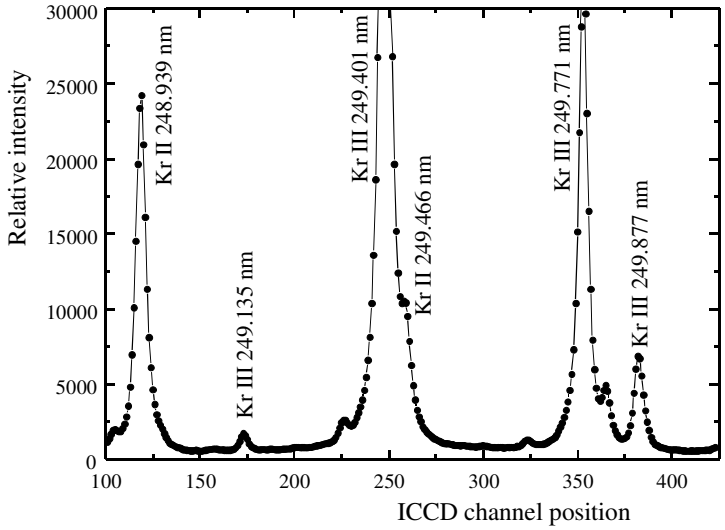

Figure 1. Part of the ionized krypton spectrum close to the 249.135 nm line.

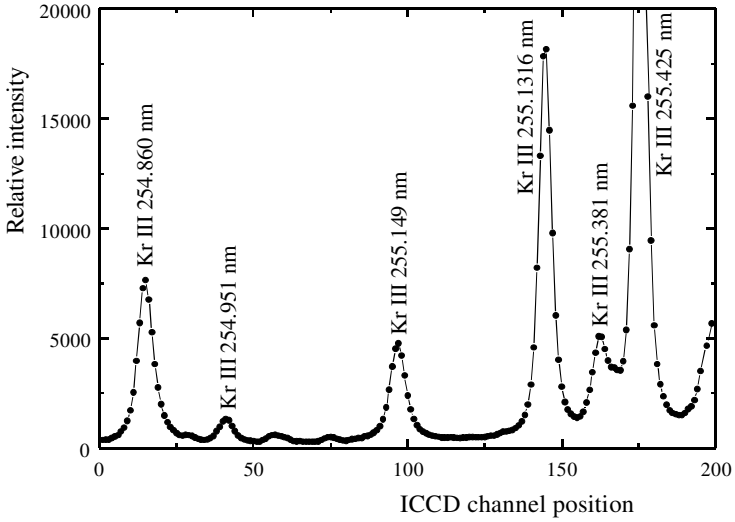

Figure 2. Part of the ionized krypton spectrum close to the 254.951 nm line.

Acknowledgements

Work of L. Gavanski and S. Djurović was supported by the Ministry of Education, Science and Technological development of Republic Serbia, under Project 171014.

M. T. Belmonte acknowledges financial support from the University of Valladolid through the FPI PhD grant.

REFERENCES

[1] A. R. Striganov and N. S. Sventitskii, *Tables of Spectral Lines of Neutral and Ionized Atoms*, Plenum, New York (1968).
[2] M. Raineri, J. G. Reyna Almandos, F. Bredice, M. Gallardo, A. G. Trigueiros, S-G. Pettersson, J. Quant. Spectrosc. Radiat. Transfer 60, 25 (1998).
[3] H. R. Griem, *Plasma Spectroscopy*, McGraw-Hill Book Company, New York (1964).
[4] M. A. Cayless and A. M. Marsden, *Lamps and Lighting*, 3rd edn. Edward Amold, London (1983).
[5] K. Shimoda, *Introduction to laser physics*, Springer Series in Optical Sciences, Springer, Berlin (1984).
[6] W. P. Bidelman, Astrophys. J. 67, 111 (1962).
[7] H. L. Dinerstein, Astrophys. J. 550, L223 (2001).
[8] R. W. P. McWhirter, Plasma Diagnostic Techniques, edited by R. H. Huddlestone and S. L. Leonard, Academic, New York (1965)
[9] G. Travaillé, O. Peyrusse, B. Bousquet, L. Canioni, K. Michel-Le Pierres, S. Roy, Spetr. Chim. Acta B 64, 931 (2009).

UNDERWATER ABLATION WITH TWO DIFFERENT LASER WAVELENGTHS

M. R. Gavrilović Božović[1], S. Jovićević[1]

[1]*Institute of physics, Belgrade, 11080 Belgrade, P.O. Box 68, Serbia*

Abstract. In this work comparative study of LIBS on a target in water using a nanosecond single-pulse laser with two different laser wavelengths 532 and 1064 nm is performed. The results revealed significant differences both in the bubble and plasma emission properties for two types of studied materials, pure metal Al and ceramic α-alumina target.

1. INTRODUCTION

The most common choice of laser wavelength in underwater laser induced breakdown spectroscopy (LIBS) studies is 1064 nm. On the other hand, second harmonic of Nd:YAG laser at 532 nm has great potential for stand-off underwater LIBS applications, since its emission wavelength lies in a transmission window of the water, where its absorption has a minimum.

Aim of this study is to obtain closer insight into the advantages and drawbacks of both laser wavelengths, especially related to the application of LIBS analysis of submerged samples.

2. EXPERIMENT

Detailed experimental setup was the described earlier [1-2]. A Q-switched laser (Molectron MY34) with a pulse duration of 20 ns was operated either at 1064 or 532 nm. The laser beam was focused perpendicular to the target plane by two quartz plano-convex lenses, where the second lens was mounted directly on the chamber wall. To estimate the losses of the input laser energy through the water column, Beer-Lambert law was used. Focusing conditions and laser energy were chosen in such a way that resulting fluence on the target surface was around 40 J/cm^2(2 GW/cm^2) for both laser wavelengths.

Fast imaging was performed through the lateral window w_1 by using a biconvex achromatic lens L_3 and objective lens OL mounted on an iCCD camera. The iCCD was controlled using a pulse generator triggered optically by a fast photodiode that captures the laser beam partially reflected on a mirror. The acquisition gate width was varied between 15 ns and 50 μs. The same optical

setup used for plasma imaging was employed for shadowgraphy with added illumination of a white light source (WLS).

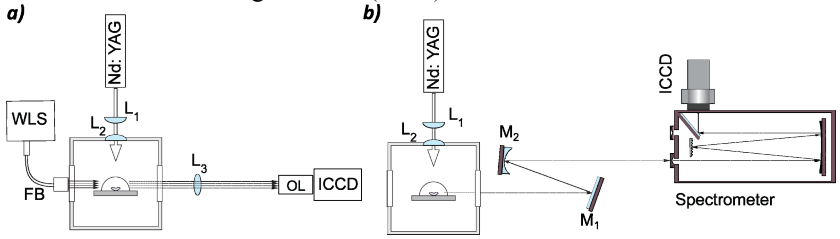

Figure 1. Experimental setup:a) fast plasma imaging and shadowgraphy, b) optical emission spectroscopy. Nd:YAG laser λ = 1064 nm or λ = 532 nm, 20 ns pulse duration, , L_1,L_2,L_3-lenses, WLS-white light source, FB-fiber bundle OL-objective lens, M_1, M_2-mirrors

In OES setup the 1: 1 image of the plasma plume was projected, by means of optical mirrors M_1 and M_2 on the entrance slit (100 μm wide) of a 0.5 m Ebert-type spectrometer, f/8.6 equipped with a grating of 1180 grooves per mm and iCCD detector.

3. RESULTS AND DISCUSSION

In Fig. 2.comparison of the bubble size obtained with two different laser wavelengths on two different types of materials is shown. Both for metallic aluminium and ceramic alumina ablation with fundamental wavelength at 1064 nm leads to the creation of larger bubbles. Maximum bubble radius on pure Al is 3.2 mm for 1064 nm and 2.7 mm for 532 nm wavelength. On the ceramic target maximum bubble size is 2.3 mm for 1064 nm and 1.9 mm for 532 nm wavelength. Besides difference in dimension, duration of the bubble is also different for two laser wavelengths. Namely, for 1064 nm wavelength, bubble collapse occurs at 475 μs and 350 μs for metal Al and ceramic alumina respectively, while with 532 nm wavelength collapse occurs at 430 μs and 330 μs. Based on the experimentally determined radius and collapse time of the bubble, the energy contained in the bubble was estimated [1].

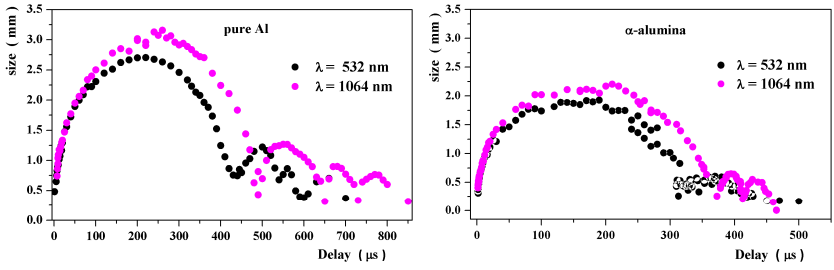

Figure 2. Size of the cavitation bubble produced with 1064 nm and 532 nm laser ablation: pure Al target (left) and ceramic α-alumina target (right)

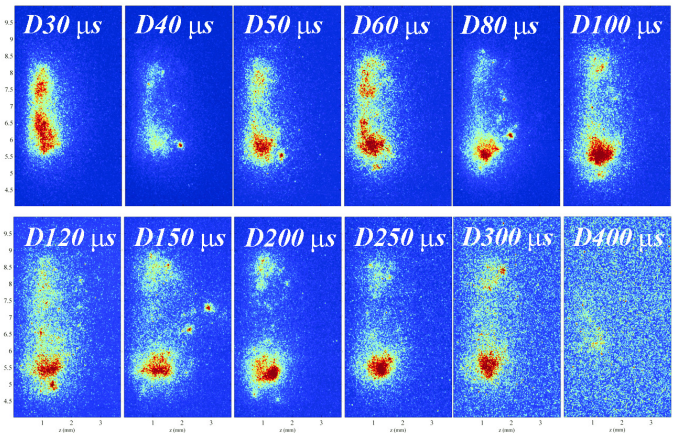

Figure 3. Secondary plasma phase on pure aluminium target produced with 532 nm laser ablation

Regarding the plasma formation, irrespective of the wavelength and target material, secondary plasma formation was always observed [1]. In Fig. 3 the appearance of the late plasma emission on the pure Al target after the ablation with the 532 nm wavelength is shown. It resembles very much the optical emission on Al with 1064 nm [1]. Here again the luminous emitting centres positioned inside the volume occupied with the cavitation bubble are observed. Since the duration of the cavitation bubble is shorter for 532 nm wavelength, consequently the optical emission also disappears earlier, ie, around 400 μs after the ablating laser pulse, while for 1064 nm ablation, optical emission lasted up to 475 μs delay.

Since the secondary plasma is formed with both laser wavelengths, clearly resolved and intense spectral lines could be recorded in both cases, see Fig. 4. Intensities of the spectral lines are however lower with 532 nm ablation. This result is in accordance with previous research on the influence of the laser wavelength on the properties of the laser induced breakdown in the bulk liquid [3]. It was found there that ablation with second harmonic of Nd:YAG results in a plasma with lower electron density and temperature, and with faster temperature decay. The explanation lies in a dominant absorption mechanism, which in laser ablation plasmas is inverse bremsstrahlung. Absorption cross sections for this process are higher for near IR wavelengths, meaning that more energy is transferred to the plasma in the case of 1064 nm wavelength. The only case when emission intensities are higher for 532 nm is molecular AlO bands emitted from Al plasma, see Fig. 4a, middle graph. But this apparent disagreement is actually further confirmation of fast temperature decay with the 532 nm wavelength, since for the molecular bands to be emitted in the plasma, the temperatures need to be low enough, i.e., around 5000 K. Although the underwater plasmas are known to have this kind of low temperature, it seems that with the 532 nm ablating laser the plasma is even colder. At later delays,

even molecular emission on Al is more intense with 1064 nm wavelength, confirming the faster temperature decay for 532 nm ablation.

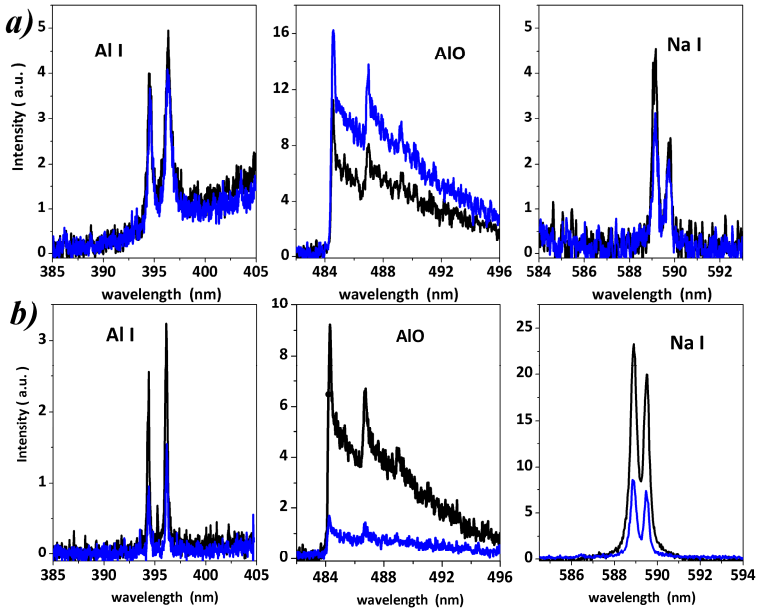

Figure 4. Spectral line emission produced with two different laser wavelengths on a) pure aluminium target b) ceramic α-alumina target. Delay for all spectra was 2 us and gate width was 10 us, blue line λ=532nm, black line λ=532 nm

The decrease in spectral line intensity with 532 nm ablation is more pronounced for ceramic alumina target. Possible explanation for this is decreased ablation efficiency[4].

Acknowledgements

This work is supported by the Ministry of Education, Science and Technological Development of Republic Serbia under Project No. 171014.

REFERENCES

[1] M. R. Gavrilović, V. Lazic, S. Jovićević, J. Anal. At. Spectrom 32, 345,(2017).
[2] M. R. Gavrilović, M. Cvejić, V. Lazic, S. Jovićević, Phys. Chem. Chem. Phys, 18, 14629 (2016).
[3] Ye Tian, B. Xue, J.Song, Y.Lu, Y. Li and R. Zheng, App. Phys. Express, 10,072401 (2017).
[4] N. N. Nedialkov, P. A. Atanasov, M. Sawczak, G. Sliwinski, Proc. SPIE 5120, XIV International Symposium on Gas Flow, Chemical Lasers, and High-Power Lasers, (10 November 2003).

TEMPORARY DEPENDENCES OF CARBON SPECTRAL LINES IN VACUUM LASER PLASMA

V. Goncharov, M. Puzyrev, V. Stupakevich

A.N.Sevchenko Institute of Applied Physics Problems,
Belarusian State University
7 Kurchatov St., 220045, Minsk, Belarus,
e-mail: puzyrev@bsu.by

Abstract. Luminescence spectrum of an erosive graphite target plume in a vacuum was observed. The target was irradiated using the YAG:Nd^{3+} laser pulses with a wavelength 1064 nm and a duration of 20 ns. Temporary dependences of luminescence lines CI, CII and CIII near a target surface are found. The brightness temperature of plasma near a target surface was about 9800 K.

1. INTRODUCTION

Diamond-like carbon films differ by exclusively high mechanical and tribological properties. One of effective ways of such films formation is the method of a pulse laser deposition [1]. The pulse laser deposition allows growing continuous ultra-thin films of various materials of single and multilayer structures with a wide range of physical properties [2].

These properties of the deposited films strong depend on the plasma parameters. In this work, we demonstrated that the control of spatial and temporary plasma parameters allows changing properties of deposited films .

2. EXPERIMENT DETAILS

The LOTIS-TII pulsed YAG:Nd^{3+} laser with a wavelength $\lambda = 1064$ nm and a pulse duration $\tau = 20$ ns (as a full width at half maximum - FWHM) was used for experiments. Laser pulse was focused on a graphite target which is placed in a vacuum chamber under pressure of 2.6×10^{-3} Pa. The target was mounted at angle of 45° with respect to the laser beam propagation and was constantly rotated to provide initial surface for ablation. The laser beam intensity was 5.7×10^{8} W/cm^2 and the diameter was about 2 mm. The sample deposition was carried out at room temperature. The target was made from highly oriented pyrolytic graphite (HOPG). This graphite has high density close to a theoretical value of the density 2.25 g/sm^3, and has diffraction of X-ray beams close to monocrystal natural graphite.

The measurement of temporary parameters of a plume luminescence was performed with an employment the double monochromator DMR-4, optical fiber and photomultiplier detector (SPM 10020). The signal from this detector transferred to Tektronix TDS2022B oscilloscope. Spectral properties of the laser plasma were studied using spectrometer of S100-2048 of SOLAR firm.

3. EXPERIMENTAL RESULTS

The Figure 1 shows the time-integrated of the spectrum on time scale of the carbon plasma near a target surface.

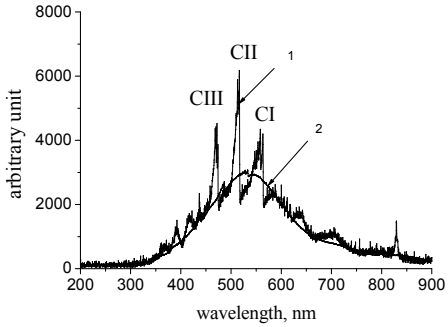

Figure 1. Integrated spectrum in time of a graphite plasma luminescence near the target surface: 1 – spectrum, 2 – the background processed by the IPC filter (infinite pulse characteristic). The power density of the irradiated laser was 5.6×10^8 W/cm^2.

In case of our experiment, the spectrum has spectral lines of carbon ions of various extents of ionization on continuous background luminescence. The brightness temperature of graphite erosive laser plasma in vacuum near a target surface has been estimated using form of continuous luminescence (see Fig. 1, (**2**)). This temperature is about ~ 9800 K.

We note, that the estimation of the temperature and the concentration of charged particles using integrated spectrum in time can be is not enough due to the appearance of the spectral lines in different time-points of the erosive laser plume recession.

The time behavior of the spectral lines CI, CII and CIII (see Fig. 1) has been determined this work. Plasma luminescence for separate spectral lines from double monochromator DMR-4 was detected on the SPM 10020 sensor. The signal from this sensor was registered by Tektronix TDS2022B oscilloscope. Results of experiments are represented on Figures 2, 3, 4.

The intensity of the luminescence line CI at 579.3 nm depends on time (see Fig. 2). The arrival time reading was covered by the starting laser pulse coincides. The line luminescence has some delay relative to the starting laser pulse. It is connected with absorption processes of the laser radiation by target, its heating, evaporation and processes of the ionization in destructions. The duration of a luminescence of an erosive laser plume much more time of the laser excitation.

The luminescence of erosion plume near a target surface begins during ~ 50 ns after starting pulse of the laser excitation. Then the time of the luminescence increases during ~ 150 nanoseconds and reaches some maximum

and during ~ 300 ns changes a little. There is a noticeable time of the luminescence growth since ~ 500 ns and maximum in a time-point 1000 ns was observed. Then luminescence intensity exponential falls off and after 3000 nanoseconds was practically zero.

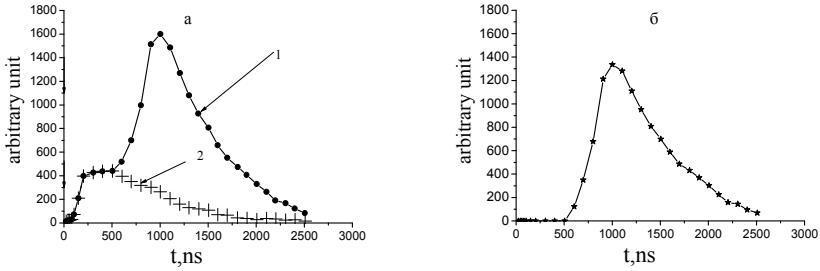

Figure 2. Dependence plasma luminescence on time: a) 1 –total signal of the line luminescence and the background, 2 – background luminescence; b) line luminescence 579.3 nm.

In Figure 2, a, shows that, the luminescence observed up to 500 ns by a total signal. The total luminescence of the line CI 579.3 nm and background ~ 530 nm is observed after 500 ns. The curve (figure 2, b) have been determine by a subtraction curve (2), of curve (1) (see Fig. 2). The luminescence of the spectral line CI begins much later, than the background luminescence (figure 2 b). These results can be explained by forming of dense nonideal plasma near a surface of graphite target at laser irradiation. This plasma luminescence is close to the luminescence of absolutely black-body radiation. Then plasma extends, with reducing density during cooling. Thus, the spectral lines luminescence appear at this time.

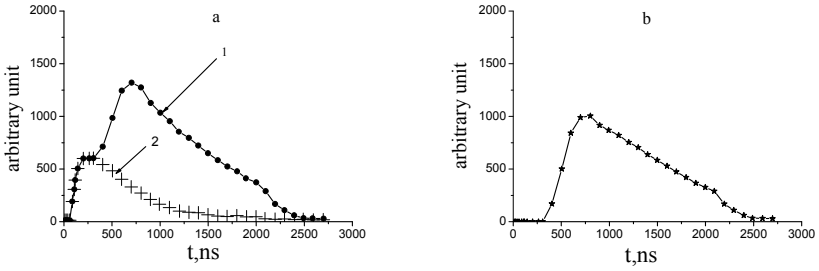

Figure 3. Temporal dependence of plasma luminescence: a) 1 – the total signal of a line luminescence and the background, 2 – the background luminescence; b) line luminescence at 514.5 nm.

The experiments have been performed at different spectral ranges. The temporal dependences of the line luminescence CII 514.5 nm and the continuous radiation for wavelength ~ 480 nm have been shown in figure 3, a. There are no spectral lines for the wavelength ~ 480 nm (figure 1). The luminescence CII 514.5 nm without a background has been illustrated in figure 3, b.

The same experiments have been performed also for lines CIII 465 nm and the background near this line too. Results of these experiments are shown in figure 4.

4. CONCLUSIONS

In order to conclude, the results of analysis illustrated in figures 1-4 allows to say that the plasma luminescence has some delay relative to the laser excitation start by the a pulse duration τ = 20 ns with a intensity 5.6×10^8 W/cm^2

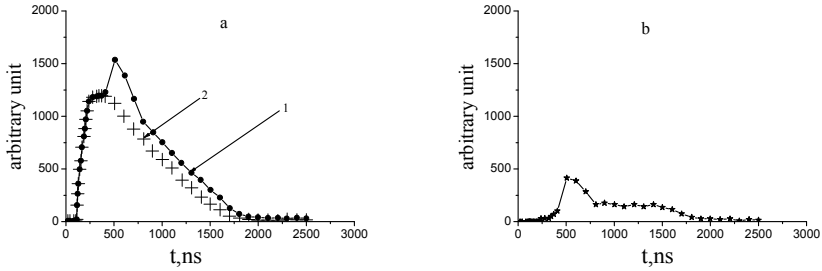

Figure 4. Dependence plasma luminescence on time: a) 1 – a total signal of a line luminescence and a background, 2 – a background luminescence; b) line luminescence 465 nm.

on the graphite target. Then near a target surface the formation of the dense destruction products in erosion plume is occurred. They are characterized by intensive luminescence in all spectral range and are close to the luminescence of absolutely black-body. It allows estimating the brightness plasma temperature near a target at the initial stage of its forming. This temperature in our experiments has value about 9800 K. Then the plasma decays, cools down and the ions lines appear. We can see (figure2, 3, and 4) that ions luminescence with higher ionization has a smaller delay relative to ions of smaller ionization degree and lines luminescence duration of ions with bigger degree ionization is less than ions with smaller level ionization.

The experiments have shown, spectral lines luminescence appear when laser plasma cooled down and all plasma formation processes have taken place, and only plasma decay processes are observed. Such processes in plasma determine many parameters of ultrathin films for the deposition regimes of coverings on different materials.

REFERENCES

[1]. S. Yasuda, T. Chikyow, S. Inoue, N. Matsuki, K. Miyazaki, S. Nishio, M. Kakihana, H. Koinuma, Appl. Phys. A 69, 925 (1999).

[2]. R. Eason, “Pulsed laser deposition of thin films: Applications-LED growth of functional materials”, 682 p (Hoboken. N.J. :Wiley-Interscience, 2007).

REGIMES OF HELIUM AND HYDROGEN BARRIER DISCHARGE AT LOWER PRESSURES

S. S. Ivković[1], N. Cvetanović[2], B. M. Obradović[1] and M. M. Kuraica[1]

[1]*University of Belgrade, Faculty of Physics, 11001 Belgrade*
[2]*University of Belgrade, Faculty of Transport and Traffic Engineering, 11000 Belgrade*

Abstract. The dielectric barrier discharge in helium and hydrogen was investigated using Stark polarization spectroscopy and electric measurements. The effect of pressure, voltage, electrode gap and surface on the electric field distribution in the pressure range 5 – 80 mbar was studied. It was found that the type of the discharge and its characteristic axial electric field distribution strongly depends on the distance between electrodes, while influence of the pressure is mostly seen as a change of the field strength. It was found that the discharge in helium is a subnormal-like for 1 mm gap while for 2 mm it is a glow-like. The discharge in hydrogen changes from a Townsend-like for 1 mm gap to a glow-like for 2 mm gap.

1. INTRODUCTION

The dielectric barrier discharges (DBDs) have been widely studied over the last two decades, mostly because of their broad fields of application [1]. The variety and ease of their implementation was demonstrated in different processes including surface modification, deposition, activation, gas purification and decontamination. Various discharge regimes have been observed and documented using high speed imaging, temporally and spatially resolved optical emission spectroscopy and simulations. One of the most important parameters of the DBD discharge is the electric field strength and its spatio-temporal distribution which determines the discharge type and characteristics [2, 3].

Hydrogen lines from the Balmer series are present in the spectrum of discharges with various working gases. Due to their high intensity they can be observed even when only traces of hydrogen are present as an impurity. For this reason the Balmer lines are commonly used as a tool for electric field measurement based on the Stark effect, see for instance [4, 5]. The advantage of the H_α line is its high intensity, even though it should be noted that it is the least sensitive line of the series, to the electric field.

Recently, the simultaneous influence of electric field and excessive line broadening on the Balmer alpha line was investigated, in the glow and DBD

discharge in a wide range of pressures [6]. The so-called excessive broadening is caused by Doppler shifted radiation from fast H atoms created in charge exchange processes [7-9]. It was shown that excessive broadening is pressure and voltage dependent, while Stark splitting can be used for electric field measurement in certain conditions. To that purpose a fitting method was developed for measurement of the macroscopic electric field [6].

Here, using the Stark polarization spectroscopy of the H_α line and the mentioned fitting method, the electric field distribution was measured in the DBD in helium and hydrogen in the pressure range from 5 to 80 mbar. Simultaneously electric measurements were performed for all conditions. The effect of pressure, voltage, electrode gap and surface on the electrical characteristics of DBD was investigated. We present different regimes distinguished in the DBDs operation, depending on pressure and gap, observed trough the electric field distribution in the discharge. Using time-resolved spectroscopy, evolution of the electric field distribution was studied during the discharge development.

2. EXPERIMENT AND METHOD

In our experiment the discharge is formed between two parallel electrodes: one metal electrode (30×30 mm^2) is covered with alumina dielectric while the other electrode is made of steel mesh and covered with pyrex glass. The distance between the barriers is set at 1 and 2 mm. The discharge chamber is firstly evacuated down to 10^{-2} mbar, and then the working gas is introduced up to 80 mbar pressure. The amplitude of the sine applied voltage was 1.1 and 1.7 kV at frequency of 19.7 kHz. Voltage is measured using a high-voltage probe, while the current waveforms are monitored using the Rogowski coil. An Echelle type monochromator was used. At the exit of the monochromator, radiation was detected using a two-dimensional ICCD (PI-MAX2, Princeton Instruments) with 1024×1024 pixels. The instrumental profile half-width was measured to be FWHM=0.02 nm, with pixel to pixel resolution of 0.0054 nm. The radiation from the discharge was polarized in the direction of the macroscopic electric field using a plastic polarizer. Thus obtained Balmer alpha line consists of Stark shifted Pi-components. The model function used for fitting is given in Ref. 6. It incorporates standard broadening mechanisms but also takes into account excessive and dissociative broadening of each component. The electric field strength, at a given time and position, is then obtained by fitting the overall line profile with the mentioned model function. The field value is a free parameter of the fit.

3. RESULTS

The analysis of the field distributions was performed for different pressures and gap distances.

Measured electric field distributions for hydrogen discharge at several pressures and 1 mm gap are shown in Figure 1. According to the nearly constant field value it can be concluded that for pure H_2 and 1 mm gap the discharge is in

the Townsend-like mode at all pressures. Additionally, it was found that for 2 mm gap it is in subnormal-like mode.

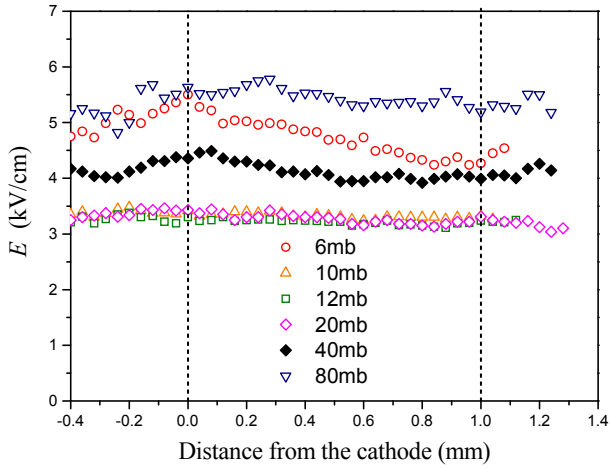

Figure 1. Electric field distributions for hydrogen discharge at several pressures and 1 mm gap.

Figure 2 shows the field distributions for the discharge in helium for the same gap of 1 mm. The small decrease of field strength with distance from the cathode indicates the discharge is in the subnormal-like mode. Analogously to hydrogen discharge, the regime changes with gap distance. Namely, the measurements for helium discharge at 2 mm gap have shown that discharge is in the glow-like mode.

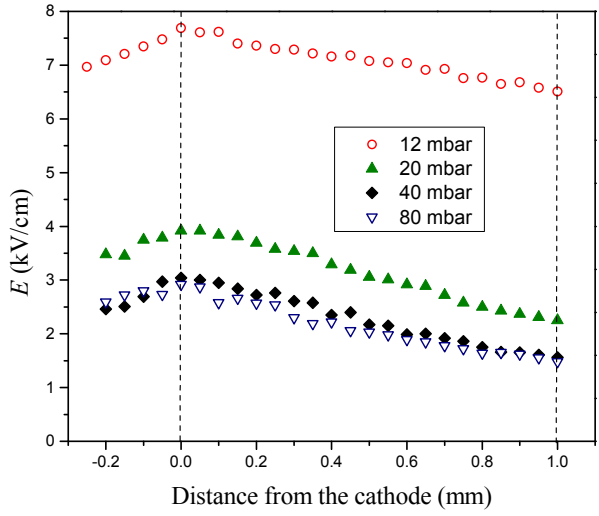

Figure 2. Electric field distributions for helium discharge at several pressures and 1 mm gap.

From a variety of obtained experimental data it was concluded that the regime of the discharge and its characteristic axial electric field distribution strongly depends on the distance between the electrodes. Influence of the pressure is mainly observed as a change in the electric field strength value, while its influence on the shape of the field distribution is of minor importance.

Acknowledgements

This work is supported by the Ministry of Education, Science and Technological Development of the Republic of Serbia through the Projects No 171034 and 33022.

REFERENCES

[1] U. Kogelschatz, Plasma Chem. Plasma Proc. 23 1–46 (2003)
[2] T. Martens, W. J. M. Brok, J. van Dijk and A. Bogaerts, J. Phys. D: Appl. Phys. 42, 122002 (2009)
[3] B.M. Obradović, N. Cvetanović, S.S. Ivković, G.B. Sretenović, V.V. Kovačević, I.B. Krstić, M. M. Kuraica, Eur. Phys. J. Appl. Phys. 77: 30802 (2017)
[4] B. N. Ganguly and A. Garscadden, J. Appl. Phys. 70, 621 (1991)
[5] T. Wujec, H. W. Janus and W. Jelenski, J. Phys. D: Appl. Phys. 36, 868 (2003)
[6] N. Cvetanović, S.S. Ivković, B.M. Obradović, M. M. Kuraica, Eur. Phys. J. D 71: 317 (2017)
[7] N. Cvetanović, M. M. Kuraica, N. Konjević, J. Appl. Phys. 97, 033302 (2005)
[8] A. V. Phelps, Plasma Sources Sci. Technol. 20 043001 (2011)
[9] N. Cvetanović, B. M. Obradović and M. M. Kuraica, J. Appl. Phys. 110 073306 (2011)

O I 645 nm TRIPLET EMITTED FROM ELECTRIC WALL STABILIZED ARC

Z. Mijatović[1], L. Gavanski[1], R. Kobilarov[1] and S. Djurović[1]

[1]*University of Novi Sad, Faculty of Sciences, Department of Physics, Trg Dositeja Obradovića 4, 21000 Novi Sad, Serbia*

Abstract. In this paper we report some investigations of 645 nm oxygen triplet lines. The electric wall stabilized arc was used as a plasma source.

1. INTRODUCTION

Excited oxygen atoms emit several groups of triplet spectral lines in visible part of spectrum (394, 543, 604, 615, 645, 725, 777, 844 nm). Up to now the 777 triplet is the most studied one in laboratory and astrophysical plasmas. Several papers consider 777 oxygen triplet in DC glow and radiofrequency discharges [1-3] and also in laser produced plasmas [4, 5]. In astrophysical plasmas this triplet is very often observed in dwarfs and giant stars [6, 7]. Contrary to triplet 777 other triplets were not mentioned in papers devoted to astrophysical plasmas. There are some discussions about 645 triplet in [8] where is radio-frequency plasma was used.

In this paper we investigated 645 triplet emitted from electric wall stabilized plasma. This triplet is consisted of the 645.36 nm, 645.44 nm and 645.59 nm lines.

2. EXPERIMENT

As a plasma source an atmospheric pressure wall stabilized arc was used [9]. The arc channel, 5 mm in diameter and 70 mm long, is formed by seven water cooled copper discs separated by 0.5 mm thick Teflon gaskets. The pure argon was introduced through holes in tungsten electrodes, placed at the ends of the channel, with flow rate of 3 l/min. In the middle part of the arc the mixture of Ar (72%) + H_2 (8%) + CO_2 (20%) was introduced with flow of 0.1 l/min. The gases were exhausted through the holes in copper discs placed next to the electrodes. The spectroscopic observations were made end on. The small percentage of the hydrogen was introduced for the electron density determination. The concentration of CO_2 was adjusted to avoid self-absorption effect. The self-absorption was checked by mirror placed behind the arc channel [10]. The measurements were performed by using eight different arc currents from 18 to 32 A.

3. PLASMA DIAGNOSTICS

The electron density was obtained from halfwidth of H_β line profile by using Griem's theoretical data [11] and was between (1.5 - 3.2) × 10^{22} m^{-3}. The estimated experimental error does not exceed ± 8%.

The electron temperatures were obtained from the [12] and measured electron densities. The data in [12] are based on Saha equation applied for pure argon. Calculation for plasma composition data [13] for mixture of argon with small percentage of other gases shows very small difference from calculations for pure argon plasma up to 11000 K. So, the temperatures determined for pure argon plasma are completely satisfying for used plasma mixture. Estimated error of electron temperature is about 10%. The numerical values of electron density and temperature are shown in Table 1 together with the halfwidth results.

4. RESULTS AND DISCUSSION

Part of the spectrum emitted from the plasma, with used gas mixtures, near the 645 oxygen triplet shows that the triplet is well isolated with no overlaping by other spectral lines.

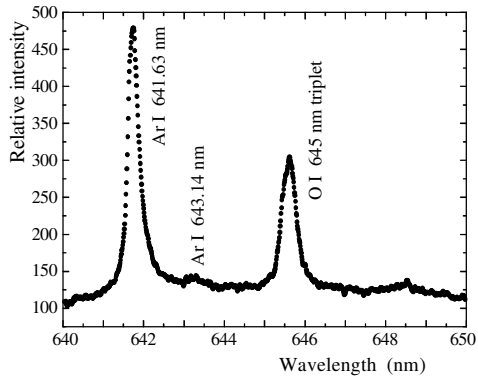

Figure 1. Part of the spectrum near to O I 645 nm triplet.

In addition to being isolated the 645 triplet is well defied. It is shown in Fig. 2. The total halfwidth of the triplet is measured as illustrated also in Fig. 2. The results, together with plasma diagnostic data are shown in Table 1. These results show that this triplet can be good candidate for the plasma diagnostic purposes.

The separation of three lines 645.36 nm, 645.44 nm and 645.59 nm by fitting procedure, for current of 30 A (N_e = 3·10^{22} m^{-3}, T_e = 10870 K), is shown in Fig. 3. All three lines are fitted by Voigt function with 0.226 nm halfwidth of each line. Ion broadening parameter for the lines is very small, about 0.08 [11]. In that case Voigt functions can describe the profiles well enough (See Fig. 3).

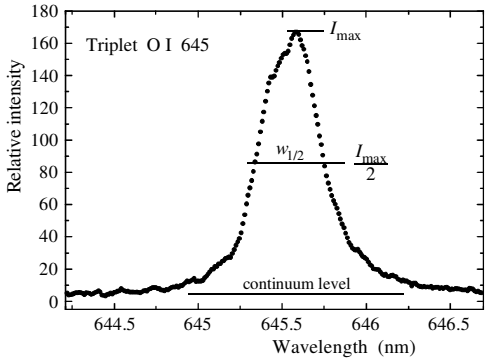

Figure 2. Oxygen 645 nm triplet with total halfwidth definition.

Table 1. The total halfwidth of O I 645 triplet with plasma diagnostic data.

N_e (m^{-3})	T_e (K)	$W_{1/2}$ (nm)
$1.5 \cdot 10^{22}$	9900	0.357
$1.8 \cdot 10^{22}$	10100	0.361
$2.0 \cdot 10^{22}$	10280	0.376
$2.3 \cdot 10^{22}$	10480	0.382
$2.6 \cdot 10^{22}$	10650	0.403
$2.8 \cdot 10^{22}$	10760	0.407
$3.0 \cdot 10^{22}$	10870	0.420
$3.2 \cdot 10^{22}$	10940	0.429

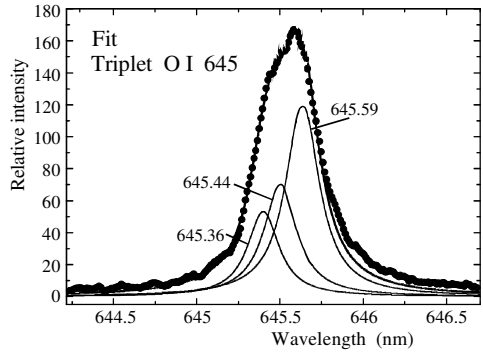

Figure 3. The Separation of three lines from O I 645 nm triplet.

The relative line intensities are I_1=30, I_2=43 and I_3=69, respectively. The ratio I_3/I_2=1.60 and I_3/I_1=2.30. It is in well agreement with line strengths (S-value) given in NIST Atomic Spectra Database [14] where S_3/S_2=1.40 and S_3/S_1=2.33. This also support absence of the selfabsorption effect.

Acknowledgements

This work is supported by the Ministry of Education, Science and Technological development of Republic Serbia, under Project 171014.

REFERENCES

[1] B. Zaniol, M. Schiorlin, E. Gazza, E. Marotta, X. Ren, M. Puiatti, M. Rea, P. Sonato and C. Paradisi, Int. J. Plasma Environ. Sci. Technol. 2, 65 (2008).
[2] M. J. Morávek, A. Kaňka, J. Čáp and V. Hrachová, WDS'15 *Proceedings – Contributed papers-Physics*, p. 227 (2015).
[3] V. Milosavljević, R. Faulkner and M. B. Hopkins, Optics Express 15, 13913 (2007).
[4] R. Stützer, M. Börner, M. Kuchelmeister and M. Oschwald, *Proceedings of Space Propulsion* SP2016, 3124870, p. 1 (2016).
[5] P. Pořízka, J. Klus, A. Hrdlička, J. Vrábel, P. Škarková, D. Prochazka, J. Novotný, K. Novotný and J. Kaiser, J. Anal. At. Spectrom. 32, 277 (2017).
[6] J. M. Vílchez, G. Stasińska and E. Pérez, *The evolution of galaxies*, p. 142 (Springer, 2001)
[7] I. Ramirez, C. A. Prieto and D. L. Lambert, *Proceedings IAU Symposium* 228, p. 271 (2005).
[8] V. Milosavljević, A. R. Ellingboe and S. Daniels, Eur. Phys. J D 64, 437 (2011).
[9] D. Nikolić, S. Djurović, Z. Mijatović, R. Kobilarov, B. Vujičić and M. Ćirišan, J. Quant. Spectrosc. Radiat. Transfer 86, 285 (2004).
[10] S. Djurović, R. Kobilarov and B. Vujičić, Bull. Astron. Belgrade 153, 41 (1996).
[11] H. R. Griem, *Spectral line broadening by plasmas*, p. 316 (Acadimic Press NJ, 1974).
[12] C. H. Popenoe and J. B. Shumaker Jr., J. Res. NBS Phys. Chem A **69**, 495 (1965).
[13] W. B. White, S. M. Jonson and G. B. Dantzig, J. Chem. Phys. **28**, 751 (1958).
[14] https://www.nist.gov/pml/atomic-spectra-Database

SPATIAL MEASUREMENTS OF LASER-INDUCED BREAKDOWN IN AIR

M. S. Rabasovic, M. D. Rabasovic, B. P. Marinkovic and D. Sevic

Institute of Physics, University of Belgrade, Serbia

Abstract. We present time resolved measurements of the plasma expansion produced by laser induced breakdown in atmospheric air. A Q-switched Nd:YAG laser is employed as the excitation source. The detection part of the acquisition system is based on a streak camera equipped with the spectrograph. A simple modification of the spectrograph enables the easy switching between the spectral and spatial measurement modes.

1. INTRODUCTION

The formation of laser induced breakdown (LIB) refers to a plasma production by focusing an intense laser beam in a gas, liquid or solid target. Parameters of laser induced plasma depend on irradiation conditions, such as laser intensity, pulse duration, laser wavelength or ambient gas. To understand the process of laser induced breakdown it is required to obtain the detailed knowledge of the initial stages of various processes involving laser duration and irradiation, plasma formation and its expansion. The nanosecond laser pulse generates plasma through thermal and non-thermal mechanisms. Studying the plasma formation with a high temporal, spectral and spatial resolution is of a great interest and formation of laser induced breakdown plasma in air has been studied by many researchers [1-6], including references therein.

After the initial breakdown, plasma plume propagates towards the focusing lens [1,3]. The bright plasma core of the LIB plasma in open air is surrounded by a layer of cold, moderately ionized gas called the sheath [1]. Glow of plasma sheath, although fainter than the core, is also visible to the naked eye. An explosive plasma expansion induces optodynamic phenomena, i.e., the propagation of a shock, acoustical and ultrasonic waves.

In this paper we present an experimental system that is capable of both spatial and spectral measurements of laser-induced plasma with picosecond temporal resolution. We performed a simple modification of our spectrograph that enables easy switching between the spectral and spatial measurement modes. Later, we became aware that this modification was already proposed and successfully used in the study of Siegel et al. [7], where imaging device was ICCD camera.

2. EXPERIMENTAL SET-UP

Time resolved LIB system implemented in our laboratory is shown in Figure 1. In this study we use the fundamental output at of OPO pumping laser (1064 nm, pulse energy up to 270 mJ, pulse duration of about 5 ns) to create an optical breakdown in ambient air. Timing considerations regarding the laser pulse and streak camera synchronization are very important in our measurements, so we added a photodiode and digital oscilloscope to our experimental setup, Figure 1.

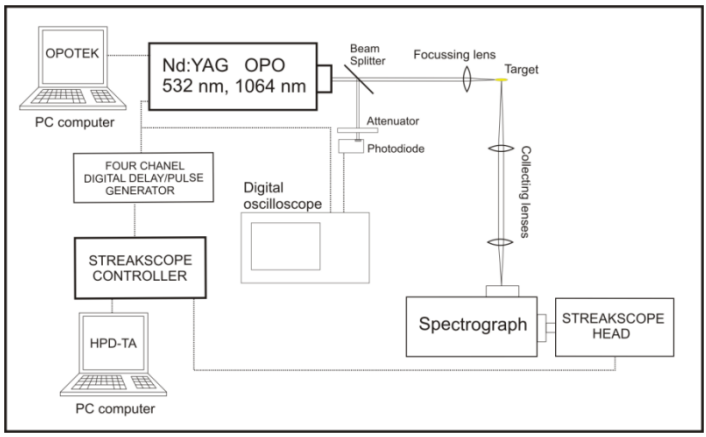

Figure 1. Setup for time-resolved laser induced breakdown measurements.

The optical emission from the plasma is collected by using a spectrograph and recorded with a streak camera. The streak images are time resolved thus enabling monitoring of temporal evolution of the ionic and atomic emission lines or spatial development of the plasma.

Our research of optical emission of plasma was limited so far to analysis of time resolved optical emission spectra acquired by the streak camera [8-10]. To make our study more comprehensive we saw the need for measuring the spatial distribution of plasma optical emission. So we improved the set up and accomplished requirement for easy switching between the spectral and spatial measurement modes of our streak camera system.

We performed a simple modification of our spectrograph that enables easy switching between the spectral and spatial measurement modes, see Figure 2. The spectrograph contains the triple grating turret. In the place of the 150 g/mm grating we mounted the plain mirror. Now, if position of turret corresponding to grating of 150 g/mm is selected, streak camera takes the image of the spatial distribution of the optical emission of the laser induced breakdown. The spectrograph entrance slit should be fully open to utilize as much as possible of the CCD camera active area. The calibration procedure showed that 1 mm on the target position corresponds to 72 pixels of the CCD camera.

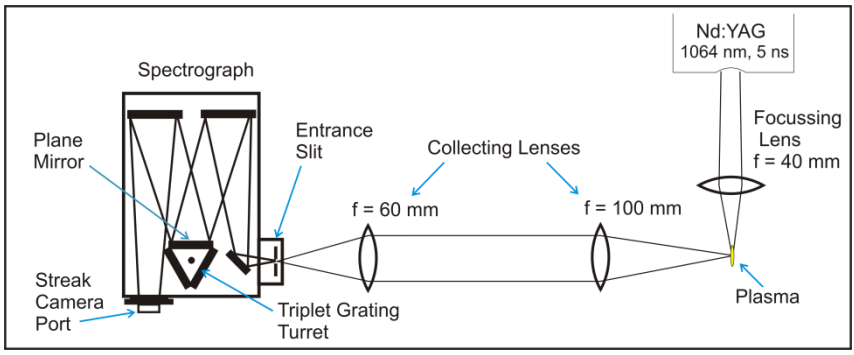

Figure 2. A simple modification of our spectrograph that enables easy switching between the spectral and spatial measurement modes.

3. RESULTS AND DISCUSSION

The streak image of the laser induced plasma (excitation at 1064 nm, energy of 51 mJ, peak intensity of 1.3 10^{11} W/cm^2) is shown in Figure 3. The time axis is vertical, with zero on top of the image. The spatial axis is horizontal. The development of the plasma is seen on the streak image as vertical development (corresponding to a passing of time) of a narrow horizontal section of plasma optical emission, seen through the camera slit, along the direction of propagation of the laser beam. In other words, two dimensional (2-D) streak image corresponds to only 1-D spatial image, represented by rows of image matrix, the other dimension being the time. White points indicate the edges and peak values of plasma brightness, detected by our image processing algorithm.

Our analysis of data provided by streak image presented in Figure 3 shows that instantaneous-velocity of plasma is about 150 km/s at the beginning, and decrease towards about 25 km/s after 16 ns. At about 20 ns plume stops expanding.

4. CONCLUSION

We have the presented the possibilities of spatial measurements of the laser induced plasma development in air by using the streak camera equipped with spectrograph, after simple modification of spectrograph turret. The presented method is suitable for plasma sheath velocity measurements from the very beginning of the laser induced breakdown by using a picosecond time resolution of our streak camera.

Acknowledgements

This work was supported by the RS MESTD, Project No. OI 171020.

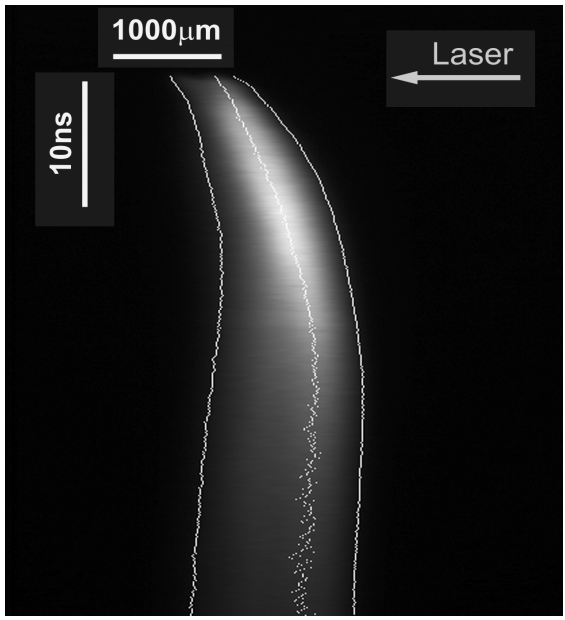

Figure 3. Streak image of the laser induced plasma (excitation at 1064 nm, energy of 51 mJ). The detected edges and peak values of brightness of the plasma plume are indicated by white points.

REFERENCES

[1] A. Robledo-Martinez, H. Sobral, M. Villagrán-Muniz, and F. Bredice, Physics of Plasmas **15**, 093510 (2008).
[2] M. Villagrán-Muniz, H. Sobral, and E. Camps, IEEE Trans. on Plasma Science **29**, 613 (2001).
[3] P. Gregorčič, J. Možina, Opt. Lett. **36**, 2782 (2011).
[4] Camacho, L. Díaz, M. Santos, L. J. Juan, J. M. L Poyato, Journal of Applied Physics **107**, 083306 (2010).
[5] N. Kawahara, J. L. Beduneau, T. Nakayama, E. Tomita, Y. Ikeda, Appl. Phys. B **86**, 605 (2007).
[6] T. Hori and F. Akamatsu, Jpn. J. of Appl. Phys. **47**, 4759 (2008).
[7] J. Siegel, G. Epurescu, A. Perea, F.J. Gordillo-Vazquez, J. Gonzalo, C.N. Afonso, Spectrochim. Acta Part B, 60, 915 (2005).
[8] D. Sevic, M. S. Rabasovic, B. P. Marinkovic, IEEE Trans. on plasma science **39**, 2782 (2011).
[9] M. S. Rabasović, D. Sevic, V. Pejčev, B. P. Marinković, Nucl. Instrum. Meth. B **279**, 61 (2012).
[10] M. S. Rabasovic, B. P. Marinkovic, D. Sevic, IEEE Transactions on Plasma Science **42,** 2388 (2014).

STARK SHIFT MEASUREMENT OF Ar I SPECTRAL LINES FOR 4s – 5p TRANSITION

I. Savić, Z. Mijatović, L. Gavanski, T. Gajo and S. Djurović

[1] *University of Novi Sad, Faculty of Sciences, Department of Physics, Trg Dositeja Obradovića 4, 21000 Novi Sad, Serbia*

Abstract. In this paper we report some Stark shift measurements of four neutral argon spectral lines emitted from agon wall stabilized arc plasma produced in DC arc regime and high current pulsed regime. under atmospheric pressure.

1. INTRODUCTION

Large number of experimental papers is devoted to study Stark parameters of many argon lines. It can be seen in [1-5]. Argon is working gas in numerous plasma sources and the Stark parameters of its spectral lines can be used for plasma diagnostic purposes for both laboratory and astrophysical plasmas. In that sense these parameters are of great importance. In the most papers Stark halfwidth data are predominated.

In this paper we report Stark shift results for four Ar I lines; 419.8317 nm, 420.0674 nm, 425.1185 nm and 426.6286 nm. All the lines correspond to the ($^2P^O_{3/2}$) 4s - ($^2P^O_{3/2}$) 4s transition. The wall stabilized electric arc working in DC and pulsed regime was used as a plasma source.

2. EXPERIMENT

As a plasma source an atmospheric pressure wall stabilized arc was used [6, 7]. The arc channel, 6 mm in diameter and 60 mm long, is formed by six water cooled copper discs separated by 0.5 mm thick Teflon gaskets. The pure argon was introduced through holes in tungsten electrodes, placed at the ends of the channel, with flow rate of 3 l/min. In DC regime arc was worked with currents of 20, 22, 24, 26, 28, 30 and 32 A.

Higher currents of 180 A and 240 A are obtained by high current pulses through arc working with current of 30 A [7]. The repetition rate of the high current pulses was 3.12 Hz.

The spectroscopic observations were made end on through 1 m spectrometer equipped with an ICCD optical system. The small percentage of the hydrogen was introduced for the electron density determination. The self-absorption was checked by mirror placed behind the arc channel [8].

2. PLASMA DIAGNOSTICS

The electron density was determined from halfwidth of H_β line profile by using Griem's theoretical data [9]. In DC regime electron density was between 0.85×10^{22} m^{-3} and 1.11×10^{22} m^{-3}. In pulsed regime electron densities was 1.09×10^{23} m^{-3} and 1.45×10^{23} m^{-3}. The estimated experimental error does not exceed ± 9%.

The electron temperatures, in the range 9600 K to 13750 K, were obtained from measured electron densities and plasma composition data according to [10] with estimated error of 10%.

3. SHIFT RESULTS

The obtained experimental shift results, measured at the peak of the lines, are presented in Table 1 and part of the results in Figure 1. The Mo I spectral lines, emitted from the hollow cathode, were used as reference lines.

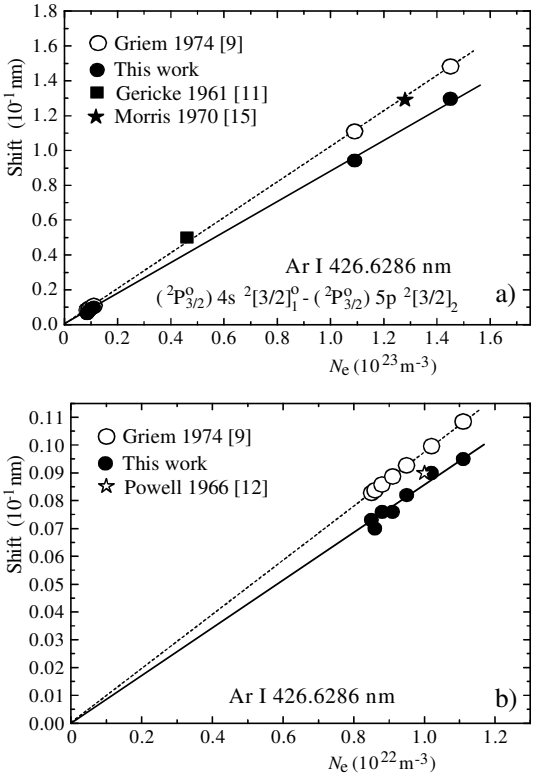

Figure 1. Shift results for Ar I 419.8317 nm line compared with theoretical [9] and experimental ones [11-15], for higher a) and lower b) electron densities.

Table 1. Experimental shift data d_m, measured at the peak of the lines, for corresponding electron densities N_e, and electron temperatures T_e. The results are compared with theoretical data d_t [9].

Wavelength (10^{-1} nm)	N_e (10^{22} m^{-3})	T_e (K)	d_m (10^{-1} nm)	d_m/d_t
4198.317	0.85	9560	0.120	0.83
	0.86	9570	0.120	0.82
	0.88	9600	0.125	0.84
	0.91	9630	0.135	0.87
	0.95	9650	0.140	0.87
	1.02	9700	0.150	0.86
	1.11	9800	0.160	0.84
	10.9	13000	1.678	0.87
	14.5	13750	2.087	0.81
4200.674	0.85	9560	0.085	0.96
	0.86	9570	0.090	1.01
	0.88	9600	0.093	1.02
	0.91	9630	0.098	1.03
	0.95	9650	0.097	0.98
	1.02	9700	0.105	0.99
	1.11	9800	0.113	0.96
	10.9	13000	0.962	0.82
	14.5	13750	1.473	0.93
4251.185	0.85	9560	0.110	0.74
	0.86	9570	0.114	0.76
	0.88	9600	0.116	0.75
	0.91	9630	0.120	0.76
	0.95	9650	0.126	0.77
	1.02	9700	0.135	0.76
	1.11	9800	0.147	0.75
	10.9	13000	1.221	0.62
	14.5	13750	1.513	0.58
4266.286	0.85	9560	0.073	0.88
	0.86	9570	0.070	0.83
	0.88	9600	0.076	0.88
	0.91	9630	0.076	0.86
	0.95	9650	0.082	0.88
	1.02	9700	0.090	0.90
	1.11	9800	0.095	0.86
	10.9	13000	0.944	0.85
	14.5	13750	1.297	0.88

The estimated experimental shift errors are between 22% and 43% for 419.8317 nm line, 20% and 35% for 420.0674 nm line, 25% and 48% for 425.1185 nm line and 23% and 38% for 426.6286 nm line.

The obtained experimental shift data were compared with theoretical [9] and other available experimental data [11-15]. The ratio $d_m/d_{[14]}$, for the line 419.8317 nm, is 0.97 and 1.13. For 420.0674 nm line the ratios are $d_m/d_{[11]}$ = 1.00, $d_m/d_{[13]}$ = 1.73, $d_m/d_{[14]}$ = 1.03 and $d_m/d_{[15]}$ = 1.02. The ratio $d_m/d_{[14]}$ for the 425.1185 nm line is 1.25 and 1.43 and for 426.6286 nm line the ratios are $d_m/d_{[11]}$ = 0.82, $d_m/d_{[12]}$ = 0.95 and $d_m/d_{[15]}$ = 0.88. The agreement is well with exception of two results, [13] for 420.0674 nm line and [14] for 425.1185 nm line.

Acknowledgements

This work is supported by the Ministry of Education, Science and Technological development of Republic Serbia, under Project 171014.

REFERENCES

[1] N. Konjević and J. R. Roberts, Phys. Chem. Ref. Data 5, 209 (1976).
[2] N. Konjević, M. S. Dimitrijević and W. L. Wiese, Chem. Ref. Data 13, 619 (1984).
[3] N. Konjević and W. L. Wiese, Phys. Chem. Ref. Data 19, 1307 (1990).
[4] N. Konjević, A. Lesage, J. R. Fuhr and W. L. Wiese, Chem. Ref. Data 31, 819 (2002).
[5] A. Lesage, New Astron. Rev. 52, 471 (2009).
[6] D. Nikolić, S. Djurović, Z. Mijatović, R. Kobilarov, B. Vujičić and M. Ćirišan, J. Quant. Spectrosc. Radiat. Transfer 86, 285 (2004).
[7] S. Djurović, Z. Mijatović, R. Kobilarov and I. Savić, Plasma Sources Sci. Technol. 21, 025007 1-9 (2012).
[8] S. Djurović, R. Kobilarov and B. Vujičić, Bull. Astron. Belgrade 153, 41 (1996).
[9] H. R. Griem, *Spectral line broadening by plasmas*, p. 316 (Acadimic Press NJ, 1974).
[10] C. H. Popenoe and J. B. Shumaker Jr., J. Res. NBS Phys. Chem A **69**, 495 (1965).
[11] W. E. Gericke, Z. Astrophys. 53, 68 (1961).
[12] W. R. Powell, Ph. D. Thesis, The Johns Hopkins University (1966).
[13] J. Chapelle, A. Sy, F. Cabannes and J. Blandin, J. Quant. Spectrosc. Radiat. Transfer 8, 1201 (1967).
[14] Bues, T. Haag and J. Richter, Astron. Astrophys. 2, 249 (1969).
[15] J. C. Morris and R. U. Morris, Aerospace Research Laboratories, Report No. ARL 70-0038 (1970).

INVESTIGATION OF STARK LINE BROADENING WITHIN SODIUM ISOELECTRONIC SEQUENCE

Nora Trklja[1], Ivan P. Dojčinović[1], Irinel Tapalaga[1] and Jagoš Purić[1]

[1]*University of Belgrade, Faculty of Physics, P. O. Box 44, 11000 Belgrade, Serbia*

Abstract. Stark broadening regularities within spectral series of the sodium isoelectronic sequence have been studied in an approach which includes both neutrals and ions. Influence of environmental conditions and certain atomic parameters on Stark widths of spectral lines have been investigated. Obtained relations were used for predictions of Stark widths for transitions within sodium isoelectronic sequence that have not been measured or calculated yet.

1. INTRODUCTION

The knowledge of Stark widths values is important in many fields of science and technology. For example, in astrophysics, line widths are useful for analysis of lines in spectra of all types of stars, investigation of chemical abundances of elements, solar opacity calculations and analysis of radiative transfer through the stellar atmospheres. Investigations in the field of solar photospheric abundances became very popular after it has been shown that abundances are less than it has been assumed, especially of low-Z metallic elements [1-3]. Different models and written codes are used for opacity research and they often use Voigt profiles for bound-bound transitions in opacity calculation. Voigt profile is defined by the convolution of the Gaussian and Lorentzian profiles. Lorentz width is due to the natural and Stark broadening. Krief et al. [4] indicated that existing uncertainties in the solar opacity calculations are due to the line broadening, they investigated effects of Stark widths values on opacity variations and pointed out the importance of Stark broadening effect in the research of solar opacity.

Theoretical calculations of the Stark width values usually use one of models given in Refs. [5-8]. Recent researches indicate importance and usefulness of searching for possible types of regularities in the framework of Stark broadening investigation. Results obtained by regularity studies have proven to be very precise and these approaches are more effective than other models in the sense that they use less parameters in calculations.

2. THEORETICAL BACKGROUND

Functional dependence of Stark widths of spectral lines on the ionization potential of the upper level of the corresponding transition, χ, and on the rest core charge of the ionized emitter, Z_e, within spectral series of Na isoelectronic sequence has been analyzed. Effects of electron density and temperature on Stark broadening of spectral lines have been analyzed, too.

General formula which indicate regularities of Stark broadening and which can be used for neutral atoms and ions can be represented by the following expression [9]:

$$\omega = Z_e^c a_1 N_e f(T) \chi^{-b} \tag{1}$$

where ω is Stark width expressed in *rad/s*, χ is defined as a positive value of the electron binding energy on the upper level of the transition of interest expressed in *eV*, Z_e =1, 2, 3… for neutrals, singly charged ions, ... respectively a_1, b and c are coefficients independent of electron density and ionization potential for a particular transition and the rest core charge of the emitter.

If reduced value of the Stark width, ω^*, is introduced, Eq. (1) has a form:

$$\log(\omega^*) = \log(\omega / Z_e^c) = a + b \cdot \chi^{-1} \tag{2}$$

where a and b are the fitting coefficients independent of χ for the chosen plasma parameters.

3. RESULTS AND DISCUSSION

Stark widths data for 276 spectral lines of Na isoelectronic sequence have been collected from literature and analyzed. Values of widths calculated by using semiclassical model and other theoretical approaches were taken from Stark B database which can be found online [10]. Other Stark broadening data used in this investigation were taken from the literature. For series for which the required atomic parameters for theoretical calculation of Stark widths are known, but calculations have not been done yet, Stark widths are calculated according to modified semiempirical formula (MSE) [8]. For this purpose, algorithm based on MSE has been made. These calculations have been done for series with small number of available data.

Beside characteristics of emitters environmental conditions affect Stark broadening data, too. The topic of present research is investigation of Stark width dependence on emitter characteristics. For the purpose of investigation, an accurate set of theoretical and experimental data is necessary, being normalized to the particular electron density and temperature. In present investigation Stark width functional dependence on electron density was tested and approximate linearity has been proven for the most of the examined spectral lines. According to [9,11,12], Stark width functional dependence on temperature is given as:

$$f(T) = A + BT^{-c} \tag{3}$$

Coefficients A, B and C are independent of temperature. Software for data normalization at temperature 100000 K has been made and it enables calculation of parameters A, B and C by using of Eq. (3). Results are given for a fixed value of electron density, 10^{22} m^{-3}.

The first step was finding the best value of parameter *c* in equation Eq. (2). This process involves monitoring the change in fit quality determined according to the value of determination factor, R^2, when changing the value of the parameter *c*. Fit has the best quality if the parameter *c* is approximately equal to 2.6.

At Fig. (1) all analyzed spectral series are represented together on the same graph, at temperature 100000 K.

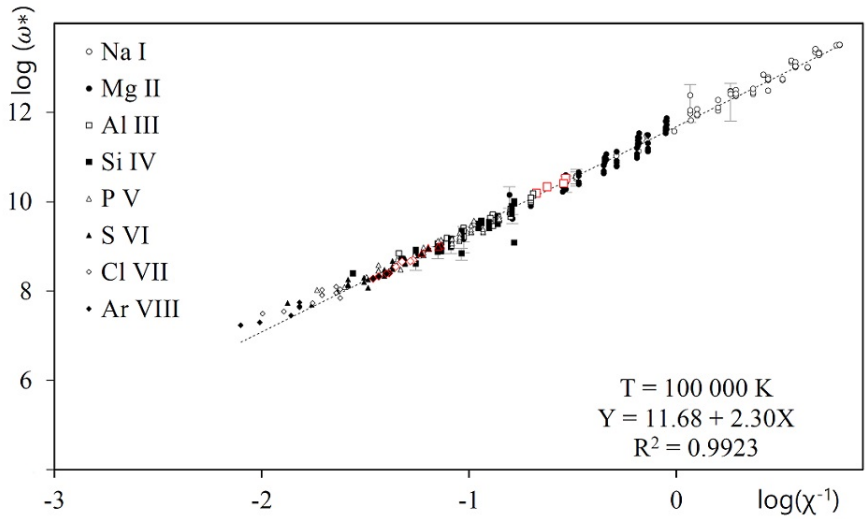

Figure 1. The electron impact contributions to Stark widths versus inverse χ for all analyzed spectral series of Na isoelectronic sequence at *T*=100000 K and at $N_e=10^{22}$ m^{-3}.

Available calculated data are represented together with data calculated in present investigation by using MSE method and with experimental data which are found in literature and represented with appropriate errors on graph. The data for each spectral series have been fitted according to Eq. (2). Values of determination factors are high for all fits which indicates good quality of the selected form of dependency.

An unique formula, which describes functional dependence of Stark width of spectral line on the ionization potential of the upper level of the corresponding transition for all spectral lines of Li isoelectronic sequence, can be obtained. This formula is given in Eq. (4) for *T*=100000 K:

$$\Delta\lambda = 4.79 \cdot 10^{-11} \cdot \frac{Z_e^{2.6} \cdot N_e}{\chi^{2.3}} \frac{\lambda^2}{2c\pi} . \qquad (4)$$

In Eq. (4) λ and $\Delta\lambda$ are expressed in m, N_e is expressed in m^{-3} and χ is expressed in eV. Constant c is the speed of light in vacuum.

4. CONCLUSIONS

Simple model proposed in this paper enable calculation of Stark broadening data for any chosen transition within sodium like emitters, by using a minimum number of parameters and it has simplest form in comparison with other methods. For spectral lines within Na isoelectronic sequence for which atomic parameters for Stark width calculation by using one of known theoretical formula are missing, presented regularity method is the only theoretical method which can be used for this purpose. Presented results are useful in extending the amount of available Stark width data. Additionally, algorithms which have been made for fast data processing enable quality control and provide verification of theoretically calculated results.

Acknowledgements

This work is financially supported by the Ministry of Education, Science and Technological Development of the Republic of Serbia within the project 171034.

REFERENCES

[1] M. Asplund, N. Grevesse, A. J. Sauval, ASP Conf. Ser. 336, 25 (2005)
[2] E. Caffau, H. G. Ludwig, M. Steffen, B. Freytag, P. Bonifacio, Solar Phys. 268, 255 (2011)
[3] P. Scott P., M. Asplund, N. Grevesse, M. Bergemann., A. J. Sauval, Astron. Astrophys. 573, A26 (2015)
[4] M. Krief, A. Feigel, D. Gazit, Astrophys. J. 821, 45 (2016)
[5] H. R. Griem, M. Baranger, A. C. Kolb, G. Oertel, Phys. Rev. 125, 177 (1962)
[6] S. Sahal-Brechot, Astron. Astrophys. 1, 91 (1969)
[7] H. R. Griem, Phys. Rev. 165, 258 (1968)
[8] M. S. Dimitrijević and N. Konjevic, JQSRT 24, 451 (1980)
[9] J. Purić and M. Šćepanović, Astrophys. J. 521, 490 (1999)
[10] https://stark-b.obspm.fr
[11] N. Trklja, I. Tapalaga, I. P. Dojčinović, J. Purić, New Astron. 59, 54 (2018)
[12] I. Tapalaga, N. Trklja, I. P. Dojčinović, J. Purić, MNRAS 474, 5479 (2018)

ELECTRIC FIELD AND ROTATIONAL TEMPERATURE DISTRIBUTION IN THE CATHODE FALL REGION OF HYDROGEN GRIMM GLOW DISCHARGE

M. M. Vasiljević[1], G. Lj. Majstorović[2], Đ. Spasojević[1], A. Jelić[1] and N. M. Šišović[1]

[1]*University of Belgrade, Faculty of Physics, 11001 Belgrade, P.O. Box 44, Serbia*
[2]*University of Defence, Military Academy, 11105 Belgrade, Pavla Jurišića Šturma 33, Serbia*

Abstract. We present the electric field and rotational temperature distribution along the axis of a cylindrical abnormal glow discharge in hydrogen at low pressure measured side on (i.e. parallel to the copper cathode surface) by the optical emission spectroscopy (OES) technique.

1. INTRODUCTION

Within the growing number of applications, Glow Discharge Sources (GDS) are successfully used as an excitation source for analytical spectroscopy of metal and alloy samples. The most of GDS applications are based on the original Grimm design with both direct-current (DC) and radio frequency (RF) excitation.

The knowledge of discharge parameters in the cathode fall (CF) region (e.g. the distributions of electric field strength F, excitation temperature, gas temperature of molecules, etc.) is of particular importance for characterization of Grimm GDS.

Here, OES technique is used to measure the electric field and gas temperature distributions in the CF region of the Grimm type glow discharge, operated in hydrogen at low pressure. In the present experiment, hydrogen Balmer lines are used for electric field strength mapping. For the rotational and gas temperature estimation $GK^1\Sigma^+_g,\ \nu' \rightarrow B^1\Sigma^+_u$, ν'' ($\nu' = \nu'' = 0$) band is recorded and analyzed.

2. EXPERIMENTAL

A detailed description of a modified Grimm GDS and experimental setup is given in [1]. The experiment has been realized in hydrogen (purity 99.999%).

The axial intensity distribution of radiation has been observed side-on through the anode slot. The discharge tube was translated in steps of d=0.125 mm. All spectral measurements were performed with an instrumental profile very close to the Gaussian form with measured full width at half maximum (FWHM) of 8.2 pm in the second diffraction order.

The axial distribution of intensity of radiation has been observed side-on through the anode slot. For the H_α and H_β experiments the radiation from discharge was polarized by a plastic polarizer. Selection of the π - polarized profile was experimentally carried out by orienting the polarizer axis parallel to the discharge axis, whereas the $GK^1\Sigma^+_g,\ \nu' \rightarrow B^1\Sigma^+_u,\ \nu''$ ($\nu'=\nu''=0$) band lines were observed without the polarizer.

3. RESULTS AND DISCUSSION

The spectral lines of atomic hydrogen exhibit linear Stark effect which was thoroughly studied so far, see for instance [2] and the references quoted therein. In a non-zero field F, the line that would be emitted at wavelength λ in zero electric field is (due to Stark effect) split into a number of Stark components. Each component is wavelength shifted by amount sF, linearly proportional to F, and has relative intensity c. In this way the Stark splitting is described by a manifold of Stark shift coefficients $s_j^{(\eta)}$ and Stark intensity coefficients $c_j^{(\eta)}$, where index j counts the Stark components for the line profile with polarization η. The number of Stark components, and their manifold coefficients $s_j^{(\eta)}$ and $c_j^{(\eta)}$, are specific for each line type and line polarization. As an example, the manifold of π-polarized H_α line is depicted in Fig. 1.

The knowledge of the Stark shift coefficients for certain type of polarized spectral line enables one to perform a spectroscopic measurement of electric field strength F from the shape of recorded line profile. In any such measurement the radiation has to be collected only from a discharge region with approximately homogeneous electric field. In side-on measurements, performed in the CF of glow discharges where F depends on distance to the cathode, this condition is satisfied in a narrow region of discharge from which the radiation should be collected.

The simplest way to perform a spectroscopic electric field measurement is to evaluate the electric field strength as $F=\Delta\lambda/s$, using the value of the Stark shift coefficient s for the chosen Stark component, and its Stark shift $\Delta\lambda=\Delta\lambda_{p\text{-}p}/2$; here, $\Delta\lambda_{p\text{-}p}$ is peak-to-peak distance, measured on the recorded line shape between two strongest Stark components that are equally shifted, one to the red, and the other to the blue wavelength side.

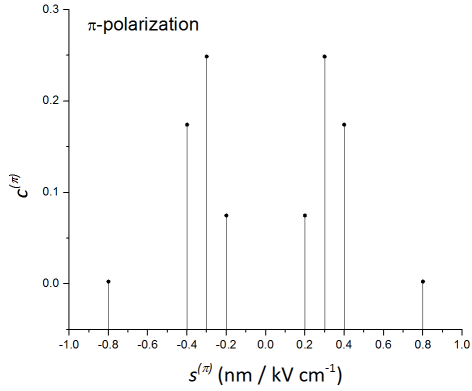

Figure 1. Stark intensity coefficients $c^{(\pi)}$ (dimensionless) versus Stark manifold coefficients $s^{(\pi)}$ scaled by the Stark constant 2.77×10^{-3} nm/(kV·cm^{-1}) in the case of the π-polarized H_α line.

The electric field strength distribution in the CF region of the Grimm type GD is determined by means of the peak-to-peak technique applied to the π-polarized profiles of the α and β hydrogen Balmer lines and σ-polarized profile of the β hydrogen Balmer line, see Fig. 3a.

In the recent study, see Ref. [3], it was found that for rotational T_{rot} and ground state $T_0(n',v')$ temperature monitoring it is possible to use first several lines of R-branch of $GK\rightarrow B$ ($v'=v''=0$) band. From the recorded spectra, see Fig. 2 it was evident that R branch lines of the electronic transition $GK\ ^1\Sigma^+_g \rightarrow B\ ^1\Sigma^+_u$ ($v'=v''=0$) are well resolved and have high enough intensities in the 453-463 nm wavelength region (wavelength data are taken from [4]). The recorded band is used for evaluation of rotational temperature $T_{rot}(n',v')$ of excited state using Boltzmann plot technique. The results obtained for T_{rot} distribution along the CF region are presented in Fig. 3b.

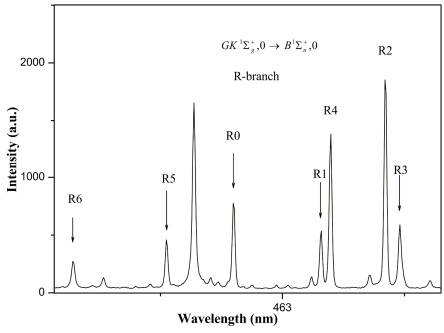

Figure 2. Emission spectra of the rotational lines for $GK\rightarrow B$ system; R-branch (with $v'=v''=0$) recorded in the second order of diffraction grating. Experimental

conditions: copper cathode; Grimm GD in H_2 at the pressure p = 4.5 mbar; discharge current I = 11 mA; discharge voltage U = 880V.

Within the framework of model discussed in [5], the rotational temperature of ground vibrational state T_0 (n', v') can be considered as a valid estimation of the ground state rotational temperatutre i.e. gas temperature. In our case the temperature recalculated [5] for the ground vibrational state $X^1\Sigma^+_g$ (v = 0) is two times larger than the rotational temperature of excited state [5].

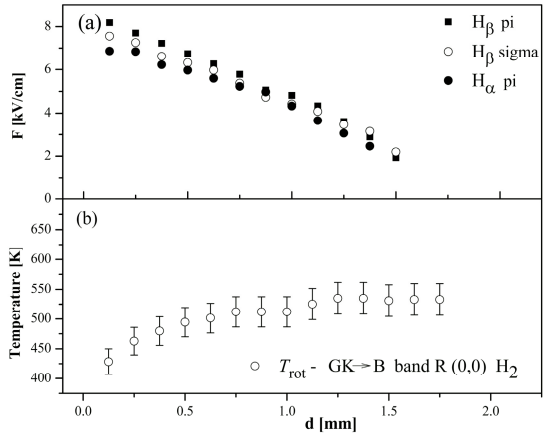

Figure 3. The dependence upon distance from cathode d of: (a) Electric field strength F (b) Rotational temperature of the excited state GK $^1\Sigma^+_g$. Experimental conditions: cooper cathode Grim GD in H_2 at p = 4.5mbar; I = 11mA; U = 880V.

Acknowledgements

This work is supported by the Ministry of Education, Science and Technological Development of the Republic of Serbia under Projects 171014 and 171027.

REFERENCES

[1] G. Lj. Majstorović, N. V. Ivanović, N. M. Šišović, S. Djurović and N. Konjević, Plasma Sources Sci. Technol. 22, 045015 (2013).
[2] N. Ryde, *Atoms and Molecules in Electric Fields* (Stockholm: Almqvist & Wiksell, 1976).
[3] M. M. Vasiljević, G. Lj. Majstorović, Đ. Spasojević and N. M. Šišović, 21th Simposium on Application of Plasma Processes (SAPP XXI), Book of Contributed Papers p. 213-217 (2017).
[4] H. M. Crosswhite. *The hydrogen molecule wavelength tables* (Gerhard Heinrich Dieke. New York: Wiley-Interscience; 1972).
[5] S. A. Astashkevich, M. Käning, E. Käning, N. V. Kokina, B. P. Lavrov, A. Ohl and J. Röpcke, JQSRT 56, 725 (1996).

NANOPARTICLES ON A SAMPLE SURFACE AS LASER INDUCED BREAKDOWN SPECTROSCOPY ENHANCERS

M. Vinić[1,2], M. R. Gavrilović Božović[1], B. Stankov[1], M. Vlainić[1] and M. Ivković[1]

[1]*Institute of Physics, University of Belgrade, Belgrade, Serbia*
[2]*Faculty of Physical Chemistry, University of Belgrade, Belgrade, Serbia*

Abstract. Signal enhancement of Laser Induced Breakdown Spectroscopy in the presence of gold nanoparticles was studied. Nanoparticles were synthesised using pulsed laser ablation of the rotating Au target immersed in liquid mediums. Stability of nanocolloids was estimated. Nanosuspensions were applied to sample surface what enabled studies of Nanoparticle Enhanced Laser Induced Breakdown Spectroscopy. The effect of spectral line enhancement was observed under the optimised conditions both for neutral and ionic lines of the studied sample material.

1. INTRODUCTION

Laser Induced Breakdown Spectroscopy (LIBS) is emission spectroscopy technique that uses a short laser pulse to create plasma on the sample surface, and analyses formed plasma to gather information about the sample studied. Despite of all its advantages (fast response, no or minimal sample treatment, simple setup, requires only optical access to the sample), lower detection limit is the largest drawback of this technique. One way of signal enhancement is deposition of metallic nanoparticles on sample surface before laser irradiation. In this way, the order of magnitude enhancement of optical signal can be obtained [1,2].

In this work, nanoparticles (NPs) were synthesised using laser ablation of the bulk gold in liquid medium, and then applied on the surface of the sample. Surface prepared in such a way was than irradiated with the laser beam, Nanoparticle Enhanced LIBS (NELIBS) plasma was formed and spectra were recorded. It was shown that application of Au NPs on the target surface prior to laser induced breakdown leads to signal enhancement of sample's element optical emission.

2. EXPERIMENT

Experiment was conducted in several steps. Firstly, it was necessary to synthesize Au NPs, uniform by size and shape. Next, the size of the NPs needed

to be evaluated, based on the position of a Surface Plasmon Resonance (SPR) band maximum. In order to do that, absorption spectra of all produced colloids were recorded with spectrophotometer [3-5]. After that, synthesised colloids of NPs ought to be applied to analysed metal target ($AlMgCu_5$), where proper volume of the colloid drop and surface coverage had to be determined experimentally. As a final step, conditions for NELIBS spectra recordings had to be optimised.

Method of choice for NPs synthesis was laser ablation in different solutions. Experimental setup consisted of laser (Nd:YAG, 2nd harmonic 532 nm), mirror for guiding the laser beam (45° angle), focusing lens of 2.5 cm focal length and rotating table on top of which cuvette with a solution and immersed Au target were positioned., see Figure 1a. In order to find the optimal conditions for NPs generation, laser energy and wavelength were changed. Also, different distances between the target and lens were set, so different energy densities on the target surface were obtained, leading to the NPs of various sizes. Duration of ablation was varied in order to obtain different colloid concentrations. NPs were synthesized in water (distilled and deionized) and in different organic solvents (DMSO, Acetonitrile and Chloroform) [6]. Characterisation of formed nanocolloids was performed with measurements of SPR band using spectrophotometer Beckman Coulter DU720. Stability of formed solutions was also estimated.

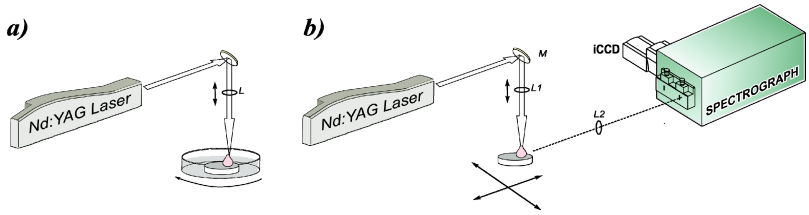

Figure 1. Experimental setup: a) for synthesis of Au nanocolloid; b) for NELIBS.

Experimental setup used for measurements of NELIBS spectra of prepared samples consisted of: laser (Nd:YAG, 2nd harmonic 532 nm), mirror (45° angle), focusing lens of 2.5 cm focal length (L_1) and lens for focusing NELIBS plasma (L_2, f=20cm) onto the entrance slit of detection system (imaging spectrometer equipped with ICCD camera), see Figure 1b. Position of the projection lens L_2 with respect to the spectrometer was varied, i.e. different portions of the plasma volume were collected by optical system, which had prove to have direct consequence on the spectral line emission enhancement.

3. RESULTS AND DISCUSION

When a metal particle is exposed to light, the oscillating electromagnetic field induces a collective coherent oscillation of conduction band electrons. The amplitude of the oscillation reaches maximum at a specific frequency, called surface plasmon resonance. The SPR induces a strong absorption of the incident light and thus can be measured using a UV–Vis

absorption spectrometer [5]. Based on the measured position of SPR band maximum, sizes of Au NPs were estimated, see Figure 2a. After few days, recordings were repeated in order to verify stability of solutions, Figure 2b. The variations in position of the SPR maximum were almost negligible after two days, leading to the conclusion that produced colloids are rather stable. Significant change in the SPR maximum position was only detected four days after the colloid synthesis.

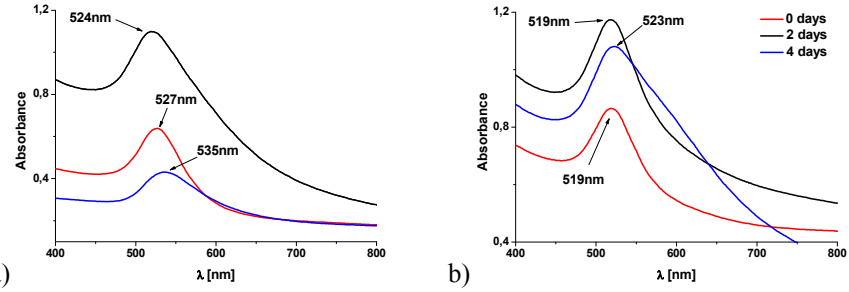

Figure 2. SPR band of formed solutions: a) size estimation; b) stability check.

Estimated sizes of Au NPs (30±5 nm) [3] were in the range of sizes that have already been reported to produce NELIBS effect [1], even two days after synthesis. Besides NPs size, important parameter for line intensity enhancement is the NP surface concentration. It was found that after certain limit, further increase of concentration does not contribute to signal enhancement [2]. In order to test that, nanocolloid was first applied on the sample surface in a form of large droplets (~10µl). In this case, the deposition of colloid was inhomogeneous such that the concentrations at the edges were higher than at the center, i.e. “"coffee-ring" effect [7], resulting in noticeable enhancement only when particular place on a drop was irradiated. This indicates that, with the large droplets, surface concentration of NPs was above critical, leading to decreased NELIBS performance [7]. Since enhancement is strongly dependent on the total amount of colloid, smaller droplets should be used. Having this in mind, further on microdroplets (0.5 µl) were applied with micropipette on the previously irradiated surface of the target.

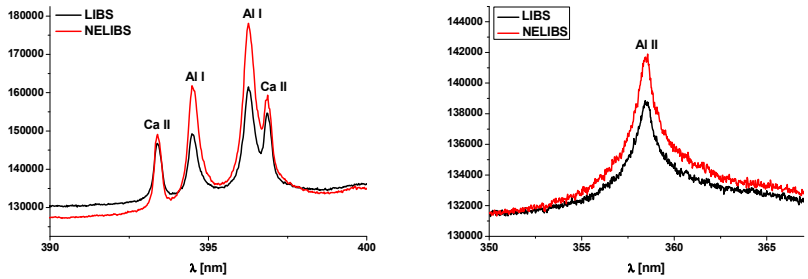

Figure 3. Comparison of LIBS and NELIBS spectra for neutral and ionic lines of main target constituent.

Spectra obtained with microdroplets are shown in Fig. 3. All presented spectra were recorded with single shot. Further enhancement of optical signal could be obtained if signal accumulation was performed. Increase of signal intensity was present in both neutral and ionic lines. Enhancement of spectral line intensity was more pronounced in case of neutral lines, possible due to larger emission volume of NELIBS plasma. Since LIBS and NELIBS plasma have similar plasma parameters [1], larger emission volume of NELIBS plasma means more contributions from "colder" layers which are emitters of mostly neutral lines. It is important to emphasize this was the reason why lens L_2 was positioned in such a way that complete plasma volume was focused to the spectrometer. This configuration corresponds to the maximum signal enhancement.

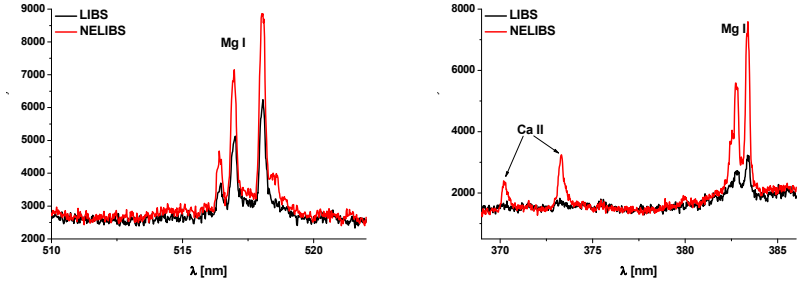

Figure 4. Comparison of LIBS and NELIBS spectra of minor elements in sample.

Fig. 4 illustrates intensity increase of spectral lines of magnesium which is minor sample constituent. Also, lines of Ca appeared in NELIBS spectra. Calcium can be present in $AlMgCu_5$ in small amounts, but also can come from water used as a medium during the NPs synthesis. Because of this uncertainty, it can be concluded that this method is not reliable for investigations of calcium containing samples.

Acknowledgements

This work was financed by the Ministry of Education, Science and Technological Development of the Republic of Serbia under Projects OI 171014 and TR 37019. Special thanks to Zoran Velikić who helped in performing spectrophotometric measurements.

REFERENCES

[1] A. De Giacomo et al, Spec. Acta Part B 98, 19 (2014)
[2] A. De Giacomo et al, Anal. Chem. 88, 9871 (2016)
[3] S. Link and M. A. El-Sayed, J. Phys. Chem. B 103, 4212 (1999)
[4] V. Amendola et al, J. Phys.: Condens. Matter 29, 203002 (2017)
[5] X. Huang and M. A. El-Sayed, J. of Adv. Research 1, 13 (2010)
[6] V. Amendola et al, J. Phys. Chem. B 110, 7232 (2006)
[7] C. Zhao and D. Dong, Anal. Chem. 88, 9869 (2016)

DEVELOPMENT OF SPECTROSCOPIC METHOD FOR MEASUREMENT OF ELECTRIC FIELD IN THE CATHODE SHEATH REGION OF AN ABNORMAL GLOW NEON DISCHARGE

N. V. Ivanović[1], N. M. Šišović[2], Dj. Spasojević[2] and N. Konjević[2]

[1]*University of Belgrade, Faculty of Agriculture, Nemanjina 6, 11080 Belgrade, Serbia*
[2]*University of Belgrade, Faculty of Physics, 11001 Belgrade, P.O. Box 44, Serbia*

Abstract. We have experimentally and theoretically studied the DC Stark shifts of several visible neon atomic lines Ne I (503.135nm; 507.421 nm; 511.367 nm; 515.196 nm; 515.443 nm; 520.390 nm; and 520.886 nm) recorded in the cathode sheath region of an abnormal glow discharge operated in neon with a small admixture of hydrogen. The electric field (up to 13.4 kV cm^{-1}) is measured from the π-polarized profile of the hydrogen Balmer line H_α using Stark polarization spectroscopy technique. Within the low electric field range, the Ne I lines exhibit a quadratic Stark effect. The values of the coefficients, correlating Stark shift and electric field strength, were determined, which enable their future use for electric field strength measurements in discharges with neon.

1. INTRODUCTION

The investigations of DC Stark effect of neutral neon lines are numerous, but most of those researches were performed at relatively high values of electric field strength F exceeding 100 kV/cm [1-5]. On the other hand, it is known that the available high F experimental data can't be always extrapolated to low F values. Recently, Ne I Stark effect studies have been directed towards lower F values in experiments carried out in the cathode sheet (CS) region of a Grimm-type glow discharge (GD). In these studies, a simple technique (based on the optical emission spectroscopy (OES) and with standard laboratory equipment) has been used for mapping of the electric field strength distribution in the CS region of a Grimm-type GD. In its essence, this is the well known Lo Surdo technique used for studies of Stark effect, but employed here with modern CCD detector for the spectral lines recording [6,7]. Here, we would also like to stress that the Ne I spectral lines have small Stark shifts which can't be measured (e.g. by measuring separation between maxima of Stark shifted lines) without introduction of a suitable model function for the shape of the recorded profiles of Ne I lines.

The aim of this work is to provide experimental values of the Stark shift coefficients for several Ne I lines which, although located in a very convenient spectral region around 510 nm, were not studied before. In the present experiment the hydrogen Balmer line H_α is used for measuring F at those positions in the CS region of an Grimm-type GD where the profiles of the studied Ne I lines are recorded. The Stark shifts of the Ne I lines are determined (with typical accuracy of 5%) from the best fit of a suitable model function to the recorded profiles.

2. EXPERIMENTAL

A modified Grimm GD source was laboratory made after the Ferreira et al. design [8,9]. Hollow anode (30 mm long with inner diameter 8 mm) has a longitudinal slot (16 mm long and 1.5 mm wide) for side-on observations along the discharge axis, see Figure 1 in [10]. The water-cooled cathode holder has tungsten electrode, 18 mm long and 7.50 mm in diameter, which screws tightly into its holder to ensure good cooling.

All experiments were carried out with the neon-hydrogen mixture (vol. 99.2% Ne + 0.8% H_2). A continuous gas flow of about 300 cm^3/min was sustained in the pressure range 5-10 mbar by means of a needle valve and two two-stage mechanical vacuum pumps. The reported values for gas pressure represent an average between measured values of gas inlet and outlet pressure. To run the discharge, a current stabilized power supply (0-2 kV, 0-100 mA) is used. The ballast resistor of 5.3 kΩ is placed in series with the discharge and the power supply. Spectroscopic observations of the Grimm GD were performed side-on through an anode slot in translation steps of approximately 1/16 mm.

For the H_α experiments prior the entering spectrometer, the radiation from discharge was polarized by a plastic polarizer. Selection of the π - or σ - polarized profile was experimentally carried out by orienting the polarizer axis parallel or perpendicular to the discharge axis, i.e. electric field direction in the CS region. Under the π - polarization is understood the component of light with linear polarization along the electric field, and under a σ - polarization the component of light that is circularly polarized in the plane perpendicular to the direction of the electric field, see schematic representation in Figure 2 in [10]. The Ne I lines were recorded without the polarizer.

The radiation from the discharge source is focused with an achromatic lens (focal length 75.8 mm) with unity magnification, through the polarizer, onto the 20 μm entrance slit (height restriction 2 mm) of 2 m focal length Ebert type spectrometer with 651 g/mm reflection grating blazed at 1050 nm. For the line shape measurements, the reciprocal dispersion of 0.37 nm/mm is used throughout this experiment. Signals from the CCD detector (1 x 3648 pixels, 8 μm pixel width) are A/D converted, collected and processed by PC. All spectral measurements were performed with an instrumental profile very close to a Gaussian with measured full width at half maximum (FWHM) of 8.2 pm.

3. RESULTS

For the electric field measurement in the CS region, Stark polarization spectroscopy of the H_α line is employed. Its Stark shifts are determined with the aid of an advanced model function, and from so obtained Stark shifts the electric field strength is calculated using the literature values, see e.g.[10], for the coefficients of the Stark shift manifold for the H_α line. For measurement of the Stark shift of Ne I lines, we have also developed an appropriate model function for the fitting procedure. Here it should be noted that due to the presence of several crossing Stark components, we had to discard from the fit the points in the spectra that do not belong to the Stark component having the greatest relative intensity. Two sets of experimental data with the corresponding best fit curves are shown in Figure 1. In panels (a - d) of both columns we present the examples of spectral profiles, recorded at four different positions inside the CS region starting from the cathode surface. The fifth one, panels e), shows the spectral profiles recorded in negative glow.

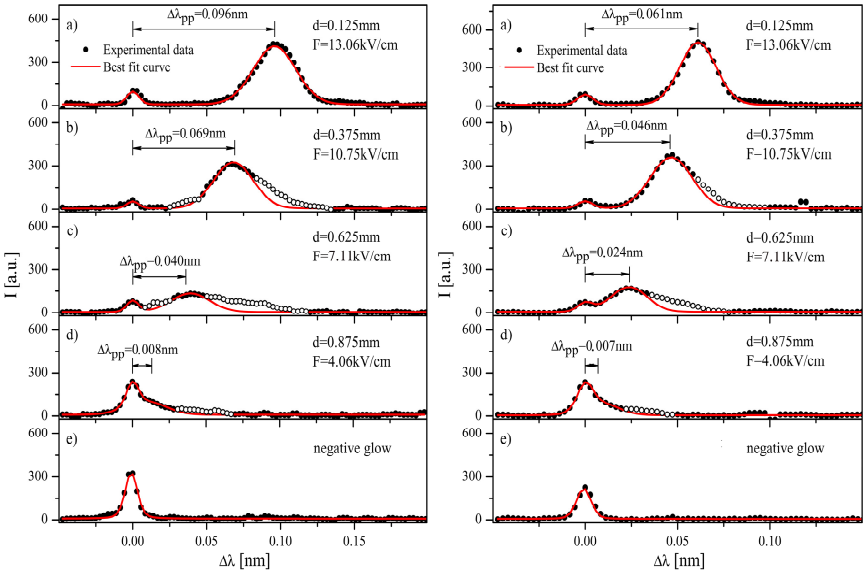

Figure 1. Experimental profiles (points) of the Ne I 507.420 nm and Ne I 520.886 nm lines recorded at different distances *d* from the cathode surface, and their best fits (red lines); hollow points are discarded in fitting. Discharge conditions: tungsten cathode, pressure p = 6 mbar, discharge current I = 12.11 mA, and discharge voltage U = 914 V. In legends, we give the corresponding values of electric field strength F and Stark shift $\Delta\lambda_{p-p}$ measured between shifted and unshifted components.

Together with the measurement that employs the model function for the spectral shape of the Ne I lines, the simple 'peak-to-peak' method of the Stark wavelength shift measurement is employed in the case of clear separation

between the maxima of the shifted and unshifted component, panels a)-c), and these two procedures gave almost the same results. For the small values of electric fields, like in our experiment, all Ne I lines exhibit a quadratic Stark effect. This is also supported with the equation given by Jäger and Windholz [2], which for the small electric field range reduces to:

$$\Delta\sigma \approx \left(\frac{A_1}{A_2} + A_3\right) F^2 = CF^2 \qquad \text{or equivalently} \qquad \Delta\lambda \approx -\lambda_0^2 CF^2 \qquad 1.$$

where λ_0 is the central wavelength of the unshifted line.

The best fits of the measured Stark shifts according to the simple quadratic function, the best fit values of constant C as well as more details will be demonstrated at the Conference.

4. CONCLUSION

For the several studied Ne I lines, coefficients for the best fit formula 1. are determined and they can be used now for low (up to 13.4 kV/cm) electric field measurement with an uncertainty less than 5%.

Acknowledgements

This work is supported by the Ministry of Education, Science and Technological Development of the Republic of Serbia under Projects 171014 and 171027.

REFERENCES

[1] N. Ryde, *Atoms and Molecules in Electric Fields*. Almqvist & Wiksell, Stockholm (1976).
[2] H. Jager and L. Windholz, Physica Scripta 29, 344 (1984).
[3] L. Windholz and C. Neureiter, Phys Rev. A 37, 1978 (1988).
[4] H. Jager, L. Windholz and R. Ch. Ziegelbecker, Phys. Scripta. 40, 740 (1989).
[5] R Ch Ziegelbecker and B Schnizer, Z. Phys. D - Atoms, Molecules and Clusters 6, 327 (1987).
[6] G. Lj. Majstorović, N. V. Ivanović, N. M. Šišović, S. Djurović and N. Konjević, Plasma Source Sci. Technol. 22, 045015 (2013).
[7] N M Šišović, N. V. Ivanović, G. Lj. Majstorović and N. Konjević, J. Anal. At. Spectrom. 29, 2058 (2014).
[8] N. P. Ferreira, H. G. C. Human and L. R. P. Butler, Spectrochim. Acta B 35, 287 (1980).
[9] M. Kuraica, N. Konjević, M. Platiša and D. Pantelić, Spectrochim.Acta 47B, 1173-86 (1992).
[10] N. V. Ivanović, N. M. Šišović, Dj. Spasojević and N. Konjević, J. Phys. D: Appl. Phys. **50**, 125201 (2017).

SIMULATION OF ELECTRON AVALANCHE SIZE DISTRIBUTIONS IN METHANE

Aleksandar P. Jovanović[1], Marjan N. Stankov[2], Suzana N. Stamenković[1] and Vidosav Lj. Marković[1]

[1]*Department of Physics, Faculty of Science and Mathematics,University of Niš, Višegradska street,18000 Niš, Serbia*

[2]*Leibniz Institute for Plasma Science and Technology (INP), Felix-Hausdorff-Strasse 2, 17489 Greifswald, Germany*

Abstract. The modeling of electron avalanches in methane is presented in this paper. The model is verified by simulating the avalanche size distribution in methane. The good agreement between simulated and measured distributions is obtained. The influence of the conditions i.e. pressure, inter-electrode distance and reduced electric field on the avalanche size distributions is discussed. The simulation results have shown that reduced avalanche size distribution only depends on the reduced electric field.

1. INTRODUCTION

The electron avalanches are important for electric breakdown of gases and inception of gas discharges, so it is important to develop accurate physical model for their description. Here we will use Monte Carlo simulation to study the electron avalanches in methane. This is often used method to study electron avalanches at various conditions [1-5]. We will use it to simulate the electron avalanche, to calculate the avalanche size, the avalanche size distributions and to study the influence of different conditions on them.

2. MODEL

In order to simulate the electron avalanche we need to track the initial electron and its descendants, until they reach the anode. In order to do this, we use Monte Carlo simulation method [6]. Initial electron is emitted from the cathode with the random initial velocity (following Maxwell distribution) and in a random direction. It starts its motion under the influence of the constant electric field E directed along the z-axis. We track the electron in the cylindrical vessel of diameter D between two plane-parallel electrodes with inter-electrode distance d. The position and velocity of the electron are calculated from the equation of motion. During its flight, electron will collide with molecules in the inter-

electrode space. The type of collision is determined by calculating collision probabilities and comparing them to random numbers. Isotropic scattering of the electron is used. For the simulation of avalanche size, only ionizing collisions are important, so we store time, position and velocity (energy) of the electron in the moment of the ionization in a local memory, similarly as in [6, 7]. The time, position and the initial velocity (energy) of the newly produced electron (which is randomly determined) are stored in separate arrays when the collision occurs. When the primary electron reaches the anode, we start to follow the last produced electron in order. The procedure is repeated until all electrons from the gap reach the anode. In this way, the total number of electrons in the avalanche is calculated. By repeating the procedure, the distribution of avalanche size is obtained.

3. RESULTS AND DISCUSSION

In order to test validity of the model, we simulated the avalanche size distribution and compared it to the experimental results measured in methane [8]. The cross sections for methane used in model are taken from [9, 10]. The good agreement between the simulated and experimental data is observed (Fig. 1).

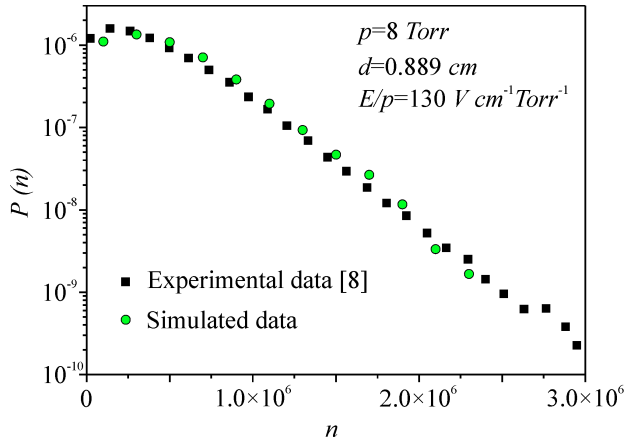

Figure 1. The comparison of measured [8] (squares) and simulated (circles) electron avalanche distributions in methane.

In ref. [8] it is observed that reduced avalanche size distribution $\bar{n} \times P(n/\bar{n})$ ($\bar{n}$ is mean avalanche size) does not depend on the inter-electrode distance for a constant pressure and reduced electric field. Similar observation is noticed in [3], where it is statistically proven that the shape of distribution is independent on the avalanche size. In order to test these statements, we carried out the simulation at various inter-electrode distances and pressures.

We simulated the reduced avalanches at the same conditions as in [8]. Since inter-electrode distances are approximately equal in [8], it is reasonable to assume that identical reduced distributions are merely coincidental. Therefore,

we carried out simulation at three more distances d=0.75, 0.5 and 0.25 *cm* in order to test this. It can be seen that good agreement is observed at all inter-electrode distances (Fig. 2), thus confirming the statement from [8].

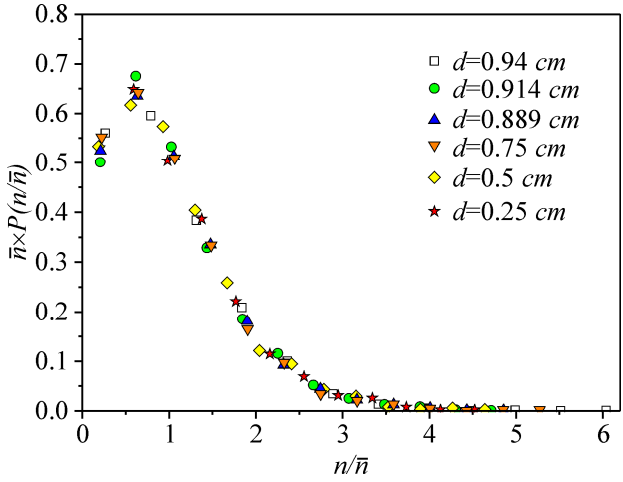

Figure 2. Simulated reduced avalanche size distributions at pressure p=8 *Torr*, reduced electric field E/p=130 $Vcm^{-1}Torr^{-1}$ and inter-electrode distances in range from 0.25 to 0.94 *cm*.

In order to study the influence of the pressure, avalanche size distributions are simulated for pressures p=100, 200 and 300 *Torr*, while inter-electrode distance d=1 *cm* and reduced electric field E/p=33 $Vcm^{-1}Torr^{-1}$ were constant (Fig. 3). It can be seen that reduced distributions are identical, i.e. they have the same shape for all pressures if the reduced electric field is constant.

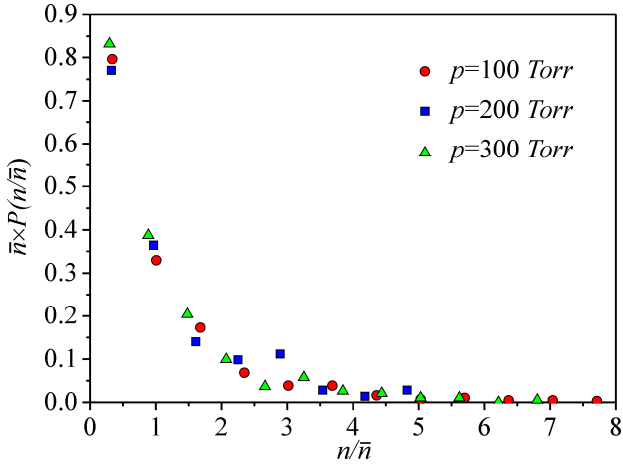

Figure 3. Simulated reduced avalanche size distributions at inter-electrode distance d=1 *cm*, reduced electric field E/p=33 $Vcm^{-1}Torr^{-1}$ and pressures p=100, 200 and 300 *Torr*.

According to simulation results, it follows that reduced avalanche size distribution is independent on inter-electrode distance for a constant pressure and reduced electric field and vice versa, confirming that the shape is independent of the mean avalanche size. Moreover, it follows that the reduced distribution, i.e. the shape of the avalanche size distribution depends only on the reduced electric field.

4. CONCLUSION

The avalanche size distributions in methane are simulated in this paper. The good agreement between the model and experimental results is observed. The reduced avalanche size distributions are discussed at different inter-electrode distance and pressure. It was confirmed that reduced distributions are independent of inter-electrode distance, when the pressure and reduced electric field are constant. In addition, the simulations shown that reduced distributions are independent of pressure, for constant inter-electrode distance and reduced electric field, as well. Moreover, it follows that reduced avalanche size distributions are independent of the mean avalanche size and only depend on the reduced electric field.

Acknowledgements

This work is supported by Ministry of Education, Science and Technological Development of the Republic of Serbia under the grant ON 171025.

REFERENCES

[1] E. E. Kunhardt, Y. Tzeng and J. P. Boeuf, Phys. Rev. A 34, 440 (1986).
[2] Z. Donkó, Phys. Rev. E 51, 3934 (1995).
[3] H. Schindler and R. Veenhof, Avalanche Statistics http://indico.cern.ch/event/58953/contributions/2048955/attachments/994694/1414528/Avalanche.pdf retrieved on November 29 2017
[4] H. Schindler, S. Biagi and R. Veenhof, Nucl. Instrum. Meth. A 624, 78 (2010).
[5] D. Bošnjaković, Z. Lj. Petrović, R. D. White and S. Dujko, J. Phys. D: Appl. Phys. 47, 435203 (2014).
[6] Z. Donkó, Plasma Sources Sci. Technol. 20, 024001 (2011).
[7] S. Dujko, R. D. White and Z. Lj. Petrović J. Phys. D. Appl. Phys. 41, 245205 (2008).
[8] G. Vidal, J. Lakaze and J. Maurel, J. Phys. D: Appl. Phys. 7, 1684 (1974).
[9] Hayashi database, www.lxcat.net, retrieved on September 29 2017
[10] IST Lisbon database, www.lxcat.net, retrieved on September 29 2017

MEMORY EFFECT IN ARGON AND ARGON-NITROGEN MIXTURE WITH DIFFERENT VOLTAGE PULSES

V. Lj. Marković[1], A. P. Jovanović[1], S. N. Stamenković[1] and M. N. Stankov[2]

[1]*Department of Physics, Faculty of Science and Mathematics,University of Niš, Višegradska street,18000 Niš, Serbia*
[2]*Leibniz Institute for Plasma Science and Technology (INP), Felix-Hausdorff-Straße 2, 17489 Greifswald, Germany*

e-mail: vidosav@pmf.ni.ac.rs

Abstract. The comparison is made between $\overline{t}_d(\tau)$ and $\overline{U}_b(\tau)$ memory curves in argon and argon-nitrogen mixture for different voltage pulses, where t_d is the electrical breakdown time delay, U_b is the dynamic breakdown voltage and τ is the relaxation time. The attention is focused on the application of $\overline{U}_b(\tau)$ memory curves to study relaxation kinetics in post-discharge conditions.

1. INTRODUCTION

The memory curve in inert and molecular gases (the electrical breakdown time delay dependence on the relaxation time) was discovered in 1956 in Electronic Industry Niš (formerly RR Zavodi) and presented at 5th International Conference on Gas Discharges in 1978 [1]. The memory curve behavior was ascribed to the decay of metastable states remaining from the preceding discharge [1]. However, metastable states are efficiently quenched in gas-phase and wall collisions and have the effective lifetimes several orders of magnitude shorter than the characteristic times of memory effect. Therefore, the memory effect in nitrogen after the plasma and charged particle decay, was explained by the surface recombination of nitrogen atoms [2-4], as well as in inert gases where nitrogen is present as impurity [5, 6]. Recently, by introducing a trace amount of nitrogen into argon in pulsed RF atmospheric pressure glow discharges Huo and co-workers [7] confirmed the surface recombination of nitrogen atoms for the explanation of late memory effect in argon. In this paper, the comparison is made between the electrical breakdown time delay $\overline{t}_d(\tau)$ and the dynamic breakdown voltage $\overline{U}_b(\tau)$ memory curves in argon and argon-

nitrogen mixture for different voltage pulses (DC, RF, linearly rising or ramp voltage pulses and others).

2. EXPERIMENTAL DETAILS

The measurements of breakdown time delay for DC voltage pulses were carried out on the gas tube filled with argon at the pressure of 200 *Pa*. The electrodes used in this tube are plane-parallel, made of oxygen-free high thermal conductivity (OFHC) copper with the diameter approximately equal to the inner diameter of the tube. The measurements of dynamic breakdown voltages U_b were performed on the cylindrical gas tube with gold-plated copper cathode at the pressure of 133 *Pa*. More details about experimental setup, procedure and tube preparation can be found in [8, 9].

3. MEMORY CURVES $\bar{t}_d(\tau)$, $\bar{t}_s(\tau)$ AND $\bar{t}_f(\tau)$ IN ARGON

The time that elapses from the moment of application of voltage greater than the static breakdown voltage U_s to the breakdown is the breakdown time delay t_d. It consists of the statistical time delay t_s (from the application of sufficient voltage and appearance of free electron initiating breakdown) and the formative time delay t_f (from this moment to the collapse of applied voltage and occurrence of a self-sustained current) [10]. The memory curves $\bar{t}_d(\tau)$, $\bar{t}_s(\tau)$ and $\bar{t}_f(\tau)$ measured by an electronic automatic system with DC voltage pulses [8] are presented in Fig. 1a, and compared to RF memory curve [7] presented in Fig. 1b.

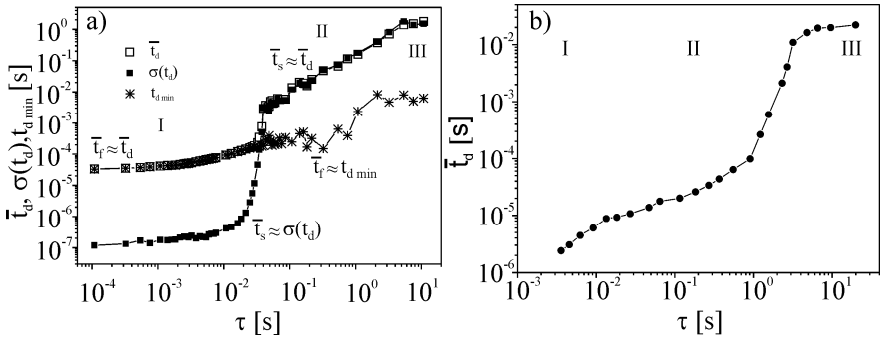

Figure 1. The $\bar{t}_d(\tau)$, $\bar{t}_s(\tau)$ and $\bar{t}_f(\tau)$ memory curves for argon [8] compared to RF memory curve from [7].

The memory curves show similar behavior with characteristic regions corresponding to different regimes of post-discharge kinetics. Three regions can be identified on the memory curves: region I caused by residual plasma and

charged particle decay, region II caused by surface recombination of nitrogen atoms and the saturation region III caused by cosmic rays and natural radioactivity. In paper [8], the memory coefficients and the memory ratios were introduced to better quantify the memory effect and the positive correlation between statistical and formative time delay [11, 12] was confirmed.

4. MEMORY CURVES $U_b(\tau)$ IN ARGON AND ARGON-NITROGEN MIXTURE FOR DIFFERENT PULSES

In papers [9, 13, 14] the electrical breakdowns and the late memory effect in argon and nitrogen were studied by applying linearly rising or ramp voltage pulses. On the basis of $\bar{U}_b(\tau)$ memory curves and the initial electron yield $Y_0(\tau)$ dependence (Fig. 2), we have concluded that the late memory effect in argon is dominated by the surface recombination of nitrogen atoms present as impurities [9].

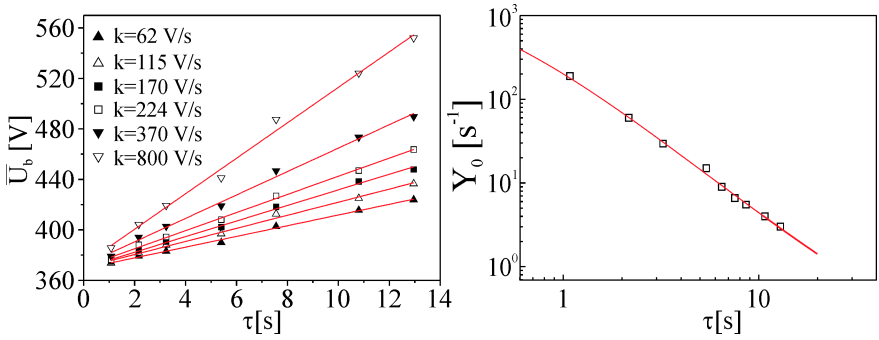

Figure 2. The dynamic breakdown voltage $\bar{U}_b(\tau)$ memory curves for ramp voltage pulses with the rates of voltage rise k and the late afterglow relaxation $Y_0(\tau)$ in argon [9].

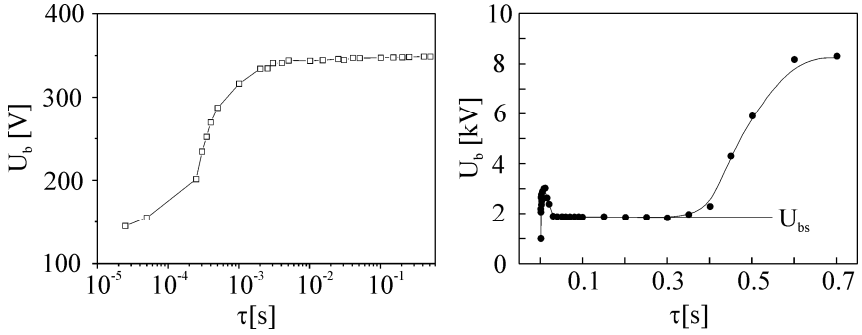

Figure 3. The $U_b(\tau)$ memory curve for RF pulses [7] and $U_b(\tau)$ memory curve from [15].

5. CONCLUSION

The memory curves have the characteristic regions dominated by plasma and charged particle decay, surface recombination of nitrogen atoms and the breakdown initiation by cosmic rays and natural radioactivity. Besides the time delay memory curves, the breakdown voltage $U_b(\tau)$ memory curves (Fig. 2 and 3) can also be used to study the relaxation in post-discharges.

Acknowledgements

The authors are grateful to the Ministry of Education, Science and Technological Development of the Republic of Serbia (project ON 171025).

REFERENCES

[1] Dj. A. Bošan, *Proceedings of 5th International Conference on Gas Discharges (Liverpool University, Liverpool, UK)*, p. 273 (IEE Conference Publishing No. 165, Stevenage, 1978).
[2] V. Lj. Marković, Z. Lj. Petrović, and M. M. Pejović, J. Chem. Phys. 100, 8514 (1994).
[3] V. Lj. Marković, M. M. Pejović, and Z. Lj. Petrović, J. Phys. D 27, 979 (1994).
[4] V. Lj. Marković, M. M. Pejović, and Z. Lj. Petrović, Plasma Chem. Plasma Process. 16, 195 (1996).
[5] V. Lj. Marković, S. R. Gocić, S. N. Stamenković, and Z. Lj. Petrović, Phys. Plasmas. 12, 073502 (2005).
[6] V. Lj. Marković, S. R. Gocić, S. N. Stamenković, and Z. Lj. Petrović, Phys. Plasmas. 14, 103504 (2007).
[7] W. G. Huo, S. J. Jian, J. Yao, and Z. F. Ding, Phys. Plasmas 21, 053505 (2014).
[8] V. Lj. Marković, B. Č. Popović, A. P. Jovanović, S. N. Stamenković and M. N. Stankov, Europhys. Lett. 109, 15002 (2015).
[9] V. Lj. Marković, S. N. Stamenković, S. R. Gocić and Z. Lj. Petrović, Contrib. Plasma Phys. 45, 476 (2005).
[10] J. M. Meek and J. D. Craggs (Editors), *Electrical Breakdown of Gases* (John Wiley & Sons, Chichester, 1978).
[11] V. Lj. Marković, S. R. Gocić, and S. N. Stamenković, J. Phys. D 42, 015207 (2009).
[12] K. Yoshino, T. Nagatomi, Y. Morita, T. Oue, N. Kosugi, M. Nishitani, M. Kitagawa, and Y. Takai, Jpn. J. Appl. Phys. 50, 026201, (2011).
[13] V. Lj. Marković, S. R. Gocić, S. N. Stamenković and Z. Lj. Petrović, Eur.Phys. J. Appl. Phys. 30, 51 (2005).
[14] V. Lj. Marković, S. N. Stamenković, S. R. Gocić and Z. Lj. Petrović, Rev. Sci. Instrum. 77, 096104 (2006).
[15] N. Dyatko, Yu. Z. Ionikh, A. V. Meshchanov and A. P. Napartovich, Plasma Phys. Rep. 44, 334 (2018).

STATISTICS OF SECONDARY AVALANCHES WITH ION-INDUCED ELECTRON EMISSION

V. Lj. Marković[1], S. N. Stamenković[1] , M. N. Stankov[2] and A. P. Jovanović[1]

[1]*Department of Physics, Faculty of Science and Mathematics,University of Niš, Višegradska street,18000 Niš, Serbia*

[2]*Leibniz Institute for Plasma Science and Technology (INP), Felix-Hausdorff-Straße 2, 17489 Greifswald, Germany*

e-mail: vidosav@pmf.ni.ac.rs

Abstract. Statistics of secondary avalanches with ion-induced electron emission is successfully modeled by negative binomial distribution (NBD) and its mixtures. The mixing weights a_j in NBD mixtures are positive correlated with μ^j for the contribution of secondary avalanche of *j*-th generation, where $\mu = \gamma_i[\exp(\alpha d) - 1]$ is an avalanche regeneration factor. The continual analogs (i.e. exponential, Gaussian and mixed Gauss-exponential distribution) for the discrete NBD and its mixtures are also applied and discussed.

1. INTRODUCTION

The operation of gaseous particle and radiation detectors is based on electron avalanches developing in applied electric field, triggered by the primary electron. By studying the fluctuation phenomena in electron avalanches initiated by one particle, Furry [1] and Wijsman [2] have derived the electron number distribution of an avalanche, which for large number of electrons can be approximated by exponential distribution. Numerous experimental distributions of carrier numbers of electron avalanches have been reported by Reather and coworkers [3, 4]. Besides the distributions of initial avalanche phase without secondary electron emission, they obtained also the electron number distributions of avalanches with ion-induced secondary electron emission on the cathode [3, 4]. In this paper, statistics of secondary electron avalanches with ion-induced electron emission is based on negative binomial distribution (NBD) and its mixtures. The experimental details for secondary avalanches of Schlumbohm [3, 4] in air are shortly summarized in Section 2. The experimental electron number distributions of Schlumbohm [3, 4] with ion-induced secondary electron emission in air are fitted by NBDs and their mixtures, as well as by their continual analogs in Section 3. Section 4 is a short conclusion.

2. EXPERIMENTAL DETAILS

The measurements analyzed in this paper for secondary electron avalanches in air originate from Schlumbohm [3, 4] at the pressure of $7\,Torr$. The vessel was first evacuated with vacuum pump and then filled with desired gas. The cathode is irradiated by the weak light of quartz lamp, so that few avalanches per second are registered. From induced current caused by motion of charged particles, Schlumbohm measured the series of electron number distributions below the sparking voltages. He measured at least 100 pulse heights of electron avalanches in single series and plotted the relative frequency of electron number in the avalanche. More details about experimental technique and measurement procedure can be found in [3, 4].

3. ELECTRON AVALANCHE STATISTICS WITH ION-INDUCED SECONDARY ELECTRON EMISSION ON THE CATHODE (γ_i PROCESS)

The measurements of number of electrons in avalanche carried out in air by Schlumbohm [3, 4] at pressure of $7\,Torr\,(933\,Pa)$, inter-electrode distance $d = 0.2\,cm$, $\mu = 0.8$, at the reduced electric field of $E/N = 8.68\times10^{-15}\,Vcm^2$ are presented in Fig. 1. In this case, the significant overpopulation of the tail of the distribution is explained by a succession of secondary electron avalanches [3, 4].

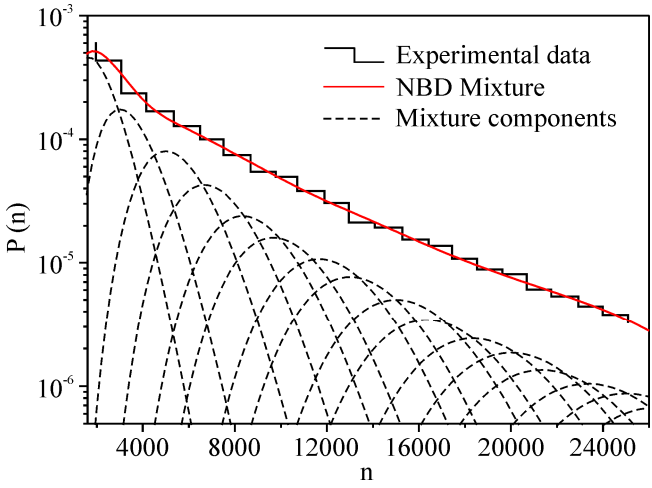

Figure 1. The fitting of electron number distribution in air for $\mu = 0.8$ by the mixture of negative binomial distributions, describing the contributions of the secondary avalanches of different generations (bars – histogram, solid line – fit by NBD mixture (1), dashed line – mixture components).

The experimental data are fitted with a mixture of several NBDs,

$$P(n) = \sum_j a_j P_j(n; k_j, p_j), \quad (1)$$

each originating from the corresponding secondary avalanche, where a_j are the mixing weights, while k_j and p_j are the parameters of mixture components. Since fluctuations of α are low, the single parameter $p = e^{-\alpha d} = 3 \times 10^{-3}$ is used, where $\alpha = 29.03\ cm^{-1}$ [5]. The values of parameters k_j and a_j along with the value of μ^j are presented in Fig. 2. From this figure the positive correlation between parameter a_j and μ^j can be noticed. By using the parameters of the distribution, the value of mean electron number in avalanche is calculated and excellent agreement with experimental data is observed (Fig. 1).

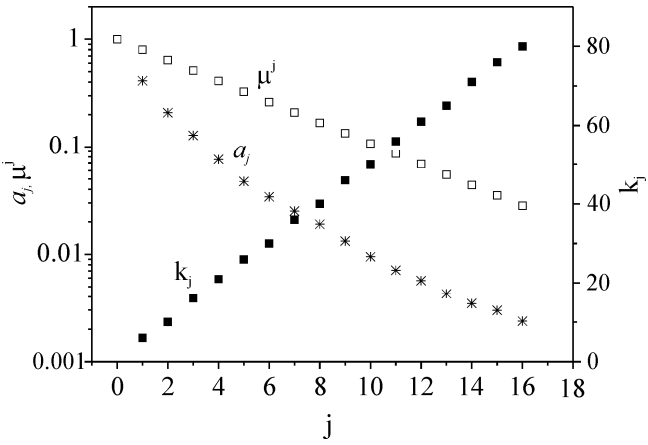

Figure 2. Left scale: The weighting factors a_j is positive correlated with μ^j for the contribution of secondary avalanche of *j*-th generation in air; Right scale: Parameters k_j in the mixture of NBDs.

In addition, since parameter *k* of NBDs takes large values, the single NBD components of mixture can be approximated with the Gaussian distribution. In this way, the experimental data are fitted with a mixture of Gaussian distributions (Fig. 3)

$$P(n) = \sum_j \frac{a_j}{\sqrt{2\pi}\sigma_j} e^{-\frac{(n-\bar{n}_j)^2}{2\sigma_j^2}} \quad (2)$$

where $\bar{n}_j$ are the mean values and σ_j is standard deviation of electron number in avalanche. The mixing weights a_j were the same as for the mixture of NBDs.

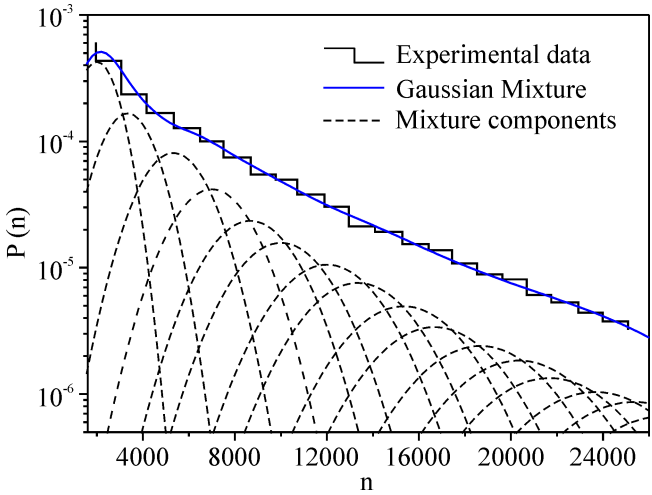

Figure 3. The fitting of electron number distributions in air for $\mu = 0.8$ by mixture of Gaussian distributions (2), describing the contributions of secondary avalanches (bars - histograms, lines - fits).

4. CONCLUSION

The statistics of avalanche growth with contributions of secondary avalanches is successfully modeled on the basis of NBDs and their mixtures. The mixing weights a_j in the mixture of NBDs for Townsend breakdown mechanism are positive correlated with μ^j. The continual analogs for the NBDs and their mixtures (i.e. exponential, Gaussian and mixed Gauss-exponential distribution) are also applied for the fitting of experimental data and have shown excellent agreement.

Acknowledgements

The authors are grateful to the Ministry of Education, Science and Technological Development of the Republic of Serbia for the partial financial support (project ON 171025).

REFERENCES

[1] H. Furry, Phys. Rev. 52, 569 (1937).
[2] R. A. Wijsman, Phys. Rev. 75, 5 (1949).
[3] H. Schlumbohm, Z. Phys. 151, 563 (1958).
[4] H. Raether, *Electron Avalanches and Breakdown in Gases* (Butterworths, London, 1964).
[5] V. Lj. Marković, et al. to be published

THE INFLUENCE OF MAGNETIC FIELD ON THE HYDROGEN BALMER ALPHA LINE IN A HOLLOW CATHODE GLOW DISCHARGE

N. V. Nedić[1], N. V. Ivanović[2], N. M. Šišović[1], Dj. Spasojević[1] and N. Konjević[1]

[1]*University of Belgrade, Faculty of Physics, 11001 Belgrade, P.O. Box 44, Serbia*
[2]*University of Belgrade, Faculty of Agriculture, Nemanjina 6, 11080 Belgrade, Serbia*

Abstract. We present the results of spectroscopic investigation of hydrogen Balmer the H_α line in external magnetic field. Hydrogen atoms were excited in a hollow cathode glow discharge operating in gas mixture of argon and hydrogen (vol. 99.2% Ar + 0.8% H_2). Homogenous magnetic field is generated along the axis of Helmholtz coils, which generated homogenous magnetic field where the hollow cathode glow discharge was located. The influence of magnetic field (B=30, 50, and 70 mT) to the parameters of hollow cathode glow discharge, total intensity, change in relative contributions and the energy of individual components of the H_α line was studied. It is shown that not only the changes in line intensity are detected, but also significant changes in the relative contributions and energy of individual components of the H_α line occur.

1. INTRODUCTION

The phenomenon of the excessive Doppler broadening of hydrogen Balmer lines was observed for the first time by Benesh and Li [1] in hollow cathode glow discharge (HCGD). Since then, it was investigated by many authors, see e.g. [2-5]. The shape of these lines emitted from low-pressure gas discharges operating in hydrogen, or hydrogen gas mixture with noble gases, exhibits unusual multi component behavior. Typical experimental profiles of the H_α line shape recordings from the central region of HCGD consists of three components, and each of them can be fitted by one Gaussian denoted here with G_1, G_2 and G_3.

The Gaussian G_1 describes the narrow central peak of the H_α line (radiation from 'cold' hydrogen atoms produced through predissociation of vibrationally excited states of H_2 molecules), G_2 describes medium width line neck (radiation from 4–8 eV hydrogen atoms produced by excitations of H_2 by electrons followed by dissociation of H_2 molecule:

$$e + \mathrm{H}_2 \rightarrow e + \mathrm{H}_2^{**} \rightarrow e + \mathrm{H}^*(n=3) + \mathrm{H}^*(nl) \qquad (1)$$

and G_3 describes the line wings, comprised of radiation from the fast hydrogen atoms, originated by neutralization and dissociation of fast hydrogen molecular ions, subsequently accelerated in the cathode sheath region, and backscattered from the cathode as fast atoms, see [6-8].

In discharges operating in mixtures of hydrogen and argon, the profiles of hydrogen H_α line has more pronounced excessive component G_3. This is the result H_2 of dominant formation of H_3^+ ions in reactions:

$$\begin{aligned} Ar^+ + H_2 &\rightarrow ArH^+ + H \\ ArH^+ + H_2 &\rightarrow H_3^+ + Ar \end{aligned} \qquad (2)$$

The group of authors [4] studied profiles of the hydrogen H_α line in an abnormal glow discharge under influence of the external axial magnetic field. They have found that the applied magnetic field predominantly increases the intensity of the central component (G_1) of the excessively broadened H_α profile. As it is known, magnetic field causes helical motion of electrons along the electric field lines and prolongs their trajectories by increasing the number of collisions with matrix gas. This explains the increase of the central component of the H_α profile and can be regarded as an experimental proof for the main contribution of electron excitation to the central part of overall profile.

Recent studies of the H_α line, carried out in a PSI-2 linear magnetized plasma device, is given in [5]. The value of the applied magnetic field was of the order of 0.1 T, and at this value the Zeeman effect causes an additional splitting of hydrogen fine-structure levels. However, the authors found that the major contribution to the lines width is provided by the Doppler broadening.

The aim of this work is to show the variation of the H_α line shape with the strength of applied magnetic field, accurately generated by Helmholtz coils.

2. EXPERIMENTAL

The hollow cathode glow discharge with copper cathode is used. Here, for completeness, minimum details will be given since the construction details follow basic concept of Pyrex-kovar design reported in [2]. The cathode was 100 mm long with 6 mm internal diameter. Kovar anodes, 5 mm long with 15 mm diameter, are located at the both ends of cathode at a distance of 15 mm. The advantage of this glow discharge construction is: the hollow cathode can be easily replaced, and cleaning of the whole discharge tube from the sputtered material is simplified.

All experiments were carried out with the argon-hydrogen mixture (vol. 99.2% Ar + 0.8% H_2). The continuous flow of the working gas is sustained in the pressure range from 2 to 5 mbar by means of needle valve and two-stage mechanical vacuum pump. To run the discharge, a current stabilized power supply (0-2 kV, 0-100 mA) is used. The ballast resistor of 5 kΩ is placed in series with the discharge and power supply. During measurements, the cathode was grounded.

The light along the axis of hollow cathode glow discharge is focused by a lens (focal length 7.58 mm) with unity magnification, onto the 10 μm entrance

slit (height restriction 2 mm) of a 2 m focal length Ebert type spectrometer with 651 g/mm reflection grating, blazed at 500 nm. For the line shape measurements, the reciprocal dispersion of 0.74 nm/mm is used throughout this experiment. Signals from the CCD detector (1 x 3648 pixels, 8 μm pixel widths) are A/D converted, collected and processed by PC. All spectral measurements were performed with an instrumental profile very close to Gaussian with measured full width at half maximum (FWHM) of 18 pm.

As the source of external magnetic field we used a pair of Helmholtz coils with N=2380 turns of wire wounded in multiple layers. The coils are mounted on a bench whose height is adjusted so that their axis coincides with the optical axis of the spectrometer. The distributions of magnetic field for three different values of generating electric current (I=1,23 A, I=1,55 A and I=3,3 A), were measured using the digital teslameter DTM 150, manufactured by Group 3, New Zealand, and are in a good agreement with the theoretical predictions for real coils, obtained by a MATLAB program, see e.g. [9].

3. RESULTS

Four excessively Doppler broadening H_α line profiles are presented in Figure 1. First one (B=0), shows the H_α line recorded without, while the remaining three are recorded with different values of external magnetic field generated by Helmholtz coil.

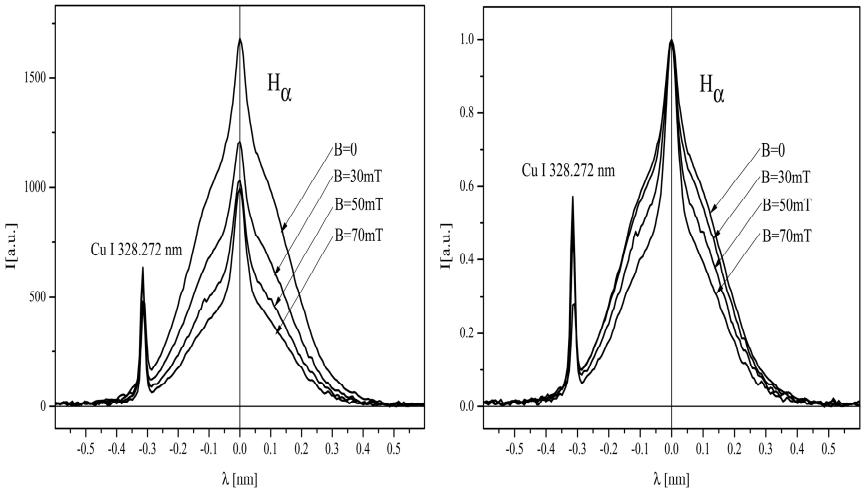

Figure 1. a) Typical profiles of the excessively Doppler-broadened hydrogen Balmer the H_α lines, recorded in a HCGD at different values of the applied magnetic field. b) Same as in panel a) but profiles are normalized to the same maximum intensity. Discharge conditions: copper cathode; working gas: vol. 99.2% Ar + 0.8% H_2; p = 4mbar; I = 45mA; and T_{wall} = 60 ºC [9].

For simplicity, in fitting procedure of the overall H_α line profiles, we used a model function consisting of only two Gaussians: (the central part) G_1 and G_3, describing the central part and the excessively broadened part, respectively. The results of fitting procedure, as well as more details regarding the influence of external magnetic field, will be reported at the Conference.

4. CONCLUSION

On the basis of spectroscopic investigation of the H_α line, several conclusions can be drawn:

- with an increase of magnetic field a significant reduction of the H_α line intensity and voltage are detected;
- relative contribution of G_1, compared to the contribution of G_3 increases with the increase of applied magnetic field
- temperature change of cathode wall in the range of 60 to 100 ºC does not affect applying voltages at the discharge source and relative contribution of G_1 and G_3 components.

Acknowledgements

This work is supported by the Ministry of Education, Science and Technological Development of the Republic of Serbia under Projects 171014 and 171027.

REFERENCES

[1] W. Benesh and E. Li, Opt.Lett. 9, 338 (1984).
[2] B. P. Lavrov, A. S. Mel'nikov, Opt. Spectrosc. 75, 1152 (1993).
[3] N. M. Šišović, G. Lj. Majstorović, N. Konjević, Eur. Phys. J. D 32, 347 (2005).
[4] B. M. Obradović, I. P. Dojčinović, M. M. Kuraica and J. Purić, Appl. Phys. Lett. 88, 141502 (2006).
[5] O. Marchuk, C. Brandt, A. Pospieszczyk, M. Reinhart, S. Brezinsek, B. Unterberg and S. Dickheuer, J. Phys. B: At. Mol. Opt. Phys. 51 025702 (2018).
[6] H. Tawara, Y. Itikawa, H. Nishimura, and M. Yoshino, J. Phys. Chem. Ref. Data 19, 617 (1990).
[7] Dj. Spasojević, V. Steflekova, N. M. Šišović, and N. Konjević, Plasma Sources Sci. Technol. 23, 012004 (2014).
[8] N. V. Ivanović, N. M. Šišović, Dj. Spasojević and N. Konjević, J. Phys. D: Appl. Phys. 50, 125201 (2017).
[9] N. M. Šišović, Doctoral thesis, Faculty of physics, Belgrade, (2012).

A SIMPLE XCOS/SCILAB MODEL OF A DBD PLASMA JET IMPINGING ON A TARGET

M.E. Pinchuk[1,2], O.M. Stepanova[1,2], A.V. Lazukin[2,3] and A.M. Astafiev[1,2]

[1] *Institute for Electrophysics and Electrical Power of the Russian Academy of Sciences, Dvortsovaya Naberezhnaya 18, Saint-Petersburg 191186, Russia*

[2] *Saint-Petersburg State University, Universitetskaya Naberezhnaya 7/9, Saint-Petersburg 199034, Russia*

[3] *National Research University Moscow Power Engineering Institute, Krasnokazarmennaya 14, Moscow 111250, Russia*

Abstract. The paper presents a XCOS/Scilab model of a dielectric-barrier discharge plasma jet impinging on a target. A model is based on the substitution of an electrical discharge system by an equivalent electrical circuit, which consists of lumped resistances and capacitances. It has a simple structure. Electrical elements are built from standard modules in XCOS/Scilab. The model allows us to conduct quantitative calculations of electrical characteristics of discharge systems.

1. INTRODUCTION

The field of possible applications of non-equilibrium atmospheric pressure plasma has been permanently expanding [1]. Many studies have increasingly been conducting in the cross-disciplinary researchers on plasma physics and life sciences [2, 3].

One of the main non-equilibrium plasma sources is a dielectric-barrier discharge (DBD) [4]. To develop a device, a number of optimization problems, namely, a necessary amount of energy deposited into a working gas, electrode geometry should be solved.

The paper considers a simple equivalent circuit, which consists of serial-parallel lumped resistances and capacitances. It has been used for calculating elements of a gas-discharge system [5, 6, 7, 8, 9]. The simplest circuit of substitution of a DBD cell with a system of series-connected capacitances, one of that simulates a gas-gap capacitance, and another one is

equivalent to a barrier capacitance. When the voltage exceeds the breakdown value, a resistance parallel to the capacitance is put into the circuit to simulate the discharge burning.

To treat a living target (biological object), plasma jet sources based on a DBD are widely used [2, 3, 4]. In this case, a plasma jet might be substituted with a chain of serial RC elements [10]. A general description of a such DBD system and applying different equivalent RC circuits is presented in [9].

Samples of using such models in XCOS/Scilab [11, 12] to simulate a system of the generation of a plasma jet in helium [13, 14, 15] are presented in the paper. Study materials on programming package can be found at [11, 12, 16]. The model has a simple structure; and it can be easily used by other researchers.

2. XCOS-SIMULATION OF A DIELECTRIC-BARRIER DISCHARGE PLASMA JET IMPINGING ON A TARGET

A system of cold plasma jet generation [13, 14, 15] based on a DBD burning in a helium flow in an axisymmetric electrode system "inner electrode (central rode) – gas gap – quartz tube (dielectric barrier) – outer electrode (outer ring)" fed by a sinusoidal voltage has been simulated. A diameter of inner electrode is 1.5 mm; an inner diameter and thickness of the quartz tube are 5.5 and 0.7 mm, correspondingly. A length of the discharge area is equal to 5 mm.

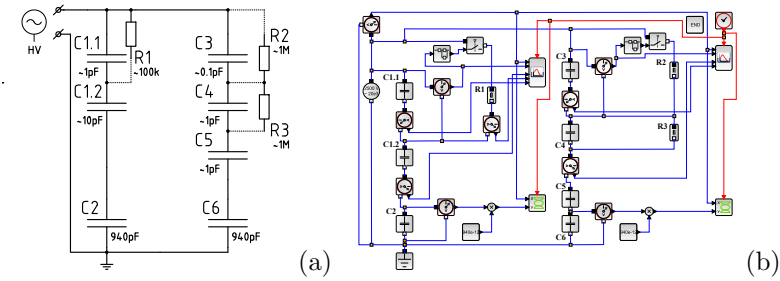

Figure 1. An equivalent circuit of a DBD plasma jet impinging on a target (a) as in [14, 15] and XCOS model to simulate it (b).

At a high frequency of applied voltage that is at a period of voltage signal which is longer than plasma relaxation time, a system "DBD – plasma jet impinging on a target" can be substituted with RC circuits, presented in Fig. 1(a). The first one (left part) is equivalent to a gas cell with a dielectric barrier. The second one (right part) is for simulating the plasma jet. An example of the equivalent circuit built in XCOS is presented in Fig. 1(b).

Here are capacitances: C1.1 — a gas gap; C1.2 — a barrier; C2 and C6 — a measuring guages; C3 — a plasma jet; C4 — a target; C5 — a substrate. R1 is an active plasma resistivity of DBD region at the breakdown of a gas gap. R2 and R3 are resistances of a plasma jet and target, corespondingly.

Values of the chain elements were calculated using geometrical sizes of the system and plasma jet parameters from [6, 17, 18, 19].

Fig. 2(a) shows a module that provides an analysis on charging the capacitance C1.1. When the voltage reaches the breakdown value, it generates a signal to switch on an active resistance R1 parallel to C1.1. The inner structure of the analysis module is shown in Fig. 2(b). Delay module provides avoiding the appearance of an algebraic loop mistake.

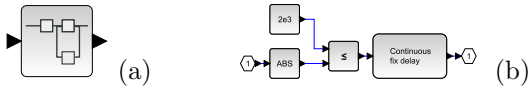

Figure 2. Analysis module of the charging of the capacitance C1.1 (a) and its inner structure (b).

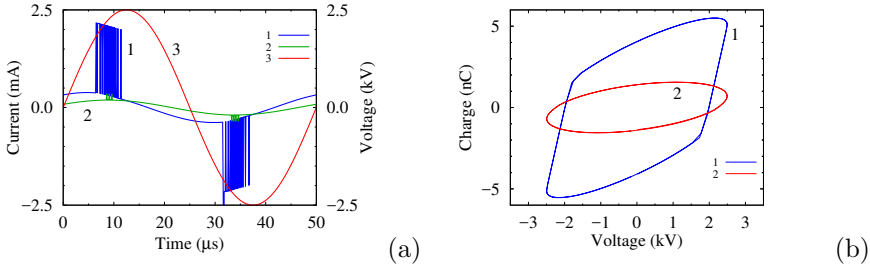

Figure 3. Calculation results: electrical (a) (1 — discharge current; 2 — plasma jet current; 3 — applied voltage) and volt-coulomb (b) (1 — discharge VCC; 2 — plasma jet VCC) characteristics.

Fig. 3(a) shows the results of calculations for the case of applying 20 kHz voltage with an amplitude of 2.5 kV. Fig. 3(b) presents corresponding volt-coulomb characteristics (VCC).

3. CONCLUSION

An implementation of a model of a DBD plasma jet in the visual programming environment XCOS/Scilab has been presented. The model is based on the substitution of a physical system by an equivalent electrical circuit, which consists of lumped resistances and capacitances. The case for simulation of DBD and DBD plasma jet impinging on the target have been described. The results of calculations of electrical and volt-coulomb characteristics of the system "DBD – plasma jet impinging on a target" have

been obtained for the case of applying 20 kHz voltage with an amplitude of 2.5 kV.

Acknowledgements

This work was supported by Saint Petersburg State University (grant no. 0.37.218.2016) and the Russian Foundation for Basic Research (grant no. 16-08-00870).

REFERENCES

[1] I. Adamovich et al, J. Phys. D: Appl. Phys. 50, 323001 (2017).

[2] S. Bekeschus et al, Plasma Processes Polym. e1800033 (2018).

[3] N. Puač et al, Plasma Processes Polym. 15, e1700174 (2018).

[4] K.D. Weltmann et al, Pure Appl. Chem. 82, n 6, 1223 (2010).

[5] V.G. Samoylovich, V.I. Gibalov, K.V. Kozlov, *Physical Chemistry of Barrier Discharge*, p. 178, (Moscow, MSU, 1989) (in russian).

[6] Yu.P. Raizer, *Gas Discharge Physics*, p. 449, (Springer, 1991).

[7] M.I. Lomaev. Atmos. Oceanic Opt. 14, 1005 (2001).

[8] A.V. Pipa et al, Rev. Sci. Instrum. 83, 115112 (2012).

[9] Ya.Z. Slutsker et al, Phys. Plasmas 24, 103510 (2017).

[10] Yu. Akishev et al, Plasma Sources Sci. Technol. 22, 015004 (2013).

[11] https://www.scilab.org

[12] https://www.scilab.org/scilab/features/xcos

[13] M. Pinchuk et al, Proc. Int. Conf. on Plasma Physics and Plasma Technology (Minsk) vol 1 (Minsk: Belarus/Kovcheg) pp 51-54, (2015).

[14] M. Pinchuk et al, J. Phys.: Conf. Ser. 830, 012060 (2017).

[15] O. Stepanova et al, Plasma Medicine 7, n3, 187 (2017).

[16] E.S. Glibin, *Simulation of Power Supplies of Electrotechnological Installations in Scilab/XCOS*, p. 48, (Togliatti, TSU, 2016) (in russian).

[17] S. Gadkari and S. Gu, Phys. Plasmas 24, 053517 (2017).

[18] G.V. Naidis, Appl. Phys. Lett. 98, 141501 (2011).

[19] G.B. Sretenović et al, J. Appl. Phys. 121, 123304 (2017).

ELECTRON ENERGY DISTRIBUTION FUNCTIONS IN A RADIO-FREQUENCY ARGON DISCHARGE – MONTE CARLO SIMULATIONS

Marija Puač[1], Dragana Marić[1] and Zoran Lj Petrović[1,2]

[1]*Institute of Physics, University of Belgrade, Pregrevica 118,11080 Zemun, Serbia*
[2]*also at: Serbian Academy of Sciences and Arts, Knez Mihailova 35, 11001 Belgrade, Serbia*

Abstract. Modeling of radio-frequency (RF) plasmas has been well developed and carried out many times and in great detail. However modeling of breakdown that precedes a fully formed plasma has been somewhat neglected. Focus of this paper is modeling of RF breakdown in argon with constant gap between electrodes of 23 mm and frequency f=13.56 MHz. Physical background of the RF breakdown has been examined through Electron Energy Distribution Functions (EEDF) for points on the voltage breakdown curve. All calculations were carried out by a Monte Carlo collision code that includes electrons only, while contribution of heavy particles will be neglected in this paper.

1. INTRADUCTION

Modeling of radio-frequency (RF) plasmas has been popular due to their large variety of applications, from nanotechnologies trough plasma cleaning and finally biomedical applications and agriculture. RF plasmas with fully formed space charge can be modeled by Particle-in-Cell simulations with Monte Carlo collisions (PIC-MCC). On the other hand our intention is to look into physical background of the breakdown itself, the development that precedes plasma formation. Breakdown may be well described as a swarm of charged particles traveling between two infinite electrodes in external RF electric field. In other words the code has been shown to represent exactly the swarms of charged particles in vanishing space charge conditions and negligible perturbation of the gas, exactly the conditions that are relevant for the breakdown initialization before the space charge effects develop.

In our previous papers [1,2] we have used spatial profiles of electron swarms to explain the Paschen like breakdown voltage curve as a function of a *pd* (pressure times the gap between electrodes). Here we add analysis of electron energy distribution functions (EEDF).

Argon was chosen to be the background gas due to its simple inelastic energy loss spectrum that can be described by four effective cross sections: elastic, two electron excitations and ionization. At this point there are no effects of the electrode surfaces and every electron that reaches electrode is absorbed and thus erased from simulation.

2. ELECTRON ENERGY DISTRIBUTION FUNCTIONS

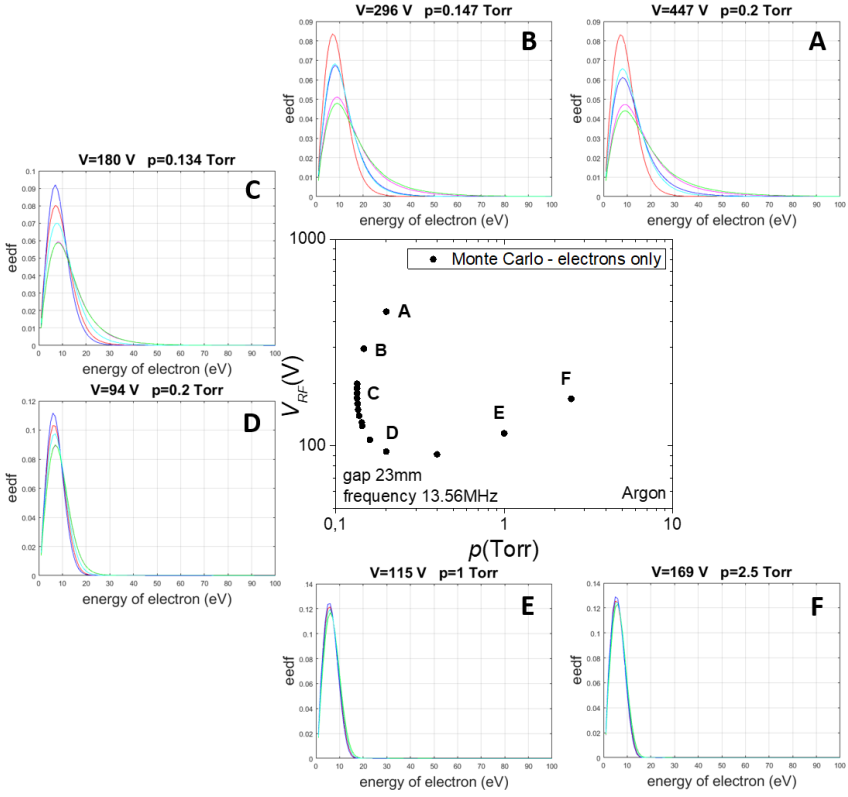

Figure 1. (Central) Voltage breakdown curve for argon at 13.56 MHz and electrode gap of 23 mm. Letters indicate the points where data are presented (A-F). EEDFs for points highlighted by letters and sampled at different times within one period.

The procedure how to determine voltage breakdown curve has been explained in our previous work [1], so we will focus on EEDFs along the voltage breakdown curve as presented in Fig.1. At first sight there is a significant difference between EEDFs at high voltages/low pressures (left hand side of the breakdown voltage curve) and high pressures/low voltages (right hand side of the curve). At high voltages, due to small number of collisions with the background gas, electrons can obtain great deal of energy from the field that leads to higher

mean energies. There are differences between EEDFs sampled over one period of the RF field (color lines in EEDF plots in Fig.1). On the other hand at high pressures there is abundance of collisions with the background gas that reduces amount of energy transferred from the field to electrons. This section of the breakdown curve exhibits smaller mean energies (as compared to the left hand side) and EEDF does not relax significantly over one period.

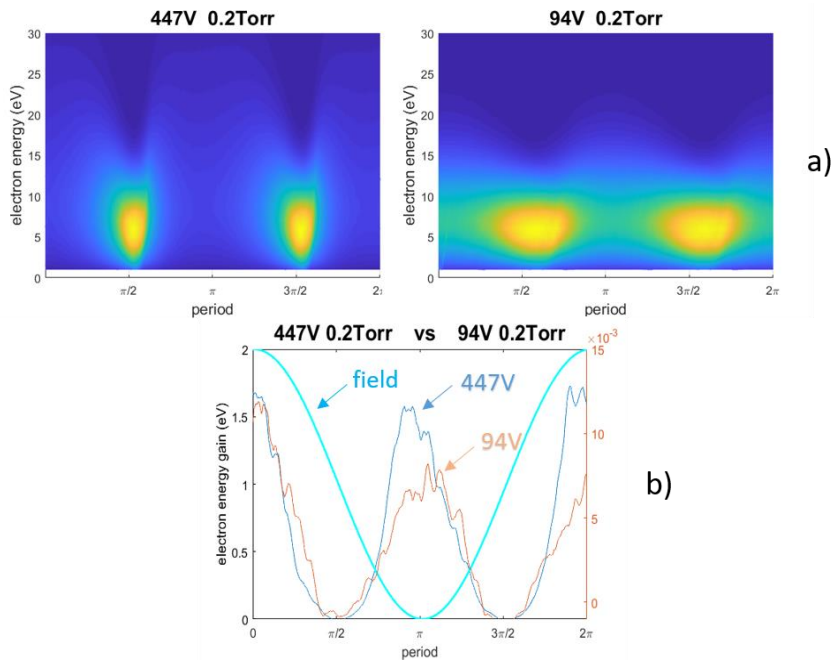

Figure 2. a) EEDF over one period of time in a 2D plot for points A and D from Fig.1 at the same pressure of 0.2 Torr and different voltages: 447 V and 94 V. b) Gain of energy transferred from the field to the electron swarm between two collisions for the same two points. L.H.S. axis is relevant for 447 V curve while for the 94 V curve it is the R.H.S. vertical axis. Background gas is argon, electrode gap is 23 mm and frequency is 13.56 MHz.

If one observes A and D from Fig.1 they have the same pressure (0.2 Torr) i.e. are on a vertical line with two possible, quite different, operating voltages (447 V and 94 V). Double valued nature of the voltage breakdown curve has been explained in [1, 2], and thus we will discuss more the energy transfer presented in Fig.2. For the lower voltage, smaller portion of energy has been transferred from the field to electrons between collisions as expected (Fig.2b). Difference between energy gains in these two cases is almost two orders of magnitude. That means that electron at 94 V experiences almost 100 times more elastic collisions while accumulating sufficient energy to ionize, as compared to the upper point at 447 V. In Fig.2a EEDF for *V*=447 V has narrower peaks but there are electrons with higher energies between those peaks (EEDF

has long "tail", brighter blue colour). At V=94 V peaks are wider and there is absence of high energy electrons depicted with darker color at higher energies (compared to EEDF for V=447 V). At the lower voltage, there is a certain time delay between the two energy gain peaks compared to the field maximum which is due to inability of energy to relax at 13.56 MHz. In other words at 447 V electrons seem to dissipate their energy faster due to their overlap with the high energy loss cross sections, while at 94 V the swarm seems to need to gather energy even after the peak in the field in order to be able to dissipate it. It is expected that such curves would be different for molecular gases.

We have presented another insight into physical background of RF breakdown that is extension of our previous work [1,2]. By examining EEDFs along voltage breakdown curve we have discussed influence of number of collisions with background gas (pressure) on mean energy. With highlighted two point on the voltage breakdown curve that have the same pressure and different voltages we have observed energy transfer between two collisions from the external field to the electrons and later electron energy dissipation through their collisions with electroneutral argon atoms.

Acknowledgements

This paper was supported through projects OI 171037 and III 41011 of the MESTD of Serbia. ZLjP is grateful to Serbian Academy of Sciences and Arts and its project F155 for its partial support.

REFERENCES

[1] M. Puač, D. Marić, M. Radmilović-Radjenović, M. Šuvakov and Z. Lj Petrović, Plasma Sources Sci. Technol., https://doi.org/10.1088/1361-6595/aacc0c (2018).

[2] M. Savić, M. Radmilović-Radjenović, M. Šuvakov, S. Marjanović, D. Marić, Z.Lj. Petrović, IEEE Trans. Plasma Sci. 39 2556 – 2557 (2011).

VOLT-AMPERE CHARACTERISTICS AND ABNORMAL GLOW DISCHARGES IN METHANOL AND ETHANOL VAPOURS

J. Sivoš[1], D. Marić[1], N. Škoro[1], G. Malović[1] and Z. Lj. Petrović[1, 2]

[1] *Institute of Physics, University of Belgrade, Pregrevica 118, Zemun, Belgrade, 11080, Serbia*
[2] *Serbian Academy of Sciences and Arts, Knez Mihailova 35, 11001, Belgrade, Serbia*

Abstract. Here we present measurements of Volt-Ampere characteristics for low-pressure discharges in methanol and ethanol vapours for electrode gap of 1.1 cm, at *pd*-s (pressure x gap) close to the Paschen minimum. We focus on changes in operating mode of discharges that are observed in abnormal glow regime. The transition occurs after certain time and it is smooth, without any instability in *V-A* waveforms.

1. INTRODUCTION

The field of non-equilibrium plasmas in liquid alcohols and their vapours have become very attractive subject of research in past years. These discharges have drawn attention due to the wide area of application from environmental remediation, biomedicine to nanotechnology. The first nanographene layers were synthesized in discharges of liquid alcohol solutions [1], the fuel industry recognizes them as suitable sources of hydrogen [2] and they are integral part of high energy particle detectors and sensors [3]. Since majority of applications work in glow discharge regime, it is important to comprehend electrical characteristics of discharges. Here we present Volt-Ampere (*V-A*) characteristics for methanol and ethanol vapour discharges measured at working conditions close to the minimum of the Paschen curve, with detailed analysis of unusual behaviour observed in abnormal glow regime of the discharge.

2. EXPERIMENTAL SET-UP

The electrode-system is placed inside tightly fitting cylindrical quartz chamber, due to prevent long-path breakdown. Plan-parallel electrode-system consists of copper cathode and quartz anode coated with transparent conductive thin film of platinum. The electrodes are 5.4 cm in diameter ($2r$) and 1.1 cm

apart. Vapours are obtained from 99 % methanol and 95 % ethanol. Volt-Ampere characteristics are measured by applying a pulse of voltage in addition to running discharge at small DC current (~ 1 μA). During the pulse, axial emission profiles are recorded by fast sensitive ICCD camera (Andor IStar DH720-18U-03). More information on the measurement technique can be found elsewhere [4].

3. RESULTS AND DISCUSSION

Volt-Ampere characteristics were recorded in a range of discharge currents from ~1 μA to several mA. In Fig. 1 we show plots of voltage and current dependence in methanol (squares) at $pd = 0.4$ Torr cm and ethanol (circles) at $pd = 0.2$ Torr cm. Operating regimes typical for low-pressure DC discharges can be clearly distinguished [5]. Evidently in both cases, abnormal regime is characterized with a very steep positive slope for currents above 800 μA.

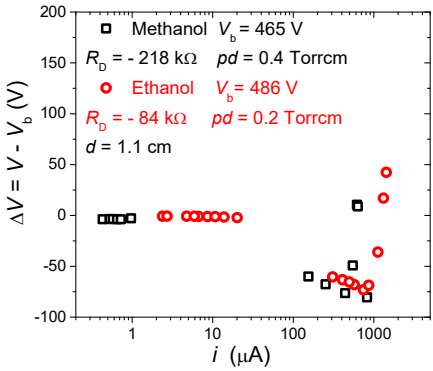

Figure 1. Volt-Ampere characteristics for discharges in methanol and ethanol vapours at $d = 1.1$ cm.

Measurements in abnormal regime of these discharges reveal changes in steady-state current and voltage values within single voltage pulse. In Fig. 2 we show examples of voltage and current waveforms for methanol and ethanol, with pronounced step-like shape, due to the mode change.

In methanol vapour discharge (Fig. 2a) initial current is 830 μA and transition in operation mode occurs after approximately 2 ms. At the beginning of the pulse, the discharge operates at lower voltage and higher current, and then it switches to ~80 V higher voltage and ~190 μA lower current. For ethanol vapour discharge (Fig. 2b) transition in operation mode occurs 30 μs after stable operation. Like in the case of methanol vapour, ethanol vapour discharge at beginning operates at higher current and lower voltage, and then switches at ~70 V higher voltage and ~320 μA smaller current. For both alcohols, transition in discharge operation is smooth, without any instabilities or oscillations in *V-A* waveforms. Furthermore, there are no significant changes in spatial structures of the discharges that could explain the mode change.

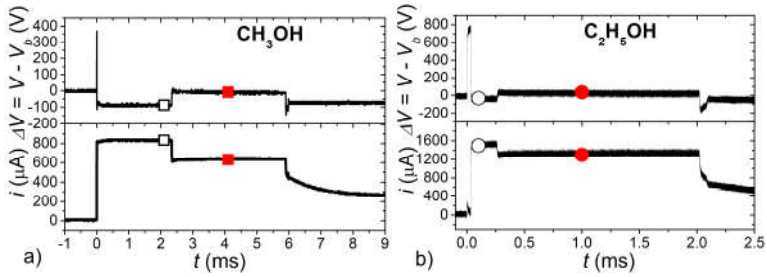

Figure 2. Waveforms of voltage and current for a) methanol abnormal discharge at pd = 0.4 Torr cm and b) ethanol abnormal discharge at pd = 0.2 Torr cm.

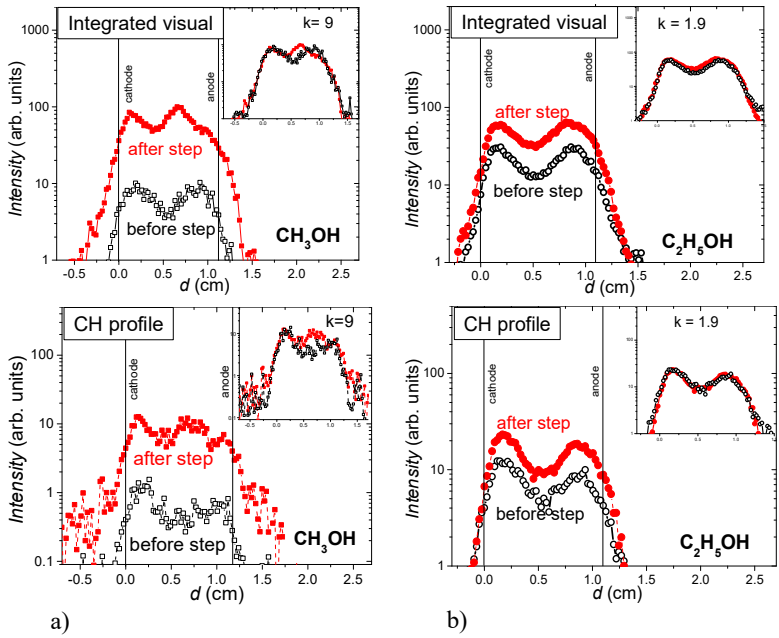

Figure 3. Axial profiles of emission from: a) methanol vapour discharge at d = 1.1 cm and pd = 0.4 Torr cm, and b) ethanol vapour discharge at d = 1.1 cm and pd = 0.2 Torr cm in abnormal regime taken in the visible range and with optical filter for CH band (431 nm). Open symbols correspond to points before the 'step' and full symbols – after the 'step'. Insets show axial profiles of emission normalized by a suitable coefficient k, for easier comparisons.

Figure 3a) and 3b) show axial profiles of emission recorded at moments marked in Figure 2a) and 2b) respectively. Axial profiles of emission in methanol (Fig. 3a) and ethanol (Fig. 3b) vapour discharges are integrated in visual range and resolved spectrally using optical filter for CH band at 431 nm.

Profiles of both alcohols reveal significant influence of heavy particles in excitation and ionization (unveiled through the peak of emission near the cathode). Furthermore, spectrally resolved profiles follow the integrated emission profiles in shape, with noticeable peak in front of the cathode indicating that heavy particles (positive ions and fast neutrals) have significant contribution to excitation of CH radical emitting at this wavelength. The profiles recorded after the transition have higher overall intensities and the emission peaks near the anode (negative glow) are slightly shifted toward the cathode in comparison with the profiles obtained before the transition, due to a change in electric field distribution. Also, the ratios of maximum intensities of profiles, recorded with and without optical filter, are the same.

Evidently, discharge after some time of stable operation slides into more preferable operating mode, with lower current and higher voltage. This behaviour is probably consequence of changes in balance of charged or excited species: ions or electronically and vibrationally excited dissociation products and adsorbed species created in discharges. This effect is, at the same time, interesting from the point of view of basic discharge properties and for applications that work in pulsed or high frequency glow regime. Further experimental investigations will provide information on processes behind the change in discharge regime.

Acknowledgements

The authors acknowledge support by MESTD of Serbia (projects ON171037 and III41011).

REFERENCES

[1] T. Hagino, H. Kondo, K. Ishikawa, H. Kano, M. Sekine and M. Hori, Appl. Phys. Express 5, 035101 (2012).
[2] G. Petitpas, J. D. Rollier, A. Darmonb, J. Gonzalez-Aguilar, R. Metkemeijer and L. Fulcheri, Int. J. Hydrogen Energy 32, 2848C (2007).
[3] P. Fonte, A. Mangiarotti, S. Botelho, J.A.C. Goncalves, M.A. Ridenti and C.C. Bueno, Nuclear Instruments and Methods in Physics Research A 613, 40 (2010).
[4] J. Sivoš, N. Škoro, D. Marić, G. Malović and Z. Lj. Petrović, J. Phys. D: Appl. Phys. 48, 424011 (2015).
[5] D. Marić, P. Hartmann, G. Malović, Z. Donko and Z. Lj. Petrović, J. Phys. D: Appl. Phys. 36, 2639–2648 (2003).

MULTIELECTRON INITIATION OF AVALANCHES BASED ON NEGATIVE BINOMIAL DISTRIBUTION AND ITS MIXTURES

S. N. Stamenković[1], V. Lj. Marković[1], A. P. Jovanović[1] and M. N. Stankov[2]

[1]*Department of Physics, Faculty of Sciences and Mathematics, University of Niš, PO Box 224, 18001 Niš, Serbia*
[2]*Leibniz Institute for Plasma Science and Technology (INP), Felix-Hausdorff-Straße 2, 17489 Greifswald, Germany*

Abstract. The generalization of electron avalanche statistics for multielectron initiation is based on negative binomial distribution (NBD) and its mixtures. In the extreme cases for one initiating electron the exponential distribution and for multielectron initiation the Gaussian distribution can be applied. With a fixed number of initial electrons, the avalanche statistics is described by a single NBD. When electron emission is a homogeneous or inhomogeneous Poisson process, the weighted mixtures of NBDs are applied.

1. INTRODUCTION

By studying the fluctuation phenomena in the passage of electrons through lead and cosmic ray showers produced by single electrons or photons, Furry [1] showed that the distribution in shower sizes $P(n,\overline{n})$ is of the form:

$$P(n,\overline{n}) = \frac{1}{\overline{n}}\left(1-\frac{1}{\overline{n}}\right)^{n-1} \tag{1}$$

where $\overline{n}$ is the mean number of observed particles. However, under the ordinary conditions, number of very small and large showers deviates from Furry law [1]. This indicates that there was not single but many initiating electrons.

Moreover, Wijsman [2] derived the probability $P(n,d)$ of finding n electrons in an avalanche for the given electron starting at the cathode

$$P(n,d) = \frac{1}{\overline{n}}\left(1-\frac{1}{\overline{n}}\right)^{n-1}, \tag{2}$$

where d is the inter-electrode gap and $\overline{n} = \exp(\alpha d)$ (α is the Townsend's first ionization coefficient). For $\overline{n} >> 1$, the Eq. (2) can be approximated by exponential dependence $P(n,d) = e^{-n/\overline{n}}/\overline{n}$.

The statistics of avalanche initiated by a single electron is completely described by Furry law [3,4]. However, when more than one electron initiates the avalanche this law is not appropriate. If k electrons are emitted from the cathode and each of them, independently, starts the avalanche, every of these avalanches can be described with Furry (geometric) distribution, but the total number of electrons in the whole avalanche will not follow it. The sum of random variables with geometric distribution will follow the negative binomial distribution

$$P(n;p,k)=\binom{n-1}{k-1}p^k q^{n-k}, \tag{3}$$

which is suitable to describe multielectron initiation. The probability $p=1/e^{\alpha d}$ will be the same, while the number of random variables with Furry distribution (number of initial electrons) will be the parameter k. In this way, NBD is physically based and its parameters p and k have the physical meaning.

The generalized electron avalanche statistics based on NBD in the limiting case of the single initiating electron ($k=1$), gives Furry distribution. When the number of initiating electrons is high ($k>>1$), Gaussian approximation for the negative binomial distribution is obtained. In the general case for the intermediate number of electrons k, the mixed Gauss-exponential distribution (as the continual analog of NBD) can be applied:

$$P_{GE}(n)=a_G\frac{1}{\sqrt{2\pi}\sigma_G}e^{-\frac{(n-\bar{n}_G)^2}{2\sigma_G^2}}+a_E\frac{1}{\bar{n}_E}e^{-\frac{n}{\bar{n}_E}}. \tag{4}$$

2. RESULTS AND DISCUSSION

The multielectron initiation causes that the electron number distributions deviate from the exponential ones. Our prediction for multielectron initiation, based on NBD for $k=3$ is presented by solid line in Fig. 1a, accompanied by continual analog i.e. the mixed Gauss-exponential distribution.

The binomial distribution successfully describes the events with two outcomes such as secondary electron emission. When a probability of electron emission tends to zero, the binomial distribution goes into Poisson distribution $P(k,\bar{k})=e^{-\bar{k}}\bar{k}^k/k!$ ($\bar{k}$ is the expected number of emitted electrons), while for neither too small nor too high probability of emission the binomial distribution goes into Gaussian one [5]. When the number of initiating electrons is random number obeying Poisson distribution [6], the mixture of NBDs is required:

$$P(n,k,p)=\sum_i a_i P_i(n,k_i,p), \tag{5}$$

where a_i are distribution weighting factors and $P_i(n,k_i,p)$ are NBDs with parameters k_i and p. The electron number distribution $P(n,k,p)$ is modeled by

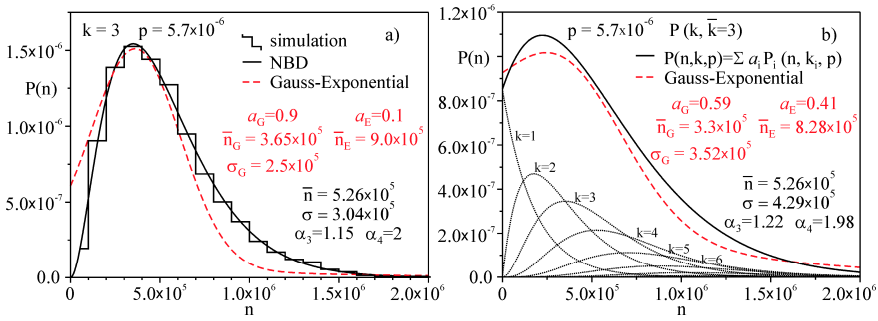

Figure 1. a) The multielectron prediction of electron number distribution based on NBD and mixed Gauss-exponential approximation. b) The electron number distribution described by mixed NBD when the number of initiating electrons obeys Poisson statistics and its mixed Gauss-exponential approximation.

the mixture of several NBDs (solid line in Fig. 1b), with the number of initial electrons $k = 1-9$ for Poisson distribution $P(k, \bar{k} = 3)$. In addition, the distribution was modeled by the mixed Gauss-exponential distribution as continual analog. The physical explanation for the use of mixture distributions is existence of many subpopulations in Poisson emission statistics caused by the fluctuation of the number of initial electrons emitted from the cathode.

The results in the literature [7,8] show that the electron emissivity of the cathode may increase/decrease with a large number of repeated measurements (sputtering, adsorption or desorption of oxygen and impurities, etc.). When the expected number of initiating electrons $\bar{k}_\lambda$ varies in time as

$$\bar{k}_\lambda = \bar{k}\, e^{\pm\lambda t} \approx \bar{k}(1 \pm \lambda t + \frac{\lambda^2 t^2}{2}), \qquad (6)$$

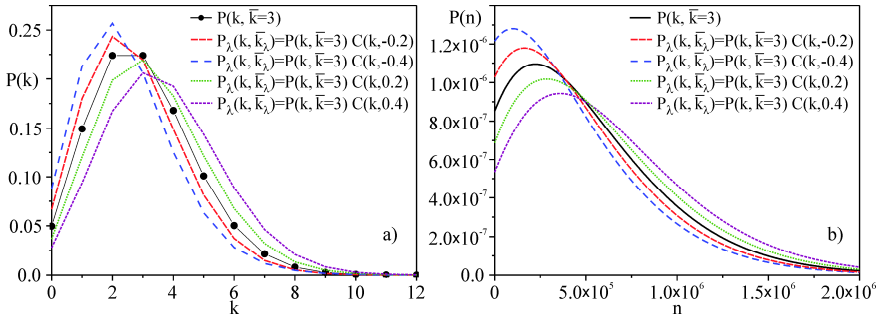

Figure 2. a) Emission statistics as inhomogeneous Poisson process $P_\lambda(k, \bar{k}_\lambda)$ with correction factor compared to homogeneous Poisson process $P(k, \bar{k})$; b) The electron number distributions with multielectron initiation described by mixed NBDs when emission statistics is inhomogeneous Poisson process compared to mixed NBDs for homogeneous Poisson process.

the electron emission is inhomogeneous Poisson process [9] (λ is the increase/decrease rate) described by modified Poisson distribution [10] (Fig. 2a)

$$P_\lambda(k,\bar{k}_\lambda) \approx P(k,\bar{k})\left\{1 \pm \frac{\lambda T}{2}(k-\bar{k}) - \frac{(\lambda T)^2}{6}\left[\bar{k} - (k-\bar{k})^2\right]\right\} = P(k,\bar{k})C(k,\lambda T), \quad (7)$$

where T is the total time of measurements. When the initial electron emission is described by inhomogeneous Poisson process, the avalanche size distribution (Fig. 2b) may be successfully described by the mixture of NBDs (Eq. 5). However, in this case $\bar{k}_\lambda$ increases/decreases and emission statistics is described by modified (or nonstationary) Poisson distribution $P_\lambda(k,\bar{k}_\lambda)$, illustrated in Fig. 2a for $\bar{k} = 3$.

3. CONCLUSION

This paper stress the importance of multielectron initiation and funds electron avalanche statistics on the negative binomial distribution and its mixtures combined with homogeneous and inhomogeneous Poisson process of initial electrons emissions. The modeling of electron avalanche distributions, both by discrete negative binomial and its mixtures, as well as mixed Gauss-exponential distribution, indicates that multielectron initiation is a more realistic assumption in experiments and applications.

Acknowledgements

The authors are grateful to the Ministry of Education, Science and Technological Development of the Republic of Serbia (project ON 171025).

REFERENCES

[1] W. H. Furry, Phys. Rev. 52, 569 (1937).
[2] R. A. Wijsman, Phys. Rev. 75, 833 (1949).
[3] H. Raether, *Electron Avalanches and Breakdown in Gases* (Butterworths, London, 1964).
[4] H. Schlumbohm, Z. Phys. 151, 563(1958).
[5] V. Lj. Marković, A. P. Jovanović, S. N. Stamenković and B. Č. Popović, *Europhys. Lett.* 100**,** 45002 (2012).
[6] R. H. Kingston, *Detection of Optical and Infrared radiation*, p. 10, (Springer-Verlag, Berlin, Heidelberg, New York, 1978).
[7] S. N. Stamenković, V. Lj. Marković, A. P. Jovanović and M. N. Stankov, Rom. Rep. Phys. 39**,** 408 (2017).
[8] S. Suzuki and H. Itoh, Plasma Sources Sci. Technol. 23, 065030 (2014).
[9] V. Lj. Marković, S. N. Stamenković, S. R Gocić and Z. Lj. Petrović, Contrib. Plasma Phys. 45, (7) 476 (2005).
[10] J. W. Müller, J. Radioanal. Chem. 61, 345 (1981).

ELECTRICAL CHARACTERISATION OF THE SURFACE DBD OPERATING IN AIR

Milica Bajić[1], Nikola Škoro[1], Nevena Puač[1] and Zoran Lj. Petrović[1,2]

[1]*Institute of Physics, University of Belgrade, Pregrevica 118, 11080 Belgrade, Serbia*
[2]*Serbian Academy of Sciences and Arts, Knez Mihailova 35, 11000 Belgrade, Serbia*

Abstract. In this paper we will present the electrical characterization of the surface dielectric barrier discharge (SDBD) source. This source has been previously used in treatments of flour and artificial bone grafts. The system operates in air at the frequency of 50 Hz. We have used commercially available HV and voltage probes in order to determine current-voltage characteristics and power transmitted to the discharge.

1. INTRODUCTION

Cold non-equilibrium plasmas are extensively used in the fields of biomedicine, stomatology, food technologies and agriculture [1, 2]. There is plethora of the plasma sources that operate at atmospheric pressure used in these fields. They are mainly distinguished by the type of applied voltage signals (pulsed, continuous), electrode geometry (DBD, jet, pin type jet etc.), feeding gas used (helium, argon, air or various mixtures) etc. Naturally, the final choice of the atmospheric plasma system is governed by the application in which it will be use. In order to be able to choose the appropriate atmospheric plasma source it is of outmost importance to have detailed characterization. One of the first characterizations that is usually performed is electrical characterization.

In this paper we will present results of the electrical characterization of the SDBD system that operates in air at atmospheric pressure. We have used the commercial high-voltage (HV) and voltage probes to perform this task. The results were obtained for the two distances between SDBD and the sample holder. We have recorded current and voltage waveforms and determined V-I characteristics of the system, as well as, the power transmitted to the plasma.

2. EXPERIMENTAL SET UP

Surface dielectric barrier discharge (SDBD) source used in the experiments is placed above glass dielectric plate (90 mm in diameter) that serves as a sample holder. The SDBD source has stripe electrodes made of 5 mm wide copper tape placed on both sides of 2 mm thick glass dielectric plate. The geometry of both powered and grounded electrode is shaped in a form of a rectangle. The copper stripes fixed to the lower part of the dielectric (facing the sample holder) were powered while the stripes on the upper part were grounded. For these treatments powered electrodes were connected to 50 Hz sine high-voltage signal that was monitored by using high-voltage probe.
The distance between the SDBD and the sample holder was adjusted with rectangular spacers. In these experiments we have used distances of 2 mm and 4 mm. The sample holder stands on a grounded metal carrier. In the grounded line, voltage drop on a 15 kΩ resistor allowed monitoring of the total current in the discharge.

3. RESULTS AND DISCUSSION

The SDBD that was previously used in treatments of flour and artificial bone grafting material was characterized by using commercially available voltage probes. The dependence of the output RMS voltage, measured at the powered electrode, on the input voltage is shown in Fig. 1. We can see that the dependence is linear and it does not change significantly with the increase of the distance from the sample holder.

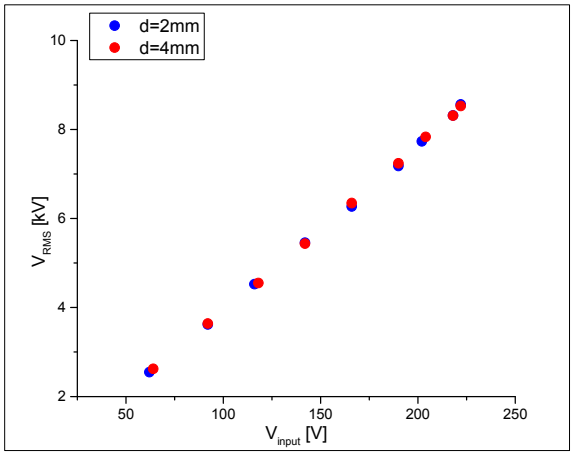

Figure 1. Dependence of the RMS voltage values on the input voltage. The distances were 2 mm and 4 mm and the discharge was operating in air.

On the other hand the voltage-current characteristics shows significant changes with the increase of the applied voltage (Fig.2). We can see that with the increase of the applied voltage at the powered electrode the current measured as the voltage drop in the grounded line is significantly increased.

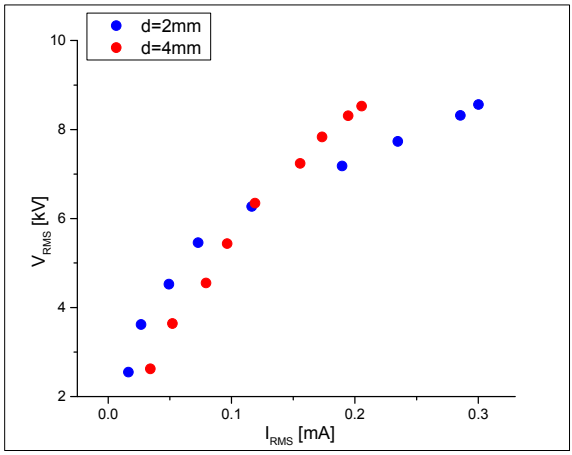

Figure 2. Voltage-Current characteristics of the SDBD. The distances were 2 mm and 4 mm and the discharge was operating in air.

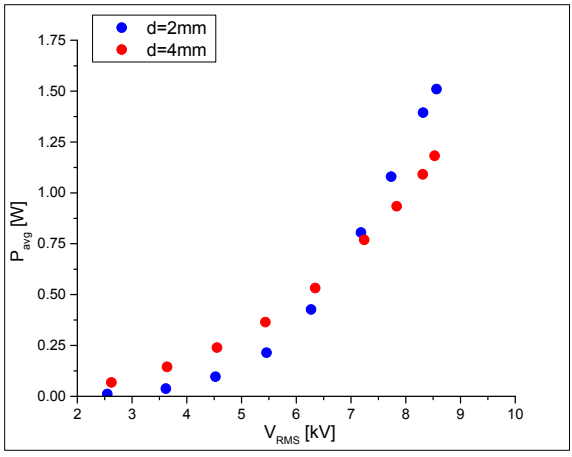

Figure 3. Power transmitted to the discharge as a function of the voltage at the powered electrode. The distances were 2 mm and 4 mm and the discharge was operating in air.

This increase is more pronounced in case of 2 mm electrode distance from the sample holder. This can be explained by the occurrence of the more streamer-type plasma channels and the increase of the current through the existing ones. In case of the 4 mm distance, this change is not that pronounced. In both cases we have drastic change in the complex impedance of the plasma system which can be observed through the changes in the slope of the V-I curves.

As expected, the similar change can be observed also in the power transmitted to the discharge shown in Fig.3. We can see that more power is transmitted to the plasma system in case of the electrode distance of 4 mm from the sample holder, but only for lower values of the RMS voltage. When the voltage crosses the 6.5 kV threshold the situation changes and more power is deposited when the distance is 2 mm. Again this can be connected with the development of more streamer discharges between the electrode and the sample holder together with higher currents flowing through already formed ones.

4. CONCLUSION

In this paper we have presented the results of the electrical characterization of the SDBD that operates in air. This plasma system is designed for treatments of granular materials. We have measured current and voltage waveforms in order to determine V-I characteristics and power deposited in the plasma. Experiments were performed for two distances between the SDBD and the sample holder. It was shown that for the smaller distance of 2 mm and for the higher values of the applied voltage we have more power deposited to the discharge than in the case of 4 mm distance. The streamer channels in this case have higher values of conduction current. This is also reflected on the complex impedance of the system that changes drastically with the increasing applied voltage.

Acknowledgements

This research is supported by the Serbian Ministry of Education, Science and Technological Development under project numbers ON171037 and III41011.

REFERENCES

[1] K. D. Weltmann, E. Kindel, T. von Woedtke, M. Hähnel, M. Stieber and R. Brandenburg, Pure Appl. Chem. 82, 1223–37 (2010).
[2] N. Puac, M. Gherardi, M. Shiratani, Plasma Proc. Polym. 15, 2 (2018).

INFLUENCE OF PLASMA AND RADIO-WAVE TREATMENT OF SEEDS ON THE ACCUMULATION OF SOME SECONDARY METABOLITES IN PLANTS

I. I. Filatova[1], V. A. Lyushkevich[1], J. N. Kalatskaja[2], S. V. Goncharik[1], V. Mildaziene[3], G. Pauzaite[3]

[1] *B.I. Stepanov Institute of Physics of the National Academy of Sciences of Belarus, 220072, Minsk, Nezavisimosti Ave., 68-2, Belarus*
[2] *V. F. Kuprevich Institute of Experimental Botany of the National Academy of Sciences of Belarus, 220072 Minsk, Academicheskaya Str., 27, Belarus*
[3] *Vytautas Magnus University, LT-44404 Kaunas, Vileikos str. 8, Lithuania*

Abstract. The effect of plasma and radio-wave treatment of seeds on the secondary metabolite content in plants is reported. The amount of anthocyanins in maize seedlings was increased up to 2.1-fold in roots, and up to 1.3 fold in leaves. Seed treatment with physical factors induces significant changes in pharmaceutically important secondary metabolite content in medicinal plant. The amount of the phenolic compounds in inflorescences of *Calendula officinalis* was increased up to 2-fold after electromagnetic field treatment, and by 2.5-fold as a result of plasma treatment.

1. INTRODUCTION

Application of cold plasma techniques in agriculture possess many advantages in particular for seed processing, owing to non-thermal, short-duration processing, without inducing damage to seeds, crops, and the environment. We showed earlier, that treatment of seeds with physical factors (electromagnetic fields or cold plasma) contributes to the increase of yield and the increase in the ecological value of agricultural products [1], causes stable changes in metabolic processes at subsequent stages, allows increasing the biomass of seedlings of perennial tree cultures [2] and the content of some secondary metabolites in plant [3]. The use of different seed treatments to improve plant performance is based on the fact that seed response to stress mobilizes the molecular mechanisms that can improve plant performance and enhance survival under stressful conditions. As it was shown microwave seed pretreatment can enhance tolerance of wheat seedlings to $CdCl_2$ stress [4] or plasma treatment can increases the ability of plants to cope with biotic and abiotic stress, such as drought and disease [5, 6].

It should be noted that the change in the content of a number of secondary metabolites in plant cells is one of the strategies of metabolic adaptation to the action of stress factors of different nature. In particular biosynthesis of anthocyanin is stimulated by diverse developmental signals and environmental stresses including drought, wounding, pathogen infection and insect attack. Plant hormones such as jasmonates, a stress-related plant hormone, also induce accumulation of anthocyanins [7, 8].

In this paper, we investigated the effect of pre-sowing plasma and radio-wave treatments of seeds on the accumulation of secondary metabolites in maize (*Zea mays* L.) one the most important grain crop and calendula (*Calendula officinalis* L.) widely cultivated due to its medicinal uses.

2. EXPERIMENTAL

Plasma treatment was carried out in a planar geometry capacitively coupled 5.28 MHz plasma reactor consisting of two plane-parallel electrodes placed in a vacuum chamber. All treatments were performed in air at a pressure of 200 Pa. The power density was not more than 0.45 W/cm^3. The duration of plasma exposure was 2 – 7 min. The following experimental conditions were used for seed treatment by radio frequency electromagnetic field (EMF): alternator frequency, 5.28 MHz; root-mean-square value of magnetic H and electric E components of EMF strength, 590 A/m (B ≈ 0.74 mT) and 12.7 kV/m, respectively; amplitude values H* = 2H and E* = 2E of 835 A/m (B ≈ 1 mT) and 17.96 kV/m, respectively. Seeds were exposed to the EMF for 5, 10, 15 and 25 min at atmospheric pressure and room temperature.

Content of anthocyanins in roots and in leaves of maize seedlings was determined using spectrophotometric method [9] with some modifications. Investigated samples (0.5 g of fresh leaves or roots) were grounded in a mortar in 5 ml 1% HCl and the homogenates were kept in a water bath at 40-45 ° C for 20 minutes. The anthocyanin content (μg/g dry weight) was measured using the formula A510-A657 subtracting the absorption of chlorophyll. Samples of inflorescences of *Calendula officinalis* was extracted several times using 70% ethanol. The resulting extract was then used to determine the total fraction of phenols and flavonoids using spectrophotometric method.

3. RESULTS AND DISCUSSIONS

It was shown that the treatment of seeds with cold plasma and electromagnetic field changed the content of anthocyanins in roots and in leaves of maize (Fig. 1). The amount of anthocyanins in plant of maize was increased up to 2.1-fold in roots, and up to 1.3 fold in leaves in dependence on treatment conditions.

The treatments caused changes in the coordination of shoot and root development, which was manifested in a change in the ratio of shoot/ root length. It was found that the slowdown of root growth and on the contrary the activation

of shoot growth is accompanied by an increase in the content of anthocyanins in these organs (Table 1).

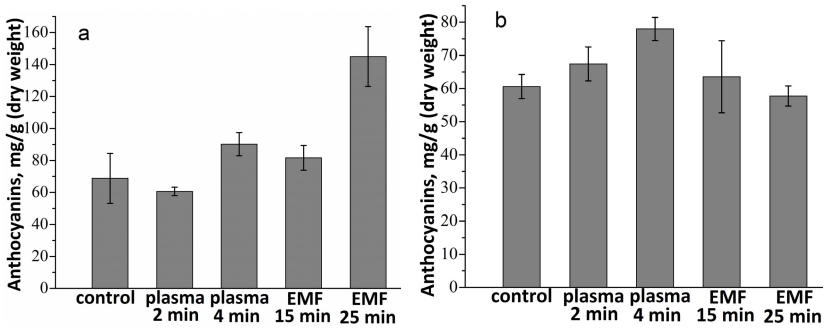

Figure 1. The average amount of anthocyanins in roots (a) and in leaves (b) of 7-day maize seedlings under various conditions of plasma and EMF treatments

Table 1. Germination and morphological parameters of maize seedlings

	Control	Plasma 2 min	Plasma 4 min	EMF 15 min	EMF 25 min
Germination (%)	95.8±2.1	100	97.9±1.0	95.8±1.2	97.9±1.7
Root length(cm±SEm)	12.8±0.14	12.7±0.17	11.5±0.16*	12.3±0.17	11.5±0.26*
Shoot length (cm±SEm)	7.2±0.17	8.1±0.20*	8.3±0.16*	8.4±0.19*	7.6±0.18

In case of medicinal plant, the results also indicate substantial changes in the amount of number of secondary metabolites. It was shown that the treatment of seeds enhanced the content of phenolic compounds (including flavonoid and ascorbic acid) in the inflorescences of calendula (Fig. 2).

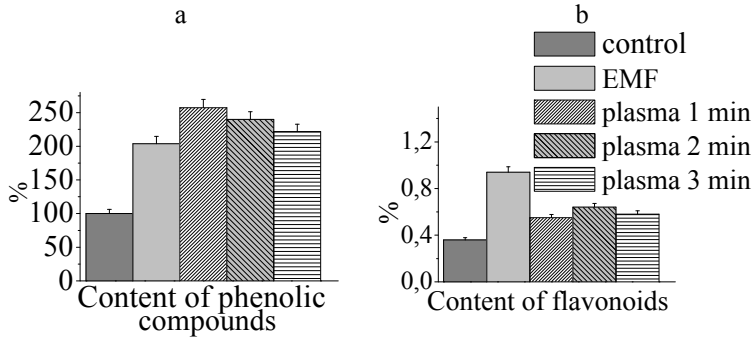

Figure 2. Accumulation of phenolic compounds (a) and flavonoids (b) in inflorescences of *Calendula officinalis* in dependence on treatment conditions

The amount of the main secondary metabolite of *Calendula officinalis* – phenolic compounds per plant was increased up to 2-fold after 10 min EMF treatment, and by 2.5-fold as a result of plasma treatment during 1 min.

So, pre-sowing seed treatment with physical stressors induces not only changes in germination and plant growth but also contributes to an increase in content of biologically active constituents in plants.

4. CONCLUSION

It is shown that plasma and radio-wave treatment of seeds acts as a stress factor that changes the plant metabolism and leads to the increase of level of secondary metabolites in plants. Thus the physical stressors might be regarded as a potential tool for the controllable modulation of plant properties.

Acknowledgements

This work is partly supported by the Belarusian Republican Foundation for Fundamental Research under the grant No Б16РА-014 and the State scientific research program «Konvergencija-2020 2.4.02».

REFERENCES

[1] Filatova I.I., Azharonok V.V., Goncharik S.V., Lyushkevich V.A., Zhukovsky A.G., Gadzhieva G.I. J. Appl. Spectrosc. 81, 250–256 (2014).
[2] Mildaziene V., Pauzaite G., Malakauskiene A., Zukiene R., Nauciene Z., Filatova I., Azharonok V., Lyushkevich V. Bioelectromagnetics. 37, 536 – 548 (2016).
[3] Mildaziene V, Pauzaite G, Naucienė Z, Malakauskiene A, Zukiene R, Januskaitiene I, Jakštas V, Ivanauskas L, Filatova I, Lyushkevich V. Plasma Process Polym. 15, e1700059 (2017).
[4] Qiu Z., Zhang J. Li, Y., Bi Z., and Wei H. Ecotoxicology and Environmental Safety. 74(4), 820–825 (2011).
[5] Huang M. J. J. Shanxi Agri. Sci. 38, 22 – 25 (2010).
[6] Jiang J. F. [et. al.] Plos one. 9, 1 – 6 (2014).
[7] Nakata, M. and Ohme-Takagi, M. Bio-protocol. 4(7), e1098 (2014).
[8] Loreti E., Povero G. et al. New Phytologist. 179 (4), 1004–1016 (2008).
[9] Mancinelli A.L. Plant Physiology. 92, 1191–1195 (1990).

NEXT GENERATION OF UNIVERSAL PULSE RESONANCE ATMOSPHERIC PLASMA SYSTEMS

Miroslav Gulan, Laurence Scally, Patrick J. Cullen, Vladimir Milosavljević

BioPlasma Research group, School of Food Sciences and Environmental Health, Dublin Institute of Technology, Ireland

Abstract. In this paper, a new configurable atmospheric plasma system that runs at pulse resonance mode with pin electrodes is presented. The plasma source is based on a pulse resonance circuit which allow create high voltage pulses with ability to control and reduce a current of the plasma discharge. This plasma system can generate a stable non-equilibrium plasma between metal electrodes without dielectric barrier-material. This configuration of plasma system can create a reproducible plasma in volume of thousands cm^3, with a changeable gap between electrodes in range of 5-65 mm. Ability to control this plasma discharge, it allows to keep a temperature of the treated sample's (organic or inorganic) material at the room temperature.

1. INTRODUCTION

In last several decades, in many papers, impact of the plasma technologies to a surface structure and functionality are studied [1, 2]. In most cases the plasma systems were operated at a low pressure (i.e. vacuum) and they are used for treatment of inorganic materials [3]. These systems were not suitable for temperature sensitive materials as organic materials. In recent years, atmospheric plasma systems based on technology known as plasma jet or microwave plasma have been used [4]. These plasma systems at atmospheric pressure, are frequently using for biological treatments. The main disadvantage of all those systems is, they are able to create only small (local) atmospheric plasma discharge. Therefore, unavailability of such plasma systems to generate atmospheric plasma discharge in volume of thousands cm^3 makes a big obstacle for those systems to be used in food industry.

A new pulse resonance atmospheric plasma systems were designed and manufactured to increase possibility of study of plasma treatment impact on sensitive organic and inorganic materials.

2. EXPERIMENTAL SETUP

A special new design of pulsing plasma power generator allows setting parameters of plasma which help to tune requested plasma treatment applying to different materials. Our plasma system allows to increase the surface-plasma interaction selectivity and to reduce plasma induced damages to the surface. The plasma system is based on pulse resonance circuit which allows reaching high voltage on electrodes and reducing current via plasma to keep temperature low.

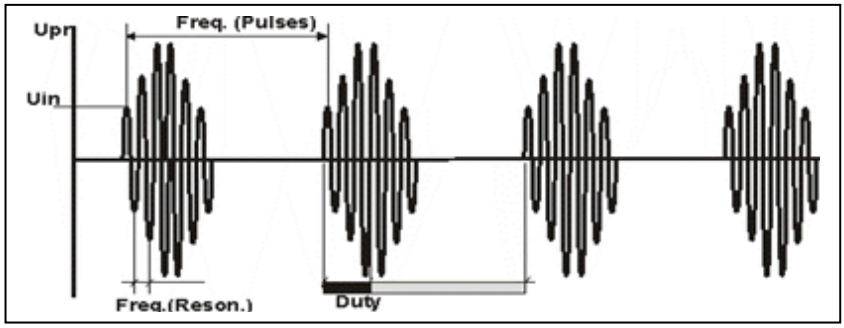

Figure 1. Pulse resonance pulses.

All parameters showed on Fig.1 can be changed. Namely, resonance frequency (Freq.(Reson.)) can be set from 30 kHz to 125 kHz and depend on configuration of the HV transformer and plasma electrodes. Correct setting of resonance frequency increase output voltage of HV transformer. Pulse frequency (Freq.(Pulses)) can be set from 100 Hz to 3000 Hz, and increasing this frequency would lead to increase the power of plasma discharge. Duty cycle influences current-power of each discharge. Input voltage is set following dielectric barrier between electrodes. Output power of system depends on the configuration of all mentioned parameters and can be set from 30W to 700W.

Figure 2. Plasma power supply unit.

The plasma generator (Fig.2) is designed to operate with the customize pin electrode such serves as a HV electrode, and ambient air such serves as a dielectric barrier. No additional dielectric material is required. This pin electrode

is used together with flat electrode which is connected to ground. This configuration of electrodes allow to reach gap up to 70 mm between the flat electrode and the pins. Output voltage can go up to 80kVpp (depends on the air gap). On Fig.3 the parallel plate electrodes configuration is presented.

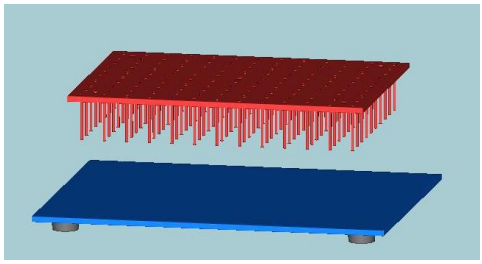

Figure 3. Pin electrodes

In Fig.4 is shown plasma discharge with the maximum gap between electrodes. This plasma generator is used to study influence of plasma treatment on organic materials and to find the optimum plasma parameters which would give the best performance of those biological samples at the minimal plasma power (W/cm^2). With increasing the plasma power over a threshold point for the bio-surface activation, the plasma effectiveness stagnate or decrease.

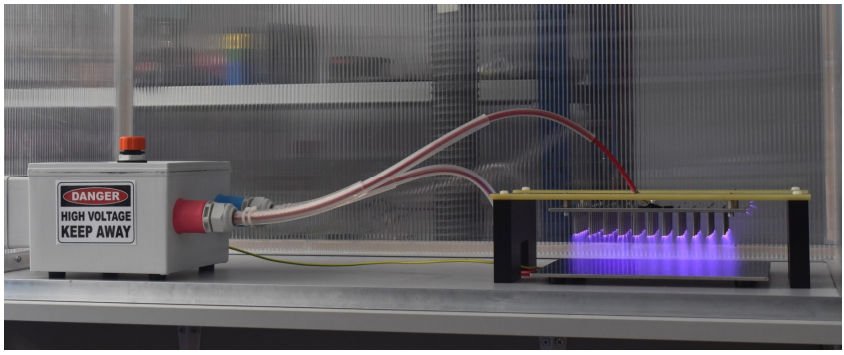

Figure 4. HV Transformer and electrodes with plasma discharge

3. RESULTS AND DISCCUSION

Measured dependence output voltage (peak to peak) in kV and air gap in mm between pin and flat electrode is showed on Fig 5.

The curve is almost linear and postpone by 10kV. Start point at 14,5kV@5mm and end point 80kV @70mm.

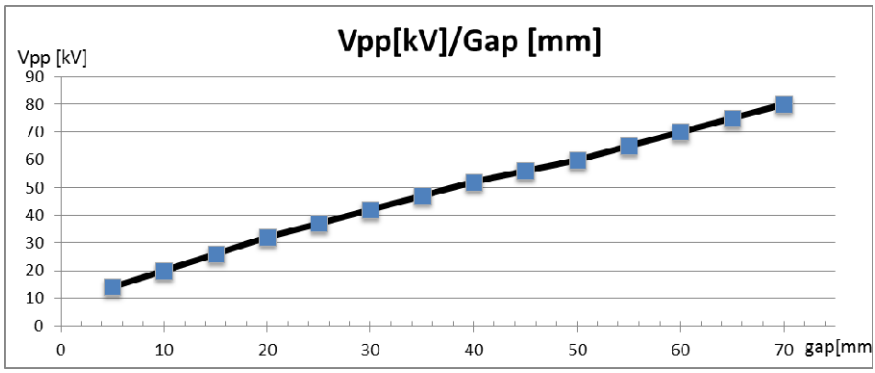

Figure 5. Output peak to peak voltage in kV and air gap in mm

4. CONCLUSIONS

The new pulse resonance plasma system, with pins electrode, allows much greater gap between electrodes, and give a possibility to be applied in food industry. Moreover, dielectric material necessary for today's DBD technology, is not required for this system. Therefore there are not issues with sterilization or decontamination of our plasma tool, on the contrary to systems which have thermally and chemical unusable dielectric (e.g. DBD).

Acknowledgements

This work was funded by the Irish Department of Agriculture, Food and the Marine, Ireland, under the Food Institutional Research Measure (FIRM) initiative (InnoFresh project - Innovative process technologies for the fresh produce industry; reference number 13F444).

REFERENCES

[1] J. Park, I. Henins, H. W. Herrmann, G. S. Selwyn, J. Y. Jeong, R. F. Hicks, D. Shim, and C. S. Chang, Appl. Phys. Lett. 76, 288 (2000).
[2] H. M. Abourayana, V. Milosavljević, P. Dobbyn, P. J. Cullen, and D. P. Dowling, Surf. Coat. Tech. 308, 435 (2016).
[3] V. Milosavljević, and P. J. Cullen, European Phys. Lett. 110, 43001 (2015).
[4] P. J. Cullen, and V. Milosavljević, Prog. Theor. Exp. Phys. 2015, 063J01 (2015).

PLASMA DECONTAMINATION OF WATER POLLUTED BY PESTICIDES FOR APPLICATION IN AGRICULTURE

Olivera Jovanović[1], Nikola Škoro[1], Nevena Puač[1] and Zoran Lj. Petrović[1,2]

[1]*Institute of Physics, University of Belgrade, Pregrevica 118, 11080 Belgrade, Serbia*
[2]*Serbian Academy of Sciences and Arts, Knez Mihailova 35, 11000 Belgrade, Serbia*

Abstract. In this work we present a method for purifying water contaminated with pesticides for further application in agriculture. For this purpose, a needle-type atmospheric pressure plasma jet (APPJ) was used, with electrode powered by a high voltage signal at frequency 330 kHz. We have used He as working gas with flow rate 2 slm. The solution of pesticide Malathion in distilled water was treated as contaminated sample. Then, the samples were used for seed imbibition. The results have shown that the plasma decontaminated water treatments had an effect on increasing the germination of maize and radish seeds.

1. INTRODUCTION

The development of plasma methods for decontamination of polluted water is caused by scarcity of freshwater. Organic compounds and microorganisms are the most common water pollutants that get into fresh water by discharging wastewater into aquatic ecosystem [1].

Plasma chemistry is rich in strongly oxidative reagents (OH, O, O_3) that can diffuse into polluted water and initiate chemical reactions such as the conversation of organic compounds in solution into water and carbon dioxide [2, 3].

In this paper we used a pin-electrode atmospheric pressure plasma jet (APPJ) for decontamination of water polluted by Malathion pesticide. After treatments we monitored germination of the seeds imbibed with the decontaminated water samples. Obtained germination percentages were compared with germination results of the control groups of seeds that were imbibed with distilled water or 500 ppm solution of Malathion.

2. EXPERIMENTAL SETUP

The Fig. 1 shows a schematic diagram of the experimental setup. Plasma source was an atmosphere pressure plasma jet which consists of a metal cylindrical body, glass tube, with the inner and outer diameters of 4 mm and 6 mm, respectively, and concentrically placed electrode with ceramic insulation. The electrode was made of stainless steel wire with the diameter of 1 mm. The end of the wire (powered electrode) is sharpened and it is protruding for 3 mm from the ceramic insulation into the glass tube. As power source we have used a commercial high voltage RF generator working at frequency of 330 kHz. In all experiments He was used as a working gas with flow rate of 2 slm.

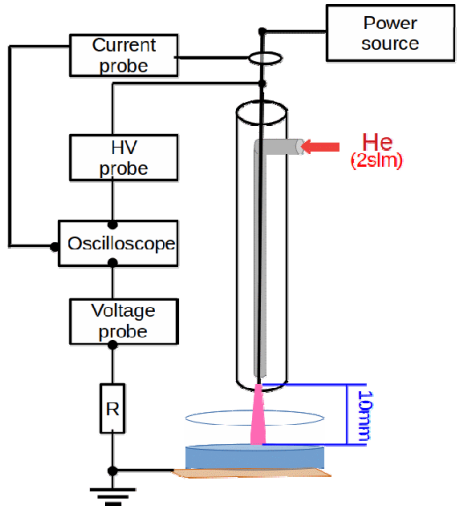

Figure 1. Schematic overview of the experimental set up.

The samples containing Malathion were treated in the wells of 6-well microtiter plate. The volume of treated solution of Malathion in the well was 4 ml and initial concentration was 500 ppm in distilled water. Treatment times were 5 and 10 minutes. At the bottom of the micro titter plate we glued copper tape that was connected to the ground through a 1 kΩ resistance. The distance between the surface of the liquid in the plate and wire was 10 mm.

3. RESULTS AND DISCUSSION

Treated solutions as well as distilled water and Malathion contaminated solution were used for the imbibition of maize and radish seeds in Petri dishes, with 12 and 40 seeds, respectively in each dish. The seeds were imbibed with 2 ml of liquid per Petri dish (5 cm in diameter). The dishes with the seeds were

left in a room with constant temperature and with day-night cycle. All experiments were done in triplicate.

For the control samples, we used seeds imbibed with distilled water and solution of Malathion (500ppm). Histogram shown in Fig. 2 presents mean value of germinated maize seeds four days after imbibition. Comparison between control groups showed that number of germinated seeds imbibed with distilled water is more than twice higher than number of seeds germinated after imbibition by Malathion solution. As for the seeds imbibed with plasma decontaminated water, we can see the positive effect of plasma treatment of water polluted by Malathion. The number of germinated seeds watered with the solutions treated for 5 minutes and 10 minutes is higher 1.5 times than in the untreated Malathion solution. Mean values in both sets of seeds imbibed with decontaminated water are the same (around the value 5) within the error bar. Nevertheless, it is still lower than the control group imbibed with distilled water where the mean value is 7.3.

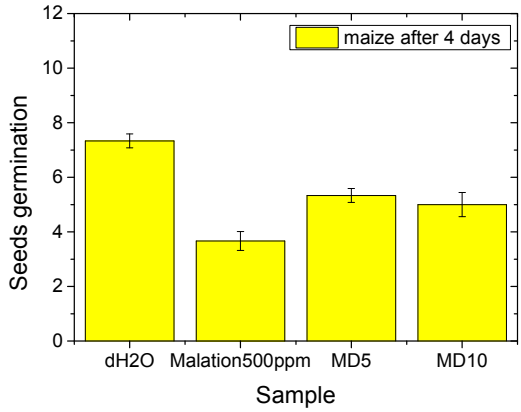

Figure 2. Mean values of maize seeds germinated after 4 days of imbibition with different water samples. dH_2O – distilled water, distilled water contaminated with 500 ppm Malathion, MD5 – contaminated water treated 5 minutes, MD10 – contaminated water treated 10 minutes.

Similar results are obtained in the case of germination of radish seeds. Fig. 3 shows mean values of germinated radish seeds 18 hours after imbibition. In this case, values in control groups with H_2O and 500ppm Malathion have difference of 1.75 times. However, the results on plasma treated samples show that in this case duration of treatment of water polluted by Malathion significantly affects germination. While the set imbibed with solution treated for 5 mins is almost the same as the Malathion sample (mean value around 15.5), the sample treated for 10 mins has the value which is 1.5 times higher.

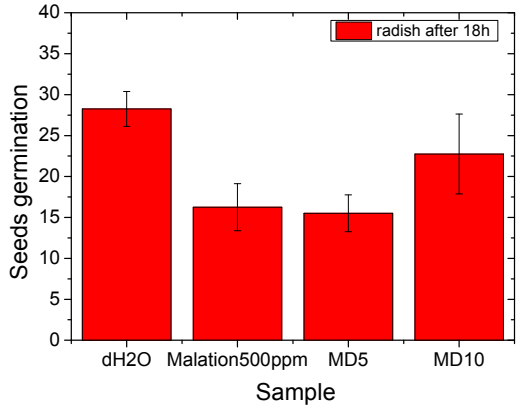

Figure 3. Mean values of radish seeds germinated after 18 hours of imbibition with different water samples. dH_2O – distilled water, distilled water contaminated with 500 ppm Malathion, MD5 – contaminated water treated 5 minutes, MD10 – contaminated water treated 10 minutes.

4. CONCLUSION

Results of germination of seeds imbibed with plasma decontaminated water showed increase in number of germinated seeds compared to the case of seed imbibition with Malathion polluted water. This proves that plasma treatments can purify water and cause decomposition of pollutant molecules to the extent suitable for the plasma treated water to be reused for plant cultivation. However, in order to achieve efficient process, one need to investigate decomposition mechanisms triggered by plasma treatment and the influence of treated solution on seed physiological processes.

Acknowledgements

This research is supported by the Serbian Ministry of Education, Science and Technological Development under project numbers ON171037 and III41011.

REFERENCES

[1] J. T. Korus and M. E. Burbach, Great Plains Res. 19, 187 (2009).
[2] J. E. Foster, Phys. of Plasmas 24, 055501 (2017).
[3] B. Jiang, J. Zheng, S. Qiu, M. Wu, Q. Zhang, Z. Yan, Q. Xue, Chem. Eng. J. 236, 348 (2014).

THE USE OF AN AIR PLASMA JET FOR TREATMENT OF PURULENT WOUNDS

A. V. Kazak[1], O. A. Emeliyanova[2], L. V. Simonchik[1] and N. V. Dudchick[2]

[1]*Institute of Physics of NAS of Belarus, Minsk, Belarus*
[2]*Republican unitary enterprise Scientific Practical Centre of Hygiene, Minsk, Belarus*

Abstract. The DC atmospheric pressure air plasma jet is realized. The bactericidal components in plasma jet are detected using infrared absorption spectroscopy. Main bioactive components for air plasma jet are RONSs. Inactivated effect at a treatment *of S.aureus* biofilm by air plasma jet is investigated. The results of treatment of purulent wounds in animal model are presented.

1. INTRODUCTION

Among a variety of low-temperature plasma sources promising for biomedical applications are developed [1]. A basic requirement for non-destructive medical applications is to provide "cold" plasma source at atmospheric pressure, wherein the gas temperature does not exceed 45 °C. Special attention is focused on the development and application of plasma jets [2] due to the possibility to treat objects of complex shapes and sizes outside a closed discharge volume. In addition, despite the extensive research and an abundance of papers the mechanisms of plasma jets action on microorganisms remain poorly understood up to now. In almost all articles about plasma medicine the accent is made on the bactericidal action of RONSs (e.g., NO, O_3, OH, H_2O_2, etc.) generated by the plasma jets [3].

2. EXPERIMENTAL SETUP

The cold plasma jet (Fig. 1) is formed by direct current glow discharge [4] in air at atmospheric pressure. The discharge chamber is composed of cylindrical 8 mm quartz tube inside of which a rod copper cathode of 6 mm in diameter is coaxially disposed. Flat copper anode (4 mm in thickness) with a central hole (1.5 mm in diameter) is located at the tube tip. Interelectrode gap is fixed at 0.7 mm. Discharge is maintained by DC or ripple current power supply with an output voltage up to 3 kV. A ballast resistor can be varied in the range of 1–300 kΩ. Air flow of 5 l/min into discharge chamber is provided through symmetrically arranged holes in cathode. Plasma generated in the discharge is

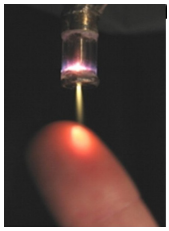

Figure1. Photo of chamber and atmospheric pressure plasma jet in air.

blown out with the gas through anode hole into surrounding air. As a result, a glow of plasma jet of 2-3 mm in diameter and several centimeters in length is observed [5].

Determination of the concentration of long-living chemically active species in the plasma jet is performed by IR absorption spectroscopy. In the absorption spectra of air jet, NO, NO_2, $HNO_2$and N_2O bands are observed. Molar fractions of these active species at the zone of the jet impact on the bacteria are 40 ppm, 20 ppm, 10 ppm and 2 ppm, correspondingly.

The suspension of microorganisms with an initial concentration of 10^9•CFU/ml is deposited uniformly onto the surface of a dense undifferentiated nutrient medium at the inactivation of bacteria in Petri dishes. Temperature of the plasma jet in the bacteria exposure zone did not exceed 30°C. Inactivation ability is determined by colony counting method. The identity of bacteria growth on untreated and pretreated agar plates by plasma jet allows us to state that inactivation occurs due plasma impact on the cells and not due to changes in nutrient medium properties.

3. RESULTS & DISCUSSION

3.1. Experiments IN VITRO

In order to carry out *in vitro* experiments, strains were applied to the surface of Petri dishes, or to the center of slide glasses with initial concentration 10^9 CFU/ml.

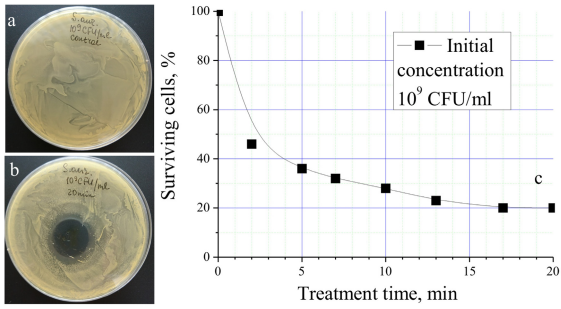

Figure 2. Photographs of treated Petri dishes with an microorganisms initial concentration of 10^9 CFU/ml (a – control, b- after 20 min treatment) and microorganism inactivation curves (c).

Prepared samples are located 4 cm from the nozzle of the plasma jet, where they are processed for 2, 5, 7, 10, 13, 17, 20 minutes. The inactivation

efficiency of the device was qualitatively estimated by inhibition zones and quantitatively by the concentrations of surviving microorganisms (Fig.2).

Previously, it was shown that for the strain of *Staphylococcus aureus* the D-times inactivation are about 2 minutes. At a concentration of 10^9 CFU/ml, the inactivation time increases to 4 minutes, this is due to the formation of a biofilm rather than a monolayer, as shown in [6].

3.2. Experiments IN VIVO

In the study of the sanifying and wound-healing effect of plasma jet *in vivo* experiment, a female rabbit of weighing 2,4 kg was used as a laboratory animal.

The animal was kept in a cage, fed on a standard ration of the vivarium, allowed to drink freely. The conditions for keeping the animal, handling it and conducting the experiment met the requirements of the Technical Regulations and were based on the international principles of bioethics in accordance with the requirements of the Geneva Convention on the Humane Treatment of Animals.

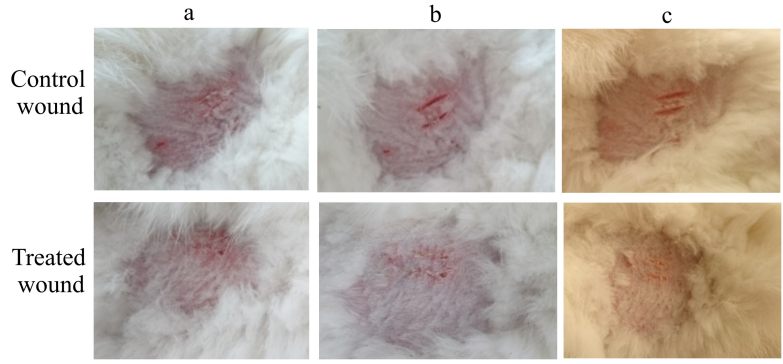

Figure 3. Photos of purulent wounds on the 4th (a), 6th (b) and 8th (c) day.

To form an infected wound on the scapula, we cut the skin in two incisions (3 cm in length) from each side. In each wound, 0.1 ml of a daily culture of *S. aureus* with a concentration of 10^9 CFU/ml was rubbed with a sterile spatula. From 2 to 4 days, visual inspection of wounds for the presence of edema, redness, purulent discharge of wounds was performed. On the 4th day, signs of the inflammatory process were revealed and the wound treatment on the right side was started by a plasma jet. The wounds on the left side were not treated and were negative control. From the 4th (Fig. 3,a) to the 9th day we were treatment with an air plasma jet at a distance of 4 cm to the surface of the skin, for 5 minutes.

After two treatment sessions for infected wounds, a noticeable decrease in their depth, hyperemia and edema of the surrounding tissues was observed compared with the negative control. Also, the beginning of regional epithelialization of wounds was noted. Purulence was practically absent, the wounds were dry, there was no pain (Fig. 3,b).

On day 8-9, the wounds on the treated side showed almost complete epithelialization and rejection of scabs formed on the surface. Control wounds healed on day 15. The treated wounds healed on the 9^{th} day. Thus, application of the device allows accelerating the process of wound healing in 2 times.

4. CONCLUSSIONS

The atmospheric pressure glow discharge air plasma jet at direct current was realized. The bactericidal components in plasma jet were detected by infrared absorption spectroscopy. It was shown that the main bactericidal components of plasma jet in air are: NO, NO_2, HNO_2 and N_2O.Axial distributions of the active components along of the plasma jet were determined.

Inactivated effect at a treatment of microorganism *S.aureus* by air plasma jet was investigated. It was demonstrated, that the biofilm *S.aureus* is more resistant to the plasma exposure than monolayer of microorganisms. For monolayer of *S. aureus* the characteristic D-times were around 2 min. In the meanwhile, D-time exceeded 4 min for the microorganism in biofilm.

In the model experiment on the animal, the possibility of treating purulent wounds with an air plasma jet was demonstrated. After two treatment sessions for infected wounds, a noticeable decrease in their depth, hyperemia and edema of the surrounding tissues was observed compared with the negative control. The treated wounds healed on the 9^{th} day (or 6^{th} day after the start of treatment). Control wounds healed on day 15 (or 12^{th} day after the start of treatment). Thus, application of the device allows accelerating the process of wound healing in 2 times.

Acknowledgements

This work is partially supported by BRFFR under the grants F17RM-050 and F17MS-030.

REFERENCES

[1] K. H. Schoenbach and K. Becker. Eur. Phys. J. D, 70: p. 29 (2016,)
[2] X. Lu, M. Laroussi and V. Puech. Plasma Sources Science Technology 21, 034005. (2012)
[3] X. Lu, G.V. Naidis, M. Laroussi, S. Reuter, D.B. Graves, K. Ostrikov, Physics Reports, 630: p. 1–84 (2016)
[4] V.I. Arkhipenko, A.A. Kirillov, Y.A. Safronau, L.V. Simonchik, S.M. Zgirouski. The European Physical Journal D, 66: 252. (2012)
[5] V.I. Arkhipenko, A.A. Kirillov, A.V. Paulava, L.V. Simonchik, N.V. Dudchik, M.M. Kuraica, B.M. Obradovirc. Proceedings of the National academy of sciences of Belarus, Physic and mathematics series, 3: p. 104-110 (2015).
[6] Kazak A.V., Kirillov A.A., Simonchik L.V., Nezhvinskaya O.E., Dudchik N.V. Plasma medicine. V. 7. № 2.P. 109 – 115 (2017)

A STUDY OF EXCITED OXYGEN SPECIES IN THE MULTI JETS NON-THERMAL ATMOSPHERIC PLASMA SYSTEM

James Lalor[1], Laurence Scally[1], Patrick J. Cullen[1] and Vladimir Milosavljević[1,2]

[1]*BioPlasma Research Group, Dublin Institute of Technology, Dublin, Ireland*
[2]*Faculty of Physics, University of Belgrade, P.O.B. 368, Belgrade 11000, Serbia*

Abstract. This work presents the development and operation of a 12 jet non-thermal atmospheric plasma system. The study is based on an absorption and emission optical spectroscopies. Densities of OH, O I, O_2 and O_3 are studied with respect to treatment time, distance, duty cycle and discharge frequency. The bulk of the chemical reactions for the 12-jet system occurs in the surrounding atmosphere and not in the jet nozzle, which is different from most other plasma jet systems.

1. INTRUDUCTION

Atmospheric pressure plasma jets (APPJs) can be configured to offer a non-thermal, resourceful plasma treatment [1]. Today these plasma sources have been used for multiple applications, including surface modification [2]. They can be generated using relatively simple designs and the associated low gas kinetic temperature properties are of particular interest to thermally sensitive surfaces including those found in biology and medicine.

APPJs have seen many applications employing single jet configurations, complex challenges associated with multi-jet arrays exist. Firstly, the supply gas and power to operate several APPJs requires a distribution network designed to deliver uniform parameters [3]. Secondly, when individual jets operate cooperatively, through individual ballasting and tailoring of the power supply and the gas flow, they do so in a localized manner with each jet coupling separately to downstream substrates [3-5] is given here. APPJs have ability to produce reactive species. In order to increase the effects and to control the production of reactive species, an understanding of the interaction between the plasma, the selected gas chemistry, and the gas flow is of major importance as well as the influence of ambient air to overall plasma chemistry [4].

Due to the low ionization energy required for ambient air species, gases such as helium or argon are used extensively as carrier gases to generate plasmas. However, these combinations are capable of producing reactive oxygen and nitrogen species. The nature, quantity and role of the plasma species generated

depends on the type of plasma device used and the carrier gas composition. The plasma radicals studied in this work are: O I (transition 3p-3s), O_2 (Atmospheric band), O_3 (Hartley band) and OH (UV band).

2. EXPERIMENTAL SETUP

A schematic diagram of the experimental apparatus is shown in Fig. 1.

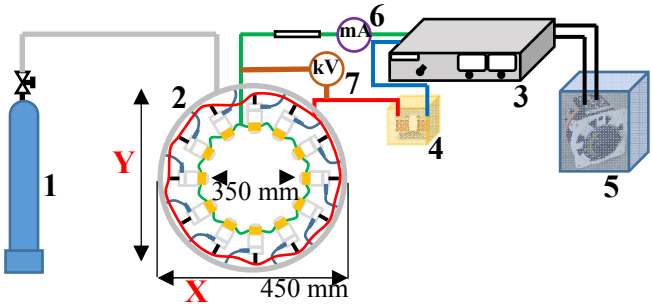

Figure 1. The set–up used in this experimental campaign. Where 1 is gas cylinders, 2 is the 12 jet circular system, 3 is the power generator, 4 is the high voltage (HV) transformer, 5 is the variac, 6 is the current probe and 7 is the voltage probe.

The customized power source (3) has a power of 2 kW, a high frequency power driver from 20 kHz to 100 kHz, a peak to peak voltage up to 40 kV (load dependent) and a duty cycle control from 10% to 90% (this control has an impact on the Q factor, with the Q values increase an energy loss decreases). The customized oil filled transformer is tailor-made for the particular range of output (load) capacities (10 pF - 20 nF). The variac is used for input voltage control.

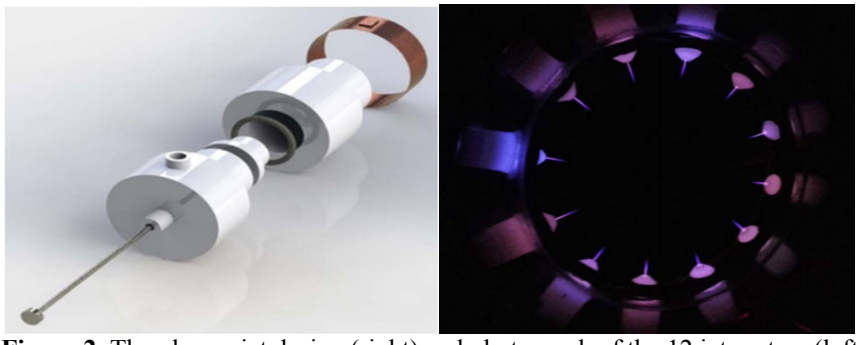

Figure 2. The plasma jet design (right) and photograph of the 12 jet system (left)

The plasma jet design (12 in-house made jets) is shown in Fig. 2. The central HV electrode is a pin and the ground electrode has a ring shape. It composes of concentric cylindrical elements. The assembled unit exists within a cylindrical

space of length 100 mm and diameter 45mm. The following are the instruments used for optical spectroscopy in this work: Edmund Optics UV-VIS Enhanced Smart CCD Spectrometer, Andor iStar 334T the 3rd generation ICCD and B&W Tek light source BDS130A (Deuterium /Tungsten Light Source). The optical techniques are based on the integration of measured signals over a line-of-sight observation. Experiments were carried out to investigate species' spectral intensities with the varying 7 external parameters (factors). The processing time, i.e. the time sequence of the recorded spectrum, was every 10 seconds for a duration of 3 minutes (plasma ON), and additional 1.5 minutes at plasma OFF (only for absorption spectroscopy). Analyzing the light emitted by neutrals, ionized atoms, radicals, and/or molecules is possible by emission spectroscopy.

3. RESULTS AND DICUSSION

Fig. 2 shows a large multi-jet array designed for continuous treatment of products by employing a conveyor belt and a surrounding tube (tunnel) to help retain the reactive species [5]. A comprehensive, four dimensional (x, y, z, t), optical diagnostic has been employed in order to study any temporal and spatial shift in radical concentrations. In the plain surface (with the 12-jets), it is important to have homogeneity of the radicals' concentration in time and space, which means the concentration is isotropic around every point.

For plasma-biological applications, oxygen is generally identified the most important of the atmospheric plasma species. This work includes optical absorption (OAS) results for the 12-jet and the single jet systems, representing both plasma on and plasma off time. OAS data correction involves a beam splitter which create a separate reference optical signal. The OAS signal recorded by the spectrometer was used to determine the molecular oxygen densities, based on the Lambert-Beer law [5].

At the short distance from the nozzle(s), O_3 concentrations show similar values (Fig. 3, 5mm). After the power source is turned off, the difference in O_3 concentrations at 5 mm could be observed. That difference is more significant for the ring jet configuration than a regular single jet system. Moreover, at a distance of 100 mm, the O_3 concentration is almost 10 times higher for the 12-jet system than the 1-jet system. For the plasma off time the O_3 concentration remains almost constant for the 12-jet system. Overall the results point to a stable O_3 concentration in both time and space for 12-jet plasma system.

Apart from ozone, O_2 plays an important role in the physical and chemical processes of plasma. The oxygen concentration is calculated from the intensity of the O_2 A-band (at 760nm). At 5 mm from the nozzle(s), there is a greater difference between O_2 concentrations between the 12-jet and 1-jet systems than observed for the ozone concentrations (Figure 3). This is due to the size of O_2 and O_3 molecules, and their associated absorption cross sections values. At 100 mm from the nozzle(s), the difference in O_2 concentration between the two systems is a factor of about 7, which remains relatively constant for an additional 150 s (plasma off time). O2 $b^1\Sigma^+_g$ is a metastable state with a low energy and long lifetime, therefore it can be populated from the ambient air molecules.

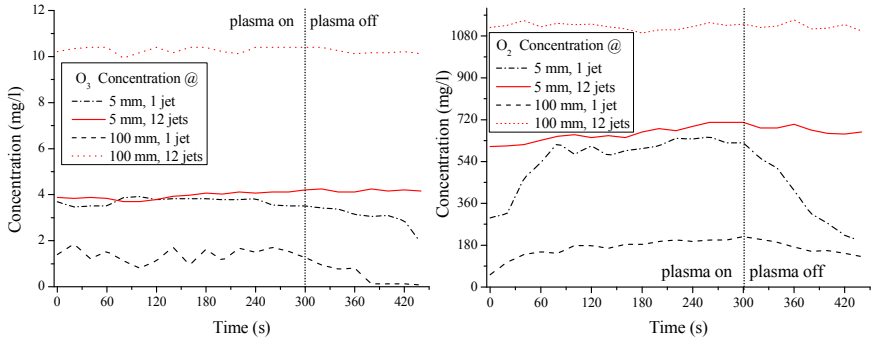

Figure 3. OAS measurement of O_3 (left) and O_2 (right) concentration in a pure argon plasma for the 12-jet system (red color) and 1-jet system (black color) as a function of processing time. Argon gas flow is 5 $Lmin^{-1}$, duty cycle is 70%, and U_{HV}=22.0 kV.

Atomic oxygen spectral emission is recorded by OES and has a higher intensity for argon than helium plasma due to a difference in the mechanisms of population of the ^5P oxygen state and the mismatch in energy of the excited argon and oxygen states [4] and helium and oxygen states [2].

4. CONCLUDIONS

The duration of plasma processing time and distance from the nozzles, for the 12-jet system is less significant than for other plasma jet systems.

Acknowledgements

This work was funded by the Irish Department of Agriculture, Food and the Marine, Ireland, under the Food Institutional Research Measure (FIRM) initiative (InnoFresh project - Innovative process technologies for the fresh produce industry; reference number 13F444). V. Milosavljević is grateful to the Ministry of Education and Science of the Republic of Serbia under Grant No. OI171006.

REFERENCES

[1] K. Inomata, N. Aoki, and H. Koinuma, Jpn. J. Appl. Phys. 33, L197 (1994).
[2] L. Scally, J. Lalor, P.J. Cullen, and V. Milosavljević, J. Vac. Sci. Technol. A 35, 03E105 (2017).
[3] Z. Cao, Q. Nie, D. L. Bayliss, J. L. Walsh, C. S. Ren, D. Z. Wang, and M. G. Kong, Plasma Sources Sci. Technol. 19, 025003 (2010).
[4] P.J. Cullen, and V. Milosavljević, Prog. Theor. Exp. Phys. 063J01 (2015).
[5] J. Lalor, L. Scally, P.J. Cullen & V. Milosavljević, J. Vac. Sci. Technol. A 36, 03E108 (2018).

PLASMA MODIFICATION OF ACOUSTICAL PROPERTIES OF TEXTILE FABRICS MADE OF NATURAL CELLULOSE FIBERS (COTTON, HEMP)

Sanja S. Pavlović[1], Vladimir M. Milosavljević[2, 3], Patrick J. Cullen[3], Snežana B. Stanković[4], Dušan M. Popović[2] and Goran B. Poparić[2]

[1]Belgrade Polytechnic, Brankova 17, 11000 Belgrade, Serbia
[2]University of Belgrade, Faculty of Physics, Studentski trg 12, P.O. Box 44, 11000 Belgrade, Serbia
[3]Bio-plasma Research group, Dublin Institute of Technology, Dublin 1, Ireland
[4]University of Belgrade, Faculty of Technology and Metallurgy, Textile Engineering Department, Karnegijeva 4, 11120 Belgrade, Serbia

Abstract. Cellulose is known as the most frequent used natural polymeric material. In the present work, acoustical properties of fabrics made from natural cellulose fibers (cotton, hemp) were modified in radio frequency (RF) argon plasma. A standard 13.56 MHz RF power supplier was employed. The power generator operated from 40 to 100 W. It has been observed that the sound absorption coefficient of the materials was increased due to the plasma treatment, especially at medium values of the applied power. Simultaneous with the treatments, the diagnostic of plasma conditions by optical emission spectroscopy and the adequate theoretical calculations on plasma parameters were performed in order to explain the plasma influence on the treated materials. The obtained results indicate that the plasma treatment could become an effective means for improving the sound absorption ability of cellulose materials.

1. INTRODUCTION

In recent years, plasma technology has been widely used as an effective method for surface modifications of textile fibers. Various plasma polymeric material modification technologies are based on plasma discharges in different gases. The most used gas is argon, which plays a very important role in a large number of applications for plasma modification [1, 2]. The argon atom is also very useful in plasma diagnostic due to sharp optical spectral lines in its optical spectrum. The plasma species can interact with solid phase substances, generating chemical, physical, and morphological changes in the uppermost portion of the exposed substrates [3]. An influence of plasma treatment to acoustical properties was expected due to the fact that it had been already observed for the polyester and jute fabrics [4].

2. EXPERIMENTAL SETUP

The method used for the modification of the cotton/hemp knitted fabrics was the plasma treatment in the RF capacitively coupled plasma (CCP) reactor filled by the argon gas. The plasma reactor was placed in the cylindrical 304 stainless steel chamber, and the center of the cylinder a copper electrode was placed. In order to control gas or gas mixture purity, a vacuum system equipped with gas mass flow controllers was used. The high voltage RF generator at standard 13.56 MHz frequency was applied for RF discharges. The argon gas was fed through mass flow controller at gas flow of 2 sccm. The pressure of the argon gas in the chamber was about 1 Torr and the maximal voltage was 1200 V peak to peak. The applied powers used during plasma discharges were in the range from 40 W to 100 W. The treated samples of materials were set in plasma reactor by using specially designed feedthrough connector and the treatments lasted for 20 minutes (this was an estimated optimum). In order to measure and control plasma conditions, the optical emission spectroscopy (OES) was employed. A high resolution optical spectrometer is used for OES at the wavelength range 300 - 1000 nm. The measurements of the sound absorption coefficient (SAC) of the examined materials were performed before and after plasma treatments. We used a standard two-microphone impedance tube which has been designed as per the ISO 10534-2:1998 standard (Acoustics-Determination of sound absorption coefficient and impedance in impedance tubes-Part 2: Transfer-function method). The diameter of the tube (29 mm) was set up for measuring SAC in the high frequency range (up to 5200 Hz).

3. RESULT AND DISCUSION

The SAC spectra, in the frequency range from 0 Hz to 5200 Hz, for both untreated and the plasma treated sample are presented in Fig 1. As can be seen from Fig 1, there is an increase of SAC of the treated material almost in the whole frequency range. We have found that the maximal effect of increase can be obtained for medium values of applied power on the RF plasma source.

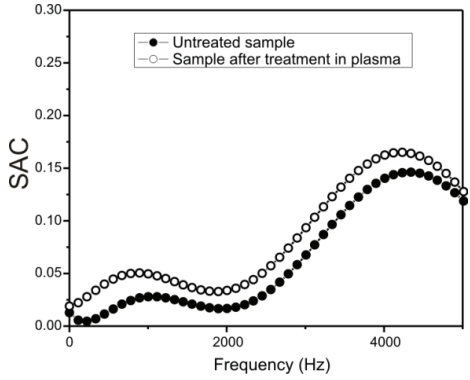

Figure 1. Sound absorption coefficients of the representative sample of treated materials.

We excluded the thermal effects as a reason of the modification of materials because the increase in temperature of samples during plasma exposition was less than 25 ^{o}C. The main processes which are responsible for the plasma polymeric material modification in inert gases are the interaction of free

electrons, and active species in an inert gas (ions, excited and metastable atoms) with polymer molecules [5]. These processes lead to bond-breaking of the polymer molecules in fibers of treated materials and making free radical parts in polymer chains. Free electrons in the argon plasma can perform such bond-breaking, especially at higher energies, due to an increase of cross sections for the processes which can break carbon-hydrogen, carbon-oxygen and carbon-carbon bonds. The second mechanism which leads to polymer modification is induced by ion bombardment of the treated materials by ions generated in the argon plasma. Beside the ions, the excited argon atoms also can take place in plasma bond-breaking processes of polymer molecules. The excited atoms emit visible or ultraviolet (VUV) radiation during their relaxation processes, which can be absorbed on polymer molecules. Energy obtained in absorption processes can lead to bond-breaking processes in polymer molecules. The excited atoms in metastable states also can cause bond-breaking processes by the non-radiative mechanisms of energy transfer. For the purpose of plasma conditions modeling, we calculated the electron energy distribution functions (EEDFs) and period averaged excitation rates of the argon atom for each of the applied power (Table 1). The calculations were conducted by using the simulation model for electron transport, excitations and ionizations of gases by electron impact in RF plasmas, which had been developed earlier and explained elsewhere [6].

Table 1. Normalized sums of relative spectral intensity and period averaged excitation rates (in 10^{-9} cm^3 s^{-1}) for various applied power values.

Power	40 W	60 W	80 W	100W
Intensity of argon spectral lines	1	2.35	2.64	2.97
Rate coefficients for excitations	1.48	2.02	2.51	3.12
Intensity of argon ion spectral lines	0.003	0.018	0.028	0.044
Rate coefficients for ionizations	0.56	1.03	1.37	1.94

To compare our results obtained by modeling with the experimental values, we used OES for plasma diagnostics. We calculated intensities of spectral lines obtained from relaxation of excited states of neutral argon atoms and of excited argon ions. We normalized these relative intensities in order to compare them with calculated excitation rates data. The values of normalized sums of relative spectral intensity for various applied power values are also shown in Table1. It can be seen from the table that the sums of relative intensities for emission from excited states increase in the same way as calculated rates for corresponding electronic states, i. e. with the increase of applied power. The same conclusion can be drawn for the sums of emission intensities from the argon ions and the calculated rates for ionization. These similar behaviors of experimentally measured relative intensities of emitted spectral lines and calculated rates by using the simulation model confirm our theoretically proposed shift of EEDFs.

4. CONCLUSIONS

The aim of this work was to investigate possible changes of the acoustical properties of natural cellulose fabrics by the argon plasma treatment. Simultaneous with the treatments, the diagnostic of plasma conditions by OES and the adequate theoretical calculations on plasma parameters were performed in order to explain the plasma influence on the treated materials. According to the conducted calculations, at medium and high applied powers, a lot of argon excited atoms and ions are created in plasma bulk. They interact with polymer molecules at the plasma sheath and cause the processes of bond-breaking between atoms in polymer molecules, which leads to surface modifications of textile fibers and increase of SAC of the treated materials.

Acknowledgements

This work was supported in part by the Ministry of Education and Science of the Republic of Serbia by the Projects No. 171006 and No. 171016.

REFERENCES

[1] Vidaurre EFC, Achete CA, Gallo F, Garcia D, Simao R, Habert AC (2002) Surface Modification of Polymeric Materials by Plasma Treatment.MaterialsResearch 5:37-41. doi:10.1590/S1516-14392002000100006

[2] Slepicka P, Slepickova Kasalkova N, Stranska E, Bacakova L, Svorcik V (2013)Surface characterization of plasma treated polymers for applications as biocompatiblecarriers. eXPRESS Polymer Letters 7: 535-545. doi:10.3144/expresspolymlett.2013.50

[3] Sahin HT (2008) RF-argon plasma induced surface modification of paper. SurfaceReview and Letters 15:503-508. doi:10.1142/S0218625X08011652

[4] Youngjoo N, Gilsoo C (2010) Sound Absorption and Viscoelastic Property of Acoustical Automotive Nonwovens and Their Plasma Treatment. Fibers and Polymers 11:782-789. doi:10.1007/s12221-010-0782-5

[5] Arefi-Khonsari F, Tatoulian M, Advanced Plasma Technology, Editors: d`Agostino R, Favia P, Kawai Y, Ikegami H, Sato N, Arefi-Khonsari F., Wiley-VCH Verlag GmbH&Co.KgaA (2008). doi:10.1002/9783527622184.ch8

[6] Ristić MM, Aoneas MM, Vojnović MM, Poparić GB, Excitation of Electronic States of N_2 in Radio-Frequency Electric Field by Electron Impact. Plasma Chem. Plasma Process. (2017) 37:1431-1443. doi:10.1007/s11090-017-9826-6.

Electrical characterization of a portable plasma needle system

Anđelija Petrović[1], Nevena Puač[1], Nikola Škoro[1], Antonije Đorđević and Zoran Lj. Petrović[1, 2]

[1]*Institute of Physics, University of Belgrade, Pregrevica 118, 11080 Belgrade, Serbia*
[3]*School of Electrical Engineering, University of Belgrade, Bulevar kralja Aleksandra 73, 11000 Belgrade, Serbia*
[3]*Serbian Academy of Sciences and Arts, Knez Mihailova 35, 11000 Belgrade, Serbia*

Abstract. In this paper we present results of the electrical characterization of a newly developed portable plasma needle system that operates at 13.56 MHz. After the calibration of the built-in derivative probes, measurements were made in different setups in order to obtain the electrical characteristics of the plasma, i.e., the current and voltage waveforms and V-I characteristics. Here we will present results obtained for the flow of the feeding gas (helium) of 2 slm and electrode-target distance of 2 mm.

1. INTRODUCTION

Many research groups have been interested in the non-thermal atmospheric plasmas due to their high efficiency in the biomedical applications. One of the pioneering plasma source systems in this field was the so called 'plasma needle' [1, 2]. One of the biggest problems with those devices was complicated and bulky power supply systems. In order to replace the large commercial systems for power supply, we have developed a novel portable power supply system that operates at 13.56 MHz.

In this paper we will present results of the electrical characterization of the home-made plasma needle device. This system has built-in derivative probes for recording current and voltage waveforms. The first task was to calibrate the probes, which was done by using derivative probes of known characteristics. Thereafter measurements were made for different electrode-target configurations and electrical characteristics of the system were determined.

2. EXPERIMENTAL SETUP

The plasma needle is a low-temperature plasma source that operates at the atmospheric pressure [1-3]. The schematic representation of the plasma needle system is presented in Fig. 1. The plasma needle consists of the powered electrode positioned centrally This electrode is a tungsten wire whose diameter is 0.5 mm. The wire was inserted in a ceramic tube, which was then placed inside a glass tube (I.D.=4 mm; O.D.=6 mm). The ceramic tube prevents ignition of the discharge between the central electrode and the glass tube, i.e., along the helium gas flow. The tip of the central electrode is positioned at a 1 mm distance from the edge of the glass tube. The plasma appears as a small glow at the tip of the tungsten wire. It operates in a mixture of the feeding gas (helium) with air.

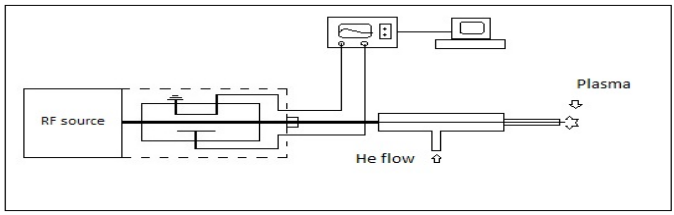

Figure 1. Schematic representation of the plasma needle setup

The novelty of the plasma needle system used in these experiments lays in the power supply system that was used. This power supply system and its electronic circuit was designed and made in the Laboratory for Gaseous Electronics. The aim was to create a small portable device that will be suitable for using in field conditions. The electric circuitry, including a set of derivative probes, is placed inside a metal body (21x20x8cm). The mass of the system is approximately 2 kg. The role of the derivate probes is to accurately measure the power transmitted in the plasma. The output of the probes was connected to a digital oscilloscope with cables of equal length. A computer collected all waveforms for further manipulation. The measurements were made in the configuration with synthetic rubber as a target positioned at a 2 mm distance from the tip of the plasma needle.

3. RESULTS AND DISCUSSION

In this study we examined electrical characteristics of the portable plasma needle device. The first task was to determine calibration characteristics of the built-in derivative probes. This was done by using derivative probes of known characteristics. After obtaining the calibration curves for the built-in derivative probes, we measured the V-I characteristics of the plasma needle setup described in Section 2.

The recorded current and voltage waveforms were transferred to the frequency domain, modified in accordance with the calibration curve given for a particular probe, and then returned to the time domain. In Fig. 2 and Fig. 3, two curves are given for current and voltage signals. The black (right axis) curve corresponds to the signal recorded directly from the oscilloscope (without numerical processing), and the red curve (left axis) is obtained the calibration.

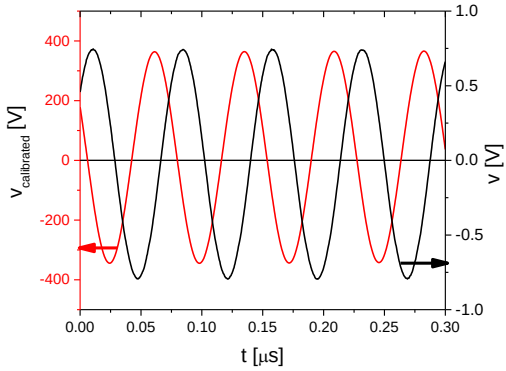

Figure 2. Voltage waveforms before and after corrections due to the calibration.

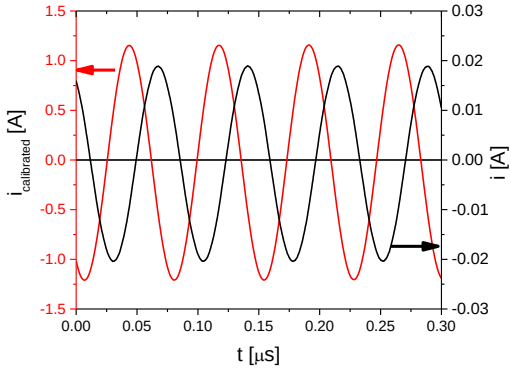

Figure 3. Current waveforms before and after corrections due to the calibration.

In order to obtain the current-voltage characteristic, the instantaneous voltage and current were monitored by using two derivate probes in the portable device, in two modes: without He flow and with a fixed flow rate of 2 slm. The obtained V-I curve is shown in Fig. 4. The moment of the plasma ignition is shown in the graph. We can see that after the plasma ignition, the total complex impedance of the system has not changed. On the other hand, the current and voltage RMS values increase significantly. This change can be also observed by visual observation of

the plasma since it starts as a small ball around the tip of the needle and then spreads towards the target. For the highest RMS values of the voltage and current, the plasma is covering at the target surface of about 4 mm in diameter.

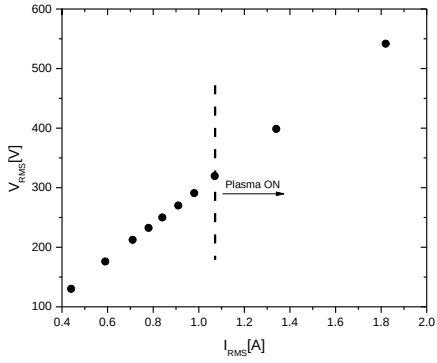

Figure 4. Volt-ampere characteristic of the plasma needle system. The flow of the feeding gas (He) was 2 slm.

4. CONCLUSION

We have developed a novel portable power supply system that operates at 13.56 MHz. In this paper we presented results obtained by measurements using the built-in derivative probes. The probes were first calibrated and then used to determine the voltage-current characteristics of the plasma needle discharge.

Acknowledgements

This research was supported by the Serbian MESTD under projects ON171037 and III41011.

REFERENCES

[1] R.E.J. Sladek and E. Stoffels, J. Phys. D: Appl. Phys., 38, 1716 (2005).
[2] N. Puač, Z.Lj. Petrović, G. Malović, A. Đorđević, S. Živković, Z. Giba and D. Grubišić, J. Phys. D:Appl. Phys. 39, 3514 (2006).
[3] S Lazović, N. Puač, M. Miletić, D. Pavlica, M. Jovanović, D. Bugarski, S. Mojsilović, D. Maletić, G. Malović, P. Milenković and Z. Petrović, New J. of Phys. 12, 083037 (2010).

Section 4.

GENERAL PLASMAS

INTERRELATIONSHIP BETWEEN LAB, SPACE, ASTROPHYSICAL, MAGNETIC-FUSION, AND INERTIAL-FUSION PLASMA EXPERIMENTS

Mark E. Koepke

Physics and Astronomy Dept., West Virginia University, Morgantown, WV, USA

Many advances in understanding space and astrophysical plasma phenomena have been linked to insight derived from theoretical modeling and/or laboratory experiments [1-3]. Advances for which (a) laboratory experiments helped explain phenomena and processes, (b) laboratory data influenced the interpretation of space data, and (c) laboratory validation of atomic and molecular spectroscopic processes contributed to telescopic probing of distant events are reviewed here. The space physics motivation of laboratory investigations and the scaling of laboratory plasma parameters to space plasma conditions are discussed. Examples demonstrating how laboratory experiments develop physical insight, validate or invalidate theoretical models, discover unexpected behavior, and establish observational signatures for the space community are presented. The various device configurations found in space-related laboratory investigations are outlined. The objectives of this review are to articulate space and astrophysical plasma physics issues that are addressable by laboratory experiments, to convey the wide range of laboratory experiments involved in this interdisciplinary alliance, and to illustrate how lab experiments on the centimeter or meter scale can develop, through the intermediary of a computer simulation, physically credible scaling of physical processes taking place in a distant part of the universe over enormous length scales.

Acknowledgement: This work is supported by DOE grant DE-SC-0012515.

REFERENCES

[1] C.-G. Fälthammar, Laboratory Experiments of Magnetospheric Interest, *Space Sci. Rev*. 15, 803–825 (1974).
[2] M. E. Koepke, Interrelated laboratory and space plasma experiments, *Rev. Geophys*. 46, RG3001 (2008).
[3] G. G. Howes, Laboratory space physics: Investigating the physics of space plasmas in the laboratory, *Phys. Plasmas* 25, 055501 (2018).

LINESHAPE MODELING: A COMPUTER EXPERIMENTALIST'S PERSPECTIVE

Evgeny Stambulchik[1]

[1] *Faculty of Physics, Weizmann Institute of Science, Rehovot 7610001, Israel*

Computer simulation (CS) methods for spectral lineshape modeling [1] have been in increasing use for a few decades since the pioneering work of Stamm and Voslamber [2]. Through the calculations, the movement of a statistically representative ensemble of perturbers over time is modeled. The resulting electric-field histories are used to obtain time evolution of the radiator, allowing for obtaining the spectrum. Such calculations are generally believed to be the most reliable type of Stark broadening models [3] as long as the very few approximations assumed are satisfied.
The scale of models being simulated by CS today far exceeds anything possible using traditional paper-and-pencil mathematical modeling. Often it is practically impossible to trace an entire execution of CS; for this reason, the results obtained using a CS are considered as results of a computer "experiment" [4]. As such, beyond the tremendous value for the data modeling and interpretation, simulations allow for uncovering new phenomena. In this paper, I will discuss a number of such discoveries.

REFERENCES

[1] E. Stambulchik and Y. Maron. Plasma line broadening and computer simulations: A mini-review. *High Energy Density Phys.*, 6(1):9–14, 2010. doi: 10.1016/j.hedp.2009.07.001.

[2] R. Stamm and D. Voslamber. On the role of ion dynamics in the Stark broadening of hydrogen lines. *J. Quant. Spectr. Rad. Transfer*, 22:599–609, 1979. doi: 10.1016/0022-4073(79)90049-9.

[3] M. A. Gigosos. Stark broadening models for plasma diagnostics. *J. Phys. D: Appl. Phys.*, 47(34):343001, August 2014. doi: 10.1088/0022-3727/47/34/343001.

[4] J. M. Haile. *Molecular Dynamics Simulation: Elementary Methods*. Wiley-Interscience, 1997. ISBN 047118439X.

Advanced helical plasma research toward steady-state fusion reactor by deuterium experiment in Large Helical Device

Y. Takeiri[1,2] for LHD Experiment Group

[1]*National Institute for Fusion Science, National Institutes of Natural Sciences*
[2]*SOKENDAI (both at 322-6 Oroshi, Toki 509-5292, Japan)*

Large Helical Device (LHD) is one of the world-largest superconducting helical system fusion-experiment devices. Since the start of experiments in 1998, it has extended its parameter regime. It has also demonstrated world-leading steady-state operation [1]. Based on these progress, LHD has been developed to the advanced research phase, that is, the deuterium experiment starting in March 2017. During the very first deuterium experiment campaign, the ion temperature of 10 keV was achieved [2,3]. This is the milestone of the helical systems research; demonstrating one of the fusion conditions. All these progress and increased understandings have provided academic bases for designing an LHD-type steady-state helical fusion reactor, which will be thoroughly overviewed in the lecture.

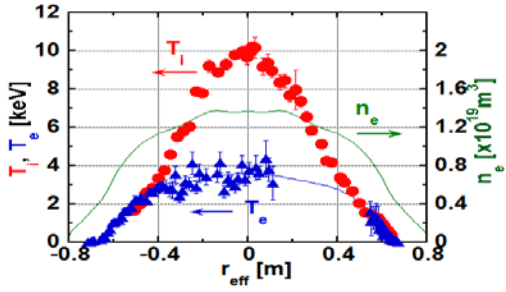

Figure 1. Temperature (ion (T_i) and electron (T_e)) and electron density (n_e) profiles for a case with achieving T_i~10 keV in the LHD deuterium experiment campaign.

Acknowledgements: The author (Y.T.) deeply acknowledges all the domestic and international collaborators for their great contributions on the LHD project.

REFERENCES

[1] Y. Takeiri, IEEE Transactions on Plasma Science 46, 1141 (2018).
[2] Y. Takeiri, IEEE Transactions on Plasma Science (Early Access) pp.1-8 (2018)
[3] H. Takahashi et al., submitted to Nuclear Fusion (2018).

FUNDAMENTAL PLANE OF ELIPTICAL GALAXIES IN $f(R)$ GRAVITY: THE ROLE OF LUMINOSITY

V. Borka Jovanović[1], P. Jovanović[2], D. Borka[1] and S. Capozziello[3,4,5]

[1] *Atomic Physics Laboratory (040), Vinča Institute of Nuclear Sciences, University of Belgrade, P.O. Box 522, 11001 Belgrade, Serbia*
[2] *Astronomical Observatory, Volgina 7, P.O. Box 74, 11060 Belgrade, Serbia*
[3] *Dipartimento di Fisica "E. Pancini", Università di Napoli "Federico II", Compl. Univ. di Monte S. Angelo, Edificio G, Via Cinthia, I-80126, Napoli, Italy*
[4] *Istituto Nazionale di Fisica Nucleare (INFN) Sez. di Napoli, Compl. Univ. di Monte S. Angelo, Edificio G, Via Cinthia, I-80126, Napoli, Italy*
[5] *Gran Sasso Science Institute, Viale F. Crispi, 7, I-67100, L'Aquila, Italy*

The global properties of elliptical galaxies are connected through the so-called fundamental plane of ellipticals, which is an empirical relation between their parameters: effective radius, central velocity dispersion and mean surface brightness within the effective radius. We investigated the connection between the parameters of fundamental plane equation and the parameters of $f(R)$ gravity potential. With that aim, we compared theoretical predictions for circular velocity in $f(R)$ gravity with the corresponding values from the large sample of observed elliptical galaxies. Besides, we consistently reproduced the values of coefficients of the fundamental plane equation as deduced from observations, showing that the photometric quantities like mean surface brightness are related to gravitational parameters. Therefore, this type of modified gravity, especially its power-law version - R^n, is able to reproduce the stellar dynamics in elliptical galaxies. Also, it is shown that R^n gravity fits the observations very well, without need for a dark matter.

APPLICATIONS OF ELECTRON-IMPACT EXCITATION OF OH IN THE SOLAR SYSTEM

L. Campbell[1] and M. J. Brunger[1]

[1]*College of Science and Engineering, Flinders University, Adelaide, South Australia*

Hydroxyl (OH) is important in studies of many solar system objects. An OH layer in the Earth's upper atmosphere is used for remote sensing of atmospheric temperatures and imaging of internal gravity waves. OH is an intermediary in the production of CO_2 in the atmospheres of Jupiter and Titan. Its emissions have been detected from meteors, comets and "clouds" around Saturn. Its presence is generally taken as an indicator of the breakdown of water, although in the Earth's atmosphere it is produced by a different chemical reaction. Emissions from OH are generally produced by prompt emission following the production of OH in an excited state, or thermal emissions. We are investigating the possibility that further information can be gained by looking at emissions produced by electron-impact excitation of OH. No experimental measurements have been made of the cross sections for such excitation, so a theoretical formulation that has been used in plasma simulations was applied. It was found that there may be problems with this formulation [1], illustrating the need for measurements. The applications addressed so far will be presented, including studies of electron-impact excitation of OH in the Earth's OH layer and of the role of OH in the meteoritic input of oxygen to the atmosphere of Jupiter. It was found in the case of the Earth that the effect of electron-impact excitation could not account for unexplained measurements, but the study led to the idea that chemical excitation of OH could transfer energy to electrons. In the case of Jupiter it was found that the ratio of OH to H_2O in the upper atmosphere is dependent on the mechanism of meteor ablation and that OH is produced by dissociation and ionization in meteor trails. Hence electron-induced emissions from OH may provide a useful method for remote sensing of meteor processes in the atmosphere of Jupiter.

Acknowledgements: This work is supported by the Australian Research Council (grant DP160102787).

REFERENCES

[1] L. Campbell and M. J. Brunger, Planet. Space Sci. 151, 11 (2018).

LARGE HELICAL DEVICE REVEALS LONG TIME-SCALE PLASMA PHYSICS

H. Kasahara[1], Y. Yoshimura[1], M. Tokitani[1] G. Motojima[1]
and LHD experiment group[1]

[1]*National Institute for Fusion Science, Oroshi 322-6, Toki 509-5292, JAPAN*

Long-pulse plasma experiments have been performed on magnetic confinement fusion devices with various plasma temperatures and electron densities. High-performance long-pulse plasma discharges with duration time over 30 min. have been frequently demonstrated on Large Helical Device (LHD), and a world record discharge (plasma temperature of 2 keV, central electron density of $1x10^{19}$ m^{-3}, duration time ~ 48 min. and injection energy of 3.4GJ) was achieved with real-time feedback controls for plasma heating and electron density [1]. With several long-pulse plasma discharges, fueling rates to keep plasma density constant were clearly different [2] from just before long-pulse operations. By comparing fueling rate between single long-pulse plasma discharge and integrated long-time plasma duration, the single long-pulse plasma discharge strongly affected wall-recycling caused through plasma-wall interaction [3] with long-time scale plasma physics. This long-time scale behavior was firstly observed on long-pulse plasma operation in LHD, and this result suggests that similar phenomena seem to be observed in fusion reactor with tungsten materials. Since future fusion devices have high power density and long-time duration, it will be one of key issues to get over long-time scale phenomena. In this lecture, high-performance long-pulse plasma operations were introduced with long-time scale plasma-wall interaction in LHD, and we suggest that what kinds of phenomena affect plasma sustainment and degrade plasma confinement through plasma-wall interaction.

Acknowledgements: This work is partially supported by the LHD projects (ULRR703, 801) and JSPS KAKENHI Grant Number JP16K06944.

REFERENCES

[1] H. Kasahara et al., in Proceedings of the 25th IAEA Fusion Energy Conference, Saint Petersburg, Russian, 13-18 October, 2014 (EX/7-3).
[2] G. Motojma, S. Masukzaki, M. Tokitani, H. Kasahara, Y. Yoshimura et al., J. Nucl. Mat. 463 (2015) 1080-1083.
[3] M. Tokitani, H. Kasahara, S. Masuzaki, G. Motojima, M. Shoji et al., J. Nucl. Mat. 463 (2015) 91-98.

PERIODICITY IN SPECTRAL VARIABILITY OF ACTIVE GALAXIES: A DIAGNOSTIC OF PHYSICAL PROCESSES IN THEIR CENTER

Andjelka Kovačević[1], Luka Č. Popović[2] and Dragana Ilić[1]

[1] *Department of Astronomy, Faculty of Mathematics, University of Belgrade, Studentski trg 16, 11000 Belgrade, Serbia*
[2] *Astronomical Observatory, Volgina 7, P.O.Box 74, 11060 Belgrade, Serbia*

Active galactic nuclei (AGN) compose the growth phases of the supermassive black holes in the core of almost every galaxy. Their electromagnetic emission presents a remarkable variety of signs even indicating the presence of periodical processes.

Here we review possible periodical signatures of their electromagnetic radiation that may follow specific source of gravitational radiation: a supermassive black hole binaries (SMBHB). Although a number of objects have been identified as SMBHB candidates through electromagnetic variability, the random nature of the main source of variability masks and makes it difficult to search for possible periodic signal.

Therefore, we will also present a new method, which we have developed for the purpose of detecting periodicity in the optical AGN observations, as well as some of the most interesting results and highlight the challenges that we have faced.

Quasars: from the Physics of Line Formation to Cosmology

P. Marziani[1], E. Bon[2], N. Bon[2], A. del Olmo[3], M. D'Onofrio[4], D. Dultzin[5], M. L. Martínez-Aldama[3], C. A. Negrete[5]

[1]*National Institute for Astrophysics (INAF), Astronomical Observatory of Padova, IT 35122, Padova, Italy*
[2]*Astronomical Observatory, Volgina 7, 11060 Belgrade, Serbia*
[3]*Instituto de Astrofisíca de Andalucía, IAA-CSIC, Glorieta de la Astronomia s/n, E-18008 Granada, Spain*
[4]*Dipartimento di Fisica & Astronomia "Galileo Galilei", Università di Padova, Padova, Italy*
[5]*Instituto de Astronomía, UNAM, Mexico D.F. 04510, México*

Quasars accreting matter at very high rates (known as extreme Population A [xA] or super-Eddington accreting massive black holes) provide a new class of distance indicators covering cosmic epochs from the present-day Universe up to less than 1 Gyr from the Big Bang. The very high accretion rate makes it possible that massive black holes hosted in quasars radiate at a stable, extreme luminosity-to-mass ratio. This in turns translates into stable physical and dynamical conditions of the mildly ionized gas in the quasar low-ionization line emitting region. In this contribution, we analyze the main optical and UV spectral properties of extreme Population A quasars that make them easily identifiable in large spectroscopic surveys at low- ($z \lesssim 1$) and intermediate-z ($2 \lesssim z \lesssim 2.6$), and the physical conditions that are derived for the formation of their emission lines. Ultimately, the analysis supports the possibility of identifying a virial broadening estimator from low-ionization line widths, and the conceptual validity of the redshift-independent luminosity estimates based on virial broadening for a known luminosity-to-mass ratio.

ON THE TIME SCALES OF OPTICAL VARIABILITY OF AGN AND THE SHAPE OF THEIR OPTICAL EMISSION LINE PROFILES

Edi Bon[1], Paola Marziani[2], Predrag Jovanović[1], Nataša Bon[1] and Aleksandar Otašević[1]

[1]*Astronomical Observatory, Volgina 7, Belgrade, Serbia*
[2]*INAF, Paddova, Itally*

Here we investigate the time scales of optical light curve variability of active galactic nuclei (AGN), for both continuum and the emission lines, and search for the connection with the shapes of their broad emission line profiles. We propose a new model that connects the shape of the optical broad emission line profiles with variability, assuming orbital time scales for continuum variability. As an application of our model, we calculate the masses of the central supermassive black holes.

Acknowledgements: This research is part of the projects 176003 "Gravitation and the large scale structure of the Universe" and 176001 "Astrophysical spectroscopy of extragalactic objects" supported by the Ministry of Education and Science of the Republic of Serbia.

DYNAMIC INSTABILITY OF RYDBERG ATOMIC COMPLEXES

M. S. Dimitrijević[1,2], V. A. Srećković[3], Alaa Abo Zalam[4], N. N. Bezuglov[4], A. N. Klyucharev[4]

[1]*Astronomical Observatory, Volgina 7, 11060, Belgrade, Serbia*
[2]*LERMA, Observatoire de Paris, PSL Research University, CNRS, Sorbonne Universites, UPMC (Univ. Pierre & Marie Curie) Paris 06, 5 Place Jules Janssen, 92190 Meudon, France*
[3]*Institute of physics, Univesity of Belgrade, P.O. Box 57, 11001, Belgrade, Serbia*
[4]*Saint Petersburg State University, 7/9 Universitetskaya nab., St. Petersburg, 199034, Russia*

The chemical composition of the Universe is mainly determined by the atoms and molecules of hydrogen, deuterium, lithium, helium, that is, by hydrogen and hydrogen-like atoms. An example is ionized hydrogen and clouds of alkali atoms in the Jupiter magnetosphere. Atoms and molecules in highly excited (Rydberg) states have a number of unique characteristics due to the strong dependence of their properties on the values of principal quantum numbers. For example, it is known that the instability of the spectral parameters of the Earth's ionosphere in the light absorption regions provided by the Rydberg states is influenced by the Solar activity and directly affects the conditions of human activity [1]. The paper discusses the results of an investigation of collisional Rydberg complexes specific features resulting in the development of dynamic chaos [2] and the accompanying diffusion autoionization processes. It is shown (experiment and theory) that in thermal and subthermal energies the global chaotic regime evolved in quasimolecular systems leads to significant changes in the Rydberg gases radiation/ionization kinetics.

Acknowledgements: This work is partially supported by Ministry of Education, Science and Technological Development of the Republic of Serbia under the grants III 44002, and 176002 and by the Russian Science Foundation under the grant NO 18-12-00313.

REFERENCES

[1] N. N. Bezuglov, G. V. Golubkov, and A. N. Klyucharev, Russian Journal of Physical Chemistry A, 11, 912 (2017).
[2] K. N. Arefieff, K. Miculis, N. N. Bezuglov, M. S. Dimitrijević, A. N. Klyucharev, A. A. Mihajlov, V. A. Srećković, Journal of Astrophysics and Astronomy 36, 613 (2015).

SPECTRAL MODELING OF HYDROGEN RADIATION EMISSION IN MAGNETIC FUSION PLASMAS

M. Koubiti and R.R. Sheeba

Aix Marseille Univ, CNRS, PIIM, Marseille, France

In magnetic fusion devices, handling the huge heat and particle loads escaping from the confined region is a major challenge as they can be very harmful for the plasma facing components (PFCs), with 20 MW/m^2 as an upper limit for the power load for the most advanced materials. A promising scenario, foreseen for future large scale fusion devices like ITER, consists in creating a radiative mantle in the divertor region in order to reach a plasma detachment regime. Such a regime can be reached by injecting impurities like nitrogen, neon or other noble gases. Therefore, a big effort is being devoted to the study of plasma detachment in both L- and H-modes especially in the framework of EUROfusion [1-2]. To support these studies, we propose the modelling of line and continuum emission of hydrogen for conditions relevant to detached plasma divertors in the aim of their characterization, i.e, providing their main plasma parameters (n_e, T_e and T_i). Under detachment conditions (n_e~10^{20}-10^{21} m^{-3}, T_e~1 eV), hydrogen spectra consisting of discrete high-n lines of the Balmer series and continuum emission can be observed. Due to the density effect on both recombination and line broadening, the continuum is shifted towards higher wavelengths [3]. Under such conditions, the high-n Balmer lines which are mainly broadened by Stark effect can be used to infer both the electron density and temperature of divertor. Indeed, the electron temperature can be inferred from the Boltzmann plot assuming a statistical equilibrium of the atomic populations over the excited levels or from the slope of the continuum. For that purpose, the discrete to continuum radiation transition will be modeled using a dissolution factor approach [4] which leads to a smooth merging of the lines into the continuum and resulting eventually in the lowering of the continuum below the theoretical limit. Modeling results will be confronted to experimental data.

REFERENCES

[1] Meyer H et al. 2017 Nucl. Fusion, 57, 102014
[2] Litaudon X et al. 2017 Nucl. Fusion, 57, 102001
[3] M. Koubiti et al. 2003 JQSRT, 81 265.
[4] Pigarov A Yu et al. Plasma Phys. Control. Fusion 40, 2055 (1998)

OPTICAL AND MID-INFRARED PROPERTIES OF ACTIVE GALACTIC NUCLEI AND DUST IN SUPERNOVA REMNANTS

Maša Lakićević[1], Luka Č. Popović[1] and Jelena Kovačević Dojčinović[1]

[1]*Astronomical Observatory Belgrade, Volgina 7, 11060 Belgrade, Serbia*

The optical and mid-infrared (MIR) radiation of AGNs come from the different regions: closer to the accretion disk, and from the torus and further, respectively. We have compared the optical and MIR spectroscopic parameters of AGNs and found several significant agreements and disagreements. These two kinds of observations do not always give the same conclusions about the starburst/AGN contribution to the AGN spectra.

Also, we will present our study on the differences between broad-line Seyfert 1 (S1), and narrow-line S1 galaxies, using MIR and optical spectroscopic parameters.

90% of dust content in the galaxies is cold dust (~20 K). Since the origin of the dust in the Universe is not well understood, it is important to study the supernovae (SNe) contribution to the dust production. SNe may be the most important dust producers in the Universe, after the asymptotic giant branch stars. The recent studies show that the young SNe and supernova remnants (SNRs) may produce ~1 solar mass of dust in their ejecta, shortly after the explosion, while some other studies show that the older remnants seem to destroy more dust than that they may earlier produce, most likely by their shocks and/or the high energetic radiation.

We explored the cold dust in SN1987A using the observations of APEX, ATCA, ALMA, Herschel, Spitzer and other telescopes. Also we performed the population study of ~60 SNRs in Large Magellanic Cloud using Herschel and Spitzer data. ALMA observations of other older SNRs are the topics of current (future) research.

SUPERNOVA REMNANTS AS COLLISIONLESS SHOCK WAVES: AN OVERVIEW OF THEORY AND OBSERVATIONS

Dušan Onić

Department of Astronomy, Faculty of Mathematics, University of Belgrade, Studentski trg 16, 11000 Belgrade, Serbia.

Supernova remnants (SNRs) are fascinating objects that are believed to be mostly responsible for the production of the Galactic cosmic rays. They strongly influence the interstellar medium through which they expand, and vice versa, the ambient interstellar matter (ISM) has a great impact on their evolution. The evolution of SNRs is closely related to the one of a particular collisionless shock wave that is actually formed ahead of the ejected material. It spreads through the ISM which is usually a low density magnetized gas plasma. The formation of such a shock wave, particle acceleration and magnetic field amplification are all coupled processes which we still do not fully understand. In fact, we still do not fully understand all these processes, such as various microinstabilities, that actually trigger collisonless shock formation. In this talk, the most important open questions regarding SNR physics are discussed. Special attention is paid to the recent study of possible equipartition between cosmic ray and magnetic field kinetic energy density in SNRs, as well as to the cosmic ray proton to electron kinetic energy density ratio.

ATOM-RYDBERG ATOM PROCESSES IN THE BROAD LINE REGION OF AGNS

Srećković A. Vladimir[1], Milan S. Dimitrijević[2,3] and Ljubinko.M Ignjatović[1]

[1]Institute of Physics, Belgrade University, Pregrevica 118, 11080 Zemun, Belgrade, Serbia
[2]Astronomical Observatory, Volgina 7, 11060 Belgrade, Serbia
[3]LERMA, Observatoire de Paris, UMR CNRS 8112, UPMC, 92195 Meudon Cedex, France

The importance of H*(n)+H(1s) collisions, for the principal quantum number n > 2, in active galactic nuclei (AGN) broad-line region (BLR) hydrogen clouds has been investigated. These processes have been treated by the mechanism of resonant energy exchange within the electron component of the considered collision system [1,2]. We calculate the corresponding collisional rate coefficients for the wide region of quantum numbers and temperatures. From the obtained results follows that these collisional atomic processes have significant influence on the free electrons and populations of hydrogen in highly excited states in moderately ionized layers of dense parts of the BLR clouds. It follows that the examined processes have to be included in the modelling and investigation of the moderately ionized parts of the BLR clouds as well as for the modelling and analysis of similar layers in the photosphere of the Sun and solar like stars [3].

Acknowledgements: The authors are thankful to the Ministry of Education, Science and Technological Development of the Republic of Serbia for the support of this work within the projects 176002 and III44002.

REFERENCES

[1] A. A. Mihajlov, V. A. Srećković, Lj. M. Ignjatović and A. N. Klyucharev, Journal of Cluster Science 23(1), 47 (2012)
[2] A. A. Mihajlov, V. A. Srećković, Lj. M. Ignjatović and M. S. Dimitrijević, Monthly Notices of the Royal Astronomical Society 458(2), 2215 (2016)
[3] V. A. Srećković, L. M. Ignjatović, D. Jevremović, V. Vujčić and M. S. Dimitrijević, Atoms 5(3), 31 (2017)

SOME IMPORTANT NOTES ON ASTA SOFTWARE: A NEW METHOD FOR ANALYSIS OF SIMPLE AND COMPLEX EMISSION/ABSORPTION SPECTRAL LINES

D. Tzimeas[1,2], D. Stathopoulos[1,3], E. Danezis[1], E. Lyratzi[1,3], A. Antoniou[1]

[1]*National and Kapodistrian University of Athens, Panepistimioupoli, Zographou 157 84, Athens, Greece*
[2]*National Hellenic Research Foundation, 48 Vassileos Constantinou Ave. 11635 Athens, Greece*
[3]*Eugenides Foundation, 387 Syngrou Av., 175 64, Athens, Greece*

ASTA is a spectral analysis software for displaying, fitting and analyzing simple or complex emission/absorption spectral lines. The software is based on the GR (Gauss-Rotation) model produced by the Astrophysical Spectroscopy Team of the National and Kapodistrian University of Athens, Greece. ASTA is able to fit, process and analyze: (i) *Simple spectral lines* that can be simulated by a classic distribution such as Gauss, Lorentz or Voigt. In these cases, ASTA has the ability to calculate the line function of an observed spectrum and compute the physical parameters of the region that produces the spectral line: Full Width Half Maximum (FWHM), Equivalent Width, Optical Depth, Column Density, (ii) *Spectral lines that exhibit complex and asymmetric profiles*, which are the product of synthesis (blend) of individual components of the same ion. Characteristic examples of this case are Broad Absorption Lines (BALs) and Broad Emission Lines (BELs) found in the spectra of Quasars, and the Discrete Absorption Components (DACs) observed in the spectra of Hot Emission Stars. Other astronomical objects exhibiting complex profiles such as Wolf Rayet, Cataclysmic Variable, O, B, Oe and Be stars can also be analyzed by ASTA. In the case of these complex and asymmetric spectral lines ASTA can provide the analysis of the complex profiles to the uniquely determined individual components it consists of. As a result, the physical parameters describing each, uniquely determined, individual component are uniquely calculated. In this paper we answer a series of questions concerning both the rationale of GR model and how ASTA software implements it. We clarify and explain the mathematical logic that we use, the method calculating the best fit of the complex spectral line (BALs, BELs, DACs) and their analysis in a uniquely series of spectral components. Finally, we present tests that guarantee the values of the calculated parameters and point out the substantial differences from other methods of spectral analysis.

STUDIES OF RUNAWAY ELECTRONS IN COMPASS TOKAMAK

Milos Vlainic[1]

[1]*Institute of Physics, University of Belgrade, P.O. Box 68, 11080 Belgrade, Serbia*

Runaway electrons present a potential threat to the safe operation of the future nuclear fusion power plants based on the tokamak principle (e.g. ITER). In the latest issue of ITER Physics Basis [1], runaway electrons are considered as the second highest priority for the ITER disruption mitigation.

The talk will give an overview of the author's work in this topic – post-disruptive runaway electron generation in COMPASS tokamak, synchrotron radiation measurements, toroidal electric field and runaway electron current estimations. The focus of the talk is on the runaway electron current and density estimation during the plasma discharge. The method uses a theoretical method developed by Fujita [2], with the difference in using experimental measurements from EFIT and Thomson scattering instead of making theoretical assumptions.

The method is explained on the COMPASS discharge number 7298, which has a significant runaway electron population. Here, it is found that at least 4 kA of the plasma current is driven by the runaway electrons. Next, the method is used on the set of plasma discharges with the variable electron plasma density. The difference in the plasma current is explained by runaway electrons, and their current is estimated using the aforementioned method. The experimental results are compared with the theory and simulations.

Acknowledgements: The 'Joint Doctoral Programme in Nuclear Fusion Science and Engineering' is acknowledged by the author for supporting the studies. The next to thank is the project MSMT LM2011021, which supports the operation of COMPASS. The authors would also like to acknowledge the work of the WP14-MST2-9 research project team. This work has been carried out within the framework of the EUROfusion Consortium and has received funding from the Euratom research and training programme 2014-2018 under grant agreement no. 633053. The views and opinions expressed herein do not necessarily reflect those of the European Commission.

REFERENCES

[1] T.C. Hender *et al.*, Nucl. Fusion 47(6), S128 (2007).
[2] T. Fujita *et al.*, J. Phys. Soc. Jpn. 60(4), 1237-1246 (1991).

Cr III STARK WIDTHS FOR STELLAR SPECTRA INVESTIGATIONS

Milan S. Dimitrijević[1] and Abhishek Chougule[1,2]

[1] *Astronomical Observatory, Volgina 7 11060, Belgrade 74, Serbia*
[2] *Institut für Astro- und Teilchenphysik, Universität Innsbruck, Technikerstr. 25/8, A-6020 Innsbruck, Austria*

Abstract. Recently, using the modified semiempirical method of Dimitrijević and Konjević, we have calculated Stark widths for six Cr III transitions, for an electron density of 10^{17} cm^{-3} and for temperatures from 5000–80,000 K, and published them in journal Atoms. In this poster contribution these data are presented and their importance discussed.

1.INTRODUCTION

Stark broadening data are needed for applications like laboratory plasma diagnostics, the research and modelling of different technological plasmas as well as for inertial fusion and laser-produced plasmas investigation. They are particularly useful in astrophysics for a number of problems like for example stellar plasma modelling, abundance determination, and stellar spectra analysis and synthesis.

Chromium III lines are present in stellar spectra. For example in [1] has been reported identification of a great number of Cr II and Cr III lines, in the spectrum of B5 Ia type star η CMa obtained by Orbiting Astronomical Observatory OAO-3 (Copernicus). A large number of Cr II and Cr III lines has been also found in the spectra of τ Her (B5 IV) and ζ Dra (B6 III), also obtained by the spectrometer on OAO-3 [2], and in the spectrum of ζ Aurigae binary system 31 Cygni (K4 Ib + B4 V), obtained by the FUSE (Far Ultraviolet Spectroscopic Explorer) satellite [3]. The contribution of the iron group elements to the observed opacity in stellar atmospheres is very significant [4], and we note as well that the spectral lines of doubly charged ions, including Cr III, are dominant in the UV spectra of hot B stars [5].

A review of the existing theoretical and experimental data for Stark broadening of spectral lines of chromium in various ionization stages is given in detail in Ref. [6] and it has been concluded that in spite of the importance

of Cr III atomic data for stellar atmospheres and abundances research, the data for Stark broadening for this ion are completely missing. So, in [6] we have calculated full widths at half intensity maximum (FWHM) due to collisions with surrounding electrons for six Cr III transitions, for an electron density of 10^{17} cm^{-3} and for temperatures from 5000–80,000 K. We performed the calculations using the modified semiempirical method (MSE) [7, 8, 9]. In this poster contribution the summary of this work is presented and the importance of the obtained results discussed.

2.Results and discussion

All details of the calculations are given in [6]. We note only that the modified semiempirical method [7, 8, 9] have been used, that the needed set of atomic energy levels was taken from [10] (see also NIST database [11]), as well as that the dipole matrix elements for considered transitions were calculated within Coulomb approximation using the method of Bates and Damgaard [12]. As an example of the obtained results, we show here in Table 1, Stark full widths at half intensity maximum for two Cr III multiplets for a perturber density of 10^{17} cm^{-3} and temperatures from 5000 K up to 80,000 K.

Since the data in [6] are the first data for the Stark broadening of Cr III lines, there is no other experimental or theoretical data for comparison.

Table 1. The example of results published in [6]. Full Width at Half intensity Maximum (FWHM, Å) for Cr III spectral lines, for a perturber density of 10^{17} cm^{-3} and temperatures from 5000 K to 80,000 K. Calculated wavelength (λ) of the transitions (in Å) is also given. $3kT/2\Delta E$ is the ratio of the energy of free electron and of the energy difference to the closest perturbing level for T = 10,000 K.

Transition	T (K)	FWHM (Å)
Cr III $3d^3(^4F)4s^5F$–$3d^3(^4F)4p^5F^o$	5000	0.723E-01
	10,000	0.511E-01
λ = 2121.8 Å	20,000	0.361E-01
$3kT/2\Delta E = 0.234$	40,000	0.256E-01
	80,000	0.181E-01
Cr III $3d^3(^4F)4s^5F$–$3d^3(^4F)4p^5G^o$	5000	0.791E-01
	10,000	0.559E-01
λ = 2241.9 Å	20,000	0.396E-01
$3kT/2\Delta E = 0.234$	40,000	0.280E-01
	80,000	0.198E-01

The obtained Stark widths have been used in [6] for the investigation of the significance of the Stark broadening in DO white dwarf atmospheres. Namely, in Refs. [13] and [14] has been demostrated the importance of

the Stark broadening mechanism in atmospheres of such stars, where its influence is usually larger than or comparable to Doppler broadening. The effective temperatures of the DO white dwarf atmospheres are within the interval 45,000–120,000 K. In [6] the atmospheric models from [15] have been used,with effective temperatures from 30,000–45,000 K, typical for the cool DO white dwarfs, marking the hot end of the so-called DB gap [16]. It has been shown that exist large atmospheric layers where Stark broadening is dominant in comparison with thermal Doppler broadening. The conclusion was also that the influence of Stark broadening increases with the increase of the value of Rosseland opacity, as well as that gravity becomes more important for atmospheric models with larger surface gravity.

Another topic for the application of the obtained results are subphotospheric layers. Namely in Ref. [17] has been underlined that Stark broadening is the dominant broadening mechanism in such layers. Consequently, if chromium exists in the stellar atmosphere, it is also the sign of its existence in various ionization stages in subphotospheric layers. Namely it is created as the result of thermonuclear reactions in stellar interiors and Stark broadening data for Cr III as well as for the chromium in other ionisation stages are useful for the modelling of such layers, and for the calculation of radiative transfer in such conditions. The application of Stark broadening data for Cr III lines for subphotospheric lyers is of interest even for cooler stars, where the influence of Stark broaening on chromium lines is negligible in stellar atmosphere.

It should be noted as well that the Stark widths of Cr III spectral lines, published in [6], will be implemented in the STARK-B database [18, 19] which is included in the Virtual Atomic and Molecular Data Center (VAMDC) [20, 21], created in order to enable a more effective search of atomic and molecular data from different databases.

Stark line widths determined theoretically in [6] contribute also to the creation of a set of such data for as large as possible number of spectral lines. This is important for a number of problems such as stellar spectra analysis and synthesis, opacity calculations, abundance determination and modelling of stellar atmospheres, but also for the diagnostics of laboratory plasmas, investigation of laser-produced and inertial fusion plasma, and for different plasma technologies.

REFERENCES

[1] A. B. Underhill, Astrophys. J. Suppl. Ser. 27, 359 (1974)

[2] A. B. Underhill, Astrophys. J. Suppl. Ser. 34, 309 (1977)

[3] W. H. Bauer and P. D. Bennett, Astrophys. J. Suppl. Ser.211, 27 (2014)

[4] S. Johansson, Phys. Scr. 36, 99 (1987)

[5] C. R. Cowley and M. Frey, Nucl. Instrum. Methods Phys. Res. B 31, 214 (1988)

[6] M. S. Dimitrijević and A. Chougule, Atoms 6,15 (2018)

[7] M. S. Dimitrijević and N. Konjević, J. Quant. Spectrosc. Radiat. Transf. 24, 451 (1980)

[8] M. S. Dimitrijević and V. Kršljanin, Astron. Astrophys. 165, 269 (1986)

[9] M. S. Dimitrijević and L. Č. Popović, J. Appl. Spectrosc., 68, 893 (2001)

[10] J. Sugar and C. Corliss, J. Phys. Chem. Ref. Data, 14, 2, 1-664 (1985)

[11] A. Kramida, Y. Ralchenko and J. Reader, NIST ASD Team,. NIST Atomic Spectra Database (2015) http://physics.nist.gov/asd

[12] D. R. Bates and A. Damgaard, Phil. Trans. R. Soc. Lond. A 242, 101 (1949)

[13] R. Hamdi, N. Ben Nessib, N. Milovanović, L. Č. Popovi, M. S. Dimitrijević and S. Sahal-Bréchot, Mon. Not. R. Astron. Soc. 387, 871 (2008)

[14] M. S. Dimitrijević, Z. Simić, A. Kovačević, A. Valjarević, A. and S. Sahal-Bréchot, Mon. Not. R. Astron. Soc., 454, 1736 (2015)

[15] F. Wesemael, Astrophys. J. Suppl. Ser. 45, 177 (1981)

[16] P. Chayer, S. Vennes, J. Dupuis and J. W. Kruk, Astrophys. J. Lett. 630, 169 (2005)

[17] M. J. Seaton, J. Phys. B, 20, 6363 (1987)

[18] S. Sahal-Bréchot, M. S. Dimitrijević and N. Moreau, STARK-B database, http://stark-b.obspm.fr

[19] S. Sahal-Bréchot, M. S. Dimitrijević, N. Moreau and N. Ben Nessib, Phys. Scr. 50, 054008 (2015)

[20] M. L. Dubernet, et al., J. Quant. Spectrosc. Radiat. Transf. 111, 2151 (2010)

[21] M. L. Dubernet, et al., J. Phys. B 49, 074003 (2016)

ADVANCES IN STATIONARY AFTERGLOW INSTRUMENTATION FOR EXPERIMENTS BELOW LIQUID NITROGEN TEMPERATURES

Á. Kálosi[1], P. Dohnal[1], D. Shapko[1], R. Plašil[1] and J. Glosík[1]

[1]*Department of Surface and Plasma Science, Faculty of Mathematics and Physics, Charles University, Prague, Czech Republic*

Abstract. We present a novel cryogenic stationary afterglow apparatus that will allow to study electron-ion recombination of simply molecular ions below liquid nitrogen temperatures in plasmatic environments. The stationary afterglow instrumentation is combined with cavity ring-down spectroscopy to monitor the rotational and translational temperatures of ions and the time evolution of ion number densities. The cryogenic core of the apparatus is connected to a closed cycle helium refrigerator and is capable if reaching temperatures as low as 25 K.

1. INTRODUCTION

The primary motivation of electron-ion recombination studies at very low temperatures originates in the fundamental nature of this process that plays a pivotal role in several plasmatic environments. In case of molecular ions the dominant process is called dissociative recombination, it has been studied both experimentally and theoretically for over 70 years [1]. From a computational point of view even triatomic systems present complex challenges when not only the vibrational and electronic structure, but also the rotational states of the molecules has to be taken into account [2]. Experimental studies aim to supply benchmarks for theoretical calculations and data for plasma modelling.

2. INSTRUMENTATION

In a stationary afterglow apparatus a plasma is ignited in a mixture of gases contained in a discharge vessel to produce the studied ions. After termination of the discharge, i.e. in the afterglow, the ion number density is

probed using a suitable diagnostic method. Recombination rate coefficients are determined from the time evolution of the measured ion number density. The design of the newly developed apparatus was based on many years of experience in afterglow instrumentation [3].

The following short description of the presented apparatus can be split into three sections: plasma generation, cryogenics and optics (for detailed description see [4]). An overview of the apparatus is shown in Figure 1.

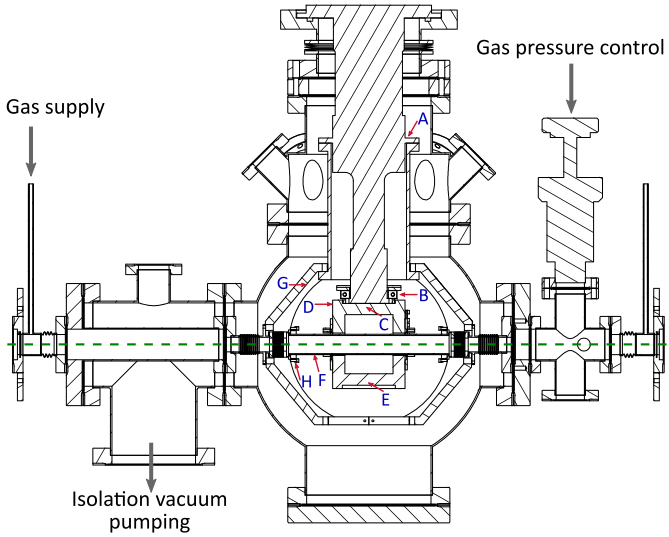

Figure 1. Cross section of the apparatus showing the positions of the temperature sensors (capital letters) and the majority of inner and outer (isolation) vacuum components. A and B: 1st and 2nd stage of the cold head, respectively. C, D and E: microwave resonator. F: discharge tube. G: heat shield. H: discharge tube holder (vacuum bellow). The dashed line is showing the line of sight of the spectrometer (axis of the plasma column).

The plasma is generated in a microwave discharge in a sapphire discharge tube along the axis of a cylindrical microwave resonator. Design parameters of the resonator were optimised to produce a homogeneous plasma column while keeping the size of the resonator as small as possible. The resonator itself is directly connected to the second stage of a cryogenic cold head, while heat transport from the discharge tube is achieved through copper braids anchored on the resonator. The discharge tube is held in place by vacuum bellows which are in turn connected to the room temperature parts of the inner vacuum system.

The cryogenic parts of the apparatus are housed in an outer isolation vacuum chamber pumped to pressures lower then 10^{-4} Pa. To achieve the lowest possible operational temperatures both the microwave resonator

and the discharge tube are further shielded from room temperature thermal radiation by a heat shield connected to the first stage of the cold head. Several temperature sensors monitor the apparatus during operation. A sample of the temperature evolutions are plotted in Figure 2 showing the cooling down, operation and warming up phases.

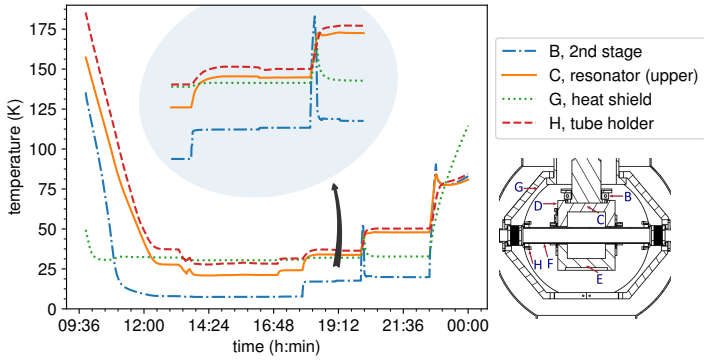

Figure 2. Temperature evolution during a typical experimental day. The highlighted region shows temperature regulation capabilities using the heating elements placed in the body of the microwave resonator.

Finally the inner vacuum system is closed at both ends of the main axis by the mirror mounts of the continuous-wave cavity ring down spectrometer. Utilizing narrow linewidth (< 10 MHz) laser sources in the range of 1250–1450 nm where the mirror reflectance is $> 99.99\%$ we can probe several rovibrational transitions of ions and molecules of interest. The distance between the mirrors is 82 cm which gives a characteristic time constant for the ring-down decay of 200 µs.

During the experiments a constant flow of the buffer and reactant gases keeps the content of impurities minimal in the discharge region while having a constant pressure of hundreds of Pascal.

3. FIRST TESTS

First tests of the newly commissioned apparatus were conducted in mixtures of helium and hydrogen gases focusing on the cooling properties. The well known H_3^+ ion was chosen as the test ion building on our previous research [5]. We probed the lowest lying rotational states of H_3^+ of both para and ortho symmetry [6] and recorded absorption spectra at different temperatures to investigate the translational temperature of the ions. A sample spectrum is plotted in Figure 3.

Further tests of the newly commissioned apparatus will include systematic studies of ion translational and rotational temperatures with varying microwave discharge conditions in order to explore the limit for the

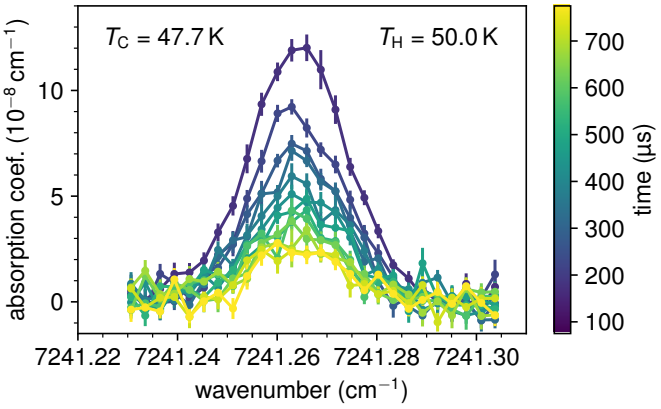

Figure 3. Absorption spectra of H_3^+ recorded at different times in the afterglow showing the time resolution capabilities of cw-CRDS. Each plotted spectrum is an average over a 50 μs time interval during the afterglow. The second overtone ro-vibrational transition originates from the lowest lying rotational state of ortho symmetry. The determined average translation temperature is (56 ± 2) K.

lowest achievable temperature. Exhaustive investigation of the plasma relaxation is also necessary before shifting our attention to recombination studies.

Acknowledgements

This work is partially supported by Czech Science Foundation projects GACR 17-08803S and GACR 17-18067S and by Charles University projects GAUK 1583517 and GAUK 646218.

REFERENCES

[1] M. Larsson and A. E. Orel, *Dissociative Recombination of Molecular Ions*, (Cambridge University Press, Cambridge, 2008).

[2] S. Fonseca dos Santos, V. Kokoouline and Ch. H. Greene, J. Chem. Phys. 127, 124309 (2007).

[3] P. Macko et al., Int. J. Mass Spectrom. 233, 299 (2004).

[4] R. Plašil et al., Rev. Sci. Instrum., submitted for publication (2018).

[5] M. Hejduk et al., J. Chem. Phys. 143, 044303 (2015).

[6] C. Lindsay and B. J. McCall, J. Mol. Spectrosc. 210, 60 (2001).

THE SPECTRAL LINES AS A TOOL FOR BLACK HOLE MASS ESTIMATION IN ACTIVE GALACTIC NUCLEI

Sladjana Marčeta-Mandić[1], Jelena Kovačević-Dojčinović[2] and Luka Č. Popović[1,2]

[1] *Mathematical Faculty, University of Belgrade, 11000 Belgrade, Serbia*
[2] *Astronomical Observatory, Volgina 7, 11060 Belgrade, Serbia*

Abstract. Here we apply two independent methods for estimation of the black hole mass in the center of Active Galactic Nuclei (AGN), using the broad Hβ lines emitted from the gaseous regions near super-massive black hole. The first is based on virial theorem and assumes that the Keplerian motion is the main broadening mechanism affecting broad emission lines (BELs). The second assumes that the gravitation influences the BELs profiles causing a red asymmetry in their shapes. We compared these masses for a sample of the 39 type 1 AGNs and discussed possible causes of differences.

1. INTRODUCTION

Active galactic nucleus (AGN) is a compact region in the center of a galaxy with luminosity much higher then of a normal galaxy, due to accretion of matter into super-massive black hole (SMBH) ($10^6 - 10^{10} M_\odot$). All AGNs have a similar structure [1]: the SMBH in it's center is surrounded by a geometrically thin and optically thick accretion disc (AD) which expands into a dusty torus. Above and below the AD is optically thick gas in the broad line region (BLR), where broad emission lines (BELs) arise (see [2]), ionized by the continuum radiation from the AD and influenced by the gravitational field of the SMBH, causing complexity of structure and kinematics of the BLR and effecting BEL shapes ([3], [4]).

Several methods are used for estimating the mass of the central SMBH (M_{BH}) in AGNs (see [5], [6]). Here we apply two independent methods for M_{BH} estimation: the first, based on the virial theorem, assumes that the Keplerian motions of the BLR gas around the SMBH is the main broadening mechanism of the BELs. The second method assumes that the gravitational redshift influences the BEL profiles, causing a red asymmetry in their shapes. Both methods are applied on the broad Hβ emission line taken from the spectra of 39 type 1 (with BELs) AGNs. Finally, we compare the SMBH masses obtained with two methods and discuss the results.

2. THE METHODS FOR SMBH ESTIMATIONS

The virial mass is defined as (see e.g. [6]):

$$M_{\rm BH} = f \ \frac{R_{\rm BLR} \ \delta v_{\rm r}^2}{G} \ , \qquad (1)$$

where f is a factor dependent of geometry and inclination of the emitting region, $R_{\rm BLR}$ is a distance of the BLR from the central SMBH, G is the gravitational constant and $\delta v_{\rm r}$ is a line broadening due to virial motion, here determined from the Full Width at Half Maximum (FWHM) of BELs. For $R_{\rm BLR}$ we used the $R_{\rm BLR} - L$ relation ([7]), which is the result of the reverberation mapping (see [8]).

The other method, when the $\rm M_{BH}$ is obtained from the gravitational redshift ($z_{\rm gr}$) of BEL, assumes that the relativistic effects in the BLR, near SMBH, is strong enough to effect the BEL shapes, and could be measured as a redshift or red asymmetry in a line profile ([9]). Jonić [10] found expected relationship between the FWHM of BELs and red asymmetry of BELs (z_{50}, intrinsic redshift at 50% of maximal line intensity, $I_{\rm max}$). This implies that the measured z_{50} is probably related to $z_{\rm gr}$ and that it could be used for calculation of $\rm M_{BH}$:

$$M_{\rm BH} \ = \ \frac{c^2 \ z_{\rm gr} \ R_{\rm BLR}}{G} \ , \qquad (2)$$

where $z_{\rm gr}$ is intrinsic redshift at 50% of $I_{\rm max}$ (z_{50}).

3. THE SAMPLE AND ANALYSIS

For our research we used the sample given in [11], who provided set of 88 AGN spectra corrected for host galaxy contribution. After elimination of 34 objects with very low S/N (signal-to-noise), and 15 objects with $z_{\rm gr} < 0$ the final sample consists of 39 type 1 AGNs.

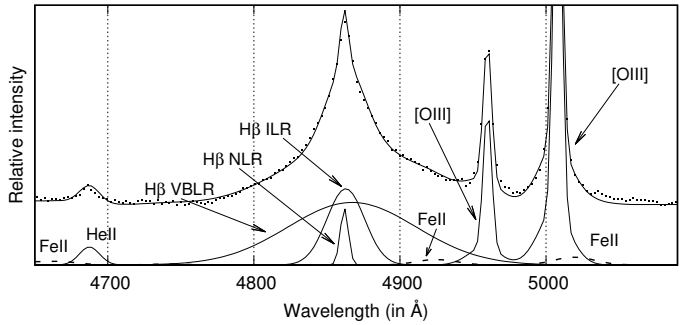

Figure 1. An example of the decomposition of Hβ in wavelength range 4650-5100Å for object SDSS J223338.41+131243.6. The observations are denoted with dots, the model with solid line, the optical Fe II templates with dashed line, and other emission line components with solid line (NLR, ILR, VBLR).

Spectra were corrected for the Galactic extinction, and for the cosmological redshift. Afterwards, the continuum emission was removed, and spectra were fitted using the multi-Gaussian model of optical emission in $\lambda\lambda 4000 - 5500 \mathring{A}$ range given in [12]. The BLR emission is described with two-component model, as assumed that the BLR consists of two different sub regions: the very broad line region (VBLR) which is closer to the SMBH, whose emission contributes to the BEL wings, and the intermediated line region (ILR), further away from the SMBH, with emission that forms the BEL cores (see [4] and references within).

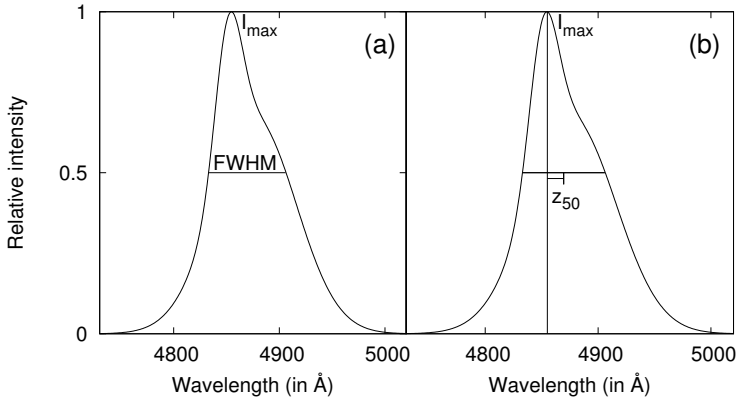

Figure 2. An example of measuring FWHM (a) and intrinsic redshift z_{50} (b) of the broad Hβ component (VBLR+ILR).

An example of the decomposition of the optical emission is shown in Fig. 1. The BEL profile is obtained as a sum of the VBLR and ILR Gaussian, and the FWHM and red asymmetry z_{50} of the BELs are measured as shown in Fig. 2. Contribution of the narrow line region (NLR) is not considered. The intrinsic redshift is measured as a difference between the centroid shift and the broad component peak at 50% of $I_{\max}$ (see [10]).

4. RESULTS

The values of M_{BH} estimated using the virial theorem $M_{BH}(vir)$ Eq.(1) and ones obtained from the gravitational redshift of BELs $M_{BH}(gr)$ Eq.(2) are in significant correlation as shown in Fig. 3a, with the correlation coefficients $\rho = 0.798$, P-value of the null-hypothesis is $P_0 = 0$ (linear best-fit coefficients: slope a=1.38, y-intercept b=-2.64). Also, it can be seen that $M_{BH}(vir)$ are systematically lower than $M_{BH}(gr)$ (see Fig 3b), as for 46% of objects $M_{BH}(gr)$ is up to 0.2 dex larger then $M_{BH}(vir)$.

As can be seen on Fig. 3, the agreement between two methods is relatively good. The detailed discussion of the results will be given in [13].

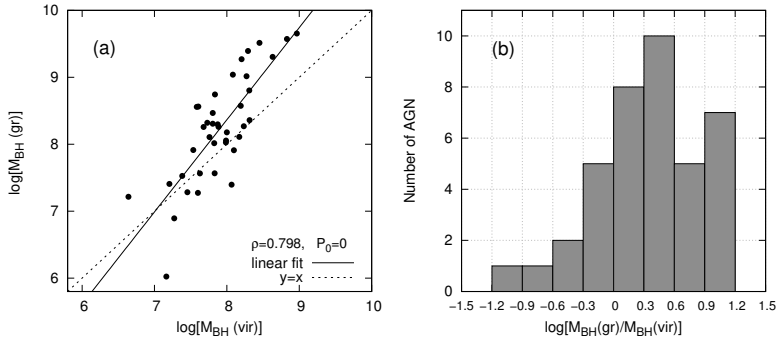

Figure 3. (a) The correlation between black hole masses calculated with two different methods, using the virial approximation and gravitational redshift of BELs. Solid line represents linear best-fit. (b) The ratio $\mathrm{M_{BH}}(gr)/\mathrm{M_{BH}}(vir)$.

Acknowledgements

This work is partially supported by the Ministry of Education, Science, Technology and Development, Republic of Serbia of under the project 176001.

REFERENCES

[1] Antonucci, R., Annual Review of ARA&A, 31, 473 (1993)

[2] D. E. Osterbrock, *Astrophysics of gaseous nebulae and active galactic nuclei*, p. 442, (University Science Books, 1989)

[3] Sulentic, J. W., Marziani, P. et al., ARA&A, 38, 521−571 (2000)

[4] Kovačević, J., Popović, L.Č, Dimitrijević, M.S., ApJS, 189, 15 (2010)

[5] Marziani, P., Sulentic, J.W., New Astron. Rev. 56, 49 (2010)

[6] Peterson, B. M., SSRev, 183. 253−275 (2010)

[7] Vestergaard, M., Peterson, B.M., ApJ, 641, 676 (2006)

[8] Peterson,B. M., MDSAI, 77, 581 (2006)

[9] Liu, H. T., Feng, H. C., and Bai, J. M., MNRAS 466 (2017)

[10] Jonić, S., Kovačević-Dojčinović, J., Ilić, D. et al., A&SS 361, 101 (2017)

[11] Shen,Y., ApJ, 805, 96 (2015)

[12] Kovačević-Dojčinović, J. and Popović, L.Č., ApJS, 221, 35 (2015)

[13] Marčeta-Mandić, S., Kovačević-Dojčinović J., Popović, L.Č., in preparation (2018)

DIFFERENCES IN THE SOLAR X-RAY FLARE INDUCED TEC_D INCREASE WITH REGARDS TO GEOGRAPHICAL LOCATION

Aleksandra Nina[1], Vladimir M. Čadež[2], Giovanni Nico[3] and Luka Č. Popović[2]

[1]*Institute of Physics, University of Belgrade, Pregrevica 118 11080 Belgrade, Serbia*
[2] *Astronomical Observatory, Volgina 7, 11060 Belgrade, Serbia*
[3] *Instituto per le Applicazioni del Calcolo, Consiglio Nazionale delle Ricerche, 70126 Bari, Italy*

Abstract. In this paper we analyze the influence of the geographical position on the increase of the total electron content in the ionospheric D-region during solar X-ray flares. We modeled the total electron content using data related to signals whose propagation paths lie in the mid and both mid and low latitude ionosphere. The obtained results indicate a larger increase of the total electron content in the perturbed equatorial D-region where the solar radiation is more pronounced and causes a larger electron density gradient with altitude.

1. INTRODUCTION

One of the most important parameters that describes the ionosphere is the total electron content (TEC) which represents the column electron number density i.e. the number of free electrons in a column of unit cross section extending from the ground to the top of the ionosphere. Knowledge of this parameter is important not only in pure scientific research but also in practical applications especially in methods based on the Global Navigation Satellite System (GNSS) and Synthetic Aperture Radar (SAR) signal propagation. Namely, these signals play a critical role in telecommunications, geodesy and land surveying, emergency response, precision agriculture, all forms of transportation (space stations, aviation, maritime, rail, road and mass transit), and deviation of their paths is most pronounced in the ionosphere due to presence of free electrons. Concerning SAR data, modelling and corrections of delays in ionosphere are more important in L-band (1 GHz – 2 GHz) even if the recent use of Sentinel-1 data for SAR meteorology applications pointed out the need for the correction of ionosphere delays also in C-band (4 GHz – 8 GHz) [1]

According to the electron density altitude distribution, the ionosphere is divided in the following regions: F (120 km – 1000 km), E (90 km – 120 km) and D (60 km – 90 km). Due to the largest electron density the F-region has the most

important contribution in TEC. The E-region has a smaller but still non negligible role in signal propagation properties, while the lowest D-region is usually ignored in TEC calculations. However, during periods of intensive Solar flare activity, perturbation of this medium may become appreciable and the electron density can be significantly increased causing the contribution to TEC coming from the D-region (TEC_D) to exceed 1 TECU (10^{16} electrons/m^2) which cannot be ignored in total TEC anymore.

In this paper we present an analysis of solar X-ray flares influence on TEC_D and perform calculations based on data collected by VLF (Very Low Frequency) receivers presented in statistical studies given in [2] and [3].

2. MODELING

If we consider electrons in a vertical column, the vertical TEC_D in the horizontal uniform D-region with the top and bottom boundaries at altitudes of h_t = 90 km and h_b = 60 km, respectively, can be expressed by the equation:

$$\mathrm{TEC}_D(t) = \int_{h_b}^{h_t} N_e(t,h)\,\mathrm{d}h \tag{1}$$

The electron density $N_e(t,h)$ in time t and altitude h can be obtained by using the equation based on Wait's model of the ionosphere [4] with parameters sharpness β (in km^{-1}) and signal reflection height H' (in km) [5]:

$$N_e(t,h) = 1.43 \cdot 10^{13} e^{-\beta(t)H'(t)} e^{(\beta(t)-\beta_0)h} \tag{2}$$

Here, β_0 = 0.15 km^{-1} while Wait's parameters can be obtained by different methods. In this paper we calculate their values as analytical functions of the X-ray intensity I during solar X-ray flares given in [6] and based on data presented in [2] and [3]:

$$\beta(I^*) = C_1 + C_2 \log(I^*) + C_3 \log(I^{*2}) \tag{3}$$

$$H'(I^*) = D_1 + D_2 \log(I^*) \tag{4}$$

where the coefficients C_1, C_2, C_3, D_1 and D_2 depend on the used data sets of Wait's parameters. In Equations (3) and (4) I^* represents the X-ray intensity (recorded by the GOES satellite in the wavelength domain between 0.1 nm and 0.8 nm) normalized on 1 W/m^2.

3. RESULTS AND CONCLUSIONS

In this paper we show the influence of geographical location on TEC variations in the D-region exposed to the increased X-radiation during a solar X-ray flare. We compare the dependence of TEC on the signal reflection height for two sets of Wait's parameters obtained β and H' in the D-region monitoring by the VLF radio waves as given in [1] and [2]. The first set is related to the area in the mid latitude ionosphere with the signal path between the UK and Serbia while the second one covers the area between the USA and New Zealand lying in the low as well as in mid latitude zone.

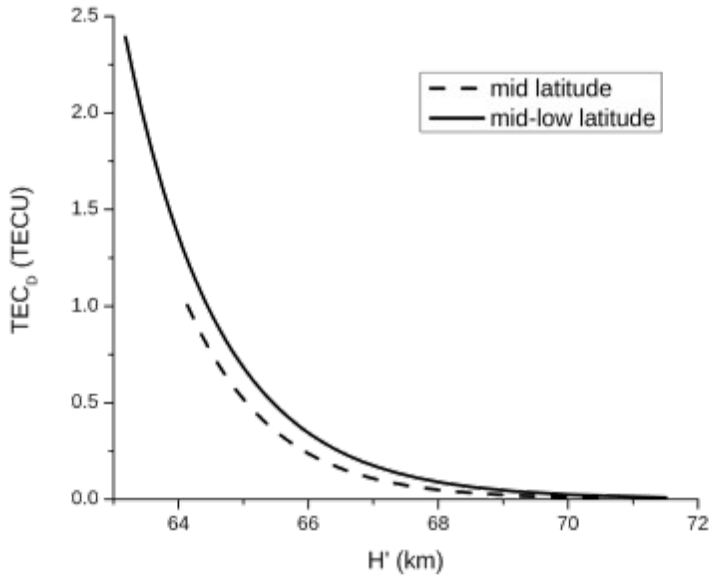

Figure 1. The TEC_D dependence on reflection height H' for signals propagating at the mid latitude [2] and mid – low latitude [3] D-region.

As seen in Figure 1, the TEC_D values at a given H' are larger in the latter than in the former case of trajectory. This difference in TEC_D increases toward lower H' which decreases with increase of the incoming X-radiation [6].

The explanation for such a behavior follows from Equation 2 showing that the electron density obtained by the explained technique depends not only on H' but also on β. This Wait's parameter characterizes the gradient of the electron density with height which is larger in the second case (the signal propagation path lies partially in the equatorial zone) at the same X-radiation intensity [5]. The obtained results show that TEC_D increases with gradient of the electron density.

Keeping in mind that this gradient increases with intensity of solar radiation [6] we can conclude that the larger influences of solar X-ray flares on the low ionospheric TEC_D are expected in the equatorial than in the mid latitude zone.

Acknowledgements

The authors thank the Ministry of Education, Science and Technological Development of the Republic of Serbia through the projects III 44002 176001, 176002 and 176004. This study is made within the COST project TD1403 and the VarSITI project.

REFERENCES

[1] P Mateus, J Catalão, G Nico, Sentinel-1 interferometric SAR mapping of precipitable water vapor over a country-spanning area, *IEEE Trans. Geosci. Remote Sens.*, 55, 2993 (2016).
[2] D. P. Grubor, D. M. Šulić and V, Žigman, Serb. Astron. J., 171, 29 (2005).
[3] N. R. Thomson, J. C. Rodger and A. M.Clilverd, J. Geophys. Res., 110, A06306 (2005).
[4] N. R. Thomson, *J. Atmos. Solar-Terr. Phys.* 55, 173 (1993).
[5] J. R. Wait and K. P. Spies, Characteristics of the Earth-ionosphere waveguide for VLF radio waves, NBS Technical Note 300, (National Bureau of Standards, Boulder, CO.S, 1964).
[6] M. Todorović Drakul, V. M. Čadež, J. B. Bajčetić, L. Č. Popović, D. M. Blagojević and A. Nina, Serb. Astron. J., 193, 11 (2016).

PHOTOABSORPTION CROSS SECTION OF A DENSE HYDROGEN PLASMA, MODEL METHOD

Nenad M. Sakan[1]*, Vladimir A. Srećković [1], Zoran J. Simić[2] and Milan S. Dimitrijević [2,3]

[1] *Institute of Physics, Belgrade University, Pregrevica 118, 11080 Zemun, Belgrade, Serbia* [2] *Astronomical Observatory, Volgina 7, 11060 Belgrade, Serbia* [3] *LERMA, Observatoire de Paris, UMR CNRS 8112, UPMC, 92195 Meudon Cedex, France.*

Abstract. Here are presented results of bound state transition modeling using the cut-off Coulomb model potential. The cut-off Coulomb potential has proven itself as a model potential for the dense hydrogen plasma. The main aim of our investigation include a further steps of improvement of the usage of model potential. The results deal with partially ionized dense hydrogen plasma. The presented results covers $N_e = 6.5 \cdot 10^{18}$ cm^{-3}, $T = 18000$ K and $N_e = 1.5 \cdot 10^{19}$ cm^{-3}, $T = 23000$ K where the comparison with the experimental data as well as with the theoretical values should take place. Since the model was successfully applied on continuous photoabsorption of dense hydrogen plasma in the broad area of temperatures and densities it is expected to combine both continuous and bound-bound photoabsorption within single quantum mechanical model with the same success.

1. INTRODUCTION

The problems of plasma opacity, energy transport and radiative transfer under moderate and strong non-ideality are of interest in theoretical and experimental research [1, 2, 3, 4]. The strong coupling and density effects in plasmas radiation were the subject of numerous experimental and theoretical studies in the last decades. In this paper we presented a new model way of describing atomic photo-absorption processes in dense strongly ionized hydrogen plasmas, which is based on the approximation of the cut-off Coulomb potential. By now this approximation has been used in order to describe transport properties of dense plasmas (see e.g. [1, 5, 6]), but it

was clear that it could be applied to some absorption processes in non-ideal plasmas too [3, 7, 8, 9]. More detailed explanation could be find in [10].

2. THEORY

2.1 The approximation of the cut-off Coulomb potential

Many body processes, namely: $\varepsilon_\lambda + (\mathrm{H}^+ + e)_i + S_{rest} \rightarrow (\mathrm{H}^+ + e)_f + S'_{rest}$, where S_{rest} and S'_{rest} denote the rest of the considered plasma are here considered simplified by the use of transformation to the corresponding single-particle processes in an adequately chosen model potential, for the detailed theory [10] should be considered.

As an adequate model potential for hydrogen plasma with such density we choose, as in [5, 3], the screening cut-off Coulomb potential, which satisfies above conditions, and is used in form

$$U_c(r) = \begin{cases} -\dfrac{e^2}{r} + \dfrac{e^2}{r_c}, & 0 < r \leq r_c, \\ 0, & r_c < r < \infty, \end{cases} \tag{1}$$

where the mean potential energy of an electron in the considered hydrogen plasma $U_{p;c} = -e^2/r_c$ is used as a energy origin of the potential. Here e is the modulus of the electron charge, r - distance from the ion, and cut-off radius r_c - the characteristic screening length of the considered plasma.
It is important that the cut-off radius r_c can be determined as a given function of N_e and T, using two characteristic lengths, $r_i = \left(k_B T/4\pi N_i e^2\right)^{1/2}$ and $r_{s;i} = (3N_i/4\pi)^{1/3}$, where N_i and $r_{s;i}$ are the ion density and the corresponding Wigner-Seitz's radius and k_B - Boltzman's constant. Namely, taking that $N_i = N_e$ and $r_c = a_{c;i} \cdot r_i$ we can directly determine the factor $a_{c;i}$ as a function of ratio $r_{s;i}/r_i$, on the basis of the data about the mean potential energy of the electron in the single ionized plasma from [11]. The behavior of $a_{c;i}$ in a wide region of values of $r_{s;i}/r_i$ is presented in Fig. 1.

2.2 The calculated quantities

In accordance with that, the behavior of the dipole matrix element is investigated here. It is given by $\hat{D}(r; r_c; n_i, l_i; n_f, l_f) = < n_f, l_f | \mathbf{r} | n_i, l_i >$, where the wave functions $|n_i, l_i >$ and $|n_f, l_f >$ are initial and final state wave functions obtained within the model of cut-off Coulomb potential.

The total absorption cross section of the line could be linked with the dipole moment directly with the help of relation

$$\sigma_0(\omega = \omega_{fi}) = \frac{1}{3}\frac{g_2}{g_1}\frac{\pi\omega_{fi}}{\varepsilon_0 \hbar c}\hat{D}(r; r_c; n_i, l_i; n_f, l_f)^2. \tag{2}$$

The total bound-bound absorption cross section for the "short" pulse from [12], $Ne = 1.5 \cdot 10^{19}$ cm^{-3}, $T = 23000$ K goes in the range

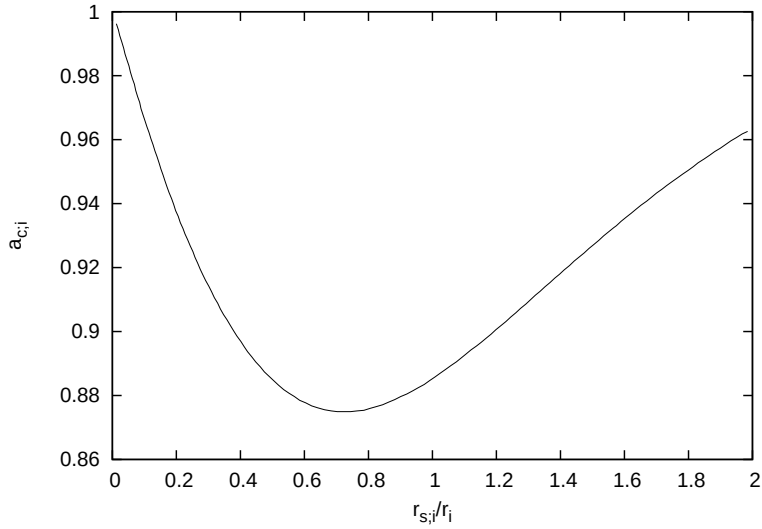

Figure 1. Behavior of the parameters $a_{c;i} \equiv r_c/r_i$, from [11], as the function of the ratio $r_{s;i}/r_i$, details on $r_{s;i}$ and r_i are in the text.

from $1,84 \cdot 10^{-7}\mathrm{m}^2(\mathrm{rad/s})^{-1}$ to $1,72 \cdot 10^{-5}\mathrm{m}^2(\mathrm{rad/s})^{-1}$, and for the "long" pulse, $Ne = 6.5 \cdot 10^{18}$ cm^{-3}, $T = 18000$ K, from $1.99 \cdot 10^{-8}\mathrm{m}^2(\mathrm{rad/s})^{-1}$ to $2.25 \cdot 10^{-5}\mathrm{m}^2(\mathrm{rad/s})^{-1}$.

3. CONCLUSION

The presented results are step forward towards inclusion of the entire photo-absorption processes for hydrogen atom in plasma within the frame of the cut-off Coulomb potential model. One of the benefits of the presented results is a completely quantum mechanical solution for considered case, obtained from wave functions that are analytical and represented with the help of special functions, e.g. the influence of additional numerical source of errors is minimized as possible. The work on including model broadening process for each of energy levels, and inclusion in calculation is going on.

REFERENCES

[1] Fortov, V.E., Iakubov, I.T. The physics of non-ideal plasma; World Scientific, 1999.

[2] Rogers, F.J., Iglesias, C.A. Opacity of stellar matter. Space Sci. Rev. 1998, 85, 61–70.

[3] Mihajlov, A.A., Sakan, N.M., Srećković, V.A., Vitel, Y., Modeling of continuous absorption of electromagnetic radiation in dense partially ionized plasmas. J. Phys. A 2011, 44, 095502.

[4] Mihajlov, A.A.; Ignjatović, L.M., Srećković, V.A., Dimitrijević, M.S., Metropoulos, A., The non-symmetric ion-atom radiative processes in the stellar, atmospheres, Mon. Not. R. Astron. Soc. 2013, 431, 589–599.

[5] Mihajlov, A.A., Djordjevi, D., Popovi, M.M., Meyer, T., Luft, M., Kraeft, W.D., Determination of the Electrical Conductivity of a Plasma on the Basis of the Coulomb cut-off Potential Model., Contrib. Plasma Phys., 1989, 29, 441–446.

[6] Ignjatović, L.M., Srećković, V.A., Dimitrijević, M.S., The Screening Characteristics of the Dense Astrophysical Plasmas: The Three-Component Systems., Atoms, 2017, 5, 42.

[7] Mihajlov, A.A., Sakan, N.M., Srećković, V.A., Vitel, Y., Modeling of the Continuous Absorption of Electromagnetic Radiation in Dense Hydrogen Plasma., Balt. Astron., 2011, 20, 604–608.

[8] Mihajlov, A.A., Srećković, V.A., Sakan, N.M., Inverse Bremsstrahlung in Astrophysical Plasmas: The Absorption Coefficients and Gaunt Factors., J. Astrophys. Astron., 2015, 36, 635–642.

[9] Sakan, N.M., Srećković, V.A., Mihajlov, A.A., The application of the cut-off Coulomb potential for the calculation of a continuous spectra of dense hydrogen plasma., Mem. S. A. I. Suppl., 2005, 7, 221–224.

[10] Sakan, Nenad M. and Srekovi, Vladimir A. and Simi, Zoran J. and Dimitrijevi, Milan S., The Application of the Cut-Off Coulomb Model Potential for the Calculation of Bound-Bound State Transitions, Atoms, 2018, 6, 1, 4

[11] Mihajlov, A., Vitel, Y., Ignjatović, L.M., The new screening characteristics of strongly non-ideal and dusty plasmas. Part 3: Properties and applications., High Temp., 2009, 47, 147–157.

[12] Vitel, Y., Gavrilova, T., D'yachkov, L., Kurilenkov, Y.K., Spectra of dense pure hydrogen plasma in Balmer area., J. Quant. Spectrosc. Radiat. Transf., 2004, 83, 387–405.

DETERMINATION N_2H^+ PRESSURE BROADENING BY MEANS OF NEAR-INFRARED CAVITY RING-DOWN SPECTROSCOPY

D. Shapko, P. Dohnal, Á. Kálosi, Š. Roučka, R. Plašil, J. Glosík

Charles University, Faculty of Mathematics and Physics, V Holešovičkách 2, Prague, Czech Republic

Abstract. A stationary afterglow apparatus with cavity ring-down spectrometer (SA-CRDS) was utilized to probe several overtone transitions of N_2H^+ ion. The pressure broadening coefficient of P(6) transition of the (200) ← (000) vibrational band was measured $B_P = (8.89 \pm 0.33)\times10^{-21}$ cm^{-1} cm^3. By utilizing the measured rate of losses of N_2H^+ ion in afterglow by ambipolar diffusion the zero field ion mobility of N_2H^+ ions in helium was determined $K_0 = (19.9 \pm 2.0)$ cm^2 V^{-1} s^{-1}.

1. INTRODUCTION

Diazenylium (N_2H^+ ion) has been observed in a number of areas in the interstellar medium (ISM). It can be used as versatile probe to the innermost dense regions of dark clouds due to their large dipole moment [1]. Since the first detection in the ISM by Turner (1974) by means of the NRAO radio telescope [2], protonated nitrogen became an important tracer for N_2, which lacks a permanent dipole moment and hence does not possess a radiofrequency spectrum [3]. The number density CO molecules in the ISM also can be determined with the help of N_2H^+ ions. In the dense clouds diazenylium is formed via proton transfer from H_3^+ and the main destruction mechanisms include proton transfer to CO and dissociative recombination with free electrons [4]. Because of its importance for astrochemistry, the recombination of N_2H^+ ions with electrons was studied for over 40 years [5].

2. EXPERIMENT

The detailed description of the SA-CRDS apparatus can be found e.g. in ref. [6] so only a short overview will be given here. The plasma is formed in a pulsed microwave discharge in a fused silica tube cooled by precooled nitrogen vapour. The discharge is ignited in a mixture of He/Ar/H_2/N_2 (a typical composition of $10^{17}/10^{14}/10^{14}/10^{13}$ cm^{-3}. A continuous-wave cavity ring-down spectroscopy [7] is used to probe the number densities of different rotational states of N_2H^+ using transitions published in ref. [4].

To study recombination of N_2H^+ ions with electrons it is important to ascertain that electron temperature T_e, kinetic temperature of the ions T_{kin} and their rotational temperature are close to the temperature of the buffer gas. The rotational temperature can be evaluated from the measured populations of different rotational states whereas the kinetic temperature can be determined from the Doppler broadening of the absorption lines. At experimental conditions used for the recombination studies (temperature below 300 K and pressure of several hundreds of pascal), the measured absorption line shape is influenced by both Doppler and pressure broadening. In order to reliably determine the kinetic temperature T_{kin} of the ions from the Doppler broadening of the absorption line, we fitted the measured data by a Voight profile. To further improve the determination of T_{kin} we first measured the rotational temperature of N_2H^+ ions from relative number densities of different rotational states of the vibrational ground state using P(5) at 6320.6311 cm^{-1}, P(6) at 6317.2682 cm^{-1}, P(7) at 6313.8544 cm^{-1} and P(8) at 6310.3902 cm^{-1} transitions in the (200) ← (000) vibrational band of N_2H^+ (for details on spectroscopic notations see ref. [4]. The obtained rotational temperature T_{rot} = (197 ± 8) K was in excellent agreement with the temperature of the discharge tube wall T_{wall} = (204 ± 1) K measured by a thermocouple. Then we measured several absorption line profiles of the P(6) transition at different values of the buffer gas pressure and fitted them by a Voight profile while keeping the Doppler width w_D constant at the value appropriate for 204 K (w_D = 0.01197 cm^{-1}). The resulting Lorentzian widths w_L of the fitted Voight profiles are plotted in Figure 1. From the slope of the straight line fitted to the dependence of the w_L on the pressure we evaluated the pressure broadening coefficient of the P(6) transition in helium B_P = (8.89 ± 0.33)×10^{-21} cm^{-1} cm^3.

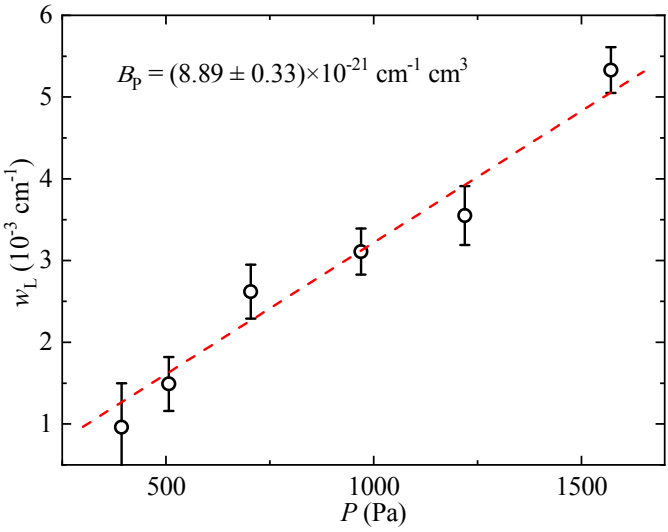

Figure 1. The dependence of Lorentzian width w_L of the P(6) overtone transition of N_2H^+ at 6317.2682 cm^{-1} on the pressure measured at 204 K. w_L was

determined by fitting the measured absorption line by a Voight profile. The evaluated pressure broadening coefficient is indicated in the figure. The dashed line is a linear fit to the data.

An example of the time evolution of the N_2H^+ number density measured at T_{wall} = (206 ± 1) K and T_{kin} = (211 ± 7) K is shown in Figure 2. The dashed line in Figure 2 denotes fit to the data that includes losses of charged particles by both recombination and ambipolar diffusion (see ref. [8] for details). From the measured time constant of diffusion losses τ_D (211 K, 519 Pa) = (5.7 ± 0.6) × 10^{-4} s the zero field ion mobility K_0 of N_2H^+ ions can be calculated using the relation given by Mason and McDaniel [9]:

$$1/\tau_D = 4.63 \times 10^{15} \times (K_0(T)/\Lambda^2) \times (T/[\mathrm{He}])\ \mathrm{s}^{-1}, \qquad (1)$$

where electrons and ions are assumed to have the same temperature T, [He] is in cm^{-3}, T in K, K_0 in $cm^2\ V^{-1}\ s^{-1}$ and $\Lambda^2 = 0.062\ cm^2$ is a factor dependent on actual length and radius of the discharge tube. The resulting zero field ion mobility of N_2H^+ ions K_0 = (19.9 ± 2.0) $cm^2\ V^{-1}\ s^{-1}$ is in good agreement with value of K_0 = (19.0 ± 0.8) $cm^2\ V^{-1}\ s^{-1}$ reported in ref. [10].

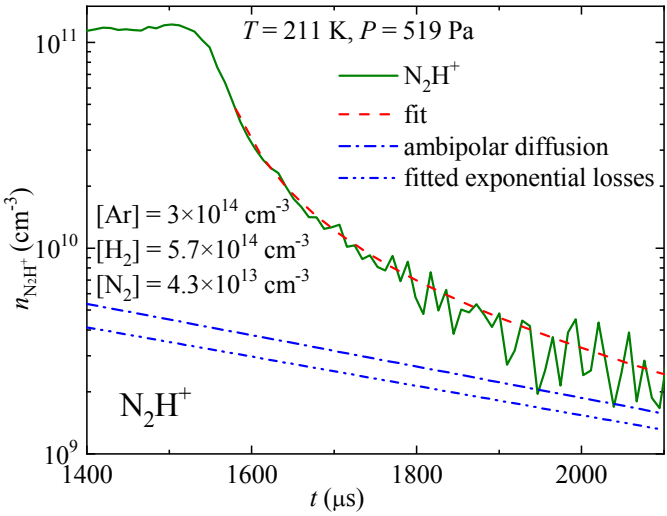

Figure 2. Time dependence of the N_2H^+ number density in discharge and early afterglow plasma. The used reactant number densities are indicated in the figure. The dashed line is a fit to the data that includes losses of charged particle by recombination and ambipolar diffusion. Calculated losses by ambipolar diffusion are indicated by the double-dot-dashed line and actual fitted exponential losses are denoted by the dot-dashed line.

3. CONCLUSION

The pressure broadening coefficient for the P(6) line of the (200) ← (000) vibrational band of N_2H^+ was determined to be B_P = (8.89 ± 0.33)×10^{-21} cm^{-1} cm^3. The measured value of zero field ion mobility of N_2H^+ in helium K_0 = (19.9 ± 2.0) cm^2 V^{-1} s^{-1} is in good agreement with previous experiments [10]. These results will be utilized in our ongoing effort to measure recombination rate coefficient of N_2H^+ ions with spectroscopically determined populations of different quantum states of recombining ions.

Acknowledgements

This work was partly supported by the Czech Science Foundation (GACR 15-15077S, GACR 17-08803S, GACR 17-18067S) and by the Charles University (projects Nr. GAUK 1583517 and GAUK 646218).

REFERENCES

[1] S. Fonseca dos Santos, N. Douguet, V. Kokoouline and A. E. Orel, J. Chem. Phys. 140 (2014) 164308.
[2] B. E. Turner, Astrophys. J. Lett. 193 (1974) L83.
[3] E. Vigren, V. Zhaunerchyk, M. Hamberg, M. Kaminska, J. Semaniak, M. af Ugglas et al., Astrophys. J. 757 (2012) 34.
[4] Á. Kálosi, P. Dohnal, D. Shapko, Š. Roučka, R. Plašil, R. Johnsen, J. Glosík, J. Instrum., 12 (2017).
[5] M. Larsson, A. E. Orel, *Dissociative recombination of molecular ions*, p. 380, (Cambridge University Press, 2008).
[6] P. Macko, G. Ban, P. Hlavenka, R. Plasil, V. Poterya, A. Pysanenko, O. Votava, R. Johnsen, J. Glosik, J. Int. J. Mass Spectrom., 233 (2004) 299.
[7] D. Romanini, A. A. Kachanov, N. Sadeghi and F. Stoeckel, Chem. Phys. Lett. 264 (1997) 316.
[8] P. Dohnal, M. Hejduk, J. Varju, P. Rubovic, Š. Roučka, T. Kotrik, R. Plašil, J. Glosík, R. Johnsen, J. Chem. Phys., 136 (2012) 244304.
[9] E. Mason and E. McDaniel, *Transport Properties of Ions in Gases* (Wiley, New York, 1988).
[10] T.T.C. Jones, J.D.C. Jones, K. Birkinshaw, N.D. Twiddy, Chem. Phys. Lett. 89 (1982) 443.

RATE COEFFICIENTS FOR THE CHEMI-IONIZATION IN ALKALI GEOCOSMICAL PLASMAS

V. A. Srećković[1], Lj. M. Ignjatović[1], M. S. Dimitrijević[2,3], N. N. Bezuglov[4] and A. N. Klyucharev[4]

[1]*Institute of Physics, University of Belgrade, P.O. Box 57 11001, Belgrade, Serbia*
[2]*Astronomical Observatory, Volgina 7 11060, Belgrade 74, Serbia*
[3]*LERMA, Observatoire de Paris, PSL Research University, CNRS, Sorbonne Universites, UPMC (Univ. Pierre & Marie Curie) Paris 06, 5 Place Jules Janssen, 92190 Meudon, France*
[4]*Saint Petersburg State University, St. Petersburg State University, 7/9 Universitetskaya nab., St. Petersburg 199034 Russia*

Abstract. The chemi-ionization processes are investigated in this contribution for the cases of Li and Na collisions, for the principal quantum numbers $n \geq 4$ and temperatures 500 K $\leq T \leq$ 1500 K. These processes were considered, with a particular accent to the applications for low temperature laboratory plasma research created in gas discharges, for example in microwave-induced discharges at atmospheric pressure. Presented results and preliminary model evaluations show that in the weakly ionized astrophysical formations of alkalis, specifically in volcanic gases on lo, chemi-ionization processes can provide effective channels for medium ionization. Also, further development of research of the chemi-ionization processes involving alkali metals in different stellar atmospheres as the factors which influence their spectral characteristics is important.

1.INTRODUCTION

The main aim of this work is to extend the investigation of Li and Na collisional ionization present in [1] for the wider region of principal quantum numbers and temperature with a particular accent to the applications for low temperature laboratory [2] and astrophysical plasma research [3, 4]. We studied the non-symmetric chemi-ionization processes

$$A^*(n) + B \Longrightarrow e + AB^+, \tag{1}$$

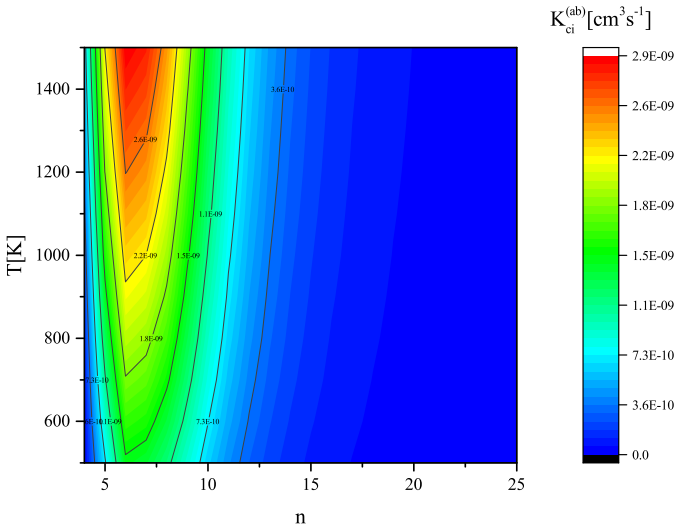

Figure 1. The total rate coefficient $K_{ci}^{(ab)}(n,T)$, Eq. (4) for chemi-ionization processes (1) and (2) in $\mathrm{Li}^*(n) + \mathrm{Na}$ collisions.

$$A^*(n) + B \Longrightarrow e + A^+ + B, \tag{2}$$

where Rydberg atom A =Li and B =Na, LiNa^+ is the molecular ion in the electronic ground state ($X^2\Sigma^+$). The resonant mechanism method is used for the calculations of the rate coefficients of the processes (1) and (2). The short description and basic theory is presented here (for details see the papers [5, 6]). The calculations of these rate coefficients are performed for the principal quantum number $4 \leq n \leq 25$ and temperatures 500 K $\leq T \leq$ 1500 K.

Interdependence of the partial $K_{ci}^{(a)}(n,T)$, $K_{ci}^{(b)}(n,T)$ and the total $K_{ci}^{(ab)}(n,T)$ rate coefficients which characterize the processes (1) and (2) is

$$K_{ci}^{(ab)}(n,T) = K_{ci}^{(a)}(n,T) + K_{ci}^{(b)}(n,T). \tag{3}$$

By definition, rate coefficients $K_{ci}^{(ab)}(n,T)$ and $K_{ci}^{(a)}(n,T)$ are given by relations

$$K_{ci}^{(ab)}(n,T) = \int_0^\infty v\sigma_{ci}^{(ab)}(n,E)f(v;T)dv, \tag{4}$$

$$K_{ci}^{(a)}(n,T) = \int_0^{E_{max}^{(a)}(n)} v\sigma_{ci}^{(a)}(n,E)f(v;T)dv \tag{5}$$

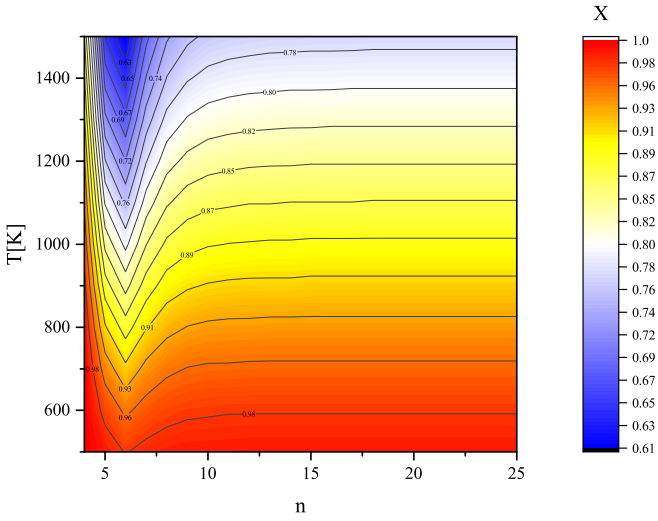

Figure 2. The ratio X of the partial rate coefficient $K_{ci}^{(a)}(n,T)$ Eq. (4) and total ones $K_{ci}^{(ab)}(n,T)$ Eq. (3) for chemi-ionization processes (1) and (2).

where the cross-sections $\sigma_{ci}^{(a,ab)}(n,E)$ are determined as in [6], $E_{max}^{(a)}(n)$ is the upper limit of the region of E relevant for the associative ionization process (1) (see [5, 6, 7]), and $f(v;T) = f_{cell}(v;T)$ is Maxwell distribution function. The rate coefficient $K_{ci}^{(b)}(n,T)$ for the process (2) is determined from the Eq. (3).

2.Results and discussion

We calculate the partial $K_{ci}^{(a)}(n,T)$, $K_{ci}^{(b)}(n,T)$ and total chemi-ionization rate coefficients $K_{ci}^{(ab)}(n,T)$, for the extended regions of principal quantum numbers $n \geq 4$ and temperatures 500 K $\leq T \leq$ 1500 K. Fig. 1 present the surface plot of total chemi-ionization rate coefficient $K_{ci}^{(ab)}(n,T)$ for all mentioned conditions. One can see that the rate coefficient $K_{ci}^{(ab)}(n,T)$ has the maximum at $n = 6$. For lower quantum numbers n the rate coefficients strongly depend on the temperature.

The relative contribution of the associative channel (1), is presented by Fig. 2. It can be noticed that in the considered regions of n and T the associative chemi-ionization (1) dominates in comparison with the non-associative chemi-ionization channel (2). Unlike the symmetric case, in the non-symmetric one associative channel changes non-monotonically with a maximum displaced to the region of small values of n.

3.Conclusions and perspectives

The rate coefficients for the chemi-ionization processes in $Li^*(n) + Na$ collisions were calculated. The results of this work confirm the possibility of application of the resonant mechanism [8] for the description of chemi-ionization collision processes, not only in the case, when the particles of the same type collide (symmetric case), but for the case of different type (non-symmetric) too.

In the near future we aim to further investigate the chemi-ionization processes and develop completely quantum-mechanical methods of their description which could be applied in the cases of extremely low temperatures.

This work is partially supported by Ministry of Education, Science and Technological Development of the Republic of Serbia under the grants III 44002, and 176002.

REFERENCES

[1] Lj. M. Ignjatović, A. A. Mihajlov, and A. N. Klyucharev, J. Phys. B 41, 2, 025203 (2008)

[2] C. Yubero, M. S. Dimitrijević, M. C. Garcia and M. D. Calzada, Spectrochim. Acta B, 62, 2, 169 (2007)

[3] A. N. Klyucharev, N. N. Bezuglov, A. A. Matveev, A. A. Mihajlov, Lj. M. Ignjatović and M. S. Dimitrijević , New Astron. Rev., 51, 7, 547 (2007).

[4] Y. N. Gnedin, A. A. Mihajlov, Lj. M. Ignjatović, N. M. Sakan, V. A. Srećković, M. Y. Zakharov, N. N. Bezuglov and A. N. Klycharev, New Astron. Rev. 53, 7-10, 259 (2009)

[5] Lj. M. Ignjatović and A. A. Mihajlov, Phys. Rev. A, 72, 2, 022715 (2005)

[6] A. A. Mihajlov, V. A. Srećković, Lj. M. Ignjatović and A. N. Klyucharev, J. Clust. Sci., 23, 1, 47-75 (2012)

[7] A. A. Mihajlov, V. A. Srećković, Lj. M. Ignjatović, Z. Simić and M. S. Dimitrijević, J. Phys. Conf. Ser., 810, 1, 012058 (2017)

[8] P. O'Keeffe, P. Bolognesi, L. Avaldi, A. Moise, R. Richter, A. A. Mihajlov, V. A. Srećković and Lj. M. Ignjatović, Phys. Rev. A, 85, 5, 052705 (2012)

STRONG SOLAR X-RAY RADIATION: INFLUENCE ON THE PLASMA IN THE IONOSPHERIC D-REGION

V. A. Srećković[1] and D. M. Šulić[2]

[1] *Institute of Physics, University of Belgrade, P.O. Box 57 11001, Belgrade, Serbia*
[2] *Union Nikola Tesla University, Belgrade, Serbia*

Abstract. Solar flare X-ray energy can cause strong enhancements in the electron density in the Earths atmosphere. This intense solar radiation and activity can cause sudden ionospheric plasma disturbances. The focus of this contribution is on the study of these changes induced by solar X-ray flares using narrowband Very Low Frequency (VLF, 3-30 kHz) and Low Frequency (LF, 30-300 kHz) radio signal analysis. The model computation is applied to obtain the electron density enhancement induced by the intense solar radiation.

1. INTRODUCTION

Lower ionosphere monitoring by the mean of the radio technique can play a crucial role for a better understanding of space weather conditions [1]. The plasma in the ionospheric D-region (50 km $\leq h \leq$ 90 km) is a very sensitive medium to external forcing like moderate solar influence, stellar explosive radiation, etc. [2, 3]. Processes like solar emission in far-UV and extreme-UV regions strongly affect the Earths atmosphere [4, 5]. This intense solar radiation and activity can cause sudden ionospheric disturbances (SIDs) and further create ground telecommunication interferences, blackouts (see [6]).

2. ANALYSIS AND RESULTS

In this contribution we analyse the amplitude and phase data of Very Low Frequency (VLF, 3 - 30 kHz) and Low Frequency (LF, 30 - 300 kHz) radio signals emitted by worldwide transmitters during SIDs. All the data were recorded at the Belgrade site with two receiver systems: Absolute Phase and Amplitude Logger (AbsPAL) system [7] and Atmospheric

Weather Electromagnetic System for Observation Modeling and Education (AWESOME) [2]. The analysis and comparison of VLF data has been carried out together with the examination of the corresponding solar X-ray fluxes. The intensity of the solar X-ray flux is taken from the database of the GOES satellites (Geostationary Operational Environmental Satellite).

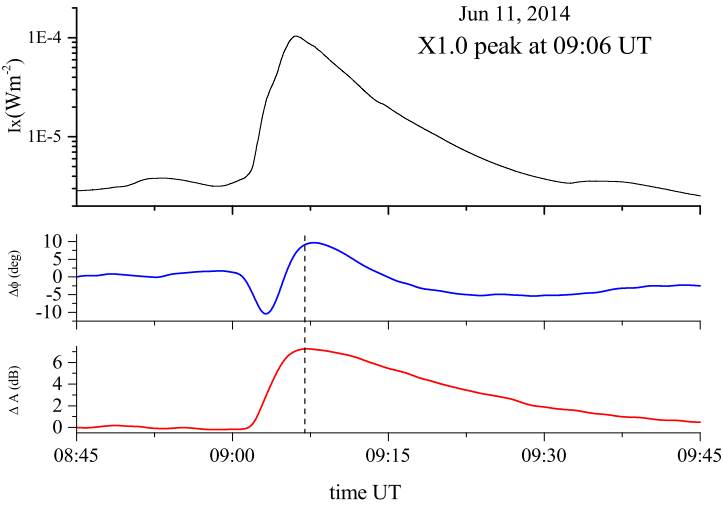

Figure 1. Variation of the X-ray irradiance, phase and amplitude in the GQD/22.10 kHz radio signal (in universal time) recorded at Belgrade on 11 Jun 2014.

2.1 SIGNAL MONITORING

Observations of amplitude (A) and phase (ϕ) in VLF/ LF signals during solar flares could be applied for investigations of the perturbed ionospheric plasma. The perturbation of the amplitude was estimated as a difference between values of the amplitude induced by some sudden event and amplitude in the normal ionospheric condition: $\Delta A = A_{\text{per}} - A_{\text{nor}}$. Here 'per' means the perturbed and 'nor' means normal condition. In the same way the perturbation of phase was estimated as $\Delta\phi = \phi_{\text{per}} - \phi_{\text{nor}}$. During the occurrence of solar flares, classified as a minor and small flare up to the C3 class[1], the amplitude of the VLF/LF signals does not have significant perturbations. A solar flare in the range from C3 to M3 classes induced an increase of the amplitude, which corresponds nearly proportional to the logarithm of the X-ray irradiance maximum [2, 8].

[1] `https://www.nasa.gov/mission_pages/sunearth/news/classify-flares.html`

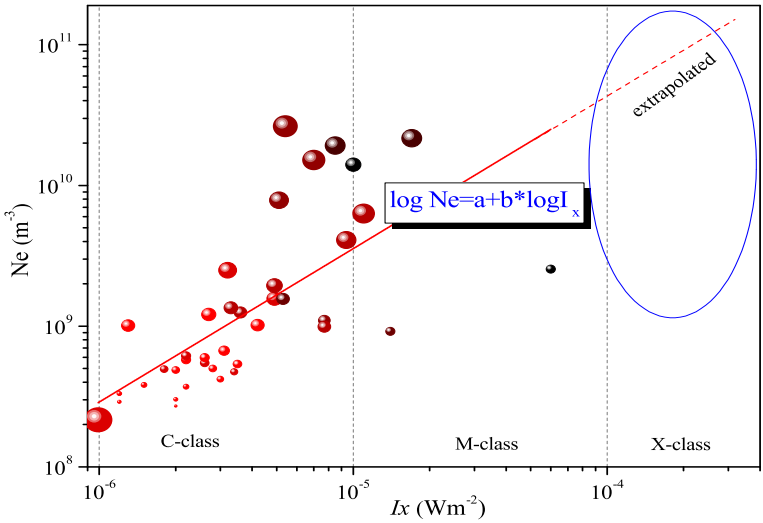

Figure 2. Electron density at height h = 74 km during flare occurrences, as a function of maximal intensity of X-ray flux. Electron density is calculated on the basis of VLF/LF propagation data recorded at Belgrade for one year. The size of the point is proportional to the amplitude change while the color depends on the phase change (the darker color indicates a larger phase change). The red line indicates linear fit and red dashed line extrapolation to stronger solar flares.

2.2 PERTURBATIONS ON RADIO SIGNAL INDUCED BY STRONG SOLAR FLARES

For studding SID VLF/LF signatures we have selected strong solar flare event whose occurrence was in time interval of few hours around local noon at Belgrade. The selected event X1.0 class solar flare was recorded on 11 Jun 2014. Our results are presented in Fig. 1. Perturbations of the GQD/22.10 kHz radio signal are presented as temporal changes of ΔA and $\Delta\phi$ during solar flare event. Fig 2. presents electron density at height h = 74 km during flare occurrences, as a function of the maximal intensity of X-ray flux. Electron density is calculated (as in [8]) on the basis of VLF/LF propagation data recorded at Belgrade for one year. From the figures we conclude:

- Changes of the phase and amplitude of radio signals during X class solar flares exibit as well defined enhancements that follow the development of the maximum in X-ray radiation.
- After occurrences of such strong solar flares the amplitude recovers

bit slower than the phase.

- Using linear fits and extrapolations we can estimate the values of electron density even for larger solar X-ray flares (oval marked area) on the base of statistical analysis.

3. CONCLUSIONS

In this contribution the effects during the enhancements of X-ray flux due to solar flares, on the propagating radio signal have been studied. The presented examples (Figs. 2 and 3) are used to qualitatively describe consequences of SIDs, during occurrences of such strong solar flares. The obtained results confirmed the successful use of applied technique for detecting space weather phenomena such as solar explosive events as well for describing and further modeling the ionospheric plasma which are important as the part of electric terrestrial-conductor environment.

This work is partially supported by Ministry of Education, Science and Technological Development of the Republic of Serbia under the grants III 44002, and 176002.

REFERENCES

[1] A. P. Mitra 1974, *Ionospheric Effects of Solar Flares*. eds. D.Reidel, Holland.

[2] D. M. Šulić & V. A. Srećković, Serb. Astron. J., 188, 45 (2014)

[3] A. Nina, V. M. Čadež, V. A. Srećković and D. Šulić, Balt. Astron., 20, 609 (2011)

[4] V. A. Srećković, A. A. Mihajlov, Lj. M. Ignjatović and M. S. Dimitrijević, Adv. Space Res., 54, 1264 (2014)

[5] A. A. Mihajlov, L. M. Ignjatović, V. A. Srećković, M. S. Dimitrijević & A. Metropoulos, Mon. Notices Royal Astron. Soc., 431, 589 (2013)

[6] M. Radovanović, J. F. P. Gomes, A. A. Yamashkin, M. Milenković & M. Stevančević, J. Geogr. Inst. Cvijic, SASA, 67(2), 213 (2017).

[7] D. M. Šulić, V. A. Srećković & A. A. Mihajlov, Adv. Space Res., 57, 1029 (2016)

[8] V. A. Srećković, D. M. Šulić, V. Vujčić, D. Jevremović and Y. Vyklyuk, J. Geogr. Inst. Cvijic, SASA, 67, 3 (2017)

THE ANOMALOUS ABSORPTION UNDER THE DECAY INSTABILITY OF X-MODE PUMP WAVE IN A PLASMA FILAMENT

A. B. Altukhov[2], V. I. Arkhipenko[1], A. D. Gurchenko[2], E. Z. Gusakov[2], A. Y. Popov[2], L. V. Simonchik[1], P. Tretinnikov[2] and M. S. Usachonak[1]

[1]*Institute of Physics of NAS of Belarus, Minsk, Belarus*
[2]*Ioffe Institute, St-Petersburg, Russia*

Abstract. The paper presents the investigation results of the absorption coefficient evolution during the pump pulse when the X-mode pump wave decay into two upper hybrid resonance plasmons occurs. It's shown that the electron density at presence of the strong anomalous absorption during the pump pulse changed by more than one order of magnitude. Maximal absorption coefficient due to X-mode pump decay in two plasmons is about 85%.

1. INTRODUCTION

It was shown at the Textor tokamak [1] that the second harmonic X-mode heating experiments are accompanied by anomalous backscattering phenomena. Theoretical model proposed recently [2] explains the anomalous backscattering as a result of the two upper-hybrid (UH) plasmons parametric decay (TUHPD) instability which has a very low threshold due to nonlinearly excited plasmons trapping in the vicinity of the density maximum that accompanies the magnetic island. The theory [2] also predicts substantial (up to 25%) anomalous absorption due to this process. The aim of this work is to test the efficiency of the X-mode anomalous absorption associated with the TUHPD leading to excitation of the trapped UH waves. The model experiment is performed in the laboratory plasma.

2. EXPERIMENTAL SETUP AND RESULTS

Plasma filament was created in a glass tube with an internal diameter of 22 mm. The tube was passed through waveguide with cross-section 72×34 mm^2 parallel to the wide walls on the axis of electromagnet (2 on Fig. 1, *a*). The initial plasma was produced in argon (pressure of 1-2 Pa) under forcing of RF power (~100 W, frequency ~27 MHz). The RF power is supplied to the ring electrodes placed outside of the tube and disposed on both sides of the waveguide at a distance of about 30 cm. At the maximal RF power the averaged plasma density

measured using the cavity diagnostics 6 (Fig. 1, *a*) is about 10^{10} см$^{-3}$. It is varying by 15-20% at the changing of the magnetic field from 0 to 45 mT. The X-mode microwave pulses (up to 200 W) were incident onto the plasma along the waveguide 3. As the frequency of the launched waves f_0 = 2.35 GHz is much higher than the upper hybrid (UH) and electron cyclotron resonance (ECR) frequencies, it seems that there were no linear mechanisms of the wave-particle interaction. The temporal behavior of the transmitted and reflected microwave signal as well as the plasma luminosity is monitored in the experiment. The radial distribution of integral plasma emission was registered with CCD-camera UC-14T32 and can be approximated by the function $(1-(r/r_0)^2)^{1.6}$. Assuming the light intensity is proportional to the plasma density, we get the maximal density in the discharge to be about 2×10^{10} см$^{-3}$.

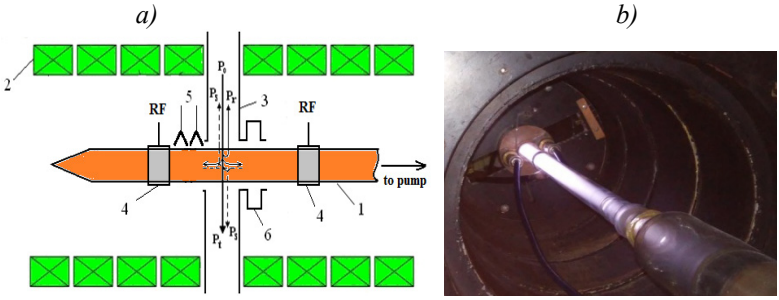

1 – quartz tube; 2 – magnetic system; 3 – waveguide; 4 – RF antenna; 5 – probing wave antenna; 6 – microwave cavity

Fig. 1. Schematic of experimental setup (*a*) and photo of the plasma filament (*b*).

The theoretical model of the low-threshold two-plasmons decay proposed in [3] consists of two parts shown schematically in Fig. 2. Firstly, it is a model of the PDI linear stage describing the absolute instability leading to extra-ordinary t_X-wave decay into two UH plasmons $l_{UH}(f_1)$ and $l_{UH}(f_2)$, which are exponentially growing from the thermal noise level. Secondly, it is a model of the absolute instability nonlinear saturation as a result of cascade of several low-threshold decays in which UH waves l_{UH}' trapped in plasma and low frequency waves (ion sound l_{IS} in the case of our experiment) are excited. The saturation level determines the efficiency of the anomalous absorption.

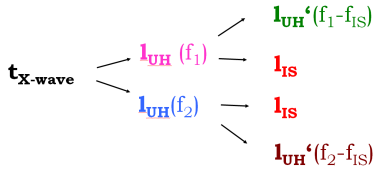

Fig. 2. The scheme of the two-plasmons decay and it's saturation.

The observations of the microwave anomalous absorption at the pump frequency higher than the second electron cyclotron harmonic are performed at the power of 210 W and magnetic field about 35 mT. At a small plasma density no distortions of the microwave pulses are observed neither transmitted through the plasma nor reflected from it (Fig. 3, *a*). The full microwave power balance is

defined as following: $P_0 = P_t + P_r + P_h$, where P_0, P_t and P_r, are incident, transmitted and reflected powers, P_h is a power irradiated through holes in waveguide (see Fig. 1, *a*). The modelling of wave transmission through the waveguide system was performed in HFSS software [4]. The simulation results are presented by stars in Fig. 3, *a* as well. Modelling and experimentally measured power balance shows that power irradiated through holes is about 1-2 W (about 1% of P_0).

However at plasma density exceeding a critical value a fast decrease of both transmitted and reflected power is observed indicating the turning on of the strong anomalous absorption (see Fig. 3, *b*). This effect is accompanied by a

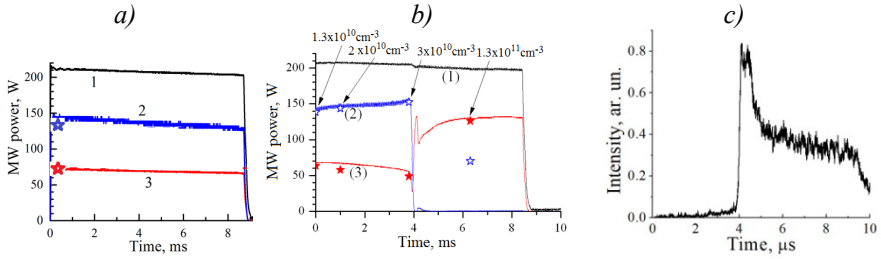

Fig. 3. Waveforms of incident (1), transmitted (2) and reflected (3) pulses and of the plasma luminosity (*c*). *a* –small plasma density, *b* – P_0 = 210 W.

sharp growth of the plasma luminosity shown in Fig. 3, *c*. The time delay of the anomalous phenomena appearance is dependent on the pump power, magnetic field and electron density of initial plasma [3]. The critical density needed for switching on of the anomalous phenomena is growing with decreasing magnetic field and this dependence is close to the theoretical UHR density dependence on the magnetic field for the half pump frequency:

$$n_e = \frac{m}{4\pi e^2}\left(\pi^2 f^2 - \left(\frac{eB}{m_e c}\right)^2\right) \quad (1)$$

For instance, at 40 mT and electron density 10^{10} cm^{-3} the threshold of strong absorption excitation is 20 W.

Using the HFSS software simulations and experimental pulse powers (Fig. 3, *b*), we can estimate the electron density during the pump pulse. In the HFSS model, the plasma filament is supposed to be homogeneous in radial direction and averaged electron density is as a variable parameter to receive an experimental ratio of transmitted and reflected signals (stars in Fig 3, *b*). At the pulse beginning, estimated average concentration is about 1.3×10^{10} cm^{-3} at collision frequency $\nu = 1.4\times10^8$ s^{-1} determined using [5]. It is close to value obtained using MW cavity. Immediately before strong absorption, the estimated average electron density reaches 3×10^{10} cm^{-3}. This concentration growth probably takes place due to collisional MW absorption. After switch on an anomalous absorption at 4th μs, the reflected signal increases. It can be connected with electron concentration growth due to anomalous absorption in result of two-plasmons decay. As it is seen, estimated average electron concentration is about 1.1×10^{11} cm^{-3} at 4.5 μs.

Localization of the microwave absorption region in the radial direction of plasma column is carried out by recording the transverse distributions of the plasma glow intensity with temporal resolution. In Fig. 4, curve 1 presents the light distribution in initial plasma column. Symbols along dashed curve 2 is the experimental profiles at 4th μs. The dashed curve 2 is fitting curve of experimental profiles. After Abel inversion, we obtain the profile 3 with two maxima close to half radius.

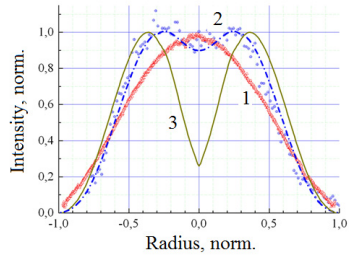

Fig. 4. Light intensity profiles.

Let's determine the efficiency of the microwave power absorption under conditions of upper hybrid resonance for half pump frequency. In the full microwave power balance, we should add power P_{abs} absorbed by plasma: $P_0 = P_t + P_r + P_h + P_{abs}$. Then an absorption coefficient k_{abs} can be expressed as $k_{abs} = 1 - (P_t + P_r + P_h)/ P_0$. It turned out that the absorption coefficient calculated using experimental power balance changes strongly during the pump pulse. It is close to zero (small collisional absorption) from 0 to 4th microsecond, 80-85% at 4th microsecond and about 40-45% after 6th microsecond.

CONCLUSIONS

The strong anomalous absorption of the microwave power is observed in the plasma filament at the density close to the UHR value for the half pump frequency by means of optical and microwave diagnostics. The threshold and growth rate of the anomalous phenomena are shown to agree with the theory results. Its dependence on magnetic field and microwave power are shown to be close to the theoretical predictions for the two-plasmon decay. The observed anomalous absorption of about 85% demonstrates the importance of this phenomenon consideration in the planning of microwave heating experiments on large installations.

The work was performed under support of the BRFBR under grant F18R-040 and RFFR under grant 18-52-00010 Bel_a.

REFERENCES

[1] S.K. Nielsen, M. Salewski, et al., Plasma Phys. Control. Fusion, 55, 115003 (2013).

[2] E.Z. Gusakov and A.Yu. Popov, Physics of Plasmas, **23,** 082503 (2016)

[3] A. Altukhov, et. al., EPJ Web of Conferences, 157, 03050 (2017).

[4] http://www.ansys.com/Products/Simulation+Technology/Electromagnetics/High-Performance+Electronic+Design/ANSYS+HFSS.

[5] http://www.laplace.univ-tlse.fr/Download/?lang=fr for BOLSIG+ 2005.

The Workshop on X-ray Interaction with Biomolecules in Gas Phase (XiBiGP)

NITROIMIDAZOLE FRAGMENTATION: A STORY OF ENERGY BARRIERS AND METASTABLE PROCESSES

Jacopo Chiarinelli

Università degli Studi RomaTre, Roma, Italy
CNR-ISM, Area della Ricerca di Roma1, Monterotondo Scalo (Roma), Italy

Nitroimidazoles are used in radiotherapy as radiosensitisers [1]. The knowledge of their physical-chemical properties and decomposition under photon irradiation allows a deep knowledge of their working principles, paving the way to a full exploitation of their potential applications. The combination of several experimental approaches, such as time of flight mass spectrometry (TOF-MS), photoelectron-photoion coincidence (PEPICO) experiments, measurement of the appearance energy (AE), and theoretical calculations have allowed to describe the most relevant photo-fragmentation paths of nitroimidazole isomers (2-, 4/5-nitroimidazole) in the vacuum ultra-violet range [2,3]. Interesting differences, that can reflect and explain the effectiveness of the different isomers as radiosensitisers, are found in the fragmentation pathways. Analysis of the peaks lineshapes in the mass spectra reveals also the presence of several metastable processes leading to the most relevant fragments. In some cases, the simulation of the time of flight measurement supported by theoretical predictions of the energy partition functions allows to reproduce the asymmetric line-shape and to extract an estimate of the dissociation rate [4].

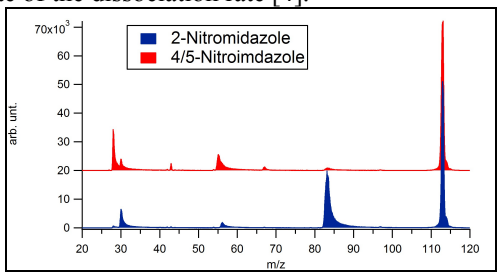

Figure 1. TOF-MS of 2 and 4/5 nitroimidazole

REFERENCES

[1] R. Baskar et al Int. J. Med Sci. 9, 193, 2012
[2] P. Bolognesi et al J. Chem. Phys. 145, 191103, 2016
[3] A. Cartoni et al J. Chem. Phys. A, 122 (2018) 4031
[4] B. Sztaray et al J. Mass Spectrom. 45 ,1233, 2010

PHOTOELECTRON SPECTROSCOPY AND DICHROISM OF SMALL BIOMOLECULES AND CLUSTERS USING ELECTRON/ION COINCIDENCE TECHNIQUES

Gustavo A. García[1]

[1]*Synchrotron SOLEIL, St. Aubin BP 48, 91192 Gif sur Yvette, France*

Despite the general title, two highly relevant and specific biological processes will be addressed. First, I will show how gas-phase data on the photoelectron anisotropy parameter of size-selected water clusters, recently recorded in VUV synchrotron radiation experiments,[1] can help parametrizing models of electron transport in liquid water, which plays a significant role in processes such as radiation damage. The second example concerns a gas-phase study on the interplay between conformational and configurational chirality in a model diol system using photoelectron circular dischroism[2] as the chiroptical probe. Through the use of theoretical models, it is seen that the former dominates the chiral response, so that induced conformational chirality could be a dominant factor in chiral molecular recognition even in small systems.[3]

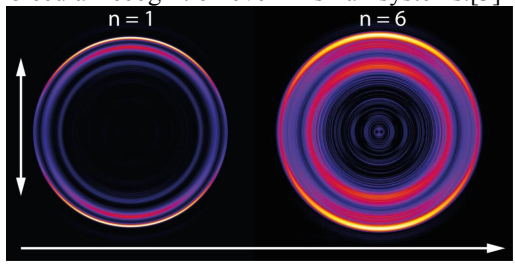

Figure 1. Reconstructed experimental photoelectron velocity map images recorded at hν = 24 eV of (a) the gas phase monomer and (b) the $(H_2O)_6$ water cluster showing the three outermost valence orbitals (See ref. [1]).

REFERENCES

[1] S. Hartweg *et al.*, "*Size-Resolved Photoelectron Anisotropy of Gas Phase Water Clusters and Predictions for Liquid Water"*, Phys. Rev. Lett. **118,** 103402 (2017)

[2] L. Nahon *et al.*, "*Valence shell one-photon photoelectron circular dichroism in chiral systems"*, J. Electron Spectrosc. Relat. Phenom. **204,** 322 (2015)

[3] S. Daly *et al.*, "*The Interplay Between Conformation and Absolute Configuration in Chiral Electron Dynamics of Small Diols"*, Angew. Chem. Int. Ed. **55,** 11054 (2016)

INTERACTION OF ENERGETIC PHOTONS AND FAST IONS WITH GAS-PHASE DNA

Wen Li[1], Xin Wang[1], Wessel Douma[1], Klaas Bijlsma[1], Ronnie Hoekstra[1], Marwa Abdelmouleh[2], Michal Ryszka[2], Mathieu Lalande[2], Jimmy Rangama[2], Violaine Vizcaino[2], Jean-Christophe Poully[2] and Thomas Schlathölter[1]

[1]*Zernike Institute for Advanced Materials, University of Groningen, Nijenborgh 4, 9747AG Groningen, The Netherlands*
[2]*CIMAP, UMR 6252 (CEA/CNRS/ENSICAEN/Université de Caen Normandie), Caen, France*

In order to improve our understanding of the molecular mechanisms underlying radiation therapy, the interaction of energetic photons and ions with gas-phase biomolecules has been intensively studied for more than 15 years [1]. Most of these studies, both experimental and theoretical, were limited to relatively small DNA building blocks. In 2011, pioneering experiments combined electrospray ionization and radiofrequency ion trapping with synchrotron and ion beamlines [2,3]. The first soft X-ray ionization study of a multiply protonated oligonucleotide proved that key findings obtained with DNA building blocks, such as high stability of nucleobases and fragile nature of deoxyribose, are also found in oligonucleotides. However, the fragmentation patterns are entirely different [4].

As DNA in living cells occurs in de-protonated form, our current experiments focus on oligonucleotide anions. In particular, we study interactions of soft X-rays (at the carbon, nitrogen and oxygen K-edges) and MeV carbon ions (at Bragg peak energies) with oligonucleotides of different structure (single and double stranded, G-quadruplex). For all systems under study, electron detachment is the dominant channel. For soft X-ray absorption, positive fragments are only observed for small oligonucleotides such as the telomeric sequence dTTAGGG. MeV carbon ions on the other hand, also lead to formation of small positive fragments when colliding with duplex DNA.

REFERENCES

[1] G. García and M. C. Fuss (Eds.), *Radiation damage in biomolecular systems*, (Springer, Netherlands, 2012).
[2] A. R. Milosavljević et al., Phys. Chem. Chem. Phys. 13, 15432 (2011)
[3] S. Bari et al., J. Chem. Phys. 134, 024314 (2011)
[4] O. Gonzalez-Magaña et al. , J. Phys. Chem. A 87, 032702 (2013)

COMPUTATIONAL STUDY OF THE FRAGMENTATION DYNAMICS OF BARE AND NANOSOLVATED PROTONATED LEUCINE-ENKEPHALINE PEPTIDE ION

A. Martin-Somer,[1] J. González-Vázquez,[1] M. Alcamí,[1] I. Corral[1]

[1]*Universidad Autónoma de Madrid, Madrid, Spain*

We report a comparative theoretical and experimental study on the photo-induced fragmentation of protonated leucine-enkephalin (Leu-Enk: YGGFL). Tandem mass (MS^2) spectrum of nanosolvated $[Leu\text{-}Enk\text{-}H\text{-}3H_2O]^+$ obtained after peptide ion exposition to vacuum UV light (VUV), shows an incredible influence of the water molecules into the backbone fragmentation pattern, while no significant changes are observed in the peptide structure by addition of the water molecules. This suggests that new fragmentation pathways are open up (for the same photon energy) by the presence of the water.

With the aim of investigating the fragmentation dynamics of both systems, we have carried out two kind of dynamical simulations. As a first approach to the problem, we have used direct dynamics simulations[1] on which $[Leu\text{-}Enk\text{-}H]^+$ ion is activated by uniformly distributing a fixed amount of energy through its vibrational modes and eventually dissociates. These simulations have allowed establishing the fragmentation pattern for statistical dissociation and how this pattern varies as a function of the ion's internal energy. The main fragment ions observed in the MS^2 spectrum are found with the dynamics simulations and thus the origin and fragmentation mechanisms of these fragments have been rationalized at a molecular level.

Since the experiments consists on activation of the ion by irradiation with VUV light. we also performed nonadiabatic molecular dynamics simulations starting from the excited state in order to study ion's relaxation from the excited state. The comparison of the output of these two kinds of simulations has allowed deciphering how the fragmentation pattern changes from vibrational excitation to electronic excitation and the fragmentation mechanisms.

Acknowledgements: This work is supported by support by the Comunidad Autońoma de Madrid and Universidad Autónoma de Madrid under Grant 2016-T2/IND-1660. We also aknowledge allocation of computing time at the CCC.

Photoelectron spectroscopy of solvated proteins at the PLEIADES beamline

C. Nicolas[1], J.-M. Guigner[2], M.-A. Hervé du Penhoat[2], A. Touati[2], S. Nandi[1], A. R. Milosavljević[1], J. Bozek[1], D. Ceolin[1], J. Palaudoux[3], L. Marichal[4], J.-P. Renault[4]

[1] Synchrotron SOLEIL, Saint Aubin - BP 48, 91192 Gif-sur-Yvette cedex, France
[2] Institut de Minéralogie, de Physique des Matériaux et de Cosmochimie, Sorbonne University, UMR CNRS 7590, MNHN, IRD UR 206, 75252, France
[3] Sorbonne Université, CNRS UMR 7614, Laboratoire de Chimie Physique-Matière et Rayonnement, 4 place Jussieu, F-75252 Paris Cedex 05, France
[4] LIONS, NIMBE, CEA, CNRS UMR 3685, Université Paris-Saclay, CEA Saclay, 91191 Gif-sur-Yvette Cedex, France

The technique of in vacuum liquid micro-jet was introduced by Faubel and co-workers [1]. A few micrometer-thick liquid jet is produced in a vacuum chamber by pushing a liquid sample through a narrow glass capillary at high backing pressure resulting in thin jet of the liquid sample exposed to the vacuum conditions. With this system, volatile liquids, such as water and solutes in water, can be studied using typical soft x-ray techniques. Electron spectroscopy experiments using liquid microjets are now available at many synchrotron facilities, such as at BESSY [2], MAX-LAB [3], SLS [4], ALS [5] and LNLS. Electron spectroscopic studies [2,6] have already been carried out on water, metallic salts solution, small biomolecules and even solution of nanoparticles. With the new liquid jet implemented at the PLEIADES beamline, we performed electron spectroscopy studies on bovine serum albumin protein in solution (40mg/ml). The results will be presented, as well as the behavior of the protein after passing through the capillary and been irradiated.

Acknowledgements: This work is partially supported the grant ANR-17-CE30-0017.

REFERENCES

[1] M. Faubel, *et al.*, ZEITSCHRIFT FUR Phys. D-ATOMS Mol. Clust. 10, 269 (1988).
[2] B. Winter and M. Faubel, Chem. Rev. 106, 1176 (2006).
[3] H. Bergersen, *et al.*, J. Phys. Condens. Matter 19, 326101 (2007).
[4] G. Olivieri, *et al.*, J. Electron Spectros. Relat. Phenomena 216, 1 (2017).
[5] D. E. Starr, *et al.*, Phys. Chem. Chem. Phys. 10, 3093 (2008).
[6] M. A. Brown, *et al.* Annu. Reports Sect. "C" 105, 174 (2009).

CORE-HOLE-STATE DYNAMICS IN AQUEOUS HISTIDINE DURING RESONANT INELASTIC X-RAY SCATTERING PROCESS

J. Niskanen[1,2], S. Eckert[2], R. M. Jay[2], P. S. Miedema[2], M. Fondell[2], B. Kennedy[2], W. Quevedo[2], M. Ianuzzi[4] and A. Föhlisch[2,3]

[1]*University of Turku, Turku, Finland*
[2]*Helmholtz Zentrum Berlin für Materialien und Energie, Berlin, Germany*
[3]*Universität Potsdam, Potsdam, Germany*
[4]*University of Zürich, Zürich, Switzerland*

Abstract. Resonant inelastic X-ray scattering (RIXS) is an element-specific and atomic-site-selective process used for spectroscopy. Owing to the two dipole transitions involved (core-level absorption and core-level emission of a photon), the RIXS spectra at a chosen K-shell resonance reflect the p-density of states around the site of excitation. This localization of the core-hole allows using RIXS spectroscopy for site-specific studies of local valence structure and its changes for second-row elements. The relative ease of interpretation of RIXS in the "electronic-loss regime" (ELR), at least when compared to resonant Auger decay, is somewhat counteracted by the low fluorescent yield of the decay process.

We will present the principles of measuring RIXS spectra in the ELR from liquids, and an orbital-based model for evaluating such spectra. We will also touch the information that could be obtained from such experiments in the quasielastic spectral features ("vibrational-loss regime"; VLR). In the end of the contribution we present our recent work on amino acid histidine [1], where we utilized RIXS in the ELR. We find the core-hole-induced dynamics of the protons to affect the spectra, which we pinpoint by applying the aforementioned model. We find intermolecular interaction to be a prerequisite for this dynamics for the model to explain the findings. As this dynamics is the driving force for lines in the VLR, we conclude that the ground-state potential energy landscape seen by the protons in aqueous amino acids may be a feasible research case for high-resolution RIXS.

REFERENCES

[1] S. Eckert, J. Niskanen, R. M. Jay, P. S. Miedema, M. Fondell, B. Kennedy, W. Quevedo, M. Ianuzzi and A. Föhlisch, Physical Chemistry Chemical Physics **19**, 32091-32098 (2017).

FEMTOSECOND TIME-RESOLVED SPECTROSCOPY OF SOME BIOLOGICAL MOLECULES

Oksana Plekan

Elettra-Sincrotrone Trieste, Strada Statale 14-km 163, 5, I-34149 Basovizza, Trieste, Italy

Femtosecond time-resolved experiments seek to provide an answer to very fundamental questions concerning the foundation of all chemical reaction, such as how atoms move when chemical bonds break, or what are the pathways of light-induced atomic motion in molecules. Free-electron lasers (FELs) have emerged as new powerful tool in this quest because of their unique features such as: ultrashort pulse duration, element and site selectivity, wavelength tunability (EUV and XUV range) temporal and transverse coherence, polarization control and high peak power. The fact that FELs can generate an output with a much higher spectral brightness and coherence than synchrotrons makes these sources very important for a number of applications, such as atomic and molecular physics, ultrafast X-ray science, advanced material studies, biology and medicine [1]. With the advent of the short wavelength FELs, the dream of exploring atomic and molecular phenomena on their own spatial (tenths of ångströms) and temporal scale (few femtoseconds) has become real.

Here, we present experimental data related to investigations of ultrafast phenomena of some isolated biomolecules (acetylacetone, thymine and 5-bromouracil) by FELs-based time-resolved spectroscopy [2, 3]. This class of spectroscopy is based on pump-probe techniques, where an optical pump pulse excites a sample and a probe pulse is used for probing the sample after an adjustable delay time.

Acknowledgements: The results of these studies have been originated from the joint effort of many international laboratories and a large number of researchers [2, 3], whose work is gratefully acknowledged.

REFERENCES

[1] L. Young et al. J. Phys. B: At. Mol. Opt. Phys. 51, 032003 (2018).
[2] R. J. Squibb et al. Nature Communications 9, 63 (2018).
[3] T. J. A. Wolf et al. Nature Communications 8, 29 (2017).

COMPUTATIONAL TOOLS FOR STUDYING X-RAY – MOLECULE INTERACTIONS: PHOTOFRAGMENTATION OF HALOTHANE

M. Radibratović[1], S. D. Tošić[2], M.C. Castrovilli[3], J. Chiarinelli[3,6], P. Bolognesi[3], L. Avaldi[3], R. Richter[4], M. Coreno[3,4], B. P. Marinković[2] and M. K. Milčić[5]

[1]*ICTM – Center for Chemistry, UB, Njegoševa 12, 11000 Belgrade, Serbia*
[2]*Institute of Physics Belgrade, UB, Pregrevica 118, 11080 Belgrade, Serbia*
[3]*Istituto di Struttura della Materia-CNR (ISM-CNR), Area della Ricerca di Roma 1, Monterotondo Scalo, Italy*
[4]*Elettra-Sincrotrone Trieste, Area Science Park, Basovizza, Trieste, Italy*
[5]*UB, Faculty of Chemistry, Studentski trg 12-16, Belgrade, Serbia*
[6]*Università degli Studi RomaTre, Roma, Italy*

Halothane ($C_2HBrClF_3$), one of the most commonly used halogenated anesthetics, play a significant role in the destruction of the earth's ozone layer [1]. Photofragmentation experiments in the VUV and soft X-ray energy regions performed at Elettra synchrotron have shown that the mass spectra of halothane is dominated by lighter mass fragments. To explain the experimental findings extensive computational studies were conducted. Low level, but fast and accurate self-consistent charge density-functional tight-binding (SCC-DFTB) theoretical method was employed to simulate the fragmentation of singly and doubly charged halothane ions from their ground state electron configurations at different temperatures. A number of fragmentation paths were simulated producing almost all fragments found in the mass spectra. For the main fragmentation pathways, the minima and the transition states on the potential energy surface were described with more accurate computational methods.
In order to obtain a better insight in the photofragmentation pathways nonadiabatic dynamics simulations were conducted using trajectory surface hopping method (Newton-X program), combined with TD-DFT (Gaussian09) and MCSCF (Columbus) electronic structure methods. The results have shown the relevance of the cation excited states in the photofragmentation processes.

Acknowledgements: Work partially supported by the MESTDRS (Grant Numbers 172065, 171020) and MAECI Serbia–Italy Joint Research Project "A nanoview of radiation-biomatter interaction".

REFERENCES

[1] A. C. Brown et al., Nature 341 (1989) 635.

OXYGEN K-SHELL SPECTROSCOPY OF ISOLATED BARE AND SOLVATED PEPTIDE

M. Lj. Ranković [1, 2], A. R. Milosavljević [3], K. Jänkälä [4], F. Canon [5], J. Bozek [3], C. Nicolas [3] and A. Giuliani [3, 6]

[1]*Institute of Physical Chemistry J. Heyrovsky, Czech academy of sciences, Dolejškova 3, 18223 Prague 8, Czech Republic*
[2]*Institute of Physics Belgrade, University of Belgrade, Pregrevica 118, 11080 Belgrade, Serbia*
[3]*SOLEIL, l'Orme des Merisiers, St Aubin, BP48, 91192 Gif sur Yvette Cedex, France*
[4]*Nano and Molecular Systems Research Unit, University of Oulu, P.O. Box 3000, 90014 Oulu, Finland*
[5]*INRA, UMR1324 Centre des Sciences du Goût et de l'Alimentation, F-21000 Dijon, France*
[6]*INRA, UAR1008, CEPIA, Rue de la Géraudière, BP 71627, 44316 Nantes, France*

The possibility to bring large macromolecules in the gas phase using the electrospray ionization technique along with mass spectrometry tools and synchrotron radiation sources, allows one to probe physicochemical properties of such systems. Since the complex interaction of natural surrounding water network plays a crucial role at molecular level [1], it is of great importance to study the hydration effects of peptides and proteins on both their electronic and spatial structure, in order to give more insights into radiation damage.
Recently, A. Milosavljević and coworkers demonstrated a pioneering studies of a protein in the gas phase, by coupling a VUV [2] and soft X-ray [3] synchrotron beamlines with the linear quadrupole ion trap mass spectrometer. In this talk, we will present the results from one of the following studies of hydrated SubstanceP peptide in the Oxygen K-shell energy region, performed at soft X-ray beamline PLEIADES of SOLEIL radiation facility near Paris, with focusing on the experimental techniques and details of the applied method.

Acknowledgements: This work was supported by ANR, France, under project ANR-08-BLAN-0065, MESTD of Republic of Serbia project #171020. We are grateful to SOLEIL general staff for running the beam smoothly.

REFERENCES

[1] O. Dopfer et al, *Chem. Rev*. **116**, 9 (2016).
[2] A. R. Milosavljević et al, *J. Synchrotron Radiat.* **19**, 2 (2012).
[3] A. R. Milosavljević et al, *J. Phys. Chem. Lett.* **16,** 6 (2015).

IONS AND MOLECULES AT THE WATER INTERFACE: A SPECTROSCOPIST'S VIEW OF SOLVATION

C. M. Saak[1], I. Unger[1], G. Gopakumar[1], C. Richter[2], J. Werner[1], C. Caleman[1] and O. Björneholm[1]

[1]*Uppsala University, Box 516, SE-751 20 Uppsala*
[2]*IOM, Permoserstr. 15, 04318 Leipzig, Germany*

Water interfaces are central to biology and the environment, from cell membranes to atmospheric aerosols. Interfaces present a complex and asymmetric environment, allowing for a diverse and rich set of behaviours and chemistry to occur [1]. However, due to their complexity, there remain many fundamental questions that are still poorly understood. For example, the origins and relative contributions of the various driving forces behind surface enrichment and ion pair formation at the interface are yet to be fully unravelled [2].

Here, we use liquid-jet X-ray photoelectron spectroscopy (XPS), a surface-sensitive experimental technique, to study the behaviour of biologically-relevant organic molecules such as amines, alcohols [3] [4], carboxylic acids [5] and amino acids, solvated at the water-air interface. Specifically, we probe the surface enrichment of these organics as a function of bulk concentration as well as the effect of inorganic salts such as sodium chloride on this enrichment. From these data we observe a significant degree of ordered monolayer formation by long-chain molecules [3] and that the intermolecular interactions between the solutes are enhanced due to reduced dielectric screening at the water-air interface.

Acknowledgements: This work is supported by STINT and VR. We thank HZB and SOLEIL for the allocation of beamtime at their facilities.

REFERENCES

[1] O. Björneholm, et al., *Chem. Rev.*, **116**, 13, 7698–7726, (2016)
[2] J. S. Hub, et al., *PCCP*, **14**, 27, 9537–45, (2012)
[3] M.-M. Walz, et al., *PCCP*, **18**, 9, 6648–6656, (2016)
[4] M.-M. Walz, et al., *PCCP*, **17**, 21, 14036–14044, (2015)
[5] N. Ottosson, et al., *PCCP*, **13**, 26, 12261–7, (2011)

Shining (synchrotron-) light on nanoparticles

R. Schürmann[1,2], T. T. Meiling[1], S. Vogel[1,2], K. Ebel[1,2], C. Nicolas[3], A. R. Milosavljević[3] and I. Bald [1,2]

[1] *Institute of Chemistry, University of Potsdam, 14476 Potsdam-Golm, Germany*
[2] *Federal Institute of Material Research and Testing, 12489 Berlin, Germany*
[3] *Synchrotron SOLEIL, L'Orme des Merisiers, Saint Aubin, BP 48, 91192 Gif-sur-Yvette Cedex, France*

Synchrotron X-ray photoelectron spectroscopy (XPS) experiments are a promising attempt to gain new insights into the photophysical and chemical properties of nanoparticles (NPs). XPS measurements on a beam of isolated gold and carbon NP-clusters have been performed at the PLEIADES beamline at the Synchrotron SOLEIL [1]. Fluorescent N-doped CNPs, synthesized in our lab, allow a precise tuning of the photoluminescence quantum yield (PLQY) up to 90%, depending on the experimental conditions [2]. Strong differences in the PLQY of CNPs with similar precursor materials and elemental composition have been observed. By monitoring the chemical species present in the core and on the surface with XPS, the origin of the PLQYs can be better understood.

Furthermore, plasmonic AuNPs equipped with 4-nitrothiophenol (4-NTP) and citrate as surface capping agents have been studied. 4-NTP is a widely used molecule to study hot electron induced reactions on NPs [3]. In order to evaluate the role of available states in the plasmon mediated electron transfer reaction, the valence band states of 4-NTP decorated AuNPs have been determined. Due to the use of an isolated beam of NPs in the XPS measurements, the X-ray damage of the molecules is prevented and the work function of the NP system can be determined. The opportunities and challenges of the experimental approach will be discussed to evaluate its potential to obtain a comprehensive understanding of the photophysics of NPs.

REFERENCES

[1] O. Sublemontier, C. Nicolas, D. Aureau, M. Patanen, H. Kintz, X. Liu, M.-A. Gaveau, J.-L. Le Garrec, E. Robert, F.-A. Barreda, A. Etcheberry, C. Reynaud, J. B. Mitchell and C. Miron, J. Phys. Chem. Lett., 5, 3399 (2014)
[2] T. T. Meiling, R. Schürmann, S. Vogel, K. Ebel, C. Nicolas, A. R. Milosavljević and I. Bald, J. Phys. Chem. C, 122, 10217 (2018)
[3] R. Schürmann and I. Bald, Nanoscale, 9, 1951 (2017)

X-RAY ABSORPTION SPECTROSCOPY OF GAS-PHASE BIOMOLECULAR IONS

Lucas Schwob[1], Simon Dörner[1], Kaja Schubert[1], Jean-Christophe Poully[2], Thomas Schlathölter[3] and Sadia Bari[1]

[1]FS-SCS, Deutsches Elektronen-Synchrotron (DESY), Hamburg, Germany
[2] Normandie Univ., ENSICAEN, UNICAEN, CEA, CNRS, CIMAP, Caen, France
[3]Zernike Institute for Advanced Materials, University of Groningen, Groningen, The Netherlands

Over the past decades, peptides and proteins have been investigated in the gas phase using state-of-art electrospray ionization source, ion guiding in radiofrequency electric field and mass spectrometric techniques. In order to shed light on the electronic and structural properties of such biomolecules, VUV and soft X-ray photo-absorption experiments have been carried out to on synchrotron facilities, offering a wide energy range and a high photon flux. In the soft X-ray regime, the resonant photon absorption at the carbon, nitrogen or oxygen K-edges allows to selectively excite or ionize the system. However, due to the large amount of C, N and O in these molecules, the energy deposited upon photon absorption is not localized. Thus, the information retrieved is averaged and the fragmentation pathways appear similar. Getting a deeper understanding on the dissociation processes would require a controlled localization of the energy deposition.

Probing the inner shells of a single sulfur atom within a biomolecule as the one and only excitation site is a promising way to overcome this obstacle. Among the natural amino acids composing the proteins, the methionine and cysteine residues, both containing a sulfur atom, are ideally suited candidates to investigate the processes following a localized excitation in such biomolecular systems. To test this hypothesis, we recently investigated sulfur containing peptides, such as Met-Enkephalin, Cytochrome *c* protein and synthetic peptides to systematically study the influence of the Met residue position, at the BESSYII (HZB, Berlin) and PETRAIII (DESY, Hamburg) synchrotron light sources. The feasibility and outcome of such experiments as well as near edge X-ray fine structure (NEXAFS) and photo-fragmentation pathways around the sulfur L-edge will be discussed.

Author Index

AUTHOR INDEX

D

E

F

G

H

I

J

K

L

M

N

O

P

Q

R

S

T

CIP - Каталогизација у публикацији - Народна библиотека Србије, Београд

537.56(082)
539.186.2(082)
539.121.7(082)
533.9(082)

SUMMER School and International Symposium on the Physics of Ionized Gases (29 ; 2018 ; Beograd)
Contributed Papers & Abstracts of Invited Lectures, Topical Invited Lectures, Progress Reports and Workshop Lectures / 29th Summer School and International Symposium on the Physics of Ionized Gases - SPIG 2018, [Aug. 28 - Sep. 1, 2018, Belgrade] ; editors Goran Poparić ... [et al.]. - Belgrade : Vinča Institute of Nuclear Sciences, University, 2018 (Beograd : Skripta Internacional). - [3], 338 str. : ilustr. ; 24 cm

Tiraž 200. - Str. [3]: Preface / Editors. - Napomene i bibliografske reference uz tekst. - Bibliografija uz svaki rad. - Registar.

ISBN 978-86-7306-146-7

a) Јонизовани гасови - Зборници b) Атоми - Интеракција - Зборници c) Плазма - Зборници
COBISS.SR-ID 267016204